University of Southampton

Faculty of Engineering, Science and Mathematics

Slat Aerodynamics and Aeroacoustics with Flow Control

Andrew K. Wells

Submitted for the degree of
Doctor of Philosophy

September 2007

Abstract

This study primarily investigated the flow and aeroacoustics associated with the slat of a three-element aerofoil in approach conditions. The study assessed importance of several factors and examined their aerodynamic impacts. The factors investigated were aerofoil incidence, slat angle, slat cusp geometry, fixing transition and blowing in the slat cove.

A combination of experimental and computational techniques investigated the factors selected. The experimental work employed PIV, pressure taps, a force balance, flush mounted microphones and an acoustic array. The computational work used DES along with the FW-H acoustic analogy to obtain the far-field directivity.

Tonal features occurred at high incidence and originated at the slat trailing edge, due to the blunt trailing edge and gap, and at the reattachment point. Fixing transition removes the tone at the reattachment point and reduces the slat gap tone at the trailing edge but does not remove the tone generated by the blunt trailing edge. All of the tones found, only occurred at certain slat and wing settings.

Broadband sound was present in all conditions but had a strong dependence on the incidence of the wing. The sound was loudest with the wing at α=5° with a reduction as the wing incidence was increased. The broadband sound also reduced as the slat angle decreased from α_S=23°. The shear incidence angle was a good indicator of the impact of these two factors on the sound generated. Extending the slat cusp reduced the broadband sound at low aerofoil incidence. However, for $\alpha \geq$10° the extension led to increased broadband sound. Neither blowing nor fixing transition had a significant impact on the broadband sound generated by the slat system.

The aerodynamic loads generated by the wing were mainly dependent on the aerofoil incidence. However, other factors did influence the forces generated. Reducing the slat angle increased the lift generated by the wing especially at low aerofoil incidence but the lift to drag ratio was unaltered. At high aerofoil incidence, extending the slat cusp reduced the lift generated. Blowing and fixing transition did not significantly alter the forces generated by the wing.

Acknowledgements

I would like to thank the following people for their assistance throughout this project. David Angland provided assistance with the design and execution of the experimental work. Dr Charlie Williams and Geoff Thomas gave input into the model design and Mike Thomas and Mike Tudor-Pole operated the wind tunnel. Ben Fenech and Al Carballo-Crespo facilitated the array work and Dr Sammie Chan provided further experimental assistance. Professor Xin Zhang, Dr Malcolm Smith and Raj Bissessur have given project guidance with further direction given by Dr Steve Chow and Dr David Sawyers.

Contents

List of Figures

List of Tables

Nomenclature

Alphanumeric Symbols

a	Speed of sound
b	Blowing rate (LPM)
c	Retracted chord length
C_D	Drag coefficient, $D/0.5\rho v^2 c$
C_{Di}	Induced drag coefficient
C_L	Lift coefficient, $L/0.5\rho v^2 c$
C_{LMAX}	Maximum lift coefficient
C_P	Pressure coefficient, $(p - p_0)/\ 0.5\rho v^2$
D	Drag per unit span
E	Total energy
f	Frequency
fn	a function, zero on the integration surface and +ve in the inner zone
F	External force
g	Gravitational force
G	Slat gap
h	Enthalpy
H_F	Flap gap
$H(x)$	Heavyside function, one when x is positive, zero at other times
I	Unit tensor
J	Diffusion
k	Turbulent kinetic energy
K	Conductivity
L	Lift per unit span
L_{TE}	Trailing edge thickness
M	Mach number
n	Velocity scale factor
N	Numerical factor, set as a positive integer
$\hat{n}$	Surface normal vector

O_H	Slat horizontal overlap
O_{HF}	Flap horizontal overlap
O_V	Slat vertical overlap
O_{VF}	Flap vertical overlap
p	Local static pressure
p'	Local acoustic pressure
p_0	Free-stream static pressure
p_{REF}	Reference pressure (0.00002Pa)
p_{RMS}	Root mean squared pressure
P_{ij}	Compressive stress tensor
Q	Q criterion value
Re	Reynolds number based on retracted chord, $\rho vc/\mu$
S	Rate of strain tensor
S_h	Additional heat source
S_m	Additional mass source
St	Strouhal number based on trailing edge thickness, fL_{TE}/u
t	Aerofoil thickness
t	Time
T	Temperature
T_{ij}	Lighthill shear stress tensor
u	Local velocity
u'	Local fluctuating velocity
v	Free-stream velocity
v_n	Normal velocity of acoustic waves
x, y, z	Cartesian coordinates, x +ve downstream, y +ve up, z +ve starboard
y^+	Non-dimensional wall distance

Greek Symbols

α	Aerofoil incidence
α_f	Flap angle
α_s	Slat angle
$\delta(fn)$	Dirac delta, infinite when $fn = 0$, else equal to zero, integrates to one
δ_{ij}	Kronecker delta, equal to one when $i = j$, else equal to zero
∇	Del operator
$\triangle t$	Time step size
$\triangle x$	Grid cell size
ε	Dissipation

θ	Polar coordinate
μ	Viscosity
ρ	Density
σ	Induced drag distribution factor ≥ 1
ς	Lift distribution factor ≥ 1
τ	Stress tensor
ϕ	Shear incidence angle
ω	Turbulence dissipation rate
Ω	Vorticity tensor

Subscripts and Others

A_{eff}	effective value (of A)
A_n	Normal component (of A
A_{2D}	Infinite wing value (of A)
A_{3D}	Finite wing value (of A)
A^T	Transpose (of A)
$\overline{A}$	Vector (A)
$\|A\|$	Magnitude (of A)
$O[A]$	Of the same order as (A)
$\Box^2$	Wave operator

Abbreviations

AR	Aspect ratio
CAA	Computational aeroacoustics
CFD	Computational fluid dynamics
CML	Continuous moldline
DES	Detached eddy simulation
EASM	Explicit algebraic stress model
EET	Energy efficient transport
ESDU	Engineering sciences data unit
FFT	Fast Fourier transform
FW-H	Ffowcs-Williams and Hawking, acoustic analogy
LDA	Laser doppler anemometry
LEBU	Large eddy break up device
LEE	Linearized Euler equations

LES	Large eddy simulation
LPM	Litres per minute
MUSCL	Monotone upstream-centred schemes for conservation laws
NASA	National aeronautics and space administration
N-S	Navier-Stokes
PIV	Particle image velocimetry
RANS	Reynolds averaged Navier-Stokes
RG	Reduced slat gap setting
RMS	Root mean squared
S-A	Spalart-Allmaras turbulence model
SPL	Sound pressure level, $20Log_{10}(p'/p_{REF})$
SST	Shear stress transport
URANS	Unsteady Reynolds averaged Navier-Stokes
ZOC	Zero operate calibrate
2D	Two-dimensional
3D	Three-dimensional

Chapter 1

Introduction to the study

1.1 Outline of the chapter

This chapter contains three main sections to introduce this study. The first section gives an overview of the issue of aircraft noise. This is followed by an introduction to the slat system, a part of the high-lift system. Finally, the aim of the project is outlined and the structure of the thesis is presented.

The second section outlines the previous work concerning aerodynamic and aeroacoustic characteristics of high-lift flows, especially those focused on slat flows. The other main area covered is the range of different methods of flow control applicable to the slat system. These areas subdivide into wind tunnel based experimental studies, computational studies and measurement of real aircraft.

The final section identifies the specific variables investigated in this study and the reasoning for their inclusion using the knowledge from the previous studies. This section first outlines the features investigated and the reasons behind their selection. The second half of this section outlines the features measured during this study to assess their importance.

1.2 Introduction

1.2.1 Background

Environmental concerns have increased in importance over the last few decades. This has led to increased regulation along with public pressure for improvements in emissions and noise levels. The aviation industry is no exception to this trend especially in the area of noise. These pressures have led to a combination of internationally agreed standards along with local regulations with the aim of reducing

the noise levels experienced around airports. Reducing aircraft noise is therefore a shared objective of aircraft manufacturers and airlines as well as the general public.

At the start of the jet age, the engine was the dominant source of aircraft noise. This was largely due to the high flow speeds generated by turbojet and low bypass turbofan engines. A lack of incentives to introduce improvements when aircraft numbers were limited delayed addressing these problems. However, over the last 50 years engine noise has significantly reduced. Switching to higher bypass ratios has been the largest step in reducing the noise levels produced. This move to higher bypass ratios originated in a desire to increase fuel efficiency rather than to reduce aircraft noise. Although noise concerns did not drive major changes, they have now developed to a point where implementation of design solutions for reducing noise level occur as long as the changes produce no major performance penalty. The engines were the dominant noise source so they were understandably the first area examined for the implementation of noise reduction technology. This area moved from utilizing improved mixing of the core and bypass flows to increasing the use of acoustic liners.

Engine noise has now reduced sufficiently to leave airframe noise as a significant noise source. Airframe noise is especially important during the landing phase due to the low thrust settings and dirty wing configuration. A dirty wing configuration refers to the aircraft configuration with deployed undercarriage and high-lift devices, making the aircraft ready for landing. The high-lift devices are the leading edge slats and trailing edge flaps, which deploy from the wing. The main airframe noise sources are the undercarriage, flap side edges and leading edge slats [1, 2, 3].

Sound levels from airframe and engine sources are now important values. However, they do not override aerodynamic and performance parameters. Hence, noise reduction steps stop when there are significant performance penalties. This study focused on the airframe sound generated by leading edge slat and examined some possible ways of reducing its impact.

1.2.2 Slat system

The slat is an aerodynamic device primarily used in the landing phase of the flight. Its main purpose is to re-energize the flow on the suction surface of the main element, delaying stall. Supplying high-speed flow through the slat gap to the suction surface achieves this aim. Deploying slats increases the aerofoil stall angle and C_{LMAX}, but has little impact on the lift generated at low aerofoil incidence. As slats have little benefit and provide increased drag they are not desirable for the cruise phase. The requirement to retract creates the largest limitation to the geometry of the slat

system. When deployed the slat is extended from the leading edge of the wing creating a cove region (Figure 1.1). Inside the slat cove, there are two main flow features.

1. A high-speed flow carrying the fluid through the slat cove and out through the slat gap. This flow separates from the slat at the cusp and reattaches close to the trailing edge before moving through the gap.

2. The recirculation region, containing slow moving flow.

These two flows form because of the requirement for the slat to retract, which forces the slat to have a convex inner surface and sharp cusp. The high-speed flow is beneficial because it replaces the upper boundary layer on the main element. However, removing the recirculation region gives a noise reduction by removing the instabilities that generate in the shear layer at the boundary of the recirculation.

In fact, the division between the recirculation region and the main flow though the slat cove generates a shear layer, which originates at the slat cusp. The shear layer is unstable and can break down into discrete vortices. The majority of the vortices remain within the recirculating flow, this leads to a feedback mechanism, increasing instabilities at the cusp. However, some vortices convect past the trailing edge of the slat where they can interact with the trailing edge and create unsteady flow in the gap.

Slat noise contains two different components with different sources:

1. Broadband noise, usually linked with unsteadiness in the recirculation region, loudest at low frequencies (below 10 kHz). This instability can grow to a point where unsteady flow passes through the slat gap generating the sound.

2. Tonal/ narrowband noise linked with laminar vortex shedding from the upper trailing edge and to a lesser extent the slat cusp. This occurs in model tests at much higher frequencies than the broadband noise. However, these features are not present in full-scale tests.

1.2.3 Geometric definitions

In order to describe an aerofoil several definitions are used. When examining an aerofoil section the key variables are (Figure 1.2):

1. Retracted chord (c), defined as the distance from the leading edge to the trailing edge of the aerofoil with high-lift devices retracted.

2. Aerofoil thickness (t), defined as the maximum thickness of the aerofoil.

3. Aerofoil incidence (α), defined as the angle between the free-stream flow direction and the aerofoil reference line.

Retracted chord is usually used rather than the chord with the slat and flap deployed (deployed chord) because it is not dependent on the slat and flap locations so it remains constant for a given aerofoil.

Four variables define the position of the slat relative to the main element (Figure 1.3):

1. Slat gap (G), defined as the distance between the slat trailing edge and the nearest point on the main element.

2. Slat incidence (α_S), defined as the angle of the slat relative to its stowed position.

3. Horizontal overlap (O_H), defined as the horizontal distance from the main element leading edge to slat trailing edge (positive downstream).

4. Vertical overlap (O_V), defined as the vertical distance from the main element leading edge to the slat trailing edge (positive up).

The first three variables are sufficient to define the slat position avoiding the need for use of the vertical overlap.

The flap uses a similar set of variables defined between the flap leading edge and the main element trailing edge to give: flap angle (α_F), flap gap (H_F), flap horizontal overlap (O_{HF}) and flap vertical overlap (O_{VF}).

1.2.4 Aims of the study

The aim of this study was to examine slat noise and in particular to assess the use of blowing as a method of reducing slat noise. The aim encompasses two main tasks.

The first task was to investigate the sources of sound generated by flow over the slat system to obtain baseline acoustic and aerodynamic values for the standard landing setting. Measurement of both the broadband and narrowband components of sound allowed comparison with other configurations.

The second task was to investigate the factors with influence over the sound generated. These factors include values that vary during flight in addition to pure flow control features such as blowing. The factors fall into two groups:

1. Factors with significant influence on the aerodynamic performance of the wing. This section contains factors such as flight speed, aerofoil incidence and slat and flap settings.

2. Factors with little or no aerodynamic influence. These are largely local geometry alterations or applications of flow control with no effect on the global flow patterns.

Having little aerodynamic impact allows optimization of the factor to reduce the sound levels. However, these alterations are mainly due to local changes to the slat, which require modification of the slat hardware. By contrast, the aerodynamic factors are often adjustable allowing avoidance of the worst flight regimes on current aircraft by controlling the flight conditions.

Airbus UK sponsored this project and they have suggested the use of blowing inside the slat cove as one possible method of reducing slat noise. This method derives from the idea that the recirculation region generates low frequency sound in the recirculation region due to movement of the reattachment point and that blowing can prevent this.

1.2.5 Outline of the thesis

Chapter two describes the methods used in the investigation. This chapter expands on the introduction chapter to specify the range of individual conditions investigated and the measurements taken to acquire data for this study.

Chapters three and four contain the results of this study. These chapters present the flow features and acoustics along with the trends observed when the flow conditions change. Chapter three presents the experimental and computational aerodynamic results. These contain the results showing the wing loading and flow patterns. Chapter four shows the aeroacoustic results from the experimental and computational work. This chapter contains the work examining the sound levels generated by the slat system and identifying the source of the sounds detected.

Chapter five then summarizes the finding. This chapter also contains recommendations on the best method of controlling slat sound generation and an outline of possible follow-on work.

1.3 Literature review

1.3.1 Aerodynamic studies

Experimental studies

Experimental studies have been a major tool over the last century for the investigation of the aerodynamic features generated by high-lift devices. Studies have investigated high-lift systems for many years in order to find the optimum geometry from a purely aerodynamic perspective. These studies have found the range of conditions where the slat is aerodynamically acceptable.

Examining the pressure distribution has shown the working of the slat system. The slat circulation is in the opposite sense to the main element circulation (Figure 1.4), reducing the suction around the nose of the aerofoil. This provides a more favourable pressure gradient on the suction surface, delaying separation [4].

Slat optimization involves altering the slat geometry and rigging locations. Alemdaroglu found the horizontal overlap had a strong impact on the pressure coefficient (C_P) [5]. The changes were largest on the main element. Reducing the slat overlap generated a smaller recirculation allowing more flow through the slat gap. The slat gap is less significant aerodynamically than the horizontal overlap. Therefore the slat can be adjusted for a given horizontal overlap to reduce the acoustics. This optimum position was also dependent on the rest of the aerofoil and highly swept aerofoils designed to operate at high aerofoil incidence need greater slat deployment angles up to α_S=45° [6].

The interaction between the slat wake and main element boundary layer influences significantly the main element. These flows can join to form a confluent boundary layer, which reduces the maximum lift achieved. A confluent boundary layer is defined as occurring where there is sufficient mixing between the boundary layer and wake that the velocity defect decreases continuously away from the wall [7]. When this occurs, the size of the boundary layer is increased resulting in a loss of lift [8]. Early confluence occurs when the slat is located low vertically relative to the main element, particularly when the gap is small [7]. This would rule out moving the slat wake closer to the main element as a method of reducing the acoustic signature. Reducing the gap reduced the slat noise by up to 10 dB but resulted in a 4% drop in lift [9].

When considering experimental work it is important to assess the relevance of the results when scaled to match real aircraft. Investigations into the impact of the Reynolds number (Re) on experimental work found significant changes in the flow

below Re=5×10^5. These changes became more significant if the Reynolds number fell further [10]. The maximum lift was also strongly Mach number dependent. The slat was particularly Re dependent due to the location of the stagnation point close to the cusp. This region changes from laminar to turbulent depending on the Reynolds number and aerofoil incidence [11]. However, on a real aircraft the cusp is turbulent over most conditions. Transition was found to start at Re=6×10^6 and finish by Re=7.8 ×10^6 [12] based on the reference chord and free-stream conditions, although this depends on the particular slat geometry.

Another study [13] found the impact of the slat gap on the flow was also Reynolds dependent. At lower Reynolds number, the gap setting at which lift rapidly drops reduced significantly because thicker boundary layers led to earlier confluence.

Flows over aerofoils show hysteresis as high-lift devices deploy. Approaching stall exaggerates the hysteresis around the aerofoil [14]. With free transition on the slat, large hysteresis effects can generate when the flap moves. Fixing transition on the slat reduced the hysteresis but this is not always practical.

Computational studies

Computational studies of high-lift devices started with simplified problems to find the mean flow features. Over time, work has moved to more complex geometries and unsteady simulations.

Early simulations to investigating an aerofoil used panel methods [15]. This method picks up the basic inviscid flow features and incorporating a boundary layer simulation improves the accuracy of the predictions. Through the addition of 3D lifting surface theory, the simulation of a 3D multi-element wing became possible [16]. However, although increasing model complexity can improve accuracy, panel method based schemes cannot generate unsteady results.

Unsteady results require the use of a form of the Navier-Stokes equations. A RANS based solver is the most common method used in industrial design. This became a possible tool for the study of 2D aerofoils from the early 1990s. Due to the complex geometries, most early studies used grids of around 5×10^{4}cells. This allows modelling of the steady flow but there are problems with separated flows. These studies often used unstructured grids [17, 18]. With an unstructured grid, it was important to focus the cells to resolve the boundary layers. Otherwise, artificially enlarged boundary layers develop, which can altered the flow [19]. A wall spacing of y^+=O[10] was found to be inadequate and y^+ =O[1] is required to accurately simulate the pressure distribution over a flap [19]. Where separation is not an issue the wall spacing was less important and a slightly larger spacing can be used. Increasing

the grid resolution by using around 2.50×10^5 cells slightly improved the simulations [20]. It is possible to automatically generate an unstructured grid concentrated around the complex flows [21]. However, the need to interpolate between points in the numerical scheme limits unstructured grids. This results in extra computational cost and makes the use of high-order schemes with larger stencils impractical.

One alternative to unstructured grids without the difficulties of a structured mesh is to use a chimera grid [22]. The grid close to the wing matches the wing elements and this overlaps with a global far-field grid. This method gives a better quality boundary layer grid than an unstructured grid without the difficulties of a fully structured grid. It is possible to apply a higher order code with this type of grid but it would still face problems in the region where the grids are overset.

Structured grids are more complex to build because all the zones have to match. However, they have the advantage of a smaller computational loading because the grid contains ordered data points that enable a simple interpolation using (i,j,k) stensils. Like other types of grid at low resolution and with a low order scheme it has problems resolving complex flows such as separated and reversed flows [23, 24]. It is possible to generate automatically suitable structured grids [25]. This is a complex task especially for high-order schemes where problems can develop if the grid is not ideal. Automatic gridding allows the development of an automatic optimization program for high-lift systems. This studies a range of configurations to find the best for given performance parameters. Currently examples of such a program only include aerodynamic factors [26, 27] but as the power of computers increases, acoustic requirements could be included in the optimization.

3D simulations have additional computational costs but pick up the features missed by a 2D simulation, such as near the tips of finite length wings [28] or on swept wings [29]. The swept wing case run by Khorrami et al. [29] used a RANS solver based on the S-A model. Modelling the entire wingspan required 1.75×10^6 cells. It was computationally expensive. However, for an un-swept wing it is acceptable to take a much smaller slice of the span. This change allows the use of periodic boundary conditions because it reduces the importance and scale of 3D features.

Work on the aerodynamic component of the flow helps to indicate the effectiveness of different turbulence models. Comparison work carried out by Rumsey and Gatski [30] found the k-ε EASM model [31] has a weakness for wall bounded adverse pressure gradients and the S-A model [32] was found to simulate separated flows poorly. A model the study found worked well for the simulation of high-lift flows including separated regions was the shear stress transport (SST) model of Menter [33, 34]. If more resources are available then DES or LES becomes a pos-

sibility and increases the ability to accurately model instabilities in separated flows [35] even near to stall [36]. Where this is not possible, a hybrid method can combine predefined discrete regions of RANS and LES regions [37], however, this works best where there is a clear division between the regions.

Flight test studies

Full-scale tests are the most expensive investigative approach for high-lift devices due to their size and the need for modification of an aircraft with specialist instrumentation. They are also the hardest to instrument due to the need to maintain the external geometry of the aircraft. Hence, there are fewer full-scale tests relative to the number of wind tunnel tests. However, after resolution of the costs and measurement difficulties, flight-testing allows testing of the full geometry without the need for the scaling or simplification, which is inherent in all computational and experimental studies.

An established flight testing technique is to fit pressure sensors to the wing to allow comparison with scale tests. A Boeing 737-100 was fitted with an array of pressure taps and hot films including on the high-lift systems [38, 39]. On approach, the hot film showed that the flow on the upper side of the slat trailing edge transitions from turbulent to laminar. This is likely to have an impact on the noise generated. On the lower surface of the slat the flow experienced transition just upstream of the cusp. This should eliminate any tones generated from a laminar separation. This study is limited by the age of the aircraft, which had an old aerofoil profile including triple slotted flaps so the flow over the slat could differ on newer designs. However, it did show real aircraft slats operate close to the boundary between laminar and turbulent flow and experiments have shown this is a determining factor in tone production.

1.3.2 Aeroacoustic studies

Experimental studies

Current studies use a variety of microphone and other measurement techniques to study the sound from a slat. The simplest method to obtain acoustic data is using a single microphone to measure the sound spectrum generated by the wing. An acoustic mirror improves on a standard microphone and allows the microphone to scan the model for sound sources. Acoustic arrays are an alternative to the acoustic mirror technique. These allow the calculation of a source map using an array of microphones [40].

Experimental tests are also very dependent on the level of details included because small design features determine the overall high-lift device noise contribution [41]. Because of the necessary complexity of these devices, slats and flaps can provide a 10 dB increase over a clean wing with slats dominating in the rear arc. Other important noise sources are the slat tracks and the engine pylons [42]. As well as acting as sources, slats destabilize the flow and can cause separation further downstream.

Olson et al. at the University of Notre Dame carried out an experimental study on the tonal noise generated by a slat [43]. This focused on variations in the tones measured by a single far-field microphone caused by alterations of the slat location. The tests used a main element with c=559mm, tested at α=10° and a flap angle of α_F=13° at 30 m/s. Tones were loudest with a moderate slat gap of around G=0.015c and a negative horizontal overlap ($O_H < 0$). Tones were angle dependent with no tones at α_S=10°, tones at α_S=20° and narrowband peaks when α_S=30°. This linked to the change in pressure gradient from adverse to favourable on the upper surface of the slat, which caused the flow to transform from turbulent to laminar. The laminar separation created strong tones but if the separating flow was turbulent, it no longer generates tonal features. This gives a reason why full-scale aircraft do not generated tonal noise. The higher Reynolds numbers mean the flow is always turbulent when it separates from the slat and it generates a largely broadband noise source. However, this does not mean the noise is purely broadband because resonance in the slat gap or the breakdown of the shear layer instabilities could generate narrowband features.

Storms et al. [44] carried out measurements using a microphone array on a three-element model and this showed the slat tones followed a v^5 power law. Hence, with flaps deployed, the sound generated by the slat increased due to increased circulation. The study also found a sharp drop in SPL for a slat angle below α_S=19°. This was similar to the pattern found by Olson et al. [43] but was not limited to tonal noise.

The slat setting also affects broadband sound generation because the sound level reduces as the flow speed past the slat trailing edge decreases [45]. Reducing α_S and increasing the slat chord minimizes acceleration through the gap but maintains lift. The sound generated at the trailing edge is also dependent on the gap setting so reducing the gap can give a noise reduction of up to 10 dB [9]. However, this restricts the gap flow leading to a 4% lift reduction.

The removal of tones by fixing transition was shown by Dobryzynski et al. [46] on a 1:10 scale Airbus wing. At α_S=12° it produced tones unless the flow was tripped at the cusp. Although v^5 scaling gave a good fit for the majority of the spectrum, above 25 kHz a v^8 law was a better fit. This represents turbulence in free space. However, as this is made of quadrapole sources it is a poor radiator so its overall

contribution is minimal. Similar tests by Andreou et al. [47] found tones increased SPL by up to 8 dB but were removed by tripping the flow at the slat cusp.

A similar divide was found when investigating a 4.7% scale model of a DC-10 using an acoustic array [48]. Low frequency noise followed v^5 scaling but high frequency noise followed v^6. This indicates a 2D source generated the lower frequencies. The slats mainly generated this low frequency sound. The higher frequencies were from a dipole and largely from the flap side edge. An earlier study on the same model also found a strong tone from the gap between the inboard and outboard slat [49]. Due to the scale of the model, this was probably a model problem. However, gaps between slats do act as noise sources and the study highlights how small features can produce strong tonal features.

When investigating a 1:10 scale A320, the slats were the dominant source in landing condition and the noise scaled with $v^{5.7}$ [2]. The sound increased with aerofoil incidence and the direction of the peak sound shifted to the rear. An earlier study using a 1:11 scale model found a scale factor of $v^{5.3}$ [50]. The lower frequencies were largely from the slat cusp but higher frequencies were from the interaction between the gap and the slat trailing edge. This model was used to investigate Strouhal dependence and some sources were found to be largely Strouhal independent, particularly at higher frequencies [51, 52]. Some tones only occur at lower speeds, indicating these were due to thicker boundary layers leading to more interactions.

As the trailing edge tones are Strouhal dependent when models are fitted with relatively thick trailing edges, this can produce unrealistically low frequency tones [9]. This is probably the main reason experimental tests frequently find slat tones but real aircraft rarely generate slat tones.

Takeda et al. at the University of Southampton studied the aeroacoustics of the national high-lift aerofoil [53]. The study used PIV, LDA and hot wire measurements along with flush mounted microphones and pressure taps. This model with c=764 mm was tested at v=30 m/s to give a Re of 1.5×10^6. Tests were carried out with α_S=25° and α_S=40° at α=5°. PIV showed vortex shedding at 15 kHz from the trailing edge and large vortical structures ejected through the gap disrupting the wake. The frequency spectrum was broadband at lower frequencies with tonal components (9 kHz and 15 kHz), which linked with the cusp and trailing edge shear layers. The 15 kHz tone gave a Strouhal number of St=0.24 based on the trailing edge thickness, a good match to the value of St=0.2 found by Storms et al. [44] and St=0.27 by Olson [43]. When the slat gap dropped below $0.015c$, the higher frequency tone fell below the broadband level so the feedback mechanism must have been broken. This was especially important because sound radiated upwards is less

of a problem as regulations only cover sound directed towards the ground.

Aerofoil incidence is also a contribution factor to slat noise. Increasing α from 6° to 16° gives a 2-3 dB reduction between 5-13 kHz [47]. However, other noise sources show the opposite trend. The slat horn (join with fuselage) increased in importance as a source as the aerofoil incidence was increased [54]. Tonal features also tend to increase as α is increased [55]. Noise generated is largely broadband in nature at low aerofoil incidence [9]. The sound generated by the wing is also dependent on the wing thickness to chord ratio. Thicker wings are generally quieter and have a greater noise reduction as the aerofoil incidence increases [56].

Studies have examined the physical causes of slat noise by observing the unsteady features in the flow around the slat. PIV showed the wake was unstable at low aerofoil incidence [57]. The number of unstable features was reduced by 40% if the aerofoil incidence was increased from α=4° to 10°. This instability was a possible source of sound and corresponded well to the reduction in sound observed at high angles of aerofoil incidence.

Periodic shedding can occur in the shear layer generated at the cusp [58]. Shedding was observed between 4 and 10 kHz and scaled with mean shear layer velocity. The aerofoil used had a finite thickness cusp and using this length the tone occurred at a Strouhal number between 0.203 and 0.215.

As well as small vortices forming in the cusp and trailing edge wakes, large spanwise rollers are intermittently ejected through the slat gap disrupting the wake [59]. These large features develop inside the slat cove region before escaping from the recirculation region.

PIV has allowed identification of three different shedding patterns through the slat gap [60] (Figure 1.5):

1. State one, all shedding from the trailing edge with vortices of both signs.

2. State two, shedding from the trailing edge and positive vortices passing through the slat gap from the cove.

3. State three, shedding formed from negative vortices from the trailing edge and positive vortices through the slat gap.

The experiment was carried out with α=4°, α=6°, α=8°. The flow alternated between the three shedding states with the state number increasing as aerofoil incidence decreases and the reattachment point moves closer to the trailing edge. This reduced the recirculation and allowed more vortices go through the gap. State one

only occurred at α=8°. This finding indicates fixing the reattachment point limits the flow to one flow type and reduces the range of vortex shedding frequencies generated.

An alternative mechanism is a whistle formed at the slat gap, which generates resonance when the waves reflected off the main element match up with the waves from the trailing edge [61]. This is possibly the source of tones but it does not take into account instabilities moving through the gap. This is similar to the system proposed by Tam and Pastouchenko [62]. The whistle frequency is determined by imposing that the time taken for and acoustic wave emitted by the trailing edge to reach the main element matches that of the reflected wave to reach the trailing edge. This forms a feedback loop that is dependent on the gap distance and normal velocity of the sound waves v_n (Figure 1.6). This gives:

$$f = \frac{N(a^2 - u^2)^{0.5}}{2G} \tag{1.1}$$

where N is an integer, a is the speed of sound, u is the local velocity and G is the slat gap. Instabilities in the slat gap generate the dominant frequency and higher harmonics. However, the experimental results in Takeda et al. [53] did not find the fundamental frequency predicted by the theory.

Component based methods

When studying the acoustics of high-lift systems, the computational methods used have evolved over time. A full simulation of the flow that resolves acoustic waves is computationally expensive, leading to the use of other methods.

The simplest way of modelling the noise generated by a wing is a component-based method. This uses standard values for different airframe components such as slats and flaps. A simple frequency distribution and directivity factor represent most components. In Fink [63], slats are simply represented by an 11 dB increase over the value for a clean wing. This type of empirical method uses a large database taken from real aircraft. The data allows the formation of an empirical relationship between the geometry of the dominant noise sources, such as the slats and flaps, and the sound produced [64]. Instead of using aircraft flyover data, it is possible to use experimental data for specific components [65]. Empirical methods give a good reading of the general noise level of an aircraft if it is of a design similar to the baseline aircraft. However, they cannot be used to model any new design or noise reduction technique unless similar flow physics and simple scaling laws can be followed.

An improvement on a purely empirical system is to include terms based on knowledge of the system. This means the terms used have more relevance and are applicable in designs incorporating some new geometric features [66]. The model is a good fit relative to general trends from the flight data but does not incorporate some of the finer flow features leading to poor modelling of tonal features.

The next step is to move from an empirical based solution to a simulation based on the geometry under investigation to identify the key features of the flow, possibly using a simplified geometry to accelerate the simulation. Examination of trailing edges over a range of conditions show sound generally increases with an increase in the aerofoil incidence [67]. Reducing the aerofoil thickness to chord ratio minimizes this trend. The trailing edge shape is also important with rounded and blunt geometries significantly louder than sharp trailing edges [68]. Trailing edge flows can be further complicated by passing vortices, as they are at the slat trailing edge. The vortex rotation direction has some influence on the sound generated, but for all vortices the radiated sound scaled with $v^{4.2}$ [69].

Acoustic analogies

Unsteady computational fluid dynamics can replace experimental models for simple flow geometries. The most common method is to combine a RANS solver with an acoustic analogy for the far-field. An acoustic analogy models the radiation of sound from a finite volume of acoustically active flow to an observer in the far-field. This approach is more computationally efficient that extending the computational domain to the far-field. The acoustic analogy approach establishes that away from major disturbances, sound propagates in a linear fashion. There are two main acoustic analogies used in CAA: the Ffowcs Williams-Hawkings analogy and the Kirchhoff analogy.

The Ffowcs Williams-Hawkings analogy builds on the acoustic theory developed by Lighthill [70, 71]. Lighthill developed a model for aerodynamic sound generation in free space in the absence of solid boundaries. A Lighthill acoustic analogy is based on replacing an unsteady flow by a uniform steady field at rest and acoustic sources. This led to the development of the Lighthill shear stress tensor T_{ij} which is applied to a uniform acoustic field to recreate the real density variations.

The shear stress tensor T_{ij} contains three components.

1. The Reynolds stresses $\rho v_i v_j$, which make up the fluctuating momentum changes.
2. The real stresses P_{ij}, which is the real stress component.

3. Hydrostatic pressure caused by density variations.

In a real flow both the Reynolds stresses and real stresses will act on the flow but a uniform acoustic field will only be exposed to hydrostatic pressure. An acoustic analogy is built using a uniform acoustic field and adding a an "external stress system" to recreate the real density variation [70]. To recreate the real density variation this must add the Reynolds and real stresses felt by the real flow and remove the hydrostatic pressure usually experienced on a uniform acoustic field. This external stress system is represented by the shear stress tensor T_{ij} [70], which is defined as:

$$T_{ij} = \rho v_i v_j + P_{ij} - a^2 \rho \delta_{ij} \tag{1.2}$$

where ρ is the density, v is the flow velocity, a is the speed of sound and P_{ij} is the compressive stress tensor made up of hydrostatic pressure and viscous stresses.

This allows the representation of disturbances by a distribution of quadrapoles allowing the calculation of the far-field pressure fluctuations without simulating their propagation. The FW-H equation uses the conservation of mass and momentum as its basis. These laws apply to an infinite region of uniform flow containing a finite region generating sound moving at a known velocity [72]. This allows to approximate the flow in the inner region by a series of sources bounded by dividing surface. The surface itself is a locus of monopole and dipole sources to maintain the conserved variables passing into the outer zone. It is modelled so the external zone contains only linearly propagating acoustic waves in a medium with a constant velocity. In the inner zone the fluid is at the same constant velocity with turbulent features replaced using the Lighthill stress tensor. A distribution of quadrapoles representing the features contained in the inner volume and monopoles and dipoles based on the surface representing the interaction with the outer zone replace the entire flow. One form of the FW-H equations is [73]:

$$\begin{aligned} \Box^2 p'(x,t) =& \frac{\partial^2}{\partial x_i \partial x_j}\{T_{ij} H(f)\} - \frac{\partial}{\partial x_i}\{[P_{ij}\hat{n}_j + \rho u_i (u_n - v_n)]\delta(fn)\} \\ &+ \frac{\partial}{\partial t}\{[\rho v_n + \rho(u_n - v_n)]\delta(fn)\} \end{aligned} \tag{1.3}$$

where $\Box^2 = [(1/a^2)(\partial^2/\partial t^2)] - \nabla^2$ is the wave operator, fn is a function that is zero on the integration surface and positive in the inner zone, v is the freestream velocity, u is the local fluid velocity, $\hat{n}$ is the outward normal to the surface, p' is the acoustic pressure and a is the speed of sound.

This form of the FW-H equation can easily be divided into the three components types of acoustic source that are used to replace the physical flow.

1. A quadrapole term $\frac{\partial^2}{\partial x_i \partial x_j}\{T_{ij}H(f)\}$, which is distributed across the area contained within the integration surface.

2. A dipole term $-\frac{\partial}{\partial x_i}\{[P_{ij}\hat{n}_j + \rho u_i(u_n - v_n)]\delta(fn)\}$, which is distributed on the integration surface.

3. A monopole term $\frac{\partial}{\partial t}\{[\rho v_n + \rho(u_n - v_n)]\delta(fn)\}$, which is distributed on the integration surface.

The acoustic analogy uses the wave operator, which linearly propagates the sound to far-field locations.

The Kirchhoff analogy evolved from the wave equation and originally applied to light but later applications included modelling sound radiated from moving surfaces [74]. As with the FW-H equation, it uses an integration surface to construct the equation. However, this formulation has the advantage of not requiring a volume integral but the disadvantage of not being possible to divide the terms into easily understandable terms such as monopoles, dipoles and quadrapoles, the Kirchhoff analogy is written as [33]:

$$\Box^2 p'(x,t) = -(\frac{\partial p'}{\partial t}\frac{v_n}{a^2} + \frac{\partial p'}{\partial n})\delta(fn) - \frac{\partial}{\partial t}[p'\frac{v_n}{a^2}\delta(fn) - \frac{\partial}{\partial x_i}[p'\hat{n}_i\delta(fn)] \tag{1.4}$$

The FW-H equation has the advantage of being based on conservation rather than on the wave equation so it is still applicable in regions where the flow is non-linear and the wave equation is not applicable [73]. If the volume integral term is not used the analogies are equivalent as long as the surface is in a linear region where the wave equation applicable. Therefore, the location of the integration surfaces is more critical for the Kirchhoff analogy. It is often difficult to spot if the surface is not located correctly resulting in errors so the FW-H equation is more robust but it has the disadvantage of requiring a volume integral to give the exact value.

Computational studies

For an analogy to produce accurate results, the integration surface must contain all the acoustic sources. This requires the simulation of a large area, leading to cost and accuracy problems, so alternative strategies were developed. One strategy is to use a Linearized Euler simulation combined with additional acoustic sources. This can

combine with a simplified geometry to model the main features. Takeda et al. [75] used this method applied to a slat. The slat was represented by a semicircle and a couple of rectangles and a dipole source was added downstream of the trailing edge of the slat. This simplification allowed the use of a relatively small grid of 5×10^4 cells and was an order of magnitude faster than a RANS/FW-H simulation. This allows rapid comparison of a range of designs. The problem with this approach is the reliance on user specified data for the acoustic sources and the simplification of the geometry makes the results less reliable. However, it is a useful method for theoretical studies and for initial investigations into acoustic changes due to variation in slat geometry and location. The simplified geometry was also investigated using RANS/FW-H to investigate the implications of trailing edge thickness and overlap settings on the acoustics [76]. The trailing edge thickness helped to determine the shedding frequency of trailing edge vortices. However, the Strouhal number increased with trailing edge thickness, indicating other factors had an influence. A reduction in the horizontal overlap reduced the feedback between the trailing edge and the main element and gave a large drop in sound radiation. However, the modified geometry made the prediction not comparable to experimental data that used a proper slat rather than a semi-circle and rectangles, so it is possible that the reduction is less significant for the real geometry. With the modified geometry, the slat was further away from the main element with the exception of the overlapping zone, which could have exaggerated the importance of the overlap.

An alternative method developed by Manoha et al. removes some of these accuracy issues. Early work [77] focused on combining a turbulent calculation close to an aerofoil (in this case LES) with the Linearized Euler Equations (LEE) to propagate the sound generated a short distance. An acoustic analogy (in this study the Kirchhoff integral) then modelled the far-field values. This allowed the simulation of a large enough area to contain the sound sources without the need to use costly LES where it gave no added physics. This gave improved accuracy but the large LES zone was still expensive when compared with a RANS simulation.

A later modification of this method reduced the drawbacks by replacing the LEE region with a RANS simulation. The LES zone was reduced in size to only contain the most complex elements of the flow [78] and was not needed in the regions which are adequately simulated using a RANS solver. The region of viscous flow increased without great expense due to the small difference in cost between LEE and RANS. This method was computationally more expensive than RANS but less expensive than the LES/LEE method because the LES zone was reduced. One study used this method to calculate the far-field acoustics of a NACA0012 aerofoil with a blunt

trailing edge. The slat cove used a LES method with 52 slices of 1.10×10^5 cells. The RANS calculation around the aerofoil used the S-A model and 4.11×10^5 cells. The FW-H analogy calculated the far-field. The main difference found compared to RANS studies was small regions of separated flow close to the slat cusp inside of the slat cove and above the leading edge of the main element. The main sound sources were these locations as well as the cusp and trailing edge. However, other studies have not detected these flow features and it is likely that they occurred due to the particular aerofoil geometry studied. This had a blunt cusp so the recirculated flow could not arrive nearly parallel to the main flow, encouraging separation. The main element leading edge was also much sharper, increasing the tendency of the flow around the aerofoil to separate.

Further work looked into different combinations of near-field, far-field and acoustic analogy [79]. This aim was to use appropriate schemes for each region without excessive computational costs. The lack of a method of assessing the accuracy of the solutions limited this work.

NASA has carried out work focused on developing the RANS based approach in order to investigate airframe noise. Macaraeg's paper lays out this project [80]. The work started by looking at the near-field using a 3D URANS simulation to model the EET as used in an earlier experimental study by Storms et al. [44]. However, this required 5.70×10^6 cells, which is not practical for most simulations, so work moved on to 2D simulations [81]. These 2D simulations used Menter's SST model on a grid of 2.71×10^5 nodes, allowing the identification of the dominant high frequency peak [82]. This work progressed to focus on the use of a RANS solver combined with the FW-H acoustic analogy to model the aerodynamics and acoustics of an aerofoil [83, 84]. The study found the majority of the flow features were identifiable using a surface mounted integration surface for the majority of its length but including the slat cove region. The result was further refined when the boundary was moved slightly away from the surface of the main element but this was not necessary on the outside of the slat. This allows the grid to be focused because the simulation only needs accurate simulation of acoustic data within integration surface.

In a related study, the grid size was increased to 4.33×10^5 nodes and a time accurate simulation was carried out to investigate the shear layer, which developed from the slat cusp [85]. However, with the RANS solution the disturbances damped out before they could break down into discrete vortices.

One possible solution to the above problem was to use the shear stress transport (SST) version of the k-ω turbulence model with the production term switched off inside the slat cove, forming a laminar zone [86, 87]. The laminar zone reduces the

dissipation of the model and allows the small acoustic features to develop. It is justifiable because the boundary layer is laminar at the cusp and the recirculating region contains low velocity flow so a laminar shear zone generates. Simulations were set at α=4°, α=6° and α=8° at M=0.2 and α_S=30°. This resulted in broadband noise components appearing below 10 kHz and tonal noise at 45 kHz. At α=8° the vorticity was carried around the outside of the slat cove in the simulations and this was a good match to experimental data. However, at α=6° the flow changed and formed a large single vortex in the centre of the cove. This resulted in an overestimate of the far-field sound by 10 dB. The study found PIV data gave a flow field in between the simulations with and without a laminar zone. However, this showed a laminar zone was still an improvement as it indicated the unstable flow [88]. It was a good match to the acoustic spectra and the main error was due to it being a 2D simulation. Experimental data follows a v^5 power law whereas 2D computational data followed a v^4 distribution and 3D simulation should give a v^5 scaling [89].

Emunds and Fisher examined a range of simulations showing the impact of slat location settings [90]. Modifications did not alter the basic dipole shape with the impact concentrated in the lower downstream direction. Increasing the gap by raising the slat reduced radiation in this direction by increasing the shielding of the slat trailing edge by the main element. The lack of a flap in the simulation possibly had an impact by reducing flow through the slat gap [91].

With a 3D simulation, many of the two-dimensional numerical effects disappear, but there is clearly a cost penalty. Studies by Choudhari et al. show that close to the cusp, the shear layer rolls into spanwise vortices similar to 2D results. However, downstream of the slat reattachment point streamwise features develop, which are not reproduced by a 2D simulation [92, 93]. Allowing 3D features increases the complexity of the flow, which increases due to interactions at the slat cusp. Low frequency vortex shedding also occurs in the cove [94]. This shedding could correspond to the ejections seen experimentally [59].

Changing the acoustic analogy allows improvements in accuracy of the simulation. The previous work used an acoustic analogy based on data from the integration surface. An assessment of the impact of adding a volumetric term of the SPL in the far-field found large differences in the noise radiating from a wing, especially in the forward and downward directions [95]. This occurred between 250 Hz and 450 Hz, where the wavelength matches the size of the vortices in the cove region.

Another area not usually covered in computational work is the impact of gusts in the oncoming airflow. These increase the magnitude of unsteady features [96]. Sim-

ilarly, as the wing vibrates significant tonal features overshadow the sound normally produced [97]. Accurately accounting of outside influences on the slat encourages the development of a full aircraft model [98]. However, obtaining the required detail is still many years away.

Flyover test studies

Full-scale acoustic tests originally used single microphones to measure total aircraft noise. However, more recently the focus has shifted to using a phased array to identify the components producing the noise during flyover tests.

Airbus A340 flyover tests confirmed the slats and flaps were the main sources [99] although these sources were loudest at the joins between the flap/slat segments. With landing gear deployed, the undercarriage dominated the noise production and contained some strong tones [2]. Tests on a Boeing 777 did not find significant noise from the slat with the exception of anti-ice holes [100]. This was different from scale-models, which produced much larger slat noise. Vortex shedding from the wing tips was an additional noise source producing low frequency tones (260-350 Hz) [101]. This tone was associated with flow separating ahead of the trailing edge outboard of the flaps. Improving slat performance in this location should reduce the amplitude of the tone by minimizing the flow separation.

While using microphone arrays, beamforming [102] allows calculation of the SPL spectra at each noise source by integrating the SPL over the area occupied the each noise source. Sijtsma and Stoker recorded sources found by beamforming as the aircraft passed overhead to observe the impact of the directionality of the sound [103]. With an Airbus A340, the engines had the highest peak power level followed by the undercarriage. The flap edges and slat horn (join with fuselage) had a peak SPL about 8 dB below the engine exhaust noise. However, the microphones were only 750 m from the runway threshold, which could have exaggerated engine noise due to the use of higher thrust settings relative to the rest of descent in preparation for the use of reverse thrust or an aborted landing. In addition, the jet engine noise had greater directionality than airframe noise so the average engine noise was less than 6 dB above the slat horn noise. Thus as engine noise reduces, the slat values being only 4 dB below the landing gear value increases in importance. By comparison, tests carried out in the same study with an older generation Boeing 737-400 showed the engine exhausts were dominant.

1.3.3 Passive flow and noise control

Several control methods potentially reduce the noise generated by the slat and the rest of the wing during the landing phase. These vary in complexity but all have limitations, which have so far prevented their wide spread use in the aviation industry. Some of the flow control methods act to improve the aerodynamics of the wing. Improved aerodynamics can give acoustic benefits by allowing lower approach speeds or reduced use of high-lift devices. Other methods aim to reduce directly the noise generated while trying to maintain the aerodynamic performance of the wing.

A possible way to reduce the noise on the ground is to move the aircraft further from the ground [104]. Possible methods of achieving this include allowing a continuous descent from cruise altitude and steeper glide slopes. Greater noise reductions would require new aircraft with a larger overall maximum lift coefficient to allow slower approach speeds. Airframe noise scales with v^5, so reducing the airspeed combined with a steeper glide slope would provide significant noise suppression during approach. As air-traffic control technology evolves, the need for international agreements on updated hardware retard quick changes. However, improvements in this area are ongoing.

Application at the slat gap

A simple method of reducing slat noise is to seal off the slat gap. This eliminates the tonal noise if the gap is completely sealed [61]. Olson et al. also showed that tones reduced significantly if the gap was nearly sealed or the gap was very large [43]. Both approaches reduce the maximum lift of the slat, so are not possible for the whole wing. Sealing the gap also reduces the broadband sound generated by the slat [47]. Leading edge droop devices allow the removal of the gap on the inboard of the wing [105]. Using a leading edge droop results in a 5% drop in maximum lift, relative to a slat, for the section but has less drag so is ideal for take off. The use of a leading edge droop is a continuation of the general trend of simplifying high-lift devices by removing gaps, which has occurred over the last 30 years. Further simplification can be achieved using continuous moldline (CML) technology (flexible ends to the droop section to avoid discrete ends becoming a source of noise) [106]. Streett et al. used CML with flaps and found that the side edge noise reduced by 5-15 dB above 2.5 kHz [107]. The same study found edge sound was also significant for slats. However, on swept wings the inboard tip generated sound 8 dB above the rest of the slat. Applying a continuous moldline device gave reductions of up to 10 dB in the peak SPL above 5 kHz.

Applications in the slat cove

A simple method to reduce slat noise is to install a slat cove cover, which extends the cusp following the direction of the shear layer. The extension gave a reduction of around 2 dB to the far-field broadband noise with local drops of 4 dB [41]. This works mainly by smoothing the flow through the slat gap by reducing the separating flow shear layer unsteadiness at the cusp. Another study [46] found a similar cover could produce up to a 5 dB drop in SPL especially at lower frequencies. A cover had a negligible impact on the efficiency of the slat aerodynamically except the small increase in friction on the air travelling through the slat cove. However, it is difficult to manufacture a device to allow the slat with cove cover to retract and form a smooth join with the main element. An alternative is to modify the direction of the cover so it follows the shape of the main wing element in the retracted configuration. This resolves the manufacturing problems with little performance penalty provided the cover is not long enough to diverge significantly from the shear layer direction when the slat is deployed. When combined with a boundary layer trip to attempt to reduce separation, a small advantage at low frequencies appears. However, at high frequencies the boundary layer trip cancels out the advantage of the cover by counteracting the smoothing action of the cover [46]. Boundary layer trips are also detrimental to cruise drag if left uncovered in the cruise settings.

A cover aligned with the main element acts as a blade seal, which provides a smooth geometry during cruise [108]. An elongated blade seal eliminates most of the small-scale vortices generated at the cusp. At low frequencies (<2 kHz), a short seal gives a 2-3 dB reduction and extending the cover provides an additional 2 dB reduction. At higher frequencies and on the slat noise tones, the cover is even more effective.

An alternative to treating the cusp is to eliminate it by smoothing it into a continuous curve. This alteration gives improved aerodynamic performance and lower levels of turbulence [109]. It maintains attached flow to a higher aerofoil incidence than a standard flap. The problem with this type of slat is the gap it leaves in the retracted configuration. This only produces a small change in efficiency in the cruise setting, but due to the high percentage of the flight in cruise setting, there is a requirement for a cover.

Another method of eliminating the sharp cusp is to fill the recirculation region of the cove with a foam filler. This was found to give significant reductions in the noise especially in the rearward radiated sound, but generated more high frequency tones [2]. On a 1/6 scale A320 wing at 60 m/s, these tones occurred at 12.5 kHz and were up to 20 dB above the surrounding frequencies. Fixing transition on both the

upper and lower surfaces of the slat, to stop laminar instabilities forming, removed the tones. There was a reduction in SPL of up to 5 dB for frequencies between 1 kHz and 4 kHz. The only penalty was an increase of around 2 dB for frequencies above 15 kHz but this still left them 8 dB lower than the lower frequencies. As with slat covers, the main problem is manufacturing the filler to allow the slat to retract and still maintain an acceptable component life. This has been tested on an A340 and combined with porous flap tips provided a 1 dB reduction in the total aircraft noise. This represented a 2 dB reduction in airframe noise between 125 Hz and 5 kHz. Similar tests on a 26% scale Boeing 777 wing [110] found a similar slat SPL reduction of 4-5 dB when the filler was added. The only exception was a small increase at 1.6 kHz. Streett et al. carried out similar tests at different aerofoil incidence values [107] and found a cove filler was effective below 3 kHz providing a 3 dB reduction but detrimental above 13 kHz, at α=10°. However, at α=14° the cove filler gave an advantage at all frequencies. Aerodynamically the cove filler gave a small improvement below α=20° but led to a 2° reduction in the stall angle [107]. Andreou et al. [47] also carried out tests using a slat cove filler and found it reduced C_{LMAX} by 50% by limiting the flow through the cove. This indicates the aerodynamic effect of a filler is aerofoil dependent, so each existing aerofoil requires extensive optimization work. One possible solution is designing the filler to obtain a slat gap with a slowly varying cross section. This would following the shape of the shear layer to avoid the aerodynamic penalties [107].

As well as smoothing the flow, cove fillers also cover the detailed features in the cove, which can cause additional sound generation. The slat track can have a noise level around 8 db above the rest of the slat [46]. This is largely because the slat tracks are perpendicular to the wing (Figure 1.7). Aligning them with the flow direction gives a 3 dB reduction and streamlining the track geometry gives further improvements . The cove region may also contain a bulb seal to seal the slat gap during cruise [108]. This device generates a dead flow region, which provides unsteadiness and destabilizes the flow at the cusp.

A porous liner can fit inside the slat and on the main element in the areas covered when the slat retracts [111]. When tested this produced a drop of up to 3.5 dB from 2-10 kHz. The liner had little aerodynamic impact as long as the liners avoided the area close to the stagnation point on the main element. The benefit of the liner was concentrated in the rear downward direction [112].

Application at the slat trailing edge

The slat trailing edge is another area of interest especially with respect to tonal features and high frequency sources. One practical solution tested was to attach brushes to the slat cusp and trailing edge. Full-scale tests on an A320 wing showed adding brushes to the cusp had little impact. However, if added to the trailing edge it reduced radiation below 1 kHz by around 1 dB. The reduction increased when brush length increased from 50 mm to 150 mm. A slat should enhance the impact of the brush because as well as shedding noise there is interaction with the flow through the gap to damp. For a flat plate, brushes led to a drop of 10 dB [113] so similar improvements could occur when applied at the trailing edge. The main limitation is the need to use relatively small brushes to prevent a reduction in the mean flow through the slat gap.

Other trailing edge modifications include adding a thin sheet to extend the slat trailing edge. This effectively sharpens the trailing edge so the shedding frequency is no longer a strong tone [114]. Thinning the trailing edge can also give significant reductions in the high frequency sound around the shedding frequency [115]. For full-scale aircraft, this is problematic because a thin trailing edge would damage easily. Also for full-scale aircraft, these tones are generally not a problem due to the greater ratio of trailing edge thickness to the wing chord [2]. A serrated trailing edge has also been tested and this provided a reduction in high frequency tones of 6-7 dB [115]. However, when testing a swept wing with serrations, peak noise increased [114]. This was possibly due to the serrations introducing additional 3D features and the average slat gap was increased. Cutting gaps in the trailing edge to form rectangular brushes arranged like a comb reduced the aerodynamic penalty compared to circular section brushes [116].

Khorrami and Choudhari studied a slat trailing edge constructed out of a porous material and found significant reductions in the tones generated by shedding from the trailing edge [117]. The remaining tones moved to a higher frequency where human hearing has a reduced sensitivity. The area treated in this study was roughly twice the trailing edge thickness. Simulation showed a reduction of up to 20 dB in the far-field noise associated with the trailing edge but debris clogging the pores would be a major issue for real applications.

Application at the slat tip

The other treatable areas of the slat are the slat tips. These can feature porous edges or brushes to stop large vortices forming. Fitting a porous edge was found to

give a reduction of up to 2 dB to the far-field, with local reduction of up to 10-15 dB for certain frequencies [2]. A similar study on flap edges by Angland et al. [118] showed that porous edges allow some flow through the porous region weakening flap tip vortices and moving them away from the surface. Alternatively, brushes fitted to the slat horn provided local noise reductions of up to 8 dB [54].

An alternative to porous or brush slat tips is to fit endplates to the slat to stop the flow along the slat cove. Tests on both full-scale components and a 0.07 scale model Bombardier CRJ-700 assessed these devices [114]. For standard slats, there was a strong source at the inboard slat tip at 3.6 kHz. At this frequency, the SPL reduced by 8 dB when the endplates are used to cover the cove region but there was no benefit at higher frequencies and a tone appeared at 30.3 kHz. In an alternative refinement of the end plate concept, the slat tip was modified to extend the slat and align the inboard tip with the free-stream direction. The tip extension reduced the sound generated at 14.1 kHz by 2 dB and did not create any tonal noise. By adding a fence to the free-stream aligned tip and adding a fillet to the main element leading edge at the join with the extended tip, the sound generated was reduced by a further 3-5 dB for all frequencies.

Separation control

Micro vortex generators are an attractive flow control strategy. They can be fitted to the inside of the slat upstream of the upper trailing edge that hides the generators during cruise conditions. The vortices influence the shedding from the trailing edge. Alternatively, if there is a separation point on the leading edge of the main element, micro-vortex generators can reduce separation. If this separation does occur, it adds an additional sound source [78]. These devices have already been shown to delay separation from a flap [119] but they were not tested inside the slat cove. However, the vortices themselves are likely to generate noise, offsetting any noise benefit from the flow control. As well as vortex generators there are a variety of riblets and large eddy break up devices (LEBU) or compliant walls, which help to smooth the incoming flow past the trailing edge [120]. Although these devices are of limited use applied directly to the slat, their main purpose is to reduce separation which can lead to a drag reduction of up to 50% and a 10% lift increase [121]. This allows slower approach speeds or reduced use of slats with alternative methods used to control the boundary layer over the aerofoil suction surface.

1.3.4 Active flow and noise control

Active control offers variations on passive techniques and other techniques. The drawback is the increased complexity and the actuator power requirements.

One family of active flow control is laminar flow control, which is aimed at reducing separation, leading to reduced drag and higher aerofoil incidences [121]. This would then allow the use of a Krueger flap or leading edge droop instead of a slat. Passive devices such as riblets and vortex generators can improve laminar flow, but active methods expand the envelope where it is feasible.

One variation on passive techniques is to replace the micro vortex generators with airjet vortex generators. The main advantage is the increased strength of the vortex that can be achieved [122], which is useful in the slat cove where the flow is quite slow. Applying the airjet generators increased aerofoil lift and delayed stall [122]. This would allow slower approach speeds.

An alternative method of vortex generation is unsteady suction and blowing via zero mass actuators [123]. This has the advantage of not generating its own tones but still delaying separation. If separation reduces sufficiently, replacing the slat by simple hinged slats becomes possible whilst still reaching $C_L \geq 2.5$ [124, 125]. This removes almost all the slat noise by eliminating the cove and the slat trailing edge and the tones these generate. Alternatively, zero mass actuators used with standard slats increase C_{LMAX} and allow steeper glide slopes. Zero mass actuators applied to the cusp potentially reduce the magnitude of instabilities in the cove region [126].

Zero mass actuators remain efficient over swept wings with lift improvements of up to 10% [127]. The zero mass actuators tested were three times more effective than constant blowing and allowed separated flows to reattach. The wing sweep generates 3D features which increase the stall angle relative to a 2D aerofoil and increase the flow control impact at the wing tips [125].

Another use of zero mass actuators is to mount one in the trailing edge of the slat to remove the shedding frequency. These actuators are compatible with a thin trailing edge that vibrates with the blowing. When applied to the trailing edge of a wing, this technique reduced the tonal sound level by 6 dB [128]. This is potentially even more significant when applied to the slat by avoiding the feedback due to interactions between the main body and the unsteady gap flow.

Instead of a blowing based system, a vibrating surface can provide a similar reduction in the size of the separated flow [129]. Similar effects occur when a strong acoustic source is located close to the wing [130]. However, this is problematic for noise control due to the additional noise source and it is impractical to implement this acoustic based flow control strategy on full size aircraft.

Another use of a vibrating surface is to mount one in the trailing edge of the slat to remove the shedding frequency. These actuators are compatible with a thin trailing edge that vibrates due to a piezo-electric plate (Figure 1.8). When applied to the trailing edge of a wing, this technique reduced the tonal sound level by 6 dB [128]. This is potentially even more significant when applied to the slat by avoiding the feedback due to interactions between the main body and the unsteady gap flow.

An alternative method of eliminating slats is to employ a jet flap, which is formed by diverting the engine exhaust though the wing trailing edge [131]. The difficulty with this technique is in maintaining the efficiency of the engines and in avoiding increased jet noise.

In most locations, separation is detrimental, but it is unavoidable at the slat cusp and trailing edge. At these locations, the aim of flow control is to avoid the formation of instabilities that generate excessive noise or reduce the aerodynamic performance. Unsteady blowing applied to the cusp can unsettle the flow and help control the flow through the cove. This type of system has already been applied to large rectangular cavities such a bomb bays [132, 133] where a similar recirculation occurs. This can result in a reduction of both tonal and broadband noise. Instead of the application of a pulsed jet it is possible to use a vibrating surface [134] to control slat flow instabilities. This could reduce the weight of the system by eliminating the array of actuators with a single vibrating surface.

Blowing air normal to the aerofoil surface, for instance by using jets, can control the flow over an aerofoil [135]. The effectiveness of this technique is sensitive to the blowing direction and amplitude but can provide increased lift when the blowing re-energizes the boundary layer. Increasing the blowing amplitude is not always a benefit because it can lead to flow separation.

Steady blowing was also effective at reducing the noise in cavities [136]. Modifying the flow by blowing achieved a steadier flow. If applied to slats, this technique could stabilize the flow in the slat cove and possibly stop the interactions with the slat trailing edge. However, the location of the steady blowing application is very important to minimize the blowing rate and maintain a good flow control performance.

A more complex system is to use a sensor in the wake to apply blowing in a closed-loop control mode, in order to cancel out slat flow instabilities [137]. Theoretically, a close-loop control system could eliminate the instabilities at the cusp and stop the shear layer destabilizing due to unsteady flows in the recirculation region. However, a practical system is unlikely in the near future due to the complexity and expense of it.

A plasma actuator can control separated flows in a cavity. At low-speeds, plasma can attenuate cavity tones [138]. However, a plasma actuator can generate high-frequency tones and could be a difficult system to integrate in real aircraft.

The slat tip also an intersting area for active flow control applications. Slat tip noise could be reduced by using blowing to stop the formation of the slat tip vortices. When applied to the side edge of a flap [139], it destroyed flap side edge vortices, resulting in a noise drop of 3-4 dB above 1.25 kHz. However, the noise reduction was no better than that from applying a fence to the suction side of the flap [140]. Slat edges do not generate a vortex as well-defined as at a flap side edge so this technique is unlikely to match this effectiveness and therefore its cost effectiveness.

A more complex system could use a controllable liner [141] or vibrating wall [142]. These devices allow aircraft to change the frequency that is absorbed to match different flow conditions, reducing the noise. However, the majority of the approach is flown at a nearly constant attitude so the complex liner and control mechanism is likely to be too expensive with respect to a non-tunable device.

Another noise reduction technique is active noise cancellation. This technology has already found limited use inside aircraft but has great potential with external flows. Application is easiest where the sound source is limited to a small source area such as the slat trailing edge. Work on applying this technique to turbofan engines [143] found the number of cancelling sources must outnumber the number of tones being cancelled. Cancellation is theoretically useful for slats because there are usually only a few major sound sources located at the slat trailing edges and reattachment point. Large reductions in sound are achievable but require a complex and expensive system, deterring the implementation of active noise cancellation on aircraft for the near future.

1.3.5 Summary

In slat flow and noise studies, new experimental and computational research techniques have moved investigations from steady aerodynamics to unsteady aerodynamics and aeroacoustics. Conventional wind tunnel work involve the measurement of the time-averaged aerodynamic forces and pressure distribution to optimize an aircraft. To understand the noise sources one of the better techniques is to use PIV to identify the flow patterns. Recent computational work has focused on unsteady features using RANS or DES and examined the far-field noise reduction using acoustic analogies. Computational complexity is increasing with computing power to improve the spacial flow resolution. There is an increasing use of 3D rather than 2D simulations.

With respect to slat acoustics, the trailing edge is the important area for high frequency tonal features. At lower frequencies, slat noise is driven by the shear flow from the cusp and unsteady ejections from the slat gap.

Reducing the noise generated by these features covers two main areas:

1. Improving the performance of the main element and flap to allow a reduced use of slats, which can be achieved by reducing the flow separation over the flap using passive devices such as riblets and vortex generators or active devices like zero mass actuators.

2. Reducing the generation of unsteady features by smoothing the flow past the slat trailing edge and slat gap, which can be done by using covers, fillers or liners in the cove to smooth the flow, or by using brushes or porous surfaces at the trailing edge of the slat.

The review of previous studies show the development of the tools used to investigate aerodynamic and aeroacoustic problems. These studies also give details of the flow and control methods. The data from these sources is useful for this investigation but like this study, they exhibit three limitations restricting real world applications:

1. Results are geometry specific rather than general.

2. Computational and wind tunnel studies both require simplifications of a real wing, either through lower Reynolds numbers or through the use of simplified geometries.

3. The durability, cost, size and complexity of a slat noise suppression system can prevent work progressing beyond an academic study.

1.4 Outline of the current study

1.4.1 Control factors investigated

This investigation used the approach of attempting to smooth the flow inside the slat cove before it passes through the slat gap. Of particular interest was the occurrence of intermittent shedding through the slat gap and finding a method to control this flow feature. The main methods of controlling this disturbance investigated here in were continuous blowing in the slat cove at the reattachment point and slat cusp

extension. The investigation of blowing as a flow control technique is novel in the context of slat flow control and was therefor pursued in this work

The investigation varied the slat angle and aerofoil incidence to cover a range of flight conditions to explore the limitations of these control methods.

Constant flow rate blowing

On source of instability in the slat cove region is that the reattachment point on the slat is not fixed increasing instabilities in the shear layer. These disturbances can then pass through the slat gap where they interact with the slat trailing edge generating noise. The aim of the blowing system was to fix the reattachment point on the inside of the slat by providing a clear dividing point (Figure 1.9). By fixing the recirculation zone, less unsteady features should travel through the slat gap. Providing an additional input into the cove will also generate a boundary layer that will move disturbances away from the slat trailing edge towards the centre of the slat gap. The blowing system was adjustable to cover a range of flow conditions and can switch off when not needed, which was an advantage. However, all blowing systems have the disadvantages of complexity and power requirements. A blowing system also acts as an additional noise source so its usefulness depends on the overall noise levels.

Slat cusp geometry

Extending the slat cusp aimed at reducing the interaction at the slat cusp by eliminating secondary recirculation zones and smoothing the main recirculation region. It also provided a sharper cusp, which should weaken the shear layer. The extension was a relatively simple device to fit and it was potentially advantageous during cruise due to the cover creating a smoother retracted profile.

Aerofoil incidence

The effect of the aerofoil incidence on slat noise was investigated by monitoring the sound levels produced at different incidences. Aerofoil incidence was a key parameter as it was the primary method of altering the lift generated.

As the aerofoil incidence increased, the size of the recirculation zone reduced and the gap velocity increased. These changes also altered the reattachment location on the aerofoil. All these flow features were important with respect to slat noise and the working of the blowing system.

Slat angle

As with the aerofoil incidence, the slat angle was a key parameter in the flow through the slat cove. Therefore, altering the slat angle was an alternative to changing the aerofoil incidence with less aerodynamic consequences.

1.4.2 Flow features measured

Flow features

The primary aim of making aerodynamic wing measurements was to quantify the performance of the entire aerofoil. Measurements of the flow also showed the patterns in the flow, which helped with the identification of slat noise sources. The aerodynamic measurements taken were:

1. Force measurements to allow the assessment of the overall lift and drag.
2. Surface pressure measurements to show the location of any significant flow acceleration and diffusion along the wing profile.
3. PIV readings in the cove to allow the identification of the local flow structure.
4. Flow simulation to gain an enhanced spacial resolution of the flow with respect to the measurements and to obtain far-field acoustic predictions by an acoustic analogy.

Acoustic features

The unsteady surface pressure of the model was measured by a set of on-surface microphones to show the local SPL values. An acoustic array was used to map the source location on the wing to augment the time-resolved wall pressure data. Both sets of microphone data collected show a broadband noise distribution. In addition, the surface mounted microphones recorded tonal features that are absent in the array data.

A computational analysis of the pressure at the monitoring points allowed the simulation of the local time dependent flow. An acoustic analogy with the simulated near-field flow allowed the calculation of the far-field acoustic radiation from the near-field aerodynamic predictions.

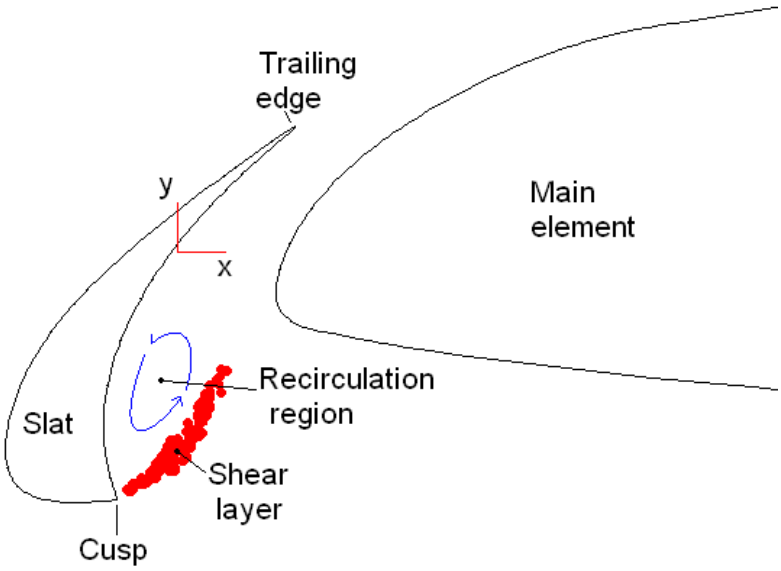

Figure 1.1: Features of the flow around a slat.

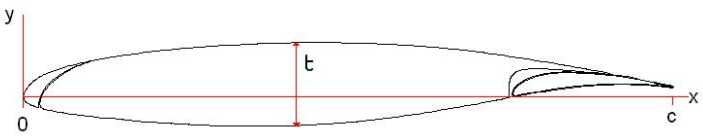

Figure 1.2: Aerofoil geometry.

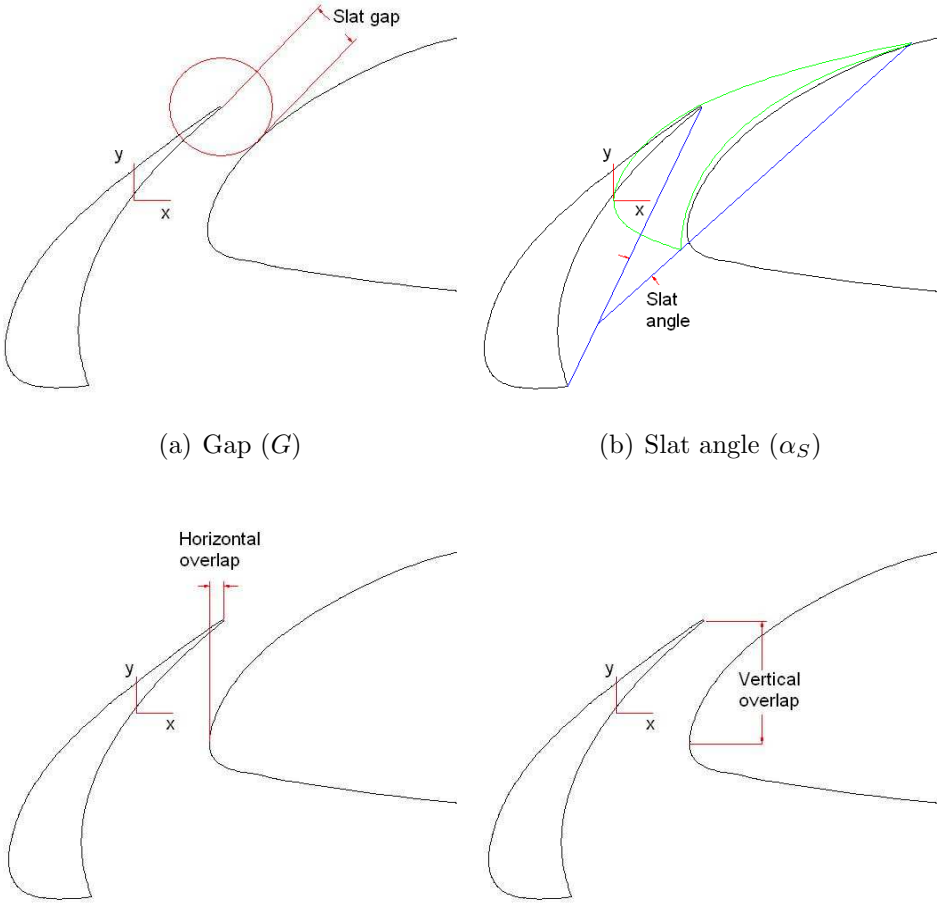

(a) Gap (G)

(b) Slat angle (α_S)

(c) Horizontal Overlap (O_H)

(d) Vertical Overlap (O_V)

Figure 1.3: Definition of slat position.

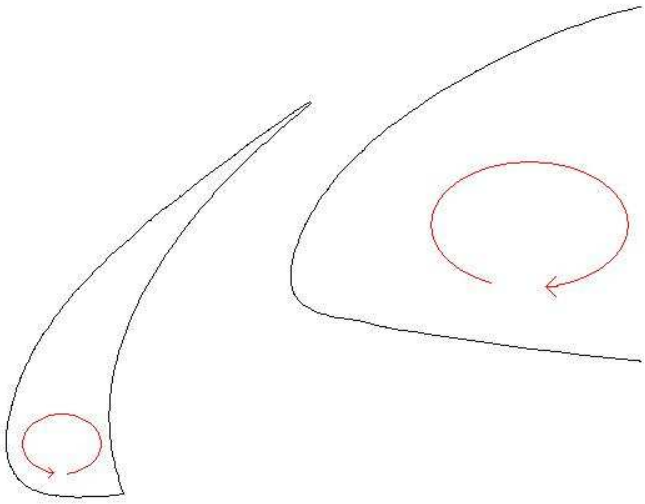

Figure 1.4: Slat and main element flow circulation.

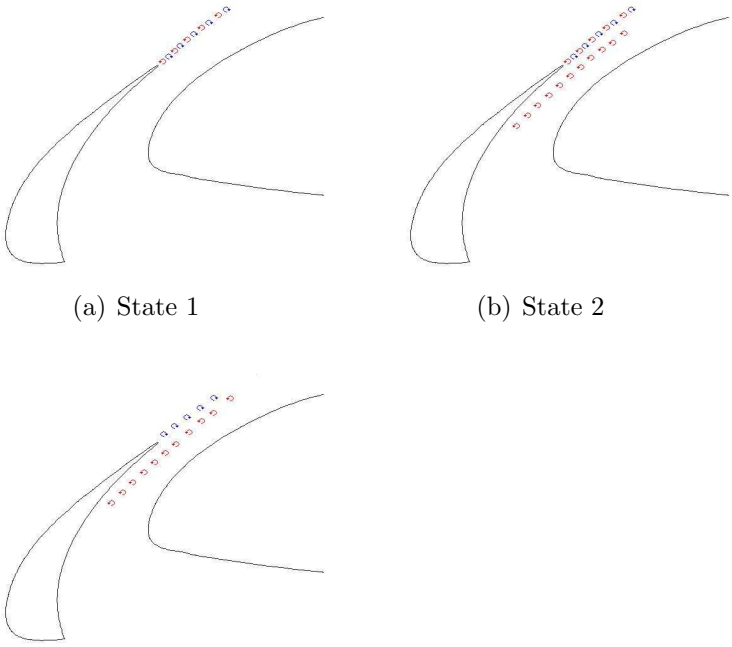

(a) State 1

(b) State 2

(c) State 3

Figure 1.5: Shedding states proposed by Jenkins et al. [60].

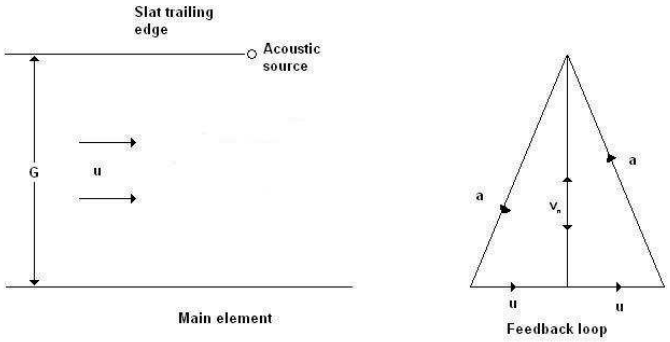

Figure 1.6: Whistle feedback mechanism proposed by Tam and Pastouchenko [62].

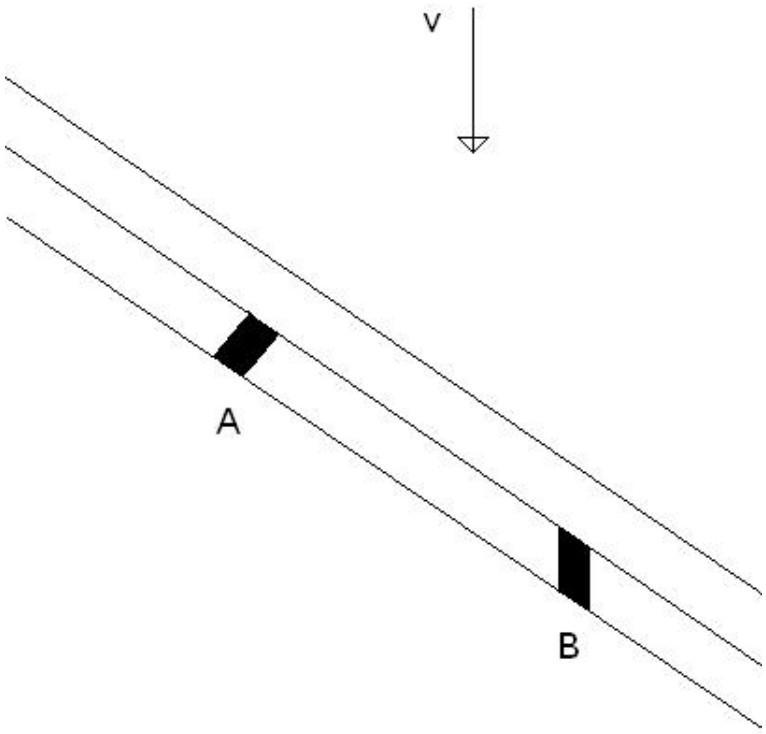

Figure 1.7: Slat track orientation. (A) Perpendicular to the wing. (B) Aligned to the flow.

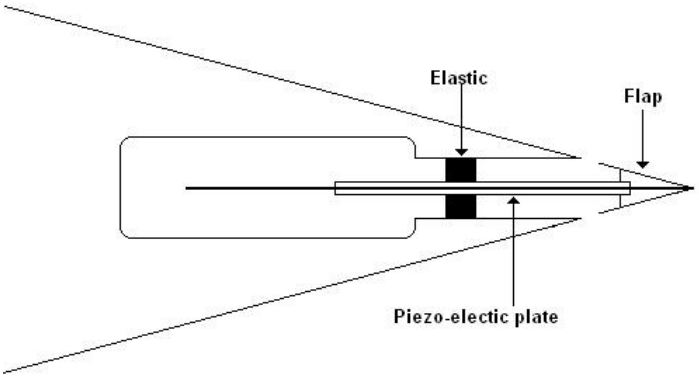

Figure 1.8: Vibrating trailing edge tested by Nakashima and Akishito [128].

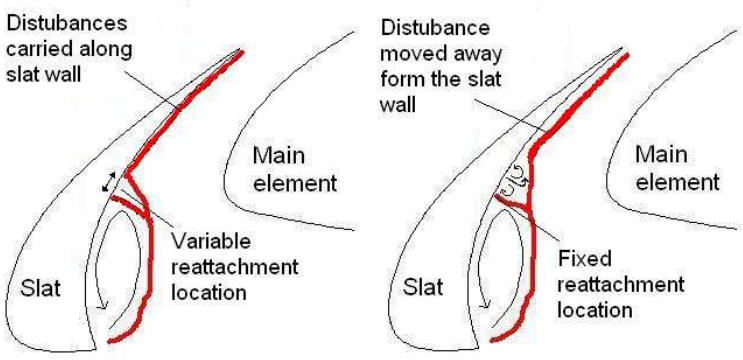

Figure 1.9: Proposed action of the blowing system.

Chapter 2

Methodology

2.1 Introduction

This chapter details the methods used in this study. The initial section outlines the geometry of the aerofoil studied along with the baseline reference settings for the slat and flap. The next section covers the experimental work starting with details of the model and experimental facilities. The experimental section finishes with details of measurement methods. The computational section starts by presenting the computational methods. It is followed by descriptions of the exact conditions investigated and the grid. The final section outlines the technique used to model the far-field sound levels based on the near-field aerodynamic predictions.

2.2 Geometry

2.2.1 Aerofoil geometry

This study used a three-element aerofoil provided by Airbus UK (Figure 2.1). All three elements of the aerofoil had finite thickness trailing edges. Table 2.1 outlines the dimensions of the elements. The study examined the aerofoil with zero sweep angle and zero taper. Experimentally the wing had a finite span with end plates but the computational work used a combination of 2D and periodic 3D simulations. Simplification of the design involved not including any slat or flap brackets, which are additional acoustic sources. However, the finite thickness trailing edges remained because they are integral to the sound sources under investigation so they were not idealized to perfectly sharp ends.

The axis system for the aerofoil used an origin located at the leading edge of the aerofoil in its retracted configuration. When orientated as an aircraft wing x points

towards the trailing edge, y points vertically upward and z along the span towards the port wing tip.

2.2.2 Reference settings

The reference settings reflected the landing configuration with both the slat and flap deployed. Table 2.2 shows the details of the locations.

This study compared the reference configuration with three other settings with reduced slat angle and slat gap. The slat angle was moved in 5° increments giving three slat angle settings of α_S=23°, 18° and 13°. Investigating the impact of changing the slat location involved reducing the slat gap from $0.017c$ to $0.01c$. For each of these positions the flap was unaltered. Table 2.3 shows the changes in the settings.

2.3 Experimental methodology

2.3.1 Experimental aims

The aim of the experimental programme was primarily to examine the near-field flow. Measurements of the near-field noise were mainly obtained through the microphone array due to the need to filter out the relatively high background noise levels present in the wind tunnel. Array measurements complemented the near-field data and gave an indication of the far-field sound levels.

Initial measurements examined the sound levels of the reference configuration. Changes in the near-field acoustics then allowed the assessment of the effectiveness of the flow control at altering the source strengths. When changes in the acoustic near-field appeared, PIV allowed the identification of the flow changes responsible for them. Measurement of the aerofoil surface pressure distribution and aerodynamic forces enabled the assessment of the aerodynamic impact of any changes in the flow field.

Achieving these aims involved the use of five main measurement techniques:

1. Flush mounted surface microphones to measure the local sound levels.
2. An acoustic array to map the sound source locations.
3. PIV to map the flow features around the slat.
4. Pressure taps to examine the mean flow and show the aerodynamic impact of changes to the aerofoil.

5. Force balance to measure the aerofoil aerodynamic forces.

The sensors were located at the centre of the slat span in order to minimize the appearance of any 3D features. These would not dominate on a real aircraft due to the large aspect ratios used.

2.3.2 Model design

Model requirements

The wind tunnel model's final configuration depended on a range of diverse requirements. These requirements include the need to

1. accurately match the geometry of the aerofoil section under investigation,
2. allow variations in the slat position,
3. allow the application of blowing at the desired location,
4. incorporate the pressure taps and flush mounted microphones,
5. allow visual access to the slat cove for PIV,
6. minimize aeroelastic deformation and vibration of the model,
7. avoid excess blockage and loading, and
8. minimize the impact of the endplates and tunnel mountings.

The five main measurement techniques influenced the model design. However, the main restrictions on the model were the need to fit the pressure taps and microphones inside the slat along with the blowing system.

The blowing system split the slat into three pressure chambers to distribute the blowing across the full span. These vented to the slat cove via blowholes located at the reattachment location. The slat required a large number of holes to give a smooth distribution across the span and to minimize the impact of the gaps between the blowholes. The size of the air supply tubing limited the size of the holes. The cross-sectional area of the tubes was set at half the size of the blowing tubes so its velocity was double the blowing rate. This was in addition to any losses in the tubing system.

The pressure chambers joined to an external compressor, which provided air compressed up to five bar via an adjustable control valve. This increased internal

pressure, while the external pressure in the cove region reduced relative to ambient pressure when the wind tunnel is running, creating the driving force for the blowing. A pressure tap located inside each chamber monitored the internal pressure. The external pressure was approximated using pressure taps located both sides of the blowing location 2 mm from the blowholes. A rotometer attached to the air supply monitored the blowing rate. A manometer measured the pressure at this location to record the density and hence mass flow rate of the blowing system.

The inside of the slat contained the pressure tap tubing and microphone cables mounted in the slat in addition to the tubes linking the air supply to the blowing system. The internal size of the slat determines the overall size of the model so this becomes the determining factor in the minimum chord length. The slat was manufactured using a carbon fibre skin of at least 1.5 mm thick and this meant the slat at the blowing location had to exceed 3 mm in width. An additional offset allowed for the glue in the slat skin to spread during construction without blocking the holes. The blowing location was fixed to coincide with the shear-layer reattachment line in the slat cove, as determined by computational fluid dynamics (Figure 3.33). This gave a minimum size of c=800 mm, representing a slat chord of 92 mm. This limited the number of sensors that could be fitted inside the slat. The span was limited to 1 m to avoid excessive blockage in the tunnel. An alternative method was to modify the profile in order to reduce the lift and blockage and allow a larger slat cross-sectional area. However, a shortened trailing edge would reduce the circulation around the wing and alter the flow around the slat.

The main element also needed fitting with pressure taps to allow monitoring of the surface pressure distribution. Additionally, the leading edge of the main element needed microphones to measure the unsteady pressure on the other side of the slat cove. The main element was larger than the slat so the sensors did not impose any additional restrictions on the main element design.

PIV had a smaller impact on the design of the model. The model needed endplates in order to achieve a quasi-2D flow in the centre span of the wing because the model did not completely span the wind tunnel. Hence, the endplates required optical access to the slat region, to allow the camera to see the flow in the cove, for the PIV measurements. PIV also required that the model did not produce strong reflections from the laser requiring the painting of the model black.

The microphone array had little impact on the model because of the array location away from the model. The main requirement of the array was a direct view of the model and minimization of acoustically reflective surfaces and other sound sources.

The model cusp extension fitted flush with the slat wall at the cove (Figure 2.2). The extension also matched to the retracted slat setting so in this configuration it would cover the gap between the slat cusp and main element. The extension was manufactured using stereo-lithography so the edges had a minimum thickness of 0.5 mm to avoid damage and vibration.

Model structure

The models 800 mm chord and 1,000 mm span also limited the forces generated to manageable values. Limiting the span had structural advantages by reducing the stiffness needed to prevent wing warping. However, a small aspect ratio required large endplates to produce a near 2D flow at its mid-span. Cherry wood made up the majority of the main element with a carbon fibre trailing edge added to prevent deformation.

The slat and flap were constructed from carbon fibre skins. This enabled the manufacture of the thin trailing edges and restricted the deformation of the slat and flap by the aerodynamic loads. The use of carbon fibre allowed shaping of the trailing edge within 0.1 mm of the design. The final design featured thirty external pressure taps on the slat along with three internal taps to measure the pressure inside the three air supply settling chambers of the slat. These were spaced out based on the pressure distribution found computationally. The distribution was set to give approximately constant change in pressure between adjacent taps around the slat (Figure 2.3). The blowholes were drilled into the slat skin, each was 1 mm in diameter and they were located in two lines each spaced every 5 mm (Figure 2.3). The lines were 2.5 mm apart with the holes alternating between the two lines (Figure 2.4). This gave 400 holes per metre of span . The slat and flap attached to the endplates via 15 mm thick aluminium ribs glued in place inside the skins. Thinner 6 mm ribs divided the slat into three internal plenum chambers.

The hardwood construction of the majority of the main element allowed the cutting of grooves in the surface to mount the sensors. After fitting the sensors, the surface required filling, smoothing and painting to avoiding light reflection during the PIV testing. There were 45 pressure taps on the main element, which were concentrated near to the leading edge along with two microphones mounted in the leading edge to monitor the pressure inside the cove (Figure 2.5).

The primary function of the endplates was aerodynamic. However, they also acted as the mounts for both the slat and the flap. The need to investigate different settings led to fitting adjustable outer windows around the slat. Slots were used to allow the adjustment of the slat gap and of its overlap. These allowed changes of

$0.01c$ in both the horizontal and vertical directions. Replacing the panels to which the slat attached allowed the slat angle to vary. Glass inner panels for the starboard endplate allow optical access to the slat cove. The endplate construction used 6 mm aluminium sheets machined to accommodate the windows. The sheets had cutouts with honeycomb inserts to reduce their weight and 1 mm aluminium sheets covering both sides to maintain the endplate stiffness. Rounding the edges of the endplates minimized separation (Figure 2.6).

The model was mounted inverted, attached at three points. The two main struts were attached to the pressure surface of the main element at x=$0.37c$ spaced 700 mm apart. They attached to steel top-hat inserts recessed into both surfaces of the wing and distributed the load preventing damage to the main element. The inserts were clamped together using an M12 bolt and covered using plasticine (Figures 2.4 and 2.7). The two main struts provide the pivot point for the model to allow alteration of the aerofoil incidence from -5° to 22.5°. The third connection was a tail bar attached to a structure mounted between the two endplates above the flap. The tail bar construction used aerodynamically shaped steel tubing to minimize its aerodynamic interference. The tubing formed a triangular structure to distribute the loading to the endplates and avoid deformation (Figure 2.8).

The initial tests of the model were in a free transition configuration. Later on, trip strips were added upstream of the slat cusp and trailing edge. The addition of the trip strips prevented laminar flow separation around the cusp [2] and gave a closer match to a higher Reynolds number flow with natural transition. The trip strips were each 12 mm wide and used 80 grit. The strips were located 4-16 mm from the cusp and 44-56 mm from the slat trailing edge on the convex side. The cove side of the trailing edge remained free transition.

2.3.3 Wind tunnel facilities

The wind tunnel tests used the 3.5 m×2.6 m R. J. Mitchell tunnel at the University of Southampton. The tunnel had a maximum velocity of 45 m/s but for these tests, the maximum speed used was 35 m/s due to the large lift forces and pitching moments generated by the wing. Above this speed, the motor holding the tail bar could not fix the aerofoil incidence at a steady value. This represented a maximum Reynolds number of Re=2.33×10^6 based on the retracted chord of 800 mm. The design of the tunnel gave a free stream turbulence level of less than 2%.

2.3.4 Measurements

Test conditions

The tests used a reference aerofoil incidence of 5° with the slat and flap in their reference positions. The test used 30 m/s as the baseline velocity. However, this was too fast for the PIV system so PIV measurements for the reference configurations were obtained at the reduced velocity of 25 m/s.

The aerofoil incidence was set at 0, 5, 10, 15 and 20° and testing was carried out at v=10, 20 and 30 m/s. The blowing system ran with the blowing set at 0, 60, 80, 100 and 120 litres per minute (LPM). Testing ran both with and without trip strips applied to both the slat trailing edge and slat cusp.

Forces

To measure the aerodynamic forces, a 6-component balance system was used. The balance was located above the model and attached to the three struts (Figure 2.8). The wind tunnel model was large so the blockage of the wind tunnel affected the force measurements. The force measurements were corrected for wind tunnel blockage using ESDU 76 028 [144]. The forces also incorporated tare values to compensate for the impact of the struts and endplates on the force readings. The force corrections are examined in Appendix A.

Oil flow

To assess 3D features on the wing, oil flow runs were carried out at α=5° and 10°. Oil flow involved applying a mixture of paraffin and titanium oxide powder to the surface of the wing. Running the wind allowed the paraffin to evaporate leaving streaks of titanium oxide, which identify the mean surface flow direction, transition and separation.

Pressure taps

The pressure taps were monitored using two ZOC systems each with 32 channels. The main element was attached to the low range zoc with a range of ±10"H^2O which corresponds to maximum of C_P±4.5 at 30 m/s. The slat pressure taps were attached to the high range zoc, which had a range of ±20"H^2O. Averaging the pressure over 40 seconds for each reading taken gave the mean pressure values. Recording each condition three times allowed further averaging. Repeating the runs helped in the detection of malfunctioning pressure ports, which had large differences

between the runs. Steel tubing with an outer diameter of 1.25 mm forms the basis of the pressure taps. A 0.6 mm hole drilled in the side of the tube exposed the tube at the measurement location. The tubes were glues in the slat, to the inside of the carbon skin and sealed through the ribs that make up the pressure bulkheads between the plenum chambers. On the main element, the tubes recessed into the surface. The tubes connected to the ZOC systems using portex tubing with an inner diameter of 1 mm.

Particle image velocimetry

The PIV system used a Dantec HiSense camera and a Gemini PIV 15 laser. The laser used two tempest Ng:YAG lasers to produce twin pulses of light at up to 120mJ per pulse. The light had a wavelength of 523nm. The system was set with the laser mounted in the roof of the tunnel to illuminate the slat cove on the tunnel centre line, at the slat mid-span. The camera was fitted outside the tunnel so it could view along the slat through the glass window in the endplate (Figure 2.9). The camera was fitted with a 60 mm lens at a distance of 1,800 mm from the measurement plane while the laser was located at a distance of around 1,250 mm.

The camera synchronizes with the laser so the two images are taken when the pair of laser pulses illuminates the flow. The typical time separation between the pair of images was around 30μs. The camera had a resolution of 1,280×1,024 pixels. This represented a plot resolution of 157×125 vector maps, constructed using an area of 32×32 pixels with an overlap of 75%. Seeding particles were provided by a smoke generator located downstream of the model allowing the smoke to become more uniform as the flow passes around the closed loop tunnel. However, it was not possible to get good readings at speeds above 25 m/s. The large size of the tunnel leads to a rapid deposition of the seeding particles and the generator cannot replace them fast enough. The tunnel size also increases the attenuation of the laser sheet intensity due to the wide angle of its lens and requires increased distance between the camera and the area recorded. The slat restricting the amount of seeding entering the cove region further complicated the situation. PIV ran at 10 m/s, 20 m/s and 25 m/s. Tests at 30 m/s did not yield usable results due to inadequate seeding in the slat cove.

The PIV data gave a map of the velocity on a plane through the slat cove. Plotting the vorticity allowed the visualization of the shear layer. The vorticity is obtained from the velocity vectors using the central differencing numerical scheme used in tecplot [145]. A vorticity plot gave the direction of the flow from the cusp and showed the size and shape of the recirculation region. The vorticity plot showed

the shear layer but was less good at picking out discrete vortices when the shear layer breaks down. Where discrete vortices are present, the Q criterion developed by Weiss and Okuba allowed their visualization [146, 147]. Subtracting the strain rate (S) from the vorticity (Ω) gave the Q value. If the value is positive, then there is a vortex.

$$Q = \frac{1}{2}(|\Omega|^2 - |S|^2) \tag{2.1}$$

$$\Omega = \frac{1}{2}(\nabla\overline{u} - (\nabla\overline{u})^T) \tag{2.2}$$

$$S = \frac{1}{2}(\nabla\overline{u} + (\nabla\overline{u})^T) \tag{2.3}$$

Microphone readings

There were six microphones fitted around the slat (Figure 2.3) and two near the leading edge of the main element. The microphones used were Panasonic WM-60A condenser microphones, each had a diameter of 6 mm and a length of only 5 mm. The microphones were sensitive from 20 Hz to 22 kHz and gave a signal to noise ratio of 58 dB. The microphones required an operating voltage of 2V, which the pre-amps provided. The microphones on the slat were labelled S1-S6, when viewed in a clockwise direction starting from the leading edge next to the cusp. On the main element, M1 was located in the nose of the main element with M5 close to the retracted trailing edge position. Performing a fast Fourier transform (FFT) analysis on the signal from the microphones generated the frequency spectra. This FFT averaged over 100 sets of data to smooth the signal and improve the signal to noise ratio. The FFT used 2,048 samples from each data set, which was sampled at 48 kHz to give a Nyquist frequency of 23 Hz on the microphone spectra.

The surface mounted microphones had a constant response over the frequency range allowing calibration at a single point. A pistonphone allowed collection of the calibration values of the microphones; this produced a tonal signal at 1 kHz and 94 dB. To give the correct amplitude the microphone fits inside the pistonphone. For the surface microphone, this was not possible because the microphones could not detach from the wing due to the need to keep the slat pressurized. This created problems in obtaining an accurate reading of the absolute value of the sound levels, but the microphones could still monitor changes in sound level caused by alterations in the test conditions.

Acoustic source distribution

Measuring the source distribution used a microphone array based on 56 Panasonic WM-61 microphones. The WM-61 microphones are similar to the WM-60 microphones except they have a reduced length of 3.4 mm and the signal to noise ratio was increased to 62 dB. After taking calibration readings, the microphone array was assembled onto a plywood panel. Cling-film covered the panel to provide a smooth cover and remove the interaction between the boundary layer and the microphone openings. The array was mounted flush with the wind tunnel ceiling 1270 mm above the model (Figure 2.10). The array recorded in 400 blocks of 512 samples at a frequency of 48 kHz to allow sufficient averaging. The array data gave the source strength in fourteen 1/3 octave bands from 1 kHz to 20 kHz. The array determined the SPL level over a 100×100 grid, located in the plane of the wing, to reconstruct the sound measured. The noise map was assembled using the beamforming method [148].

2.4 Computational methodology

The computational work divided into two main steps, computational fluid dynamics (CFD) and computational aeroacoustics (CAA). The first step involved solving the Reynolds averaged Navier-Stokes (RANS) equations to simulate the flow close to the aerofoil. An unsteady simulation gave a time history of the near-field conditions, which included the time-dependent near-field pressure fluctuation.

The simplest acoustic analysis used the near-field pressure history to estimate local sound levels. An acoustic analogy estimated the far-field sound levels.

2.4.1 Computational aims

The computational work was complementary to the experimental work, filling in the gaps in the data provided by the experimental study. The overall target was to generate the near-field data necessary to employ an acoustic analogy. The experimental work allowed the validation of the near-field simulation by comparing the flow features around the slat. The experimental data was limited to the near-field, so the computational work became the sole source of far-field SPL levels, which were used to test flow control method effectiveness in aerodynamic noise reduction.

Simulations were also useful in the investigation of the shape of the unsteady flow features, complementing the PIV work. The simulation gave a clearer image of the small-scale features, enabling an improved analysis of the flow patterns.

The computational work had the advantage of allowing higher Reynolds numbers relative to the experimental work. However, simulations were time-consuming, so the number of cases run was significantly limited.

2.4.2 Computational formulation

As with all CFD simulations, the basis of the method was a set of conservation laws. To simulate the flow around the aerofoil section, the Navier-Stokes equations were used to give conservation of mass, momentum and energy [149].

$$\frac{\partial \rho}{\partial t} + \nabla.(\rho \overline{u}) = S_m, \tag{2.4}$$

$$\frac{\partial \rho \overline{u}}{\partial t} + \nabla.(\rho \overline{u} \overline{u}) = -\nabla p + \nabla.\overline{\tau} + \rho \overline{g} + \overline{F}, \tag{2.5}$$

$$\frac{\partial}{\partial t}(\rho E) + \nabla.(\overline{u}(\rho E + p)) = -\nabla.(K_{eff} \nabla T - \Sigma_j h_j \overline{J}_j + \overline{\tau}.\overline{u}) + S_h, \tag{2.6}$$

where $\overline{\tau}$ is the stress tensor

$$\overline{\tau} = \mu[(\nabla \overline{u} + (\nabla \overline{u})^T) - \frac{2}{3} \nabla.\overline{u} I]. \tag{2.7}$$

In the above equations, ρ is density, t is time, $\overline{u}$ is the velocity vector, S_m is a mass source, p is the static pressure, $\overline{F}$ is an external body force, E is total energy, K_{eff} is the effective conductivity, T it the absolute temperature, h_j is enthalpy of species j, $\overline{J}_j$ is diffusion of species j, $\overline{\tau}$ is the viscous stress tensor, S_h is a term for additional heat sources, μ is the molecular viscosity and I is a unit tensor.

For an adiabatic non-reacting, neutrally buoyant flow equations 2.4- 2.7 become:

$$\frac{\partial \rho}{\partial t} + \nabla.(\rho \overline{u}) = 0, \tag{2.8}$$

$$\frac{\partial \rho \overline{u}}{\partial t} + \nabla.(\rho \overline{u} \overline{u}) = -\nabla p + \nabla.\overline{\tau}, \tag{2.9}$$

$$\frac{\partial}{\partial t}(\rho E) + \nabla.(\overline{u}(\rho E + p)) = -\nabla.(K_{eff} \nabla T - \Sigma_j h_j \overline{J}_j + \overline{\tau}.\overline{u}). \tag{2.10}$$

All aerodynamic flows satisfy the Navier-Stokes equations, however, the equations cannot be solved exactly for most real flows. Hence, CFD uses finite difference and finite volume schemes to approximate their solution. As with all numerical calculation, the size of the numerical grid is a key factor in determining the accuracy of the predictions. Computational limitations make it impossible to generate a grid fine enough to capture the smallest scales of motion in engineering flows.

One method of reducing the computational cost is to use Reynolds averaged Navier-Stokes equations (RANS). These equations are based on the conservation of mass and momentum equations that form part of the N-S equations. The RANS equations are formed by replacing all the velocity components and pressure by time mean and fluctuation about the mean components. The resulting values are averaged. When averaged the fluctuating components average to zero when not combined with another fluctuating component. Assuming the fluctuations in density, and moecular viscosity are negligible, this leaves the $-\rho u'u'$ term, which is needed to close the equations. This term is known as the Reynolds stresses and is modelled by a turbulence model in RANS simulations. The RANS equations are [149]:

$$\frac{\partial \rho}{\partial t} + \nabla.(\rho \overline{u}) = 0, \tag{2.11}$$

$$\frac{\partial \rho \overline{u}}{\partial t} + \nabla.(\rho \overline{u}\overline{u}) = -\nabla p + \nabla.\overline{\tau} - \nabla.(\rho \overline{u'u'}) \tag{2.12}$$

Where $\overline{u}$ and p are averaged values and $\overline{u'}$ is the fluctuating velocity component.

RANS simulations model all of the Reynolds stresses. However, if the grid is fine enough, the large-scale turbulent features are resolvable. If the large-scale turbulence is simulated and modelling only covers the small scales, the simulations becomes a large eddy simulation (LES). Detached eddy simulation (DES) is a combination of RANS and LES where the simulation covers the large turbulent scales away from walls but the full Reynolds stresses are modelled close to walls. The greater the percentage of the unsteady flow simulated rather than modelled the better the result. However, the simulation of the flow unsteadiness can only occur where the grid resolution is adequate.

This study used Reynolds averaged Navier-Stokes equations and DES with a finite-volume scheme applied on the computational grid built around the wing. The solution then employed time marching to allow the solution to evolve temporally. The use of sub-iterations improved the accuracy of the temporal scheme. For computational cost reasons, the grid did not cover all small-scale features present in a real flow, necessitating the use of a turbulence model.

Flow conditions

The CFD work concentrated on the reference geometry and α=5°. The simulations used the slat and flap in their reference positions. The simulations were carried out at M=0.2, which is a standard landing velocity.

Both blowing and no-blowing cases were modelled. Initial 2D simulations had

the blowholes replaced by a slot. Clearly this was not a realistic case so later work used a narrow 3D grid which allowed the use of discrete blowholes. However, due to the size of the computation, it was necessary to simplify the geometry by replacing the round blowholes by square holes. This allowed simulation of the small-scale 3D features around the blowholes.

Simulation technique

The simulation work was carried out using Fluent. Initial work used a 2D grid using a variety of turbulence models in URANS simulations. These simulations did not pick up any unsteady feature in the slat cove due to excessive numerical dissipation.

To reduce the numerical dissipation in the cove region, the turbulent production term in the $k-\omega$ shear stress transport (SST) turbulence model was switched off in the area shown in Figure 2.11. This technique to reduces the eddy viscosity in the cove region was developed by Khorrami et al. [86, 87] and assumes that the large flow acceleration through the cove keeps the flow laminar. Some supporting evidence for this is that the slat system featured a laminar separation from the slat cove for a large part of the flight envelope. With the turbulent kinetic energy production term suppressed, unsteady features developed in the slat cove allowing the investigation of the application of flow control.

Including blowing in the cove simulation gave an initial assessment of the blowing system. The main limitation was that the 2D simulation modelled blowing through a slot rather than through small holes as used in the experiment (Figure 2.4). Therefor the 2D simulation was not representative of the experimental setup.

To allow the simulation of the discrete blow holes, a narrow 3D simulation was set up. Using periodic boundaries in the spanwise direection partially compensated for the limited span of the model. The scale of the blowhole distribution, which was set at $6.25\times10^{-3}c$, gave two blowholes across the numerical model span and fixed the span of the simulation domain. Replacing the round blowholes by square holes allowed the use of an extruded grid and avoided excessively skewed cells, simplifying the geometry. Transition was modelled by suppressing the kinetic energy production terms around the leading edge of the slat up to the location where the trip strip was placed on the experimental work.

For the 3D simulations detached eddy simulation (DES) was used. This allowed to resolve the main flow unsteadiness in the cove, removing the need for a laminar zone. At the start of the time-resolved computations the conservative velocities were initialized using the results from a Spalart-Allmaras steady RANS simulation.

The time step for the 2D time resolved computations was set at $\triangle t$=1×10^{-5}

seconds. A numerical experiment was performed on the selection of the time step. It was found that increasing $\triangle t$ to 1×10^{-4} seconds did not give enough time steps for the shear layer to break down before the vortices leave the cove. The 3D simulations used the same time step size as the 2D simulations.

Grid

The 2D grid design was a multi-block structured C type grid, which fits around the outside of the aerofoil. This extended out to a distance of ten chords downstream and eight chord lengths upstream from the aerofoil reference point (Figure 2.12). This reference point was located at the leading edge of the slat when it was in the retracted position (Figure 2.1(a)). All grids were fully one-one block matched grids so they require no interpolation across internal domain computational boundaries. This reduced the impact of the joins between the blocks. The drawback of the selected computational mesh geometry was that a large number of cells was generated away from the slat, particularly in the wake region. The cells were concentrated around the slat and the cell size expands rapidly to the far-field to keep the number of cells to an acceptable number. In most directions the geometric stretching was kept below 1.10 but it was higher at the far-field boundary and away from the slat cove, which is the primary area of interest (Table 2.4).

The grid structure was complicated by the addition of the slat and the flap, especially the near right angles at the slat cusp and upstream of the flap cove. These make it impossible to use a conformal C type grid. The grid was smoothed to minimize skewness and reduce the cell aspect ratios where possible (Figures 2.13 and 2.14).

Close to the wall, the wall-normal first interior cell is $\triangle x=1\times10^{-5}c$. This gives a y^+ value of one, which allows to resolve of the boundary layers. The cell size at the far-field increased to $\triangle x=0.5$, which results in a range of scales of 5×10^4. This was acceptable in a 2D simulation, because the cells expand in both directions, so the cell aspect ratios remain within acceptable limits. The use of large cells in the far-field keeps the number of cells to an acceptable number of around 2.50×10^5.

The 3D simulations used a teardrop shaped grid. The grid was based on a 2D grid produced by Zhaokai Ma [112] (Figures 2.15 and 2.16). The grid used a teardrop rather than a circular geometry to reduce the skewness of the cells above the suction surface of the aerofoil. The grid placed the outer computational domain boundary at a distance of ten chord lengths from the aerofoil reference point.

Forming the 3D grid required reducing the resolution away from the walls and adding the discrete blow holes. For the narrow geometry, eleven equally spaced slices

constituted the spanwise direction to allow the creation of simplified blow holes on the inside of the slat (Figure 2.17). The grid contained 1.18×10^6 cells and had a width of $6.25\times10^{-3}c$.

Boundary conditions

The far-field boundary of the grid used a pressure far-field boundary condition, which fixed the pressure, Mach number and flow direction, at the boundary, allowing the other values to vary. Therefore it must be located far enough from the aerofoil to allow the fixing of those variables. The grid had an aerofoil incidence of α=0° so the free-stream direction of the flow determined the aerofoil incidence. The pressure far-field was a non-reflecting condition designed for compressible flow and uses Riemann invariants for incoming and outgoing waves [150].

For the 3D simulations, periodic boundary conditions were used in the spanwise direction.

Simulation settings summary

The 3D simulations used the following settings:

1. The code used was Fluent 6.2.
2. The simulation used a coupled, DES formulation, with the ideal gas law and the energy equation to allow compressible flow.
3. The pressure was set with gauge pressure at 0, and operating pressure at 101,325 Pa.
4. The boundary used the pressure far-field condition. This was set with a Mach number of 0.2, x component of 0.996, y component of 0.087 and a temperature of 288°K.
5. The temporal scheme had a time step size of 1×10^{-5} with 30 sub-iterations per time step using a third order MUSCL scheme [151].
6. The spatial scheme used a third order MUSCL formulation.

Analysis methods

Two main methods obtained the acoustics from the simulations. The simplest was to record the data at a point and use a FFT to calculate the acoustic spectra. However,

this is a point analysis so it was hard to build up a picture of the acoustics of the entire system.

The second method was an acoustic analogy to give the far-field directivity.

2.5 Far-field noise prediction

2.5.1 Acoustic analogy

The FW-H acoustic analogy generated the far-field data for this study. This took the pressure data on an integration surface to obtain the pressure history at monitoring points in the far-field. The far-field calculations used the FW-H solver developed as part of sotonCAA (aka SHOCASE3D), which is a high-order CFD package with an FW-H solver developed at the University of Southampton [152]. In this project only the FW-H component was used which is based on the FW-H formulation developed by Farassat and Succi [153, 154].

A total of 100 monitoring points were set up to form a ring 100 m from the slat in the centre span plane. The pressure history at these points was calculated by the numerical solution of the FW-H equation. The pressure history at the far-field points was then analyzed to find the RMS pressure at each point and hence the directivity of the radiated sound.

2.5.2 Integration surface

The integration surface used was located on the slat wall rather than away from the surface. The integration surface was on the wall for two reasons:

1. The acoustic analogies did not work well where turbulent flow features pass through the integration surface [155]. This was unavoidable for an integration surface location close to the walls.

2. If the surface was located further from the walls, the grid resolution was not as high as in the cove region and the simulation of sound waves was less accurate.

The analogy separately calculated the far-field contributions from the three aerofoil elements using surface data. Combining the three values gave the total unsteady pressure at the monitoring points. This was valid because all three far-field simulations use the data from the same simulation so there was a common time at the monitoring points during the combination process. The limitation of this technique was that the quadrapole terms and the sound shielding provided by neighboring surfaces were not included in the analogy.

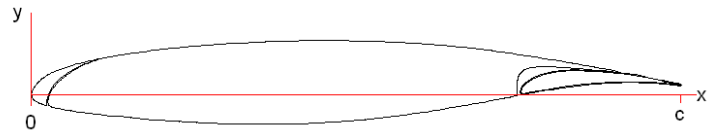

(a) Retracted geometry.

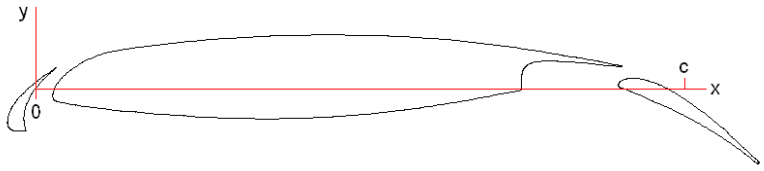

(b) Reference geometry.

Figure 2.1: Slat geometry.

Geometric feature	Value
1) Thickness to chord ratio (t/c)	0.128
2) Main element chord	$8.76\times10^{-1}c$
3) Main element trailing edge thickness	$1.51\times10^{-3}c$
4) Slat chord	$1.15\times10^{-1}c$
5) Slat trailing edge thickness	$6.62\times10^{-4}c$
6) Flap chord	$2.48\times10^{-1}c$
7) Flap trailing edge thickness	$3.11\times10^{-3}c$

Table 2.1: Aerofoil dimensions.

Geometric feature	Value
1) Flap angle (α_F)	30°
2) Flap gap (H_F)	$1.65\times10^{-2}c$
3) Flap overlap (O_{HF})	$5.00\times10^{-3}c$
4) Slat angle (α_S)	23°
5) Slat gap (G)	$1.68\times10^{-2}c$
6) Slat horizontal overlap (O_H)	$5.06\times10^{-3}c$
7) Slat vertical overlap (O_V)	$4.25\times10^{-2}c$

Table 2.2: Reference slat and flap settings.

Position	G	O_H	α_S
Ref	$1.68\times10^{-2}c$	$5.06\times10^{-3}c$	23°
18°	$1.68\times10^{-2}c$	$5.06\times10^{-3}c$	18°
13°	$1.68\times10^{-2}c$	$5.06\times10^{-3}c$	13°
13°RG	$1.01\times10^{-2}c$	$1.51\times10^{-3}c$	13°

Table 2.3: Slat positions investigated.

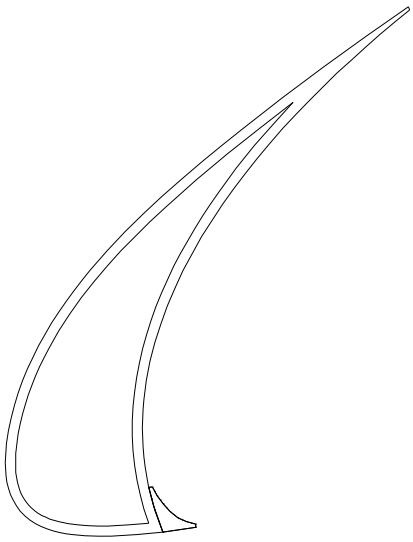

Figure 2.2: Geometry of the slat cusp extension.

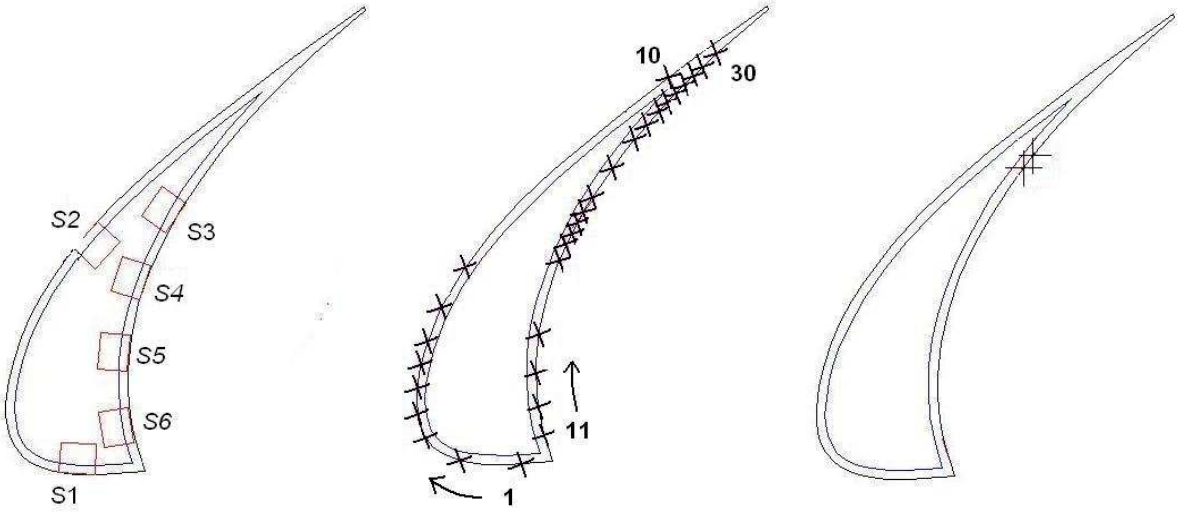

(a) Microphone locations (b) Pressure tap locations (c) Blow hole locations

Figure 2.3: Sensor locations on slat.

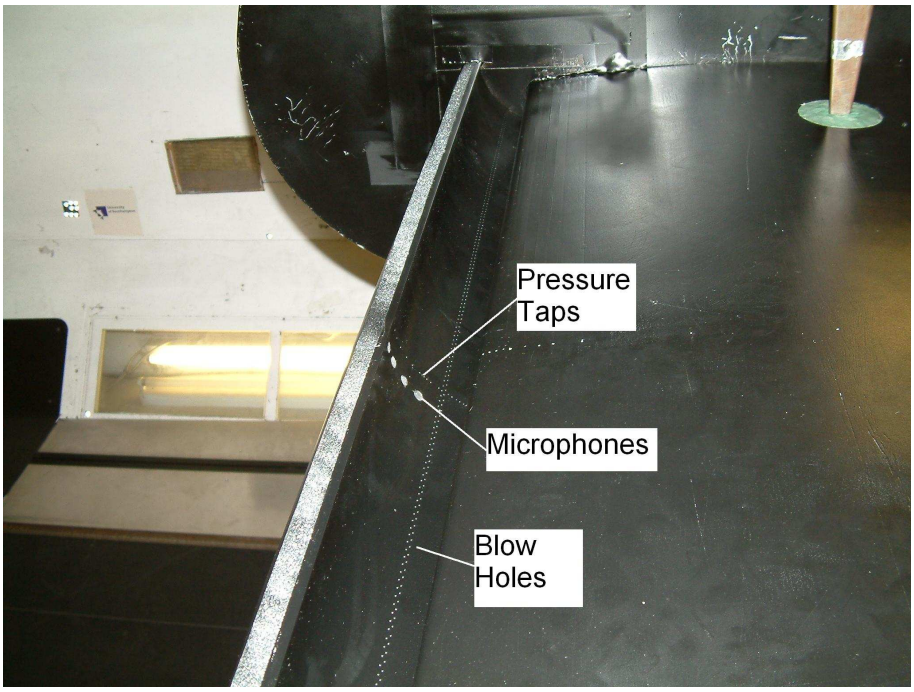

Figure 2.4: Photo showing the blow holes, microphones and pressure taps.

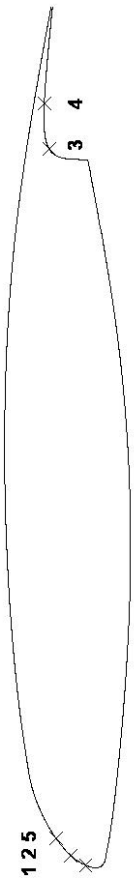

(a) Microphone locations

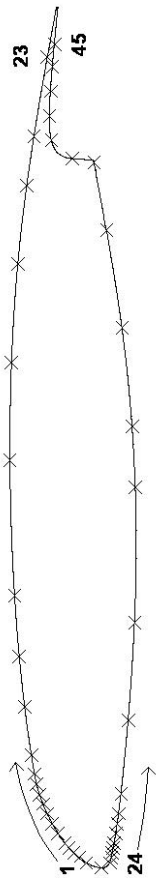

(b) Pressure tap locations

Figure 2.5: Location of sensors on the main element.

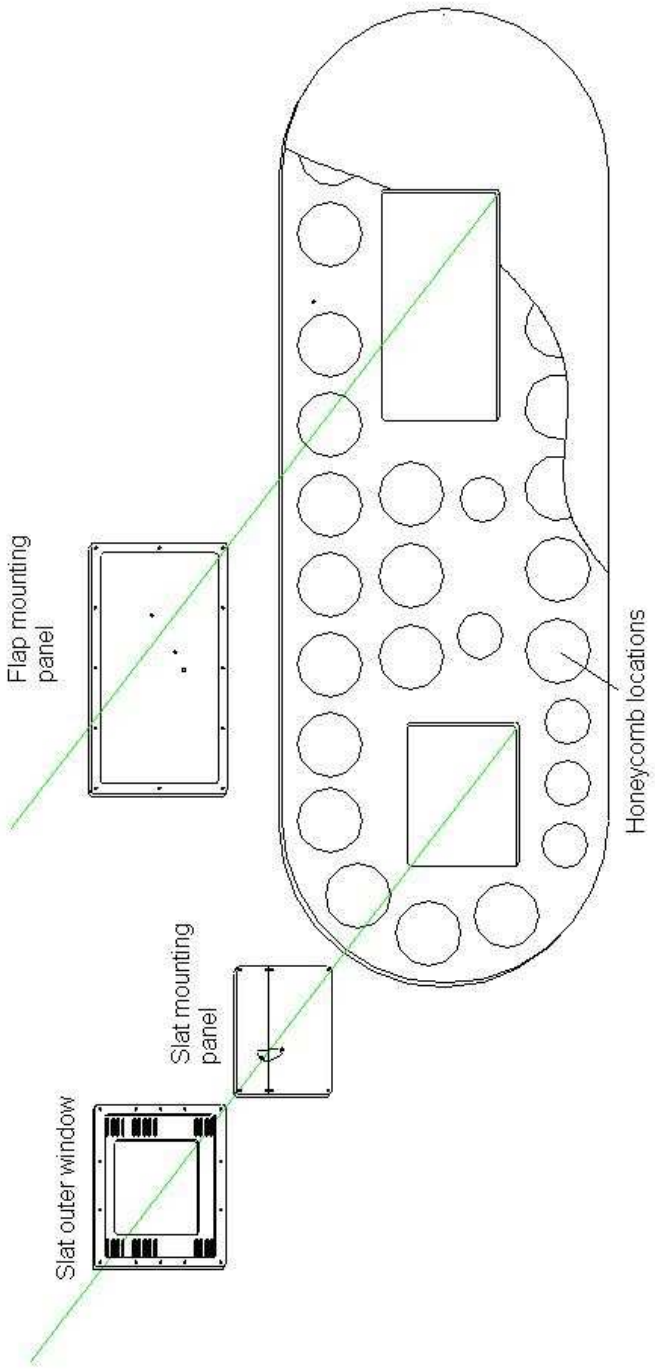

Figure 2.6: Design of endplate showing location of windows and the honeycomb sections.

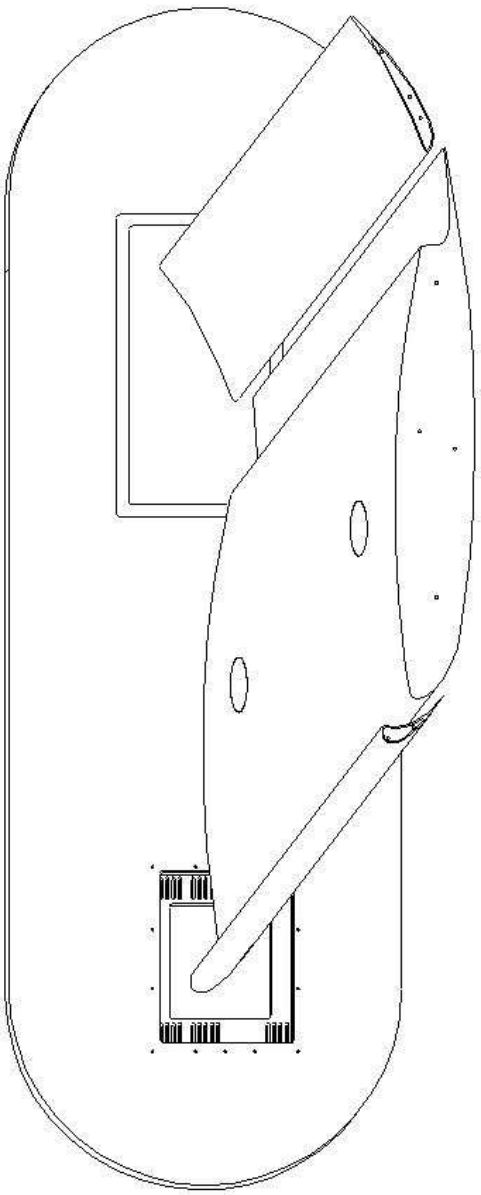

Figure 2.7: Design of the three-element aerofoil and endplates.

Figure 2.8: Model mounted in the R. J. Mitchell wind tunnel.

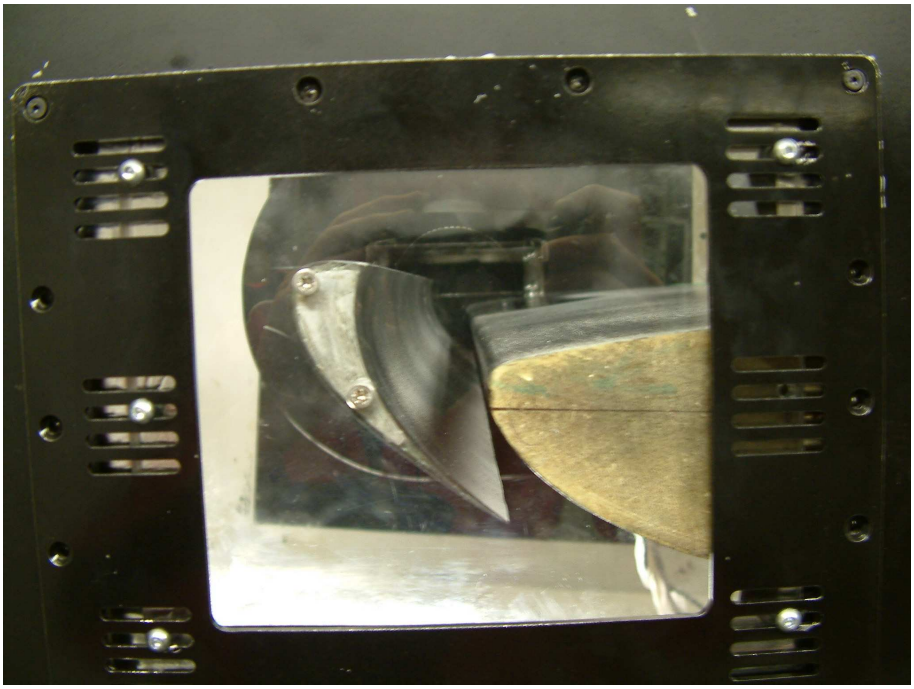

Figure 2.9: Slat viewed through window in endplate.

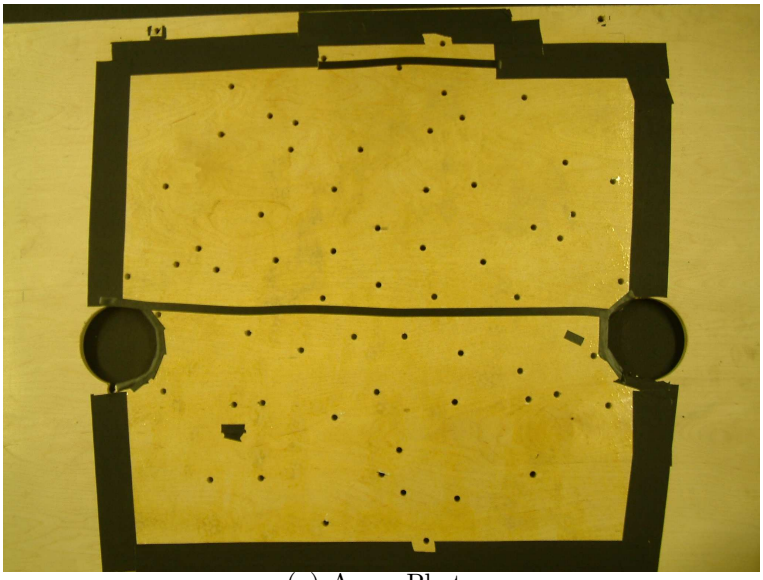

(a) Array Photo

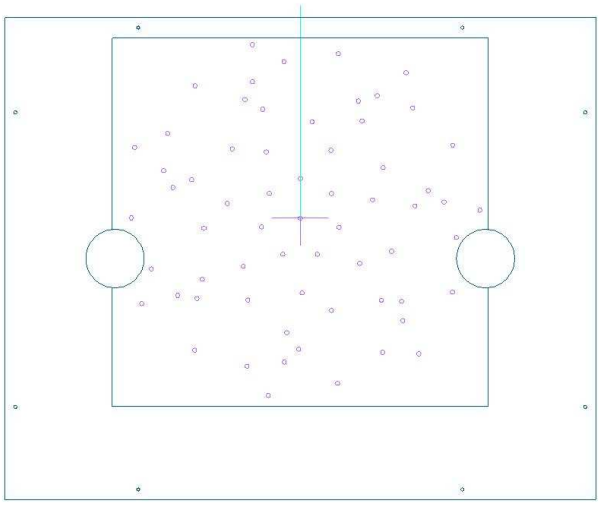

(b) Array Design

Figure 2.10: Microphone array design.

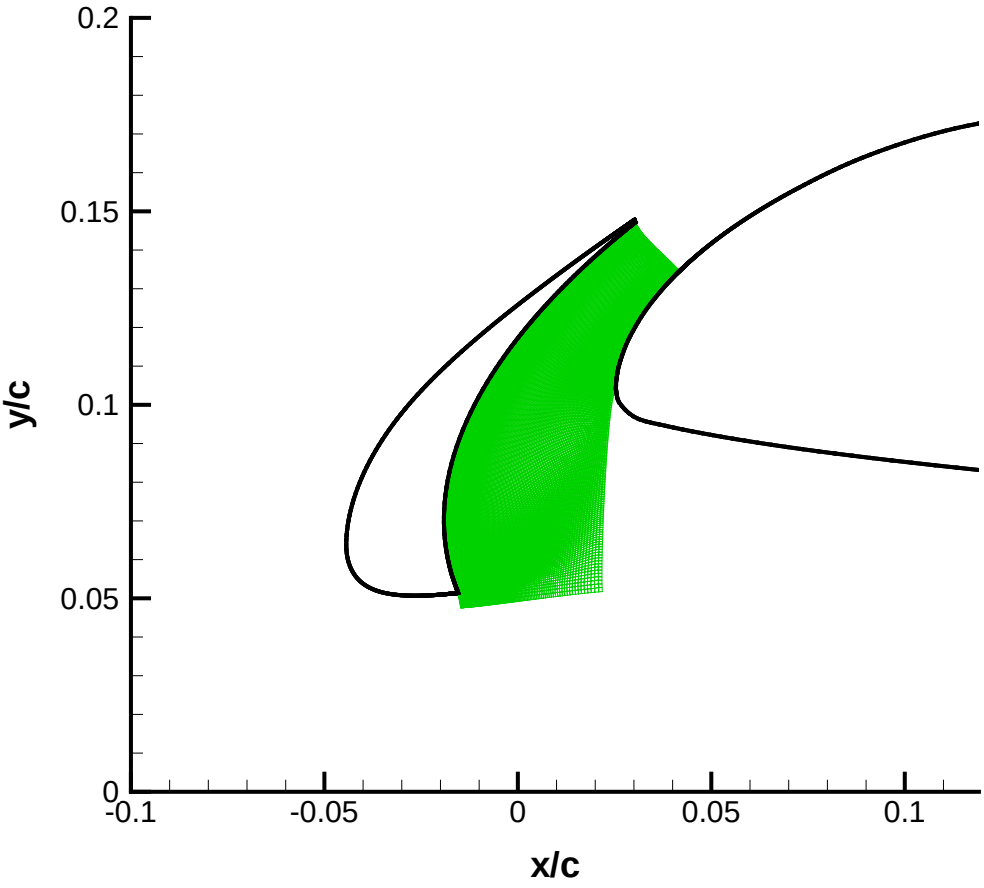

Figure 2.11: Location of the laminar zone.

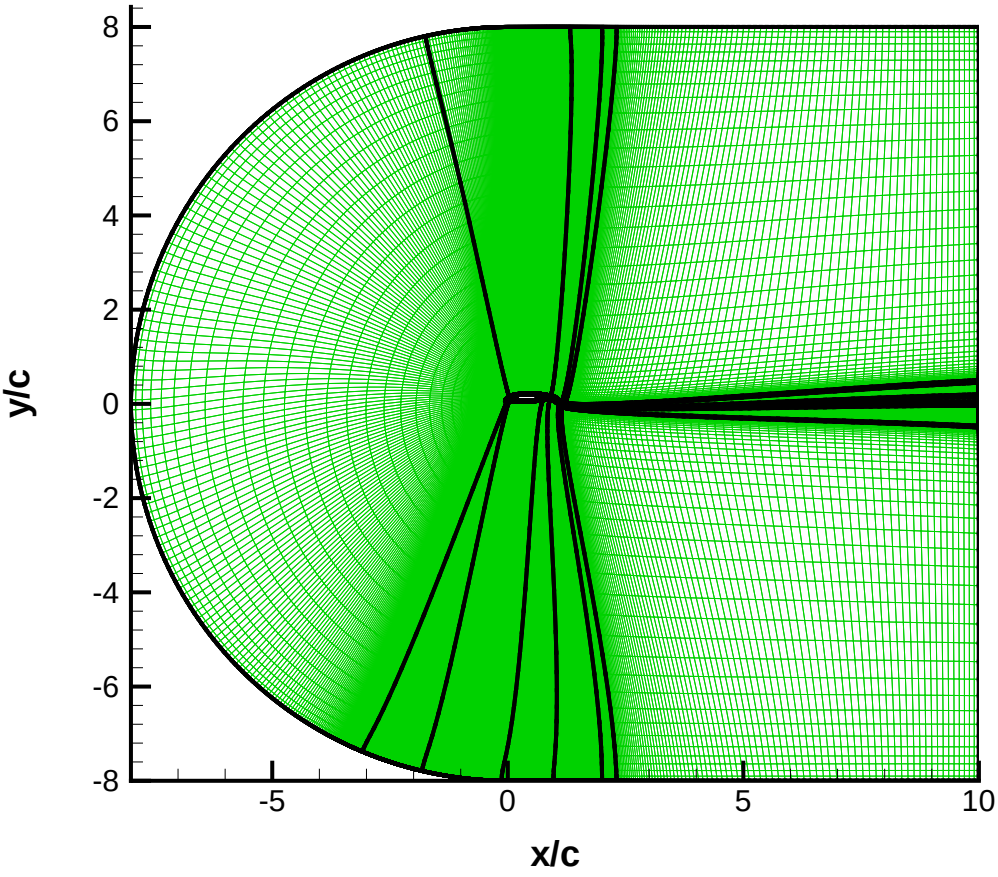

Figure 2.12: Size and shape of the 2D grid.

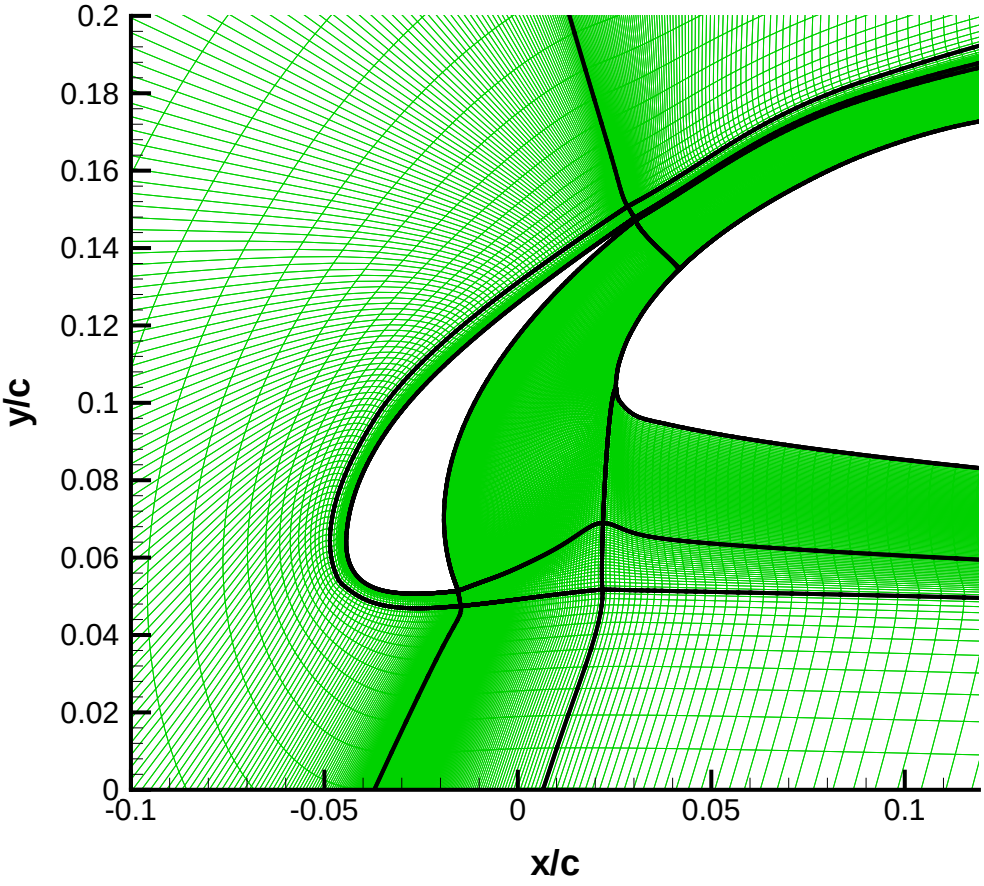

Figure 2.13: Detail of 2D grid around the slat.

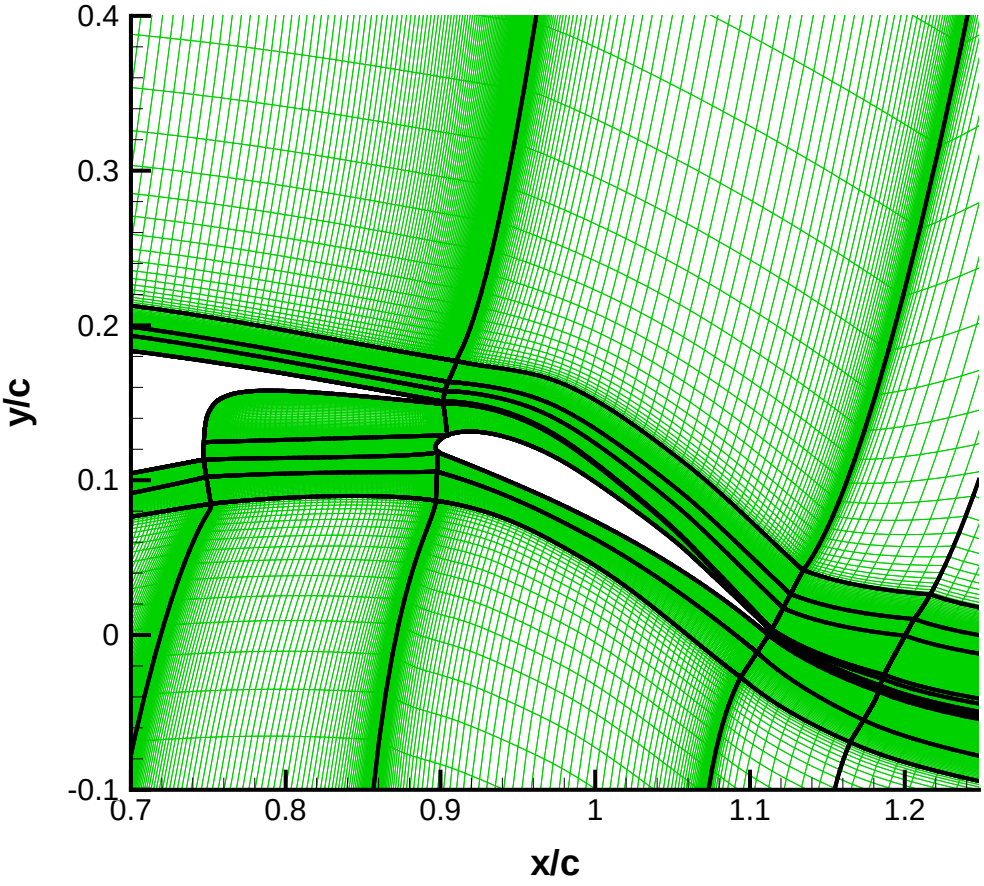

Figure 2.14: Detail of 2D grid around the flap.

Surface	2D grid	3D grid
Slat outer surface	1.16	1.24
Slat cove surface	1.03-1.08	1.17
Slat trailing edge	1.04	1.10-1.15
Main element suction surface	1-1.07	1.10-1.11
Main element pressure surface	1-1.05	1.11-1.15
Main element trailing edge	1.12	1.41
Flap suction surface	1.02-1.18	2.00-2.05
Flap pressure surface	1.06	1.35-1.79
Flap trailing edge	1.44	1.24
Far-field boundary	1.30-1.26	1.03-1.21

Table 2.4: Grid stretching factors measured on the block boundaries from the first to second cell.

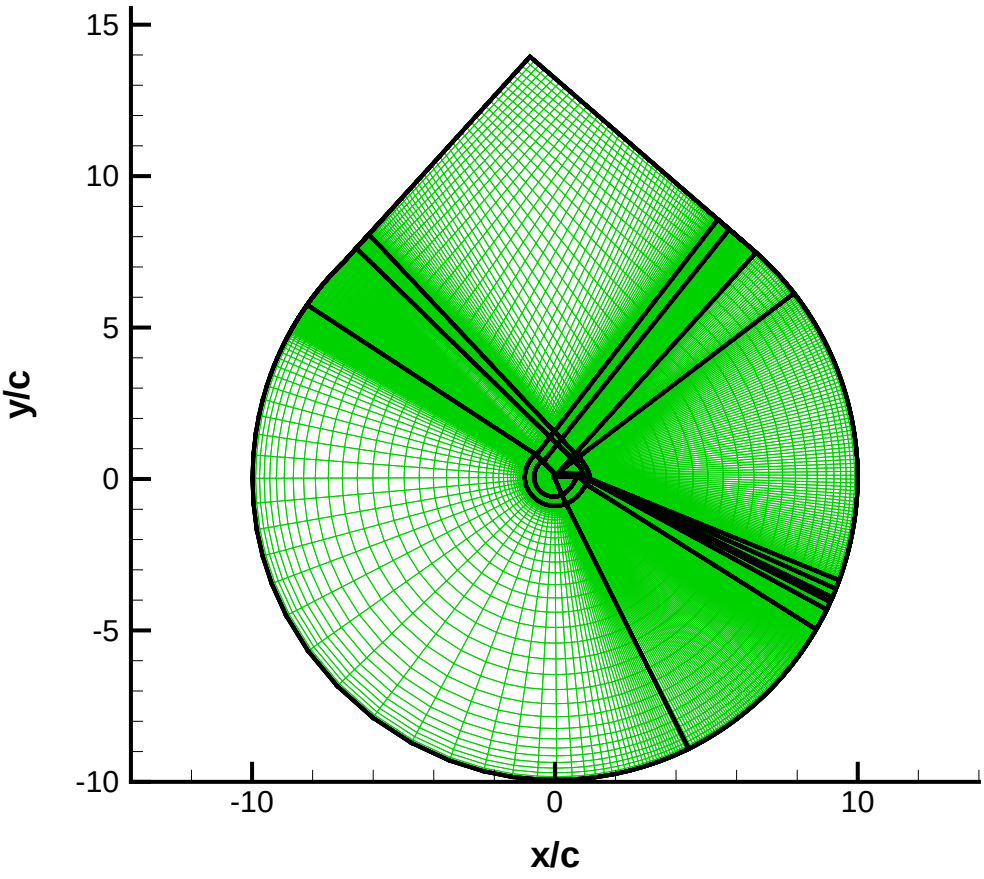

Figure 2.15: Size and shape of the 3D grid.

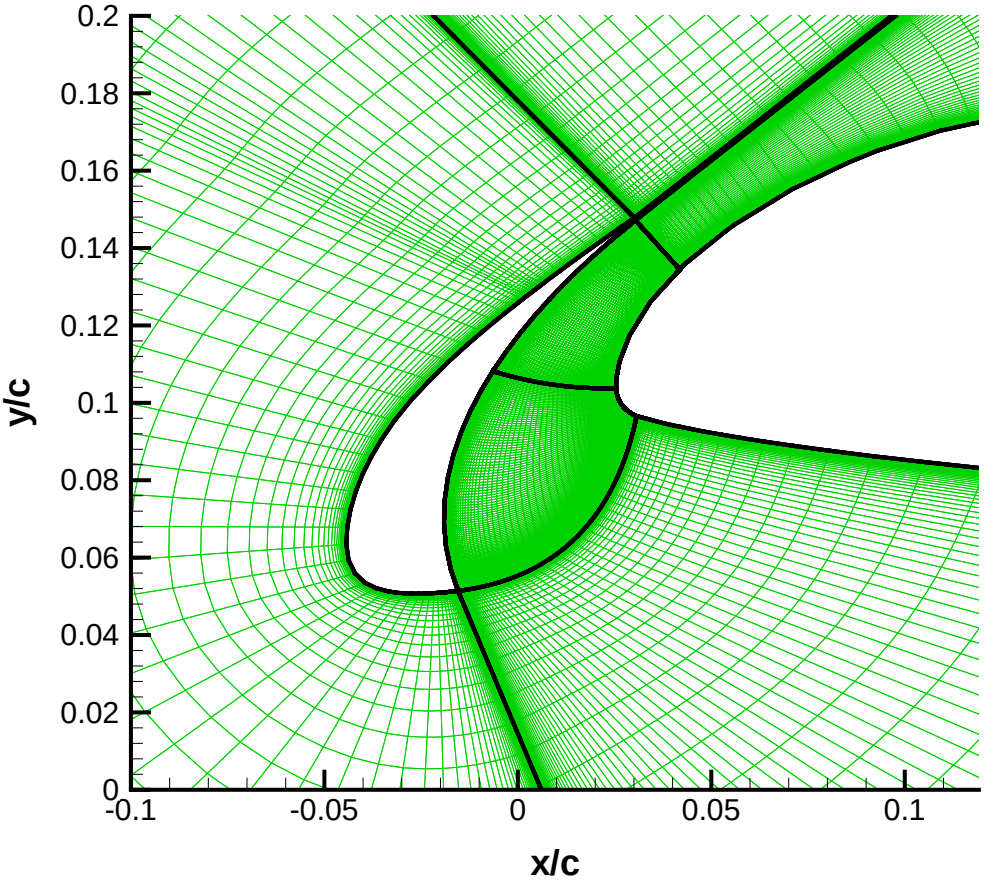

Figure 2.16: Detail of 3D grid around the slat.

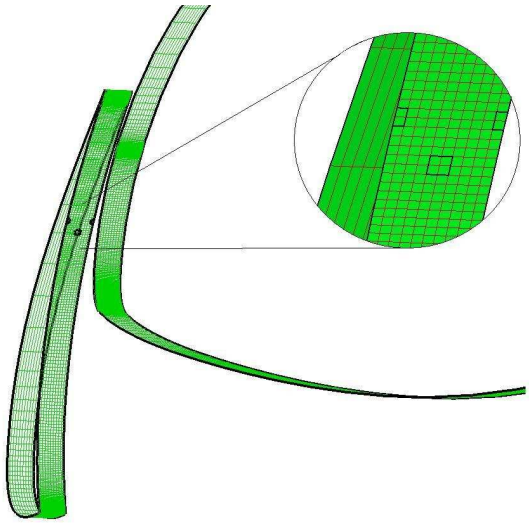

(a) Surface Grid

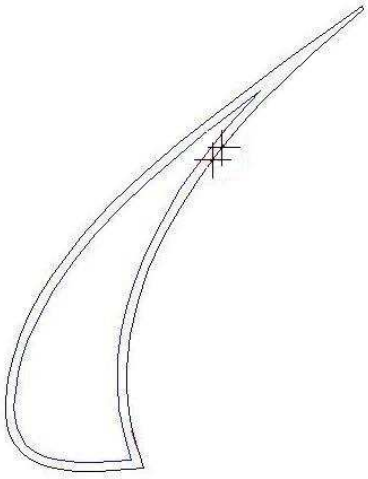

(b) Blow hole locations

Figure 2.17: Detail of the grid on the surface of the aerofoil showing the blow holes on the slat wall. The blow holes are located at $4.133\times10^{-2}c$ and $4.446\times10^{-2}c$ from the slat trailing edge.

Chapter 3

Aerodynamic Results

3.1 Introduction

This chapter covers the aerodynamic work and has experimental and computational sections. In both sections, the first subsection contains the results for the reference configuration. This establishes the unmodified flow pattern and the reference aerodynamic force levels. The following subsections then focus on the influence of the four factors under investigation: α, α_s, cusp geometry and blowing. An examination of the reliability of the results and the reasons for differences are given at the end of the chapter.

The experimental aerodynamic work covered three main areas

1. force measurements,
2. C_P distribution measured from the pressure taps, and
3. flow pattern measured using PIV.

The computational work shows the baseline flow patterns from both 2D and 3D simulations with a baseline flow speed of M=0.2. The 3D grids at both flow speeds allowed the assessment of the impact of blowing on the aerodynamic performance of the aerofoil. The low blowing rate matched the experimental work to give 120LPM across a 1 m span. With the flow speed at M=0.2 the blowing rate was increased to 270LPM to keep the ratio of blowing the free-stream velocities constant.

The computational modelling allowed the generation of three main types of results:

1. Force values.
2. Wall static pressure from which to calculate C_P.

3. Flow pattern plots showing variables such as pressure, velocity and vorticity.

The force readings gave the overall aerodynamic impact of changes to the aerofoil settings. The C_P and flow patterns showed changes to the local flows. Examination of near-field flow helped to explain the physics of the aerodynamic and acoustic changes.

3.2 Experimental results

3.2.1 Baseline results

The baseline conditions consisted of the reference slat and flap locations at α=5°. In this configuration at v=30 m/s, the wing was producing a lift force of 625N which corresponds to C_L=1.47, with a lift to drag ratio of 5.52. Figure 3.1 shows the chordwise surface pressure distribution for this configuration where only 24 out of 30 slat measurement taps were operational. The distribution shows stagnation points on both the main element and slat. In the slat cove there is a pressure rise, however, C_P does not rise above zero. The peak suction occurs around the slat cusp and on the main element at the slat gap. Peaks should have also occurred on the trailing edge of the slat. However, the geometry of the slat made it impractical to add taps to this location, preventing pressure measurement.

Figure 3.2 shows the flow pattern with both the mean and instantaneous readings for the reference setting. At the reference conditions, the PIV measurements show that the shear layer generated at the slat cusp did not significantly deviate from the free-stream direction until it is close to the main element. This led to a large recirculation zone with minimal flow through the gap. In this configuration, the slat did not add to the lift of the aerofoil and, due to the low aerofoil incidence, separation was not a major concern. The shear layer did not completely break down close to the cusp but, after it reached the main element, the shear layer formed discrete features. Fixing the transition point increased the vorticity in the shear layer but reduced the formation of discrete vortices. Away from the walls, the shear layer was clearly resolved. However, close to the walls, and at the gap, reflections from the wall and areas of shadow distorted the image. These areas then generated unphysical features in the spanwise vorticity plot. The PIV pattern is similar to the one from studies by Jenkins et al. [60] and Takeda et al. [53] but the flow at the cusp was altered by the lack of a cusp extension, which allowed a larger amplitude shear layer greater instability to develop.

Plotting the Q value for the same PIV data shows the discrete vortices located

within the shear layer (Figure 3.3). With free transition, the cove contained a large number of small vortices convecting around the recirculation region, but few were carried up to the main element stagnation point. With fixed transition, all the vortices travelled towards the main element stagnation point significantly reducing the number of vortices within the cove region.

3.2.2 Dependence on incidence

Over the aerofoil incidence range, the lift and drag increased, as the incidence was increased (Figures 3.4 and 3.5). The range of angles measured did not reach the stall point. The curves were close to linear from α= 0° to α=20°. However, close to α=0° there was a small drop in lift possibly caused by the pressure side of the flap moving into the wake of the main element. This was an indication of the wing approaching stall. For a symmetrical wing the negative angle stall would match the standard stall angle. However, the deployed slat greatly increased the camber of the wing and made it easy for the separated flow in the cove to expand, leading to a loss in lift. The loss of lift would be an issue below α=0°, however, this setting does not have many practical uses in aircraft operations and the drop in lift could be reduced by reducing the slat angle or retracting the slat. The drag curve does show some curvature but appears almost linear rather than the expected form of C_D=a+bC_L^2. This difference is partly down to the plot only containing a limited aerofoil incidence range disguising the shape of the drag curve. The other main factors are that the endplates will reduce the contribution of the induced drag and that the wing is in a landing configuration. The landing configuration means that the aerofoil experiences significant regions of separation around the slat cove and behind the flap trailing edge. These regions are aerofoil incidence dependent and will alter the profile drag component unlike with a clean wing setting.

As α increased, the C_P minimum increased on the wing suction side although the general pattern remained constant (Figure 3.6). The exception was at α=0° where the shear layer from the cusp did not enter the cove generating a long recirculation zone (Figure 3.7). Where this recirculation zone ended there was stagnation point, but away from the leading edge, the spacing of the taps increased so the surface pressure records missed the stagnation point resulting in an under-estimate of the maximum C_P. However, this setting was clearly not a realistic condition for slat utilization. The aerofoil incidence trend followed the same pattern as earlier tests by Jenkins et al. [60] but this study included more taps in the cove, which expanded the data available to include the reattachment point.

As α increased, the PIV (Figures 3.8 and 3.9) showed that the size of the re-

circulation zone shrunk significantly from occupying the entire cove region at α=5° to being restrained close to the slat at α=20°. The reduction in the size of the re-circulation region allowed an increased flow through the slat cove. However, above α=10°, as the gap became more aligned with the free-stream, the acceleration of the gap flow was reduced, leading to a slight reduction in the suction generated around the cusp. The flow velocity through the gap is likely to have a major impact on the acoustics at the trailing edge but the total forces are more dependent on the overall recirculation rather than on a localized feature. Fixing transition did not have a significant impact on the mean flow and hence, on the aerodynamic forces of the wing over the range of angles investigated (Figures 3.10 and 3.11). The trajectory of the shear layer defining the size of the recirculation region, matched the pattern found by earlier simulations by Storms et al. [44].

Under all conditions, the Q value showed the presence of discrete vortices formed within the shear layers (Figure 3.12). As the aerofoil incidence increased, the number of vortices increased up to α=15° while their size decreased. This reduction insize is because the vortices were increasingly constrained to the shear layer. At α=20°, the number of vortices reduced along with the size of the recirculation zone.

3.2.3 Dependence on slat angle

The total force values were similar for the different slat positions. However, reducing the slat angle did give a slight increase in lift generated (Figure 3.13). At α=5° reducing α_S from 23° to 13° gave a 5% lift improvement. However, by α=20° the improvement was reduced to 1.6%. This occurred because the slat's design conditions were at high aerofoil incidence so at low aerofoil incidence the slat became more effective when deployed at a reduced angle. Reducing the gap had no significant impact at the conditions measured. The increase in lift was reflected in a similar increase in drag so the lift to drag ratio was unaffected by the slat changes (Figure 3.14). The slat was likely to become more important towards the stall point but, over the range considered, α_S=13° was a better setting.

At α_S=13°, the variation of C_P with α (Figure 3.15)was similar to the pattern at the reference slat position (Figure 3.6). On the main element, the largest change of C_P with decreasing α was around the leading edge, where there was a drop in the peak suction indicating a drop in the flow velocity through the gap (Figure 3.15). On the slat, increasing α_S moved the stagnation point closer to the cusp (Figure 3.16). Moving the stagnation point increased the acceleration of the flow over the upper surface of the slat giving increased lift from the slat. The stagnation point was clearly also dependent on α (Figure 3.15). As α increased, the stagnation

point moved towards the cusp and the peak suction moved from the cusp side to the trailing edge side. For the reference slat, this change occurred at α=10° but at α_S=13° this occurred before α=10° (Figure 3.17). Inside the cove, the reduced gap velocity resulted in increased pressure on the slat wall, indicating a reduction in the velocity in the recirculation region.

The PIV results for α_S=13° (Figures 3.18 and 3.19) show why this slat setting was more effective at low aerofoil incidence. The increased distance between the cusp and main element and closer alignment with the flow allowed the shear layer to go through the slat gap rather than impinge on the main element at α=5°. The increased size of the cove left increased the space between the shear layer and main element, leading to the lower peak suction values observed. The Q value showed the discrete vortices at α_S=13° were contained within the shear layer (Figures 3.20 and 3.21). Relative to the reference slat angle the cove was larger, allowing the shear layer to move further from the slat wall. This appears to have reduced the interaction at the cusp creating more order in the shear layers leading to a reduction in the size of the shed vortices. With free transition, the size of the vortices increased with respect to fixed transition measurements but the pattern remained with few vortices leaving the shear layer. At α=15° with free transition, the vortices seem to form into a staggered pattern similar to a von Karman vortex street (Figure 3.22).

3.2.4 Influence of blowing

The aim of the blowing system was to influence the unsteady features in the slat cove to alter the acoustics of this wing. Producing significant changes in the aerodynamic forces by blowing was therefor not an aim of this study. Hence the blowing rates were relatively small with respect to the free-stream flow. For this reason, the blowing system did not have a significant impact on the total forces generated by the wing.

The blowing system did have an influence on the local flow in the cove as shown on the C_P plot of Figure 3.23. Adding the blowing produced localized pressure peaks (a) and (b) either side of the blowing location. These probably formed due to the flow splitting either side of the jet, giving a clear dividing point as shown in the schematic. These changes in the cove altered the shape of the recirculation, creating a pressure peak located closer to the cusp. This indicated a fixed secondary recirculation zone was formed, giving a high-pressure point. Without the blowing, this upstream pressure peak was absent so there was either no secondary vortex or this was intermittent. The flow was also altered slightly upstream of the cusp where the pressure is slightly reduced (c).

The PIV images of the slat showed that the blowing did not significantly change

the flow pattern in the cove (Figures 3.24-3.25). The jet was not visible on the PIV because the blow rate of 120LPM corresponds to a mass flow rate of less than 0.01 kg/s (Appendix B), which was much smaller than the mass flow rate through the cove of approximately 0.5 kg/s. The small size of the jet limited it to close to the wall, where it was not resolved by the PIV due to surface reflections of the laser sheet.

3.2.5 Dependence on cusp geometry

The addition of the cusp extension did not alter the forces generated by the wing at a low aerofoil incidence. However, above α=10°, the cusp extension gave a reduction in the lift generated (Figure 3.26). With the reference slat angle at α=10°, there was a 2.5% drop in the lift generated by the wing. A 4% drop in drag at this configuration accompanied this.

The C_P distribution around the wing reflected the change in the flow pattern (Figure 3.27). The addition of the extension moved the reattachment point in the cove closer to the cusp, as shown by the localized pressure change located around x/c=0. Moving the reattachment point increased the flow through the gap increasing the suction at the gap. However, further downstream, there was a reduction in the suction generated, leading to the loss of lift. The loss in suction was probably due to a mismatch between the gap flow and the flow over the suction surface of the main aerofoil element, leading to a region of recirculating flow on the upper surface of the aerofoil. The pressure distribution along the aerofoil pressure side was essentially unaffected by the cusp extension.

3.3 Computational results

3.3.1 Baseline results

The baseline flow condition of α_S=23° was simulated using both the 2D and 3D grids at a free-stream speed of M=0.2. Both simulations gave lift values significantly above the experimental results with C_L=2.39±0.003 for the 3D DES simulation and C_L=2.35 for the 2D RANS simulation. This increase relative to the experimental values was clearly due to the simulations modelling an infinite wing so none of the losses associated with a low aspect ratio wing are included. Although the model did use end plates to reduce 3D effects these were not large enough to remove all of the spanwise variations. The lift to drag ratio was also relatively high due to the low incidence of the wing. At high incidence, although the lift was increased the

drag increase was greater, leading to a reduced lift to drag ratio. For a complete aircraft, there would be a further drag increase due to the presence of the fuselage and empennage. The drag for the 3D simulation was C_D=0.045±0.003, giving a lift to drag ratio of 53. There was a significant difference in the drag values, with the 2D value approximately double the 3D value.

The pressure distribution around the 3D grid at M=0.2 shows that there was a pressure rise located in the slat cove at the reattachment point located at x=0 (Figure 3.28). Suction peaks were formed at both sides of the slat cusp where C_P=-3.6. On the main element, there was a localized suction peak of C_P=-4.1 around the leading edge followed by a more extended suction plateau of C_P=-3.4. The pressure then increased away from the leading edge with a flap suction peak of C_P=2.4.

Examining the velocity distribution in the slat region showed the acceleration through the slat gap (Figure 3.29). The high-speed flow, formed by the acceleration around the main element leading edge, reached a velocity magnitude approximately twice the free-stream value. Low-speed flow was located around the slat and main element stagnation points and around the reattachment point in the slat cove. There is also low-speed flow near the centre of the recirculation zone and in the cove close to the cusp. The region close to the cusp featured complex velocity fluctuations, indicating an unstable interaction between the recirculated and gap flows at this point, highlighted by the vorticity in the cove (Figure 3.30). The cusp generated most of the vorticity; however, there was an additional source located where the recirculating flow in the cove separates from the slat wall, before the cusp, where indicated by arrow 1. These two sources interacted near the cusp and influenced significantly all the unsteady features in the cove. The majority of the vorticity was located in the recirculation zone with some elongation of the vortex structure through the gap close to the slat trailing edge. The pressure plots show the large low-pressure region in the cove generated by the flow accelerating through the cove (Figure 3.31). There was also a low-pressure region at the cusp, which identified the start of the cove flow acceleration. The pressure plot also clearly shows the location of the reattachment point and suction on the upper surface of the main element.

The pressure distribution for 2D simulations gave the same general pattern as the 3D results (Figure 3.32). The main changes were the lack of the localized high suction points on the main element at the slat gap and an increase in the pressure at the reattachment point. The velocity pattern from 2D simulations was similar to the 3D results; the largest difference was at the cusp where a clearly defined secondary vortex forms (Figure 3.33). There was also an increase in the size of the centre of the main recirculation zone that affected the flow past the main element.

Examining the vorticity showed that the 2D simulation matched the main features in the cove but did not capture the fine details, which will involve a 3D component (Figure 3.34). The restriction to the 2D shear layer means that growth is slower and explains the rise in pressure at the reattachment point by not allowing the force to spread over a wider area. Specifically, 2D vortices in the 3D shear layer break down into 3D vortices. This process is not modelled in the 2D predictions. Generally, the 2D simulations gave a good match to the 3D simulations but the local features contained 3D elements that limited the use of 2D simulations. The 2D method matched the method used by Khorrami et al. [86] which also found significant shear layer breakdown and this is matched to the 3D DES simulations. The domain of the 3D simulation was narrower in the spanwise direction than those employed by Choudhari and Khorrami [92], but this allowed compatibility with the discrete blow holes used in this study.

3.3.2 Influence of blowing

The 3D simulations allowed assessment of the impact of blowing on the aerodynamics of the wing. In the simulation carried out at M=0.2, there was a small increase in the lift generated when a low blowing rate was applied. The change increased the lift from C_L=2.38 to C_L=2.45. However, the higher blowing rate did not generate a further lift increase. At the same time, there was a larger increase in drag of 20% rising to 33% at maximum blowing. This magnitude of drag increase was significant but during the landing phase, the lift value had a greater importance than the drag level.

Adding a low blow rate of 120LPM to the simulation at M=0.2 produced some localized changes in the pressure distribution (Figure 3.35). Increasing the blowing rate further to 270LPM did not produce any further change. Compared with the no-blowing case, the most noticeable change was an increase in pressure at the slat cusp from C_P=-0.8 to C_P=-0.7, indicating a reduction in the local flow velocity. The cove wall, close to the cusp, was nearly vertical, so the change in pressure on this wall did not alter the lift generated. However, the pressure coefficient displayed relative to the y-axis shows this surface had a significant impact on the overall drag value (Figure 3.36). The plot shows the blowing significantly altered the cove flow. As the blowing increased, the suction increased on this surface leading to the drag rise measured. The changes only occurred on the cove side of the reattachment point and the pressure on the slat wall through the gap was not blowing dependent. However, there was an increase in the suction applied to the main element at the slat gap indicating the blowing moved the gap flow closer to the main element. The

final change occurred on the upper surface of the flap where the blowing increased the suction level. Of the three changes, the change to the main element reduced drag, the other two increased the drag level and led to the overall increase in drag.

The impact of blowing is clearly indicated in the velocity plots at both low and high blowing rates (Figures 3.37 and 3.38). As the rate increased, the size of the zone of separated flow at the cusp was increased and the recirculation zone became restrained closer to the slat. The blowing also acted to move the main gap flow away from the slat trailing edge producing lower velocities close to the wall. The vorticity plot confirmed the shear layer movement away from the slat wall and also showed how the recirculation moves away from the cusp (Figure 3.39).

The experimental work showed the size of the recirculation zone was aerofoil incidence dependent. Hence, without blowing, an increase in incidence moved the reattachment point anticlockwise around the slat towards the slat trailing edge. For the reference condition the blowing moves the reattachment point slightly closer to the slat trailing edge Figure 3.36). The blowing acts to provide a clear division on the slat wall (Figure 3.23b) so the movement of the reattachment point due to blowing will be dependent on the non-blowing location.

3.4 Experimental/ computational agreement

The force and C_P values obtained computationally were significantly higher than those found experimentally. This was due to the simulations modelling infinite span wings caused by the use of periodic boundary conditions. The difference in overall loading reflected in the flow patterns inside the cove. The increased wing loading reduced the size of the recirculation zone for the reference condition. This flow was closer to the pattern observed at α=10°. These 3D effects make it inappropriate to consider the experimental and computational work as relating to the same case. However, both put forward information useful to understanding the slat flow. To bridge this gap an estimation of the impact of a finite aspect ratio is required. Lifting line theory can be used to approximate this value [156].

For an elliptical lift distribution, lifting line theory gives the induced drag as:

$$C_{Di} = \frac{C_L^2}{\pi AR} \tag{3.1}$$

where C_{Di} is the induced drag and AR is the wing aspect ratio. The induced drag is created by accounting for the downwash behind the wing due to the circulation needed to generate lift. The downwash effectively alters the aerofoil incidence cre-

ating a component of lift in the drag direction. The lift remaining can be found by adjusting the lift by the induced drag angle. For an elliptical lift distribution, the lift can be found using:

$$C_L = 2\pi(\alpha - \frac{C_L}{\pi AR}) \tag{3.2}$$

when α is measured from the zero lift angle. This assumes that the aerofoil matches the lift slope of 2π that derives from thin aerofoil theory. Rearranging the equation gives:

$$C_L = 2\pi\alpha\frac{AR}{AR+2} \tag{3.3}$$

so

$$C_{L_{3D}} = C_{L_{2D}}\frac{AR}{AR+2} \tag{3.4}$$

For non-elliptical distributions, these equations are not exact due to variation in the lift and downwash across the span leading to the need to add efficiency factors. Modifying the equations for C_{Di} and C_L gives:

$$C_{Di} = \frac{(1+\varsigma)C_L^2}{\pi AR} \tag{3.5}$$

$$C_{L_{3D}} = C_{L_{2D}}\frac{AR}{AR+2(1+\sigma)} \tag{3.6}$$

where both σ and ς are positive values based on the lift distribution.

The experimental model had large endplates, which force the model to act as if it had a higher aspect ratio than the physical value of 1.2. The Effective aspect ratio can be found by assuming that the difference in the drag value between the computational and experimental work was due to the induced drag, which was not calculated in the computational work. Hence:

$$AR = \frac{(1+\varsigma)C_{L_{3D}}^2}{\pi\Delta C_D} \tag{3.7}$$

$$C_{L_{3D}} = C_{L_{2D}}\frac{\frac{(1+\varsigma)C_{L_{3D}}^2}{\pi\Delta C_D}}{\frac{(1+\varsigma)C_{L_{3D}}^2}{\pi\Delta C_D}+2(1+\sigma)} = C_{L_{2D}}\frac{C_{L_{3D}}^2}{C_{L_{3D}}^2+2\pi\Delta C_D\frac{1+\sigma}{1+\varsigma}} \tag{3.8}$$

Using the assumption used by Anderson [156] that $\sigma \approx \varsigma$ reduces the equation to:

$$C_{L_{3D}} = C_{L_{2D}}\frac{C_{L_{3D}}^2}{C_{L_{3D}}^2+2\pi\Delta C_D} \tag{3.9}$$

$$C_{L_{2D}} = \frac{C_{L_{3D}}^2 + 2\pi\Delta C_D}{C_{L_{3D}}} \tag{3.10}$$

Substituting the values for $C_{L_{3D}}$= 1.47, $C_{D_{3D}}$=0.266 and $C_{D_{2D}}$=0.045 gives $C_{L_{2D}}$=2.39 matching the measured value of 2.39.

Although force values could be partially adjusted for 3D effects this is not as easy with the acoustic values limiting quantitative comparison between the results. The aspect ratio difference was also clear in the flow patterns from the computational and experimental sections. The computational work had an infinite span so did not include the impact of induced drag and downwash, which had a similar impact as increasing the aerofoil incidence.

The adjusted forces show a link between the experimental and computational results and this extends to the flow patterns the generate the wing loading. Examining the surface pressure distribution show a common distribution from the computational (Figure 3.28) and experimental data(Figure 3.6). However as with the forces the computational values, which were simulated at α=5° are a better match experimental data taken at an increased aerofoil incidence of between α=15° and α=20° due to the lack of the downwash. Inside the slat cove there is also a similarity in the shape of the recirculation region between the computations (Figure 3.30) and experimental PIV data (Figure 3.9).

3.5 Summary

The experimental results show the incidence of the model had by far the largest aerodynamic influence of the factors investigated. The incidence largely determined the total forces generated along with the flow pattern inside the slat cove controlling the recirculation size and reattachment point. The Q value plots showed discrete vortices form within the shear layer, but fixing transition significantly reduced their production.

The slat angle also had an influence on the flow in the slat cove. With reduced slat angle, the cove was larger increasing the size of the recirculation region. With the larger recirculation region, the shear layer appeared to have increased stability with less formation of large discrete vortices, which can leave the shear layer. However, the slat angle had a limited impact on the overall force values, reducing the slat angle gave a 5% lift improvement at α=5° and as incidence was increased this improvement reduced. The aerodynamic impact of altering the cusp geometry was limited but produces a small lift reduction above α=10°. The blowing had little global aerodynamic impact and changes were limited to small pressure changes in

the slat cove region.

The simulations generated a lift of C_L=2.39 for the reference wing with a small drop when 2D simulations were used. Addition of blowing generated a small lift improvement but led to a drag rise when applied at M=0.2.

The pressure distribution featured suction peaks at the slat trailing edge and main element leading edge. Pressure peaks are located at the reattachment points on the slat, main element and cove walls. The impact of the blowing focused on the slat cusp region. Velocity and vorticity plots show the blowing moved the reattachment point and recirculation zone as a whole, altering the size of the separated flow region at the cusp.

The results are generally consistent with the trends from other, earlier studies and introduce new work on the cusp extension and blowing.

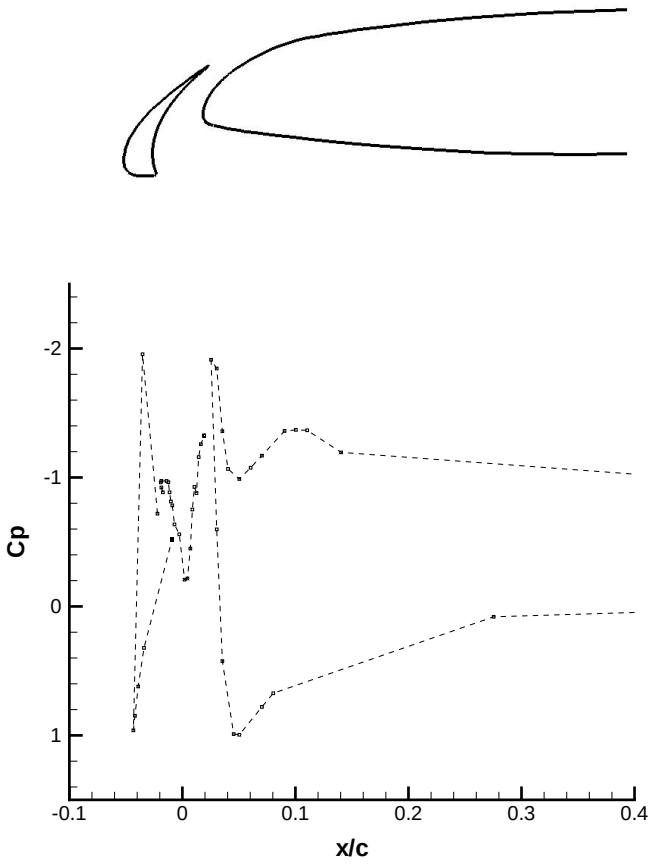

Figure 3.1: Experimental C_P plot of the reference conditions. v=30 m/s.

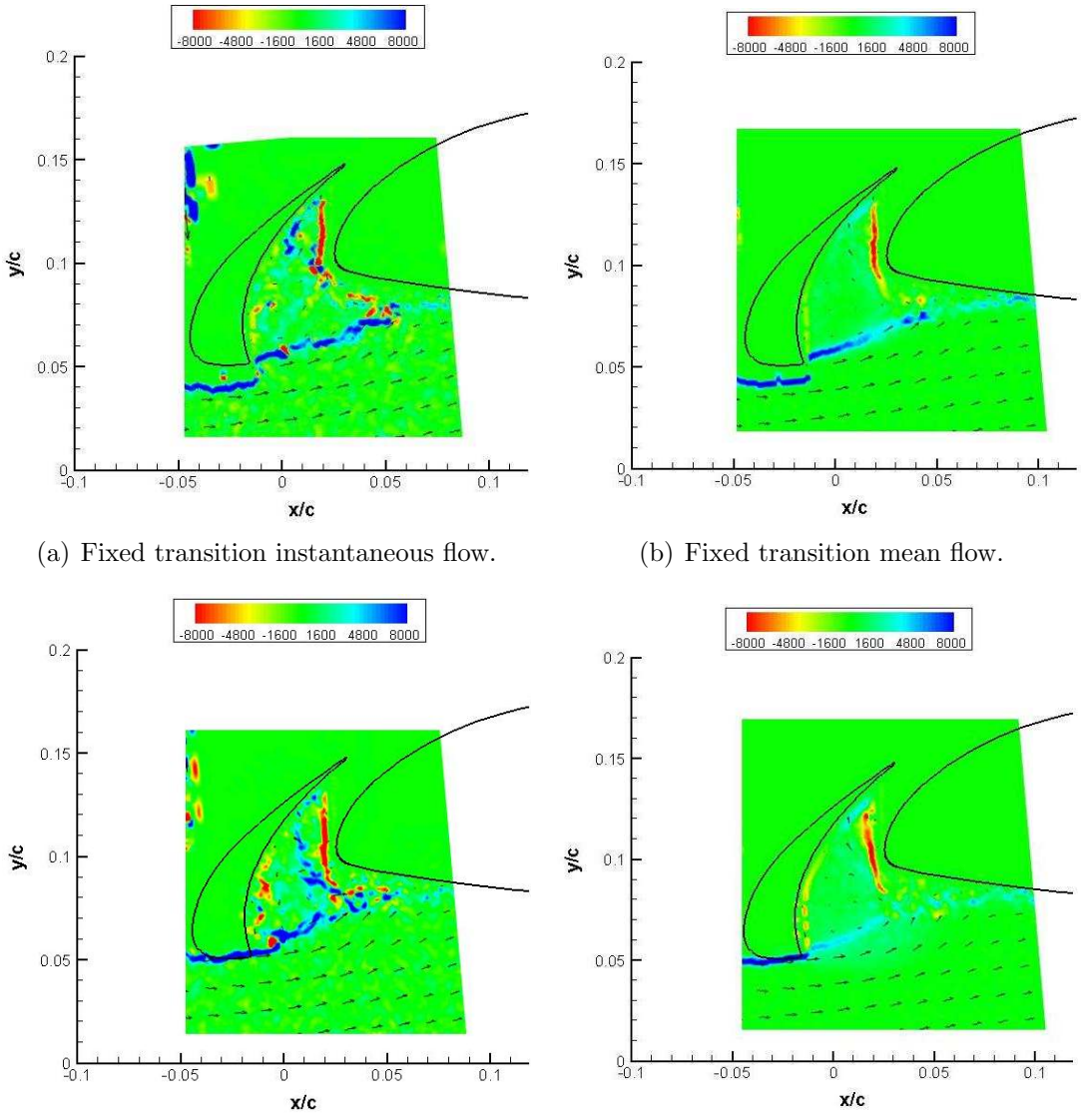

(a) Fixed transition instantaneous flow.

(b) Fixed transition mean flow.

(c) Free transition instantaneous flow.

(d) Free transition mean flow.

Figure 3.2: PIV spanwise vorticity plots (s^{-1}) of the reference configuration with free and fixed transition. v=25 m/s.

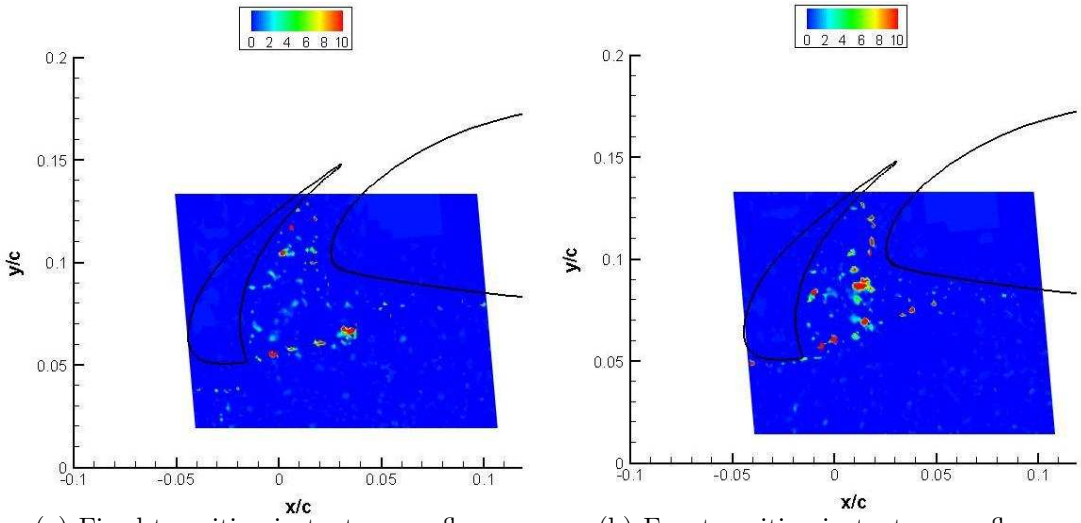

(a) Fixed transition instantaneous flow. (b) Free transition instantaneous flow.

Figure 3.3: Q value (s^{-2}) of the PIV data at the baseline configuration with free and fixed transition. v=25 m/s.

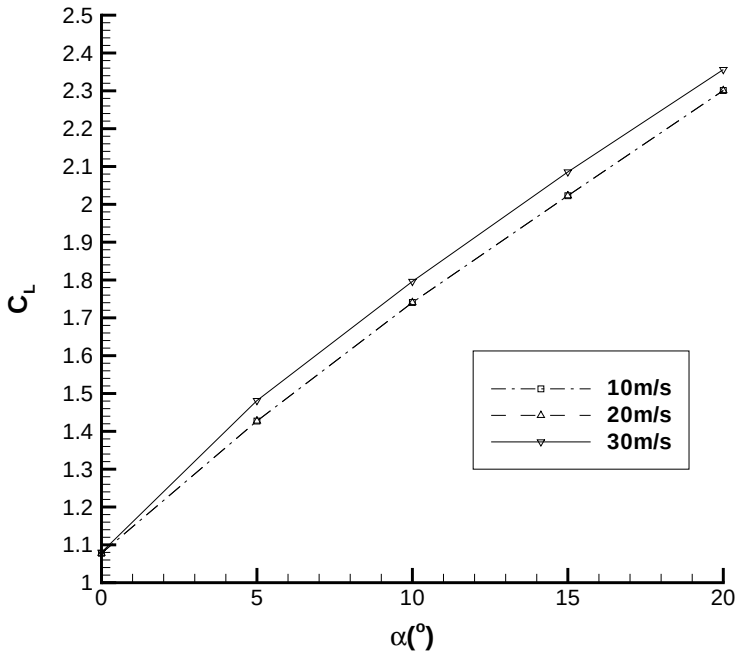

Figure 3.4: Experimental C_L vs α plot at the reference conditions.

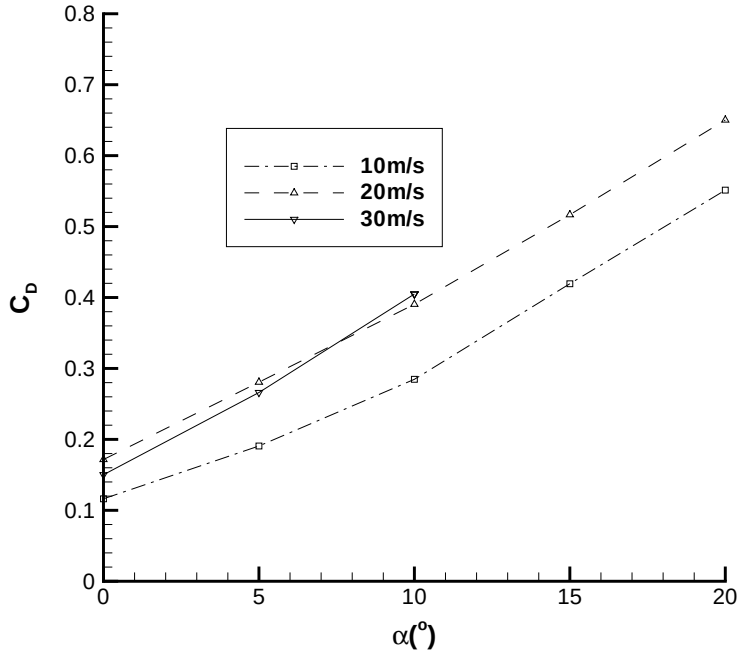

Figure 3.5: Experimental C_D vs α plot at the reference conditions.

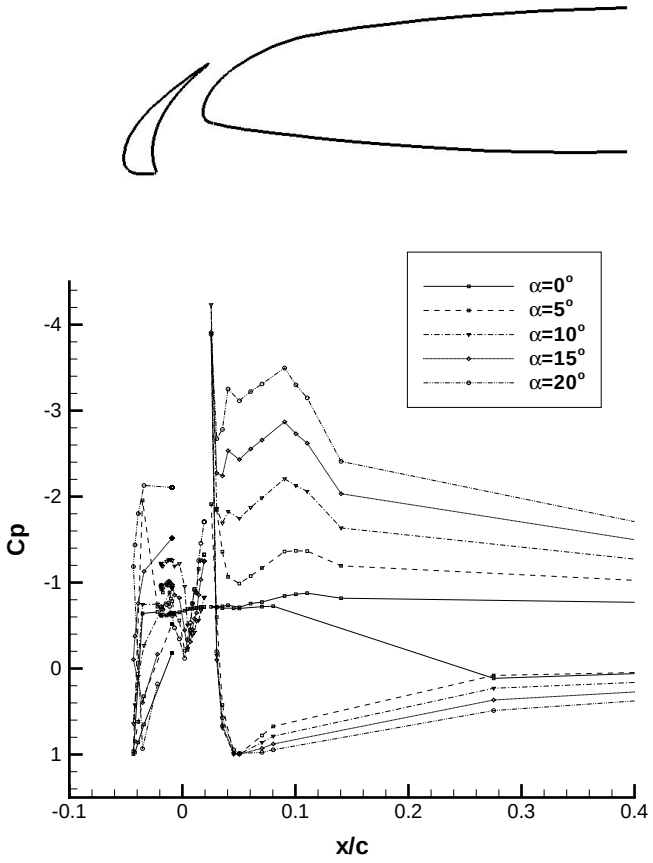

Figure 3.6: Experimental C_P plot showing the impact of the aerofoil incidence. v=30 m/s, α_S=23°.

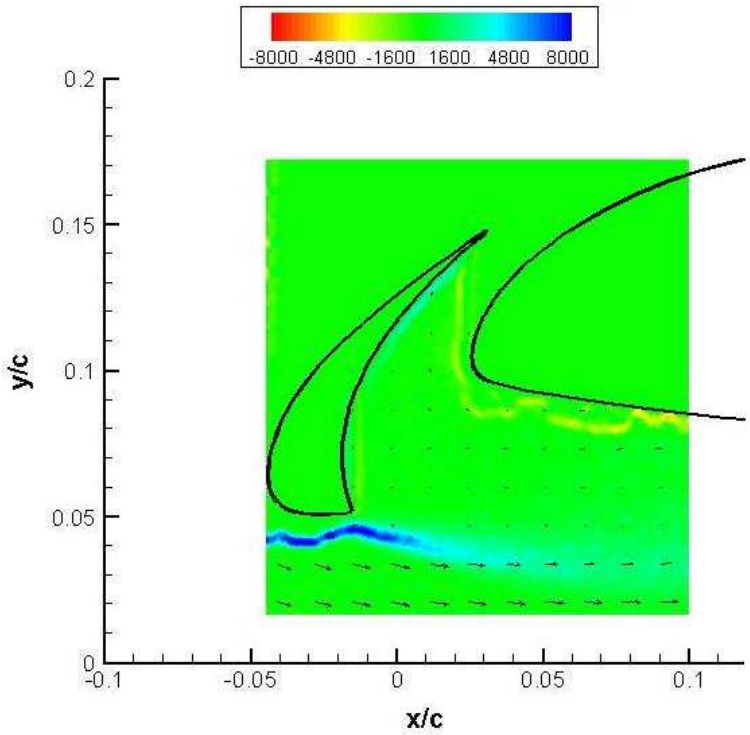

Figure 3.7: PIV mean spanwise vorticity plot (s^{-1}) at α=0°, v=25 m/s.

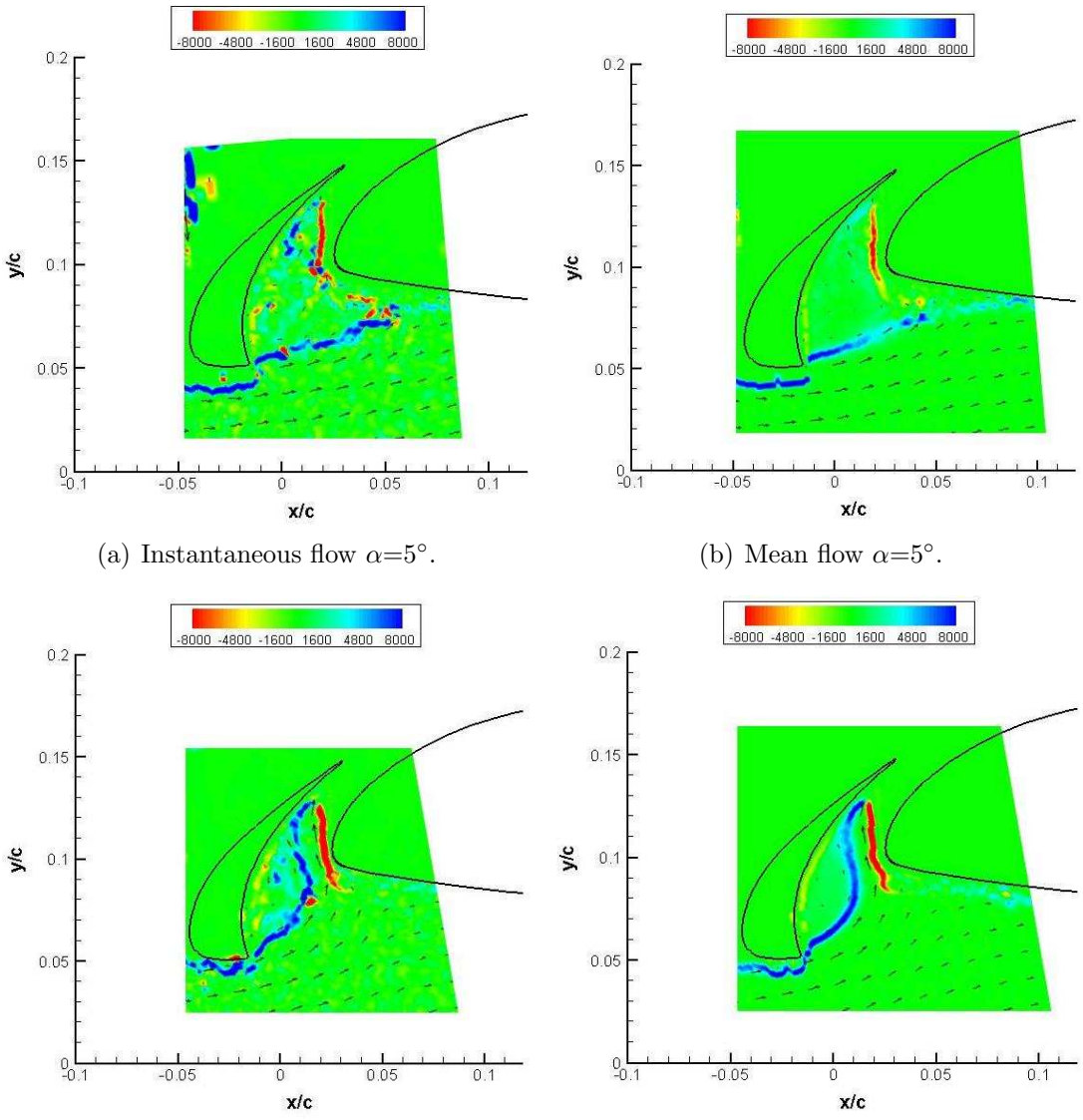

(a) Instantaneous flow α=5°.

(b) Mean flow α=5°.

(c) Instantaneous flow α=10°.

(d) Mean flow α=10°.

Figure 3.8: PIV spanwise vorticity plots (s^{-1}) over the aerofoil incidence range. v=25 m/s, α_S=23°, α=5°, 10°.

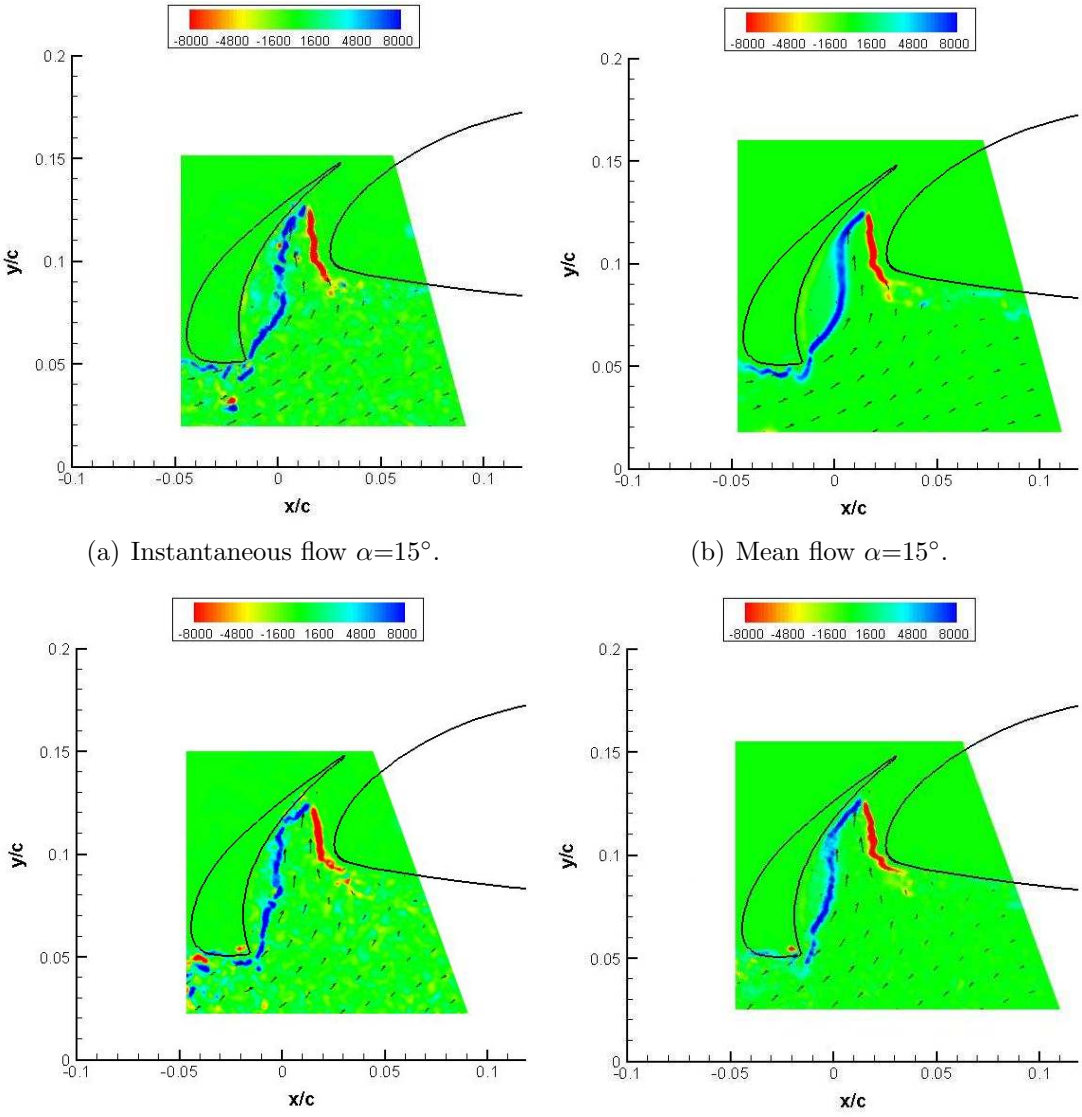

(a) Instantaneous flow α=15°.

(b) Mean flow α=15°.

(c) Instantaneous flow α=20°.

(d) Mean flow α=20°.

Figure 3.9: PIV spanwise vorticity plots (s^{-1}) over the aerofoil incidence range. v=25 m/s, α_S=23°, α=15°, 20°.

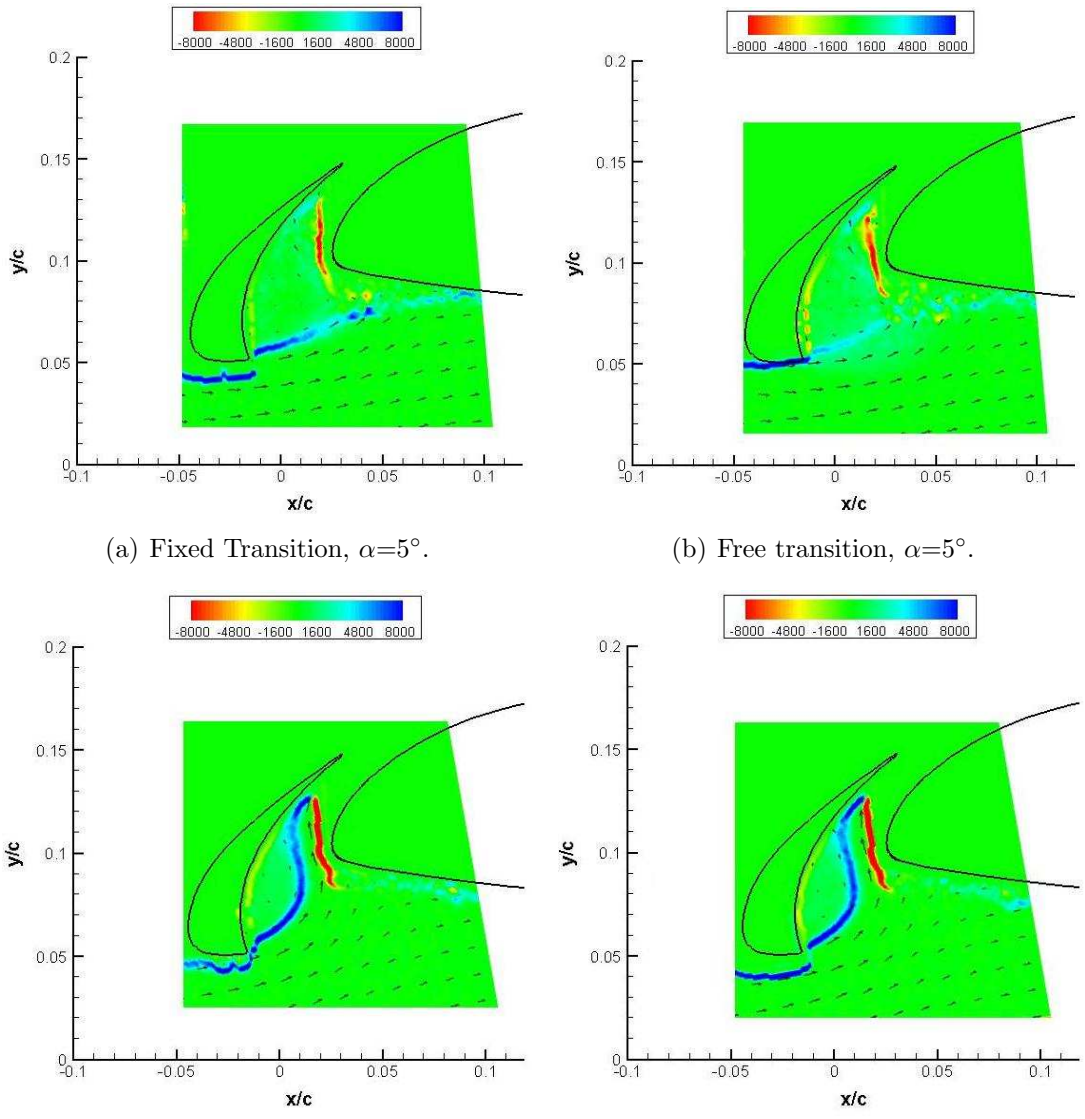

(a) Fixed Transition, α=5°.

(b) Free transition, α=5°.

(c) Fixed Transition, α=10°.

(d) Free transition, α=10°.

Figure 3.10: PIV spanwise vorticity plots (s^{-1}) showing the impact of transition on the mean slat flow patterns. v=25 m/s, α=5°, 10°.

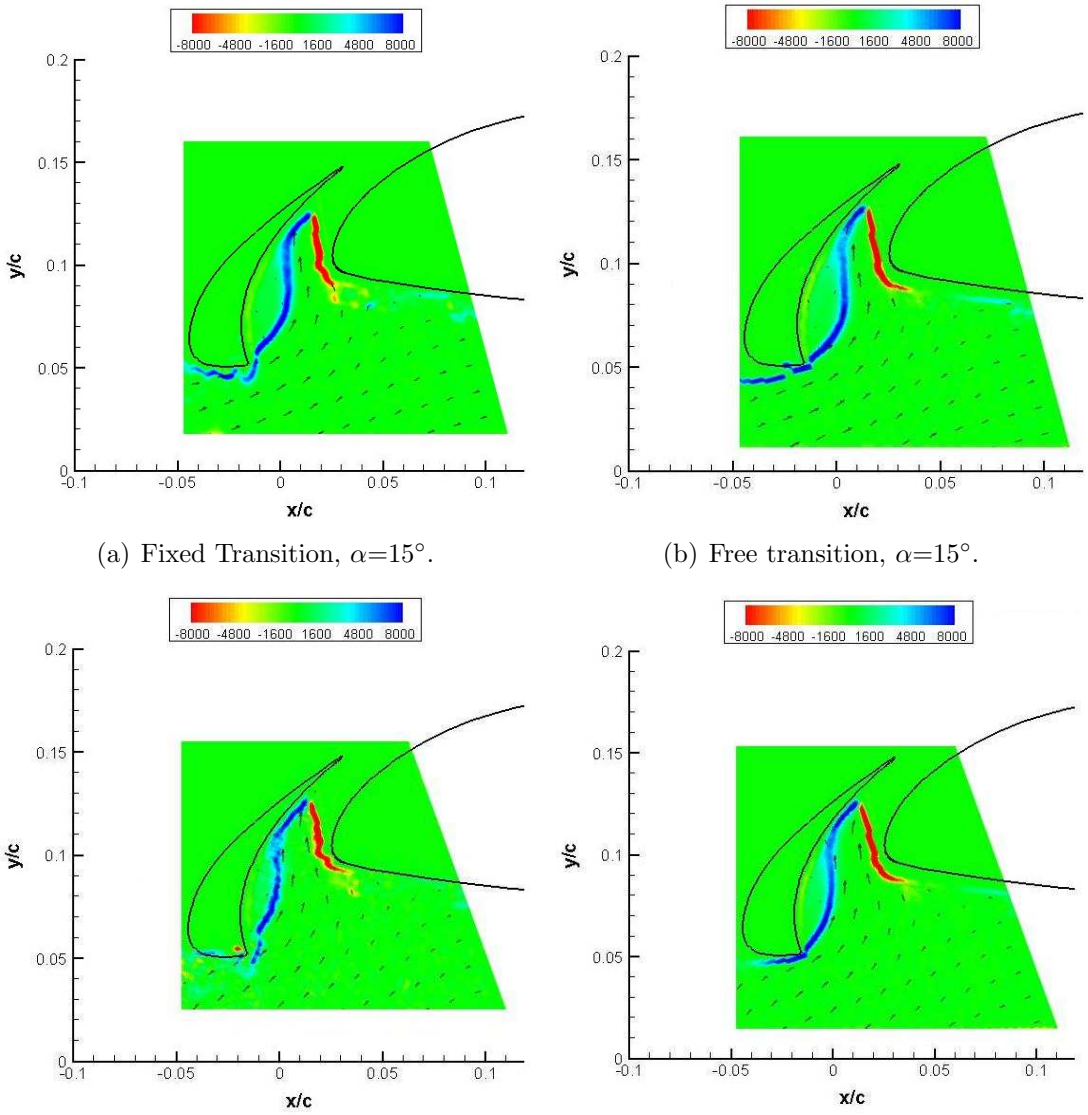

(a) Fixed Transition, α=15°.

(b) Free transition, α=15°.

(c) Fixed Transition, α=20°.

(d) Free transition, α=20°.

Figure 3.11: PIV spanwise vorticity plots (s^{-1}) showing the impact of transition on the mean slat flow patterns. v=25 m/s, α=15°, 20°.

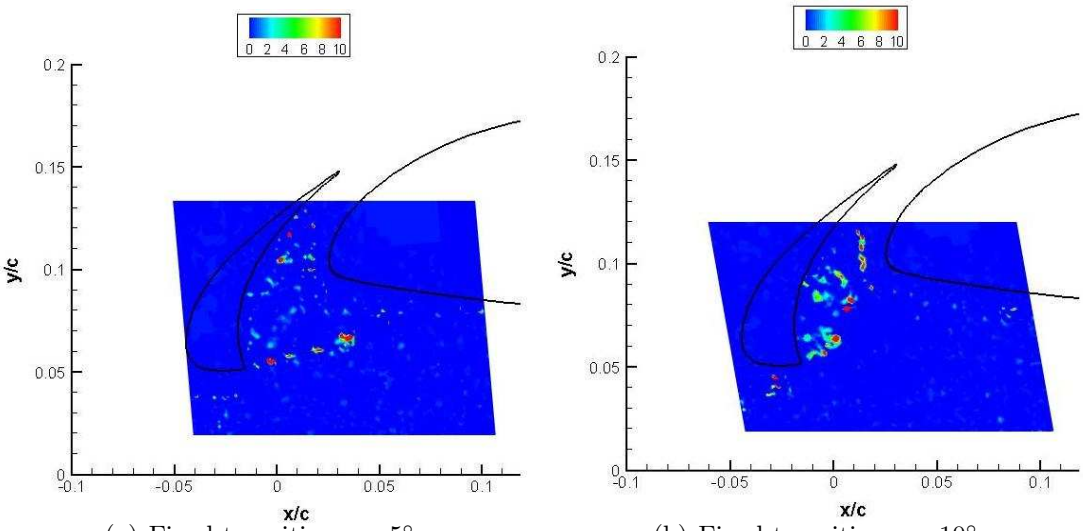

(a) Fixed transition, α=5°.

(b) Fixed transition, α=10°.

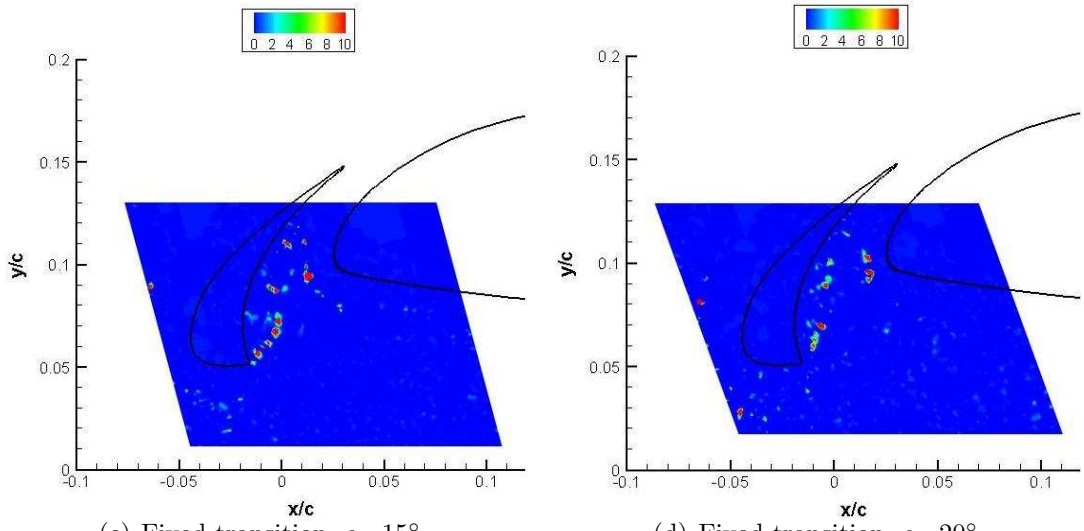

(c) Fixed transition, α=15°.

(d) Fixed transition, α=20°.

Figure 3.12: Q value plots (s^{-2}) using the PIV data showing the impact of the aerofoil incidence on the mean slat flow patterns, v=25 m/s.

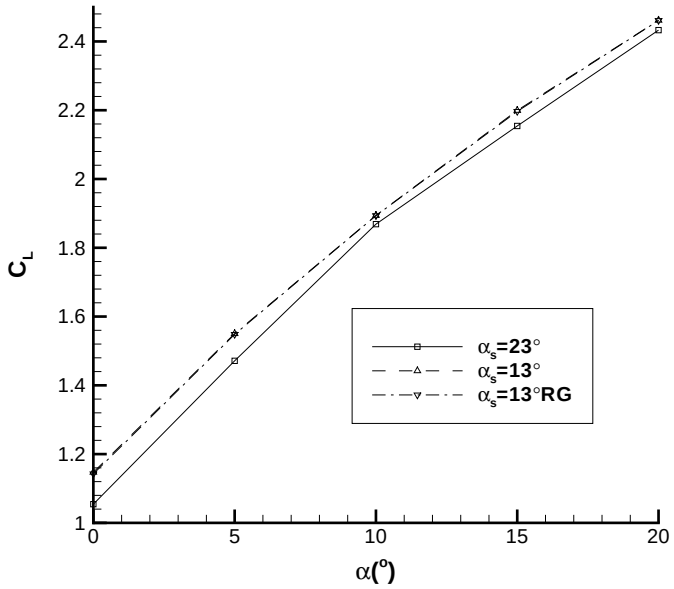

Figure 3.13: Experimental C_L vs α plot with the slat angle altered, v=30 m/s.

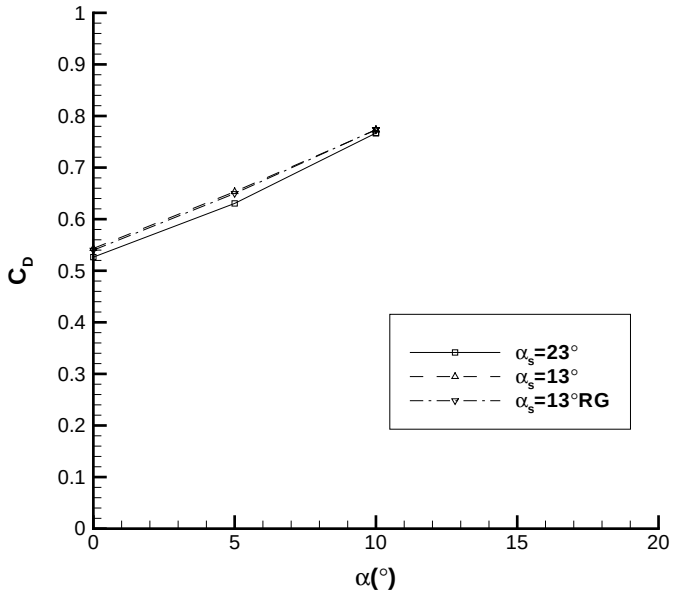

Figure 3.14: Experimental C_D vs α plot with the slat angle altered, v=30 m/s.

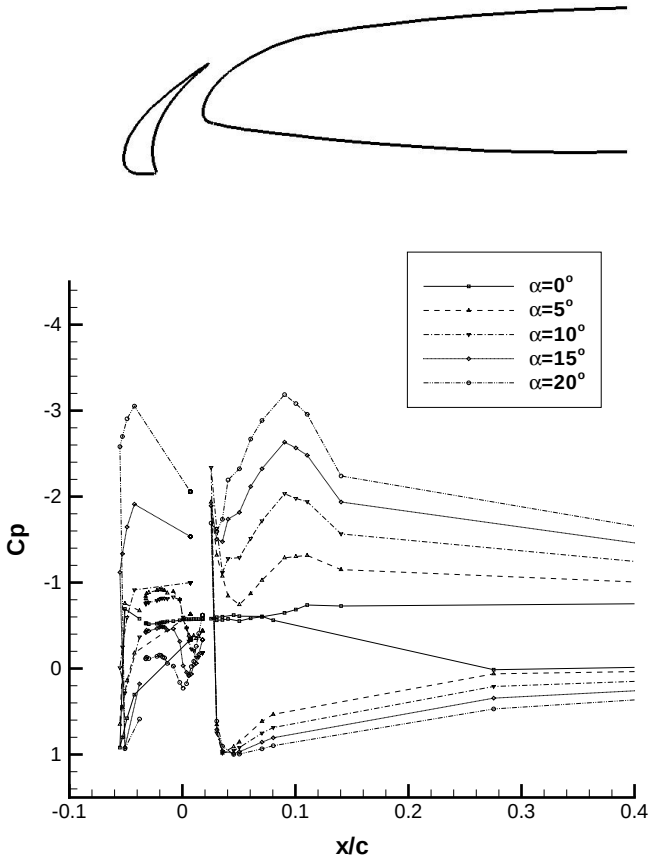

Figure 3.15: Experimental C_P plot showing the impact of the aerofoil incidence. v=30 m/s, α_S=13°.

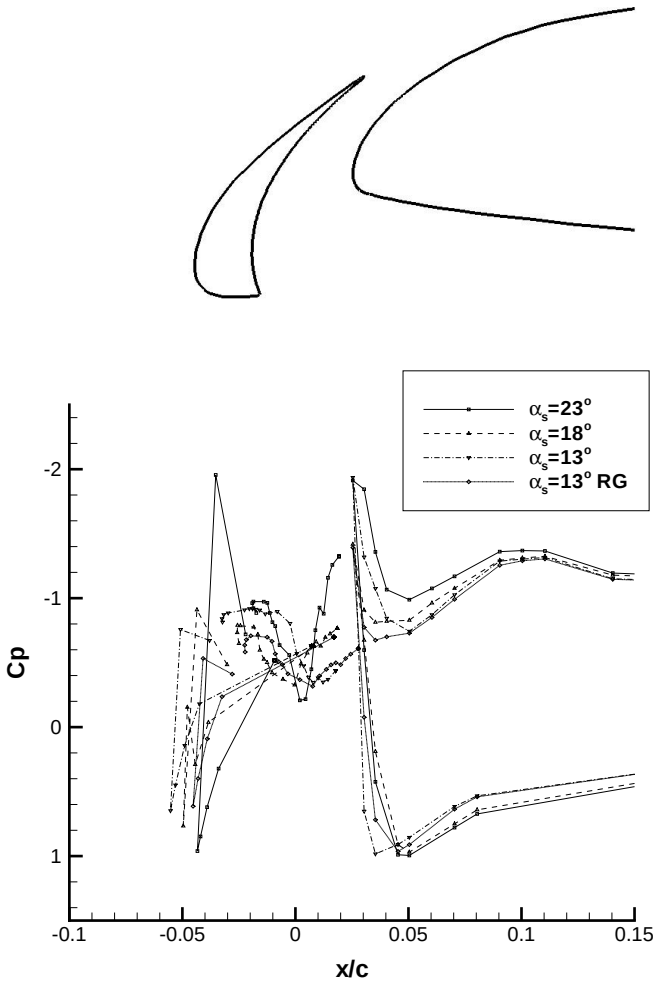

Figure 3.16: Experimental C_P plot showing the impact of the slat angle. v=30 m/s, α=5°.

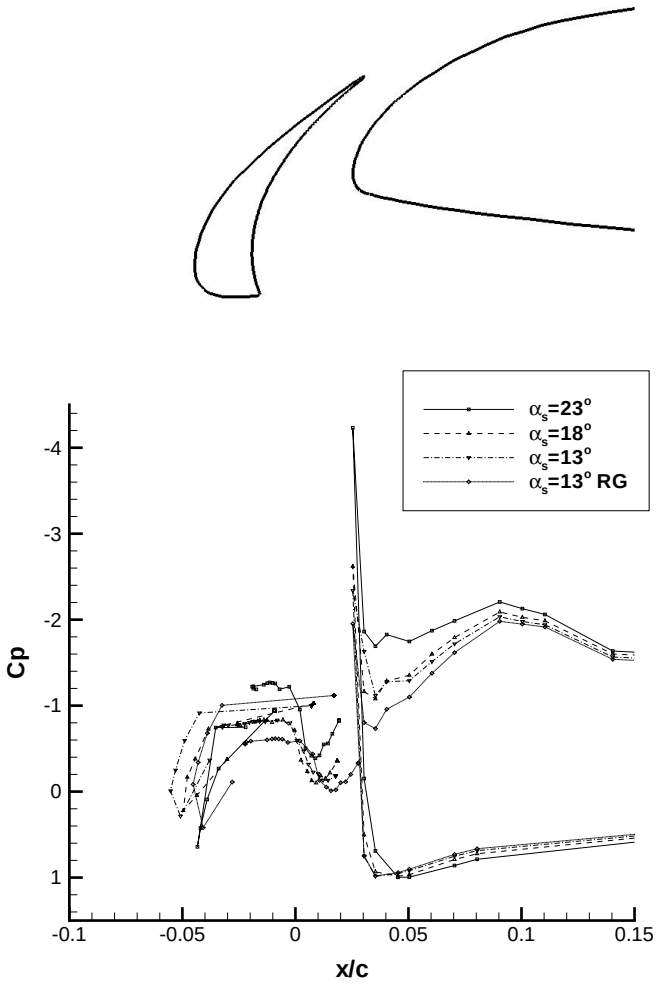

Figure 3.17: Experimental C_P plot showing the impact of the slat angle. v=30 m/s, α=10°.

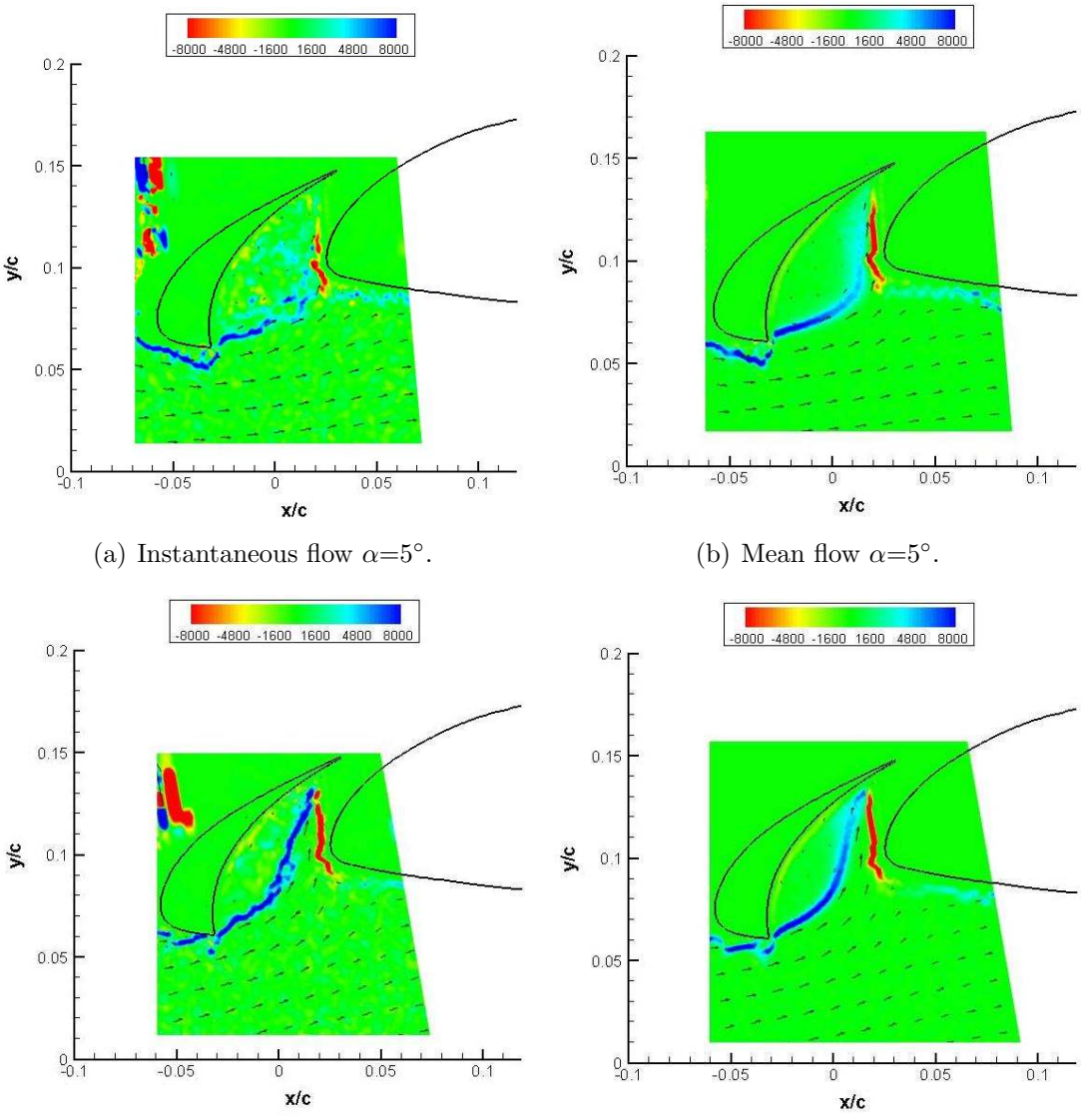

(a) Instantaneous flow α=5°.

(b) Mean flow α=5°.

(c) Instantaneous flow α=10°.

(d) Mean flow α=10°.

Figure 3.18: PIV spanwise vorticity plots (s^{-1}) over the aerofoil incidence range. v=25 m/s, α_S=13°, α=5°, 10°.

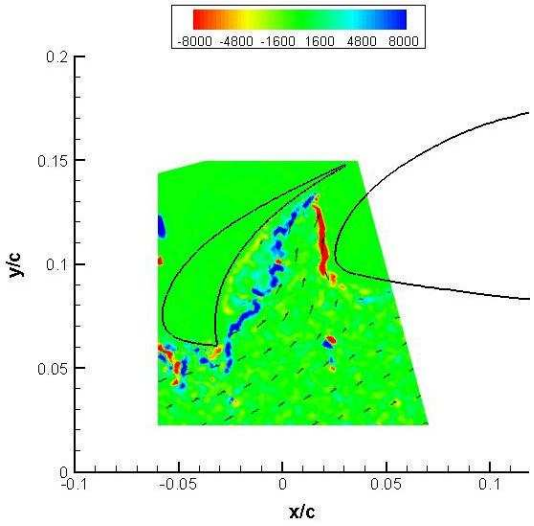

(a) Instantaneous flow α=15°.

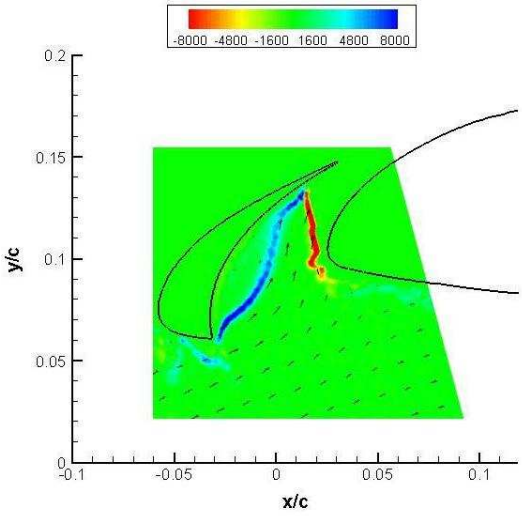

(b) Mean flow α=15°.

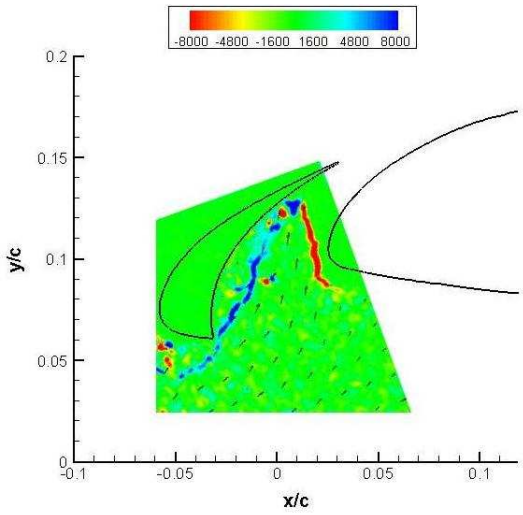

(c) Instantaneous flow α=20°.

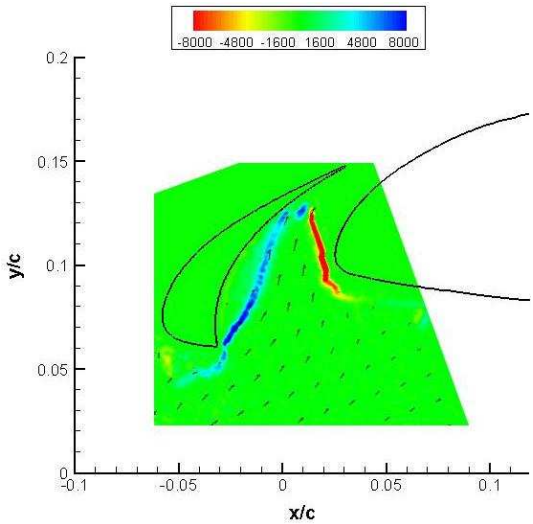

(d) Mean flow α=20°.

Figure 3.19: PIV spanwise vorticity plots (s^{-1}) over the aerofoil incidence range. v=25 m/s, α_S=13°, α=15°, 20°.

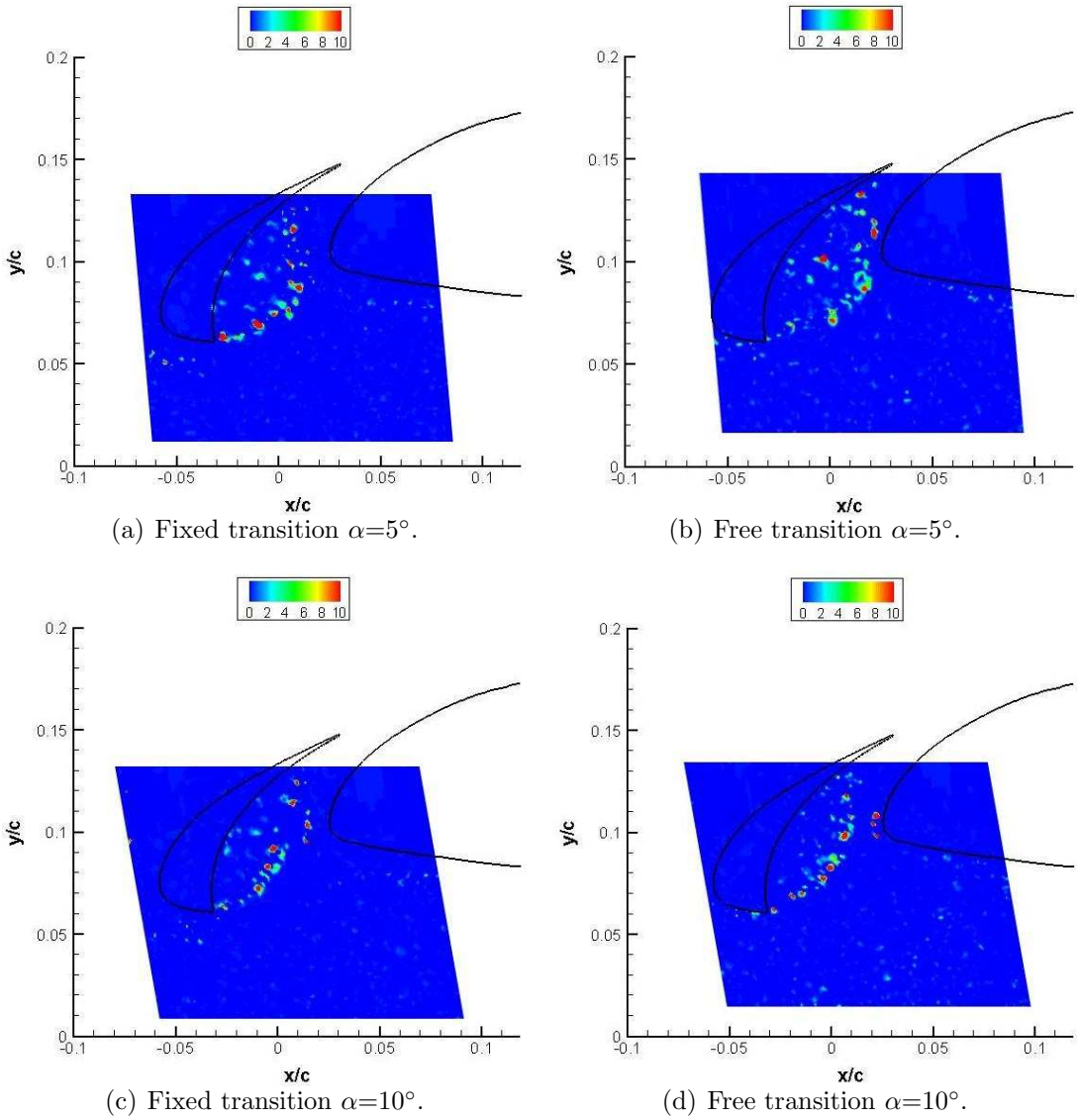

(a) Fixed transition α=5°.

(b) Free transition α=5°.

(c) Fixed transition α=10°.

(d) Free transition α=10°.

Figure 3.20: Q value plots (s^{-2}) using the PIV data over the aerofoil incidence range. v=25 m/s, α_S=13°, α=5°, 10°.

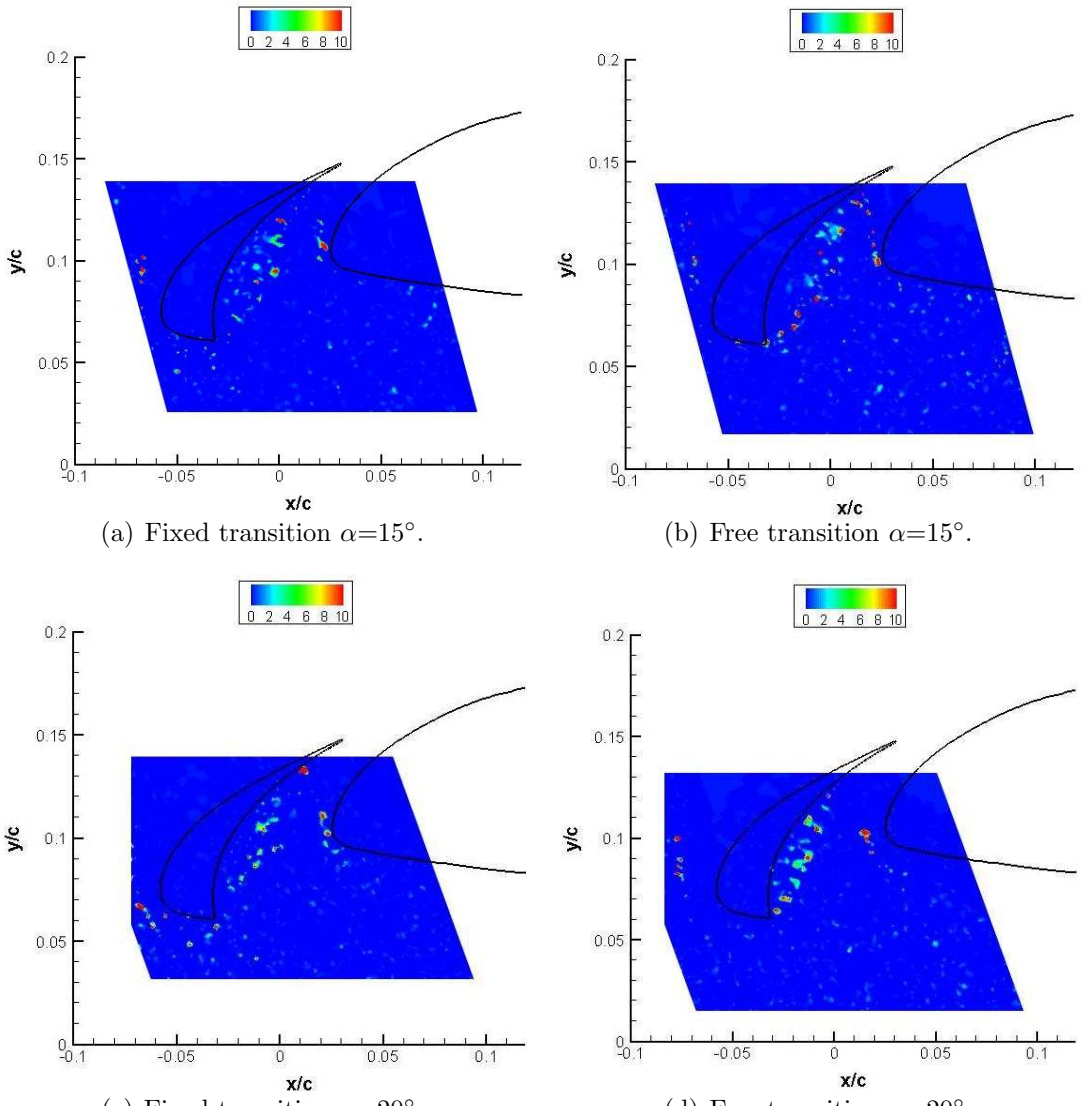

(a) Fixed transition α=15°.

(b) Free transition α=15°.

(c) Fixed transition α=20°.

(d) Free transition α=20°.

Figure 3.21: Q value plots (s^{-2}) using the PIV data over the aerofoil incidence range. v=25 m/s, α_S=13°, α=15°, 20°.

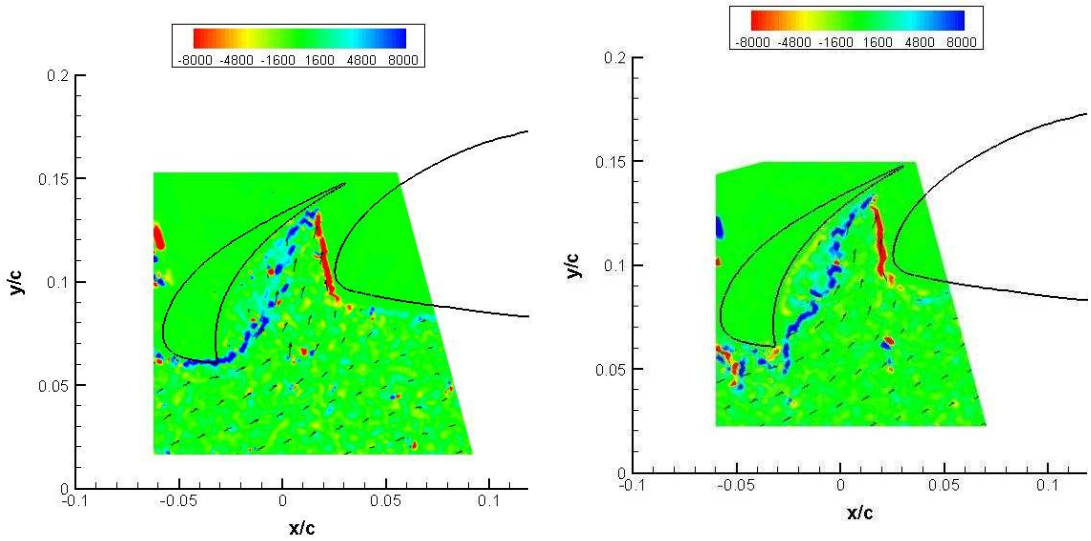

(a) Instantaneous flow, free transition.

(b) Instantaneous flow, fixed transition.

Figure 3.22: PIV spanwise vorticity plots (s^{-1}) for the free transition case and no tone with fixed transition. α=15°, α_S=13°, v=30 m/s.

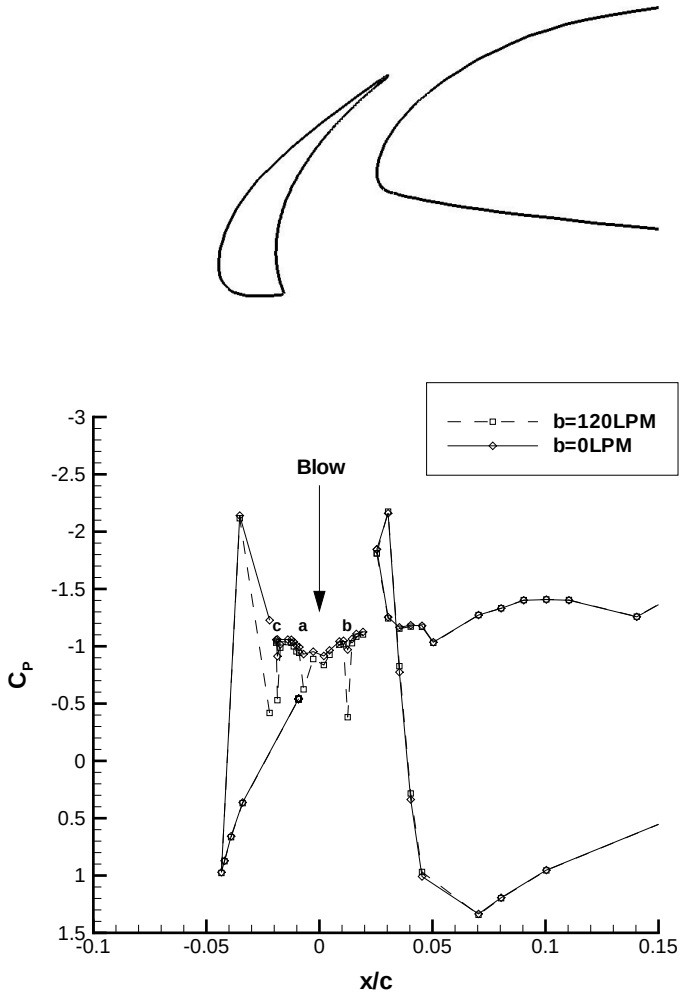

(a) C_P.

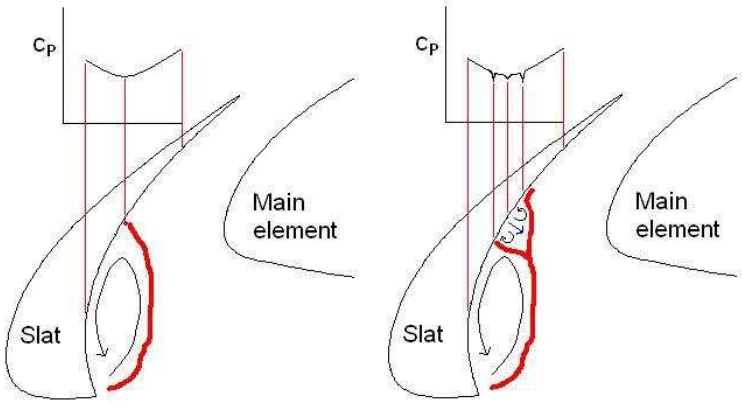

(b) Schematic showing the direction of the shear layer with and without blowing along with the corresponding C_P distribution on the cove side of the slat.

Figure 3.23: Experimental C_P plot showing the impact of blowing and schematic showing changes in the slat cove. v=30 m/s.

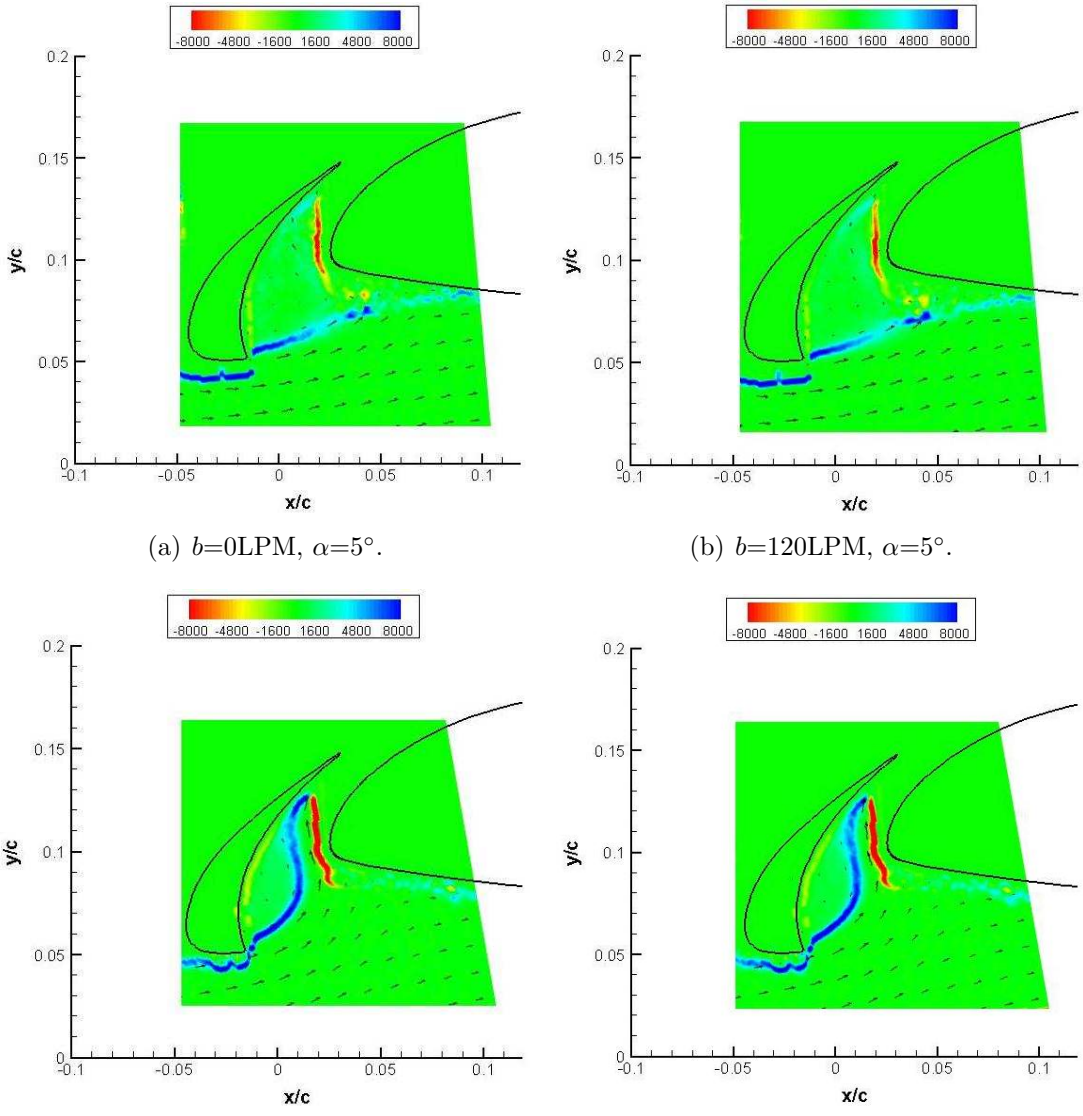

(a) b=0LPM, α=5°.

(b) b=120LPM, α=5°.

(c) b=0LPM, α=10°.

(d) b=120LPM, α=10°.

Figure 3.24: PIV spanwise vorticity plots (s^{-1}) showing the impact of blowing on the mean flow. v=25 m/s, α=5°, 10°.

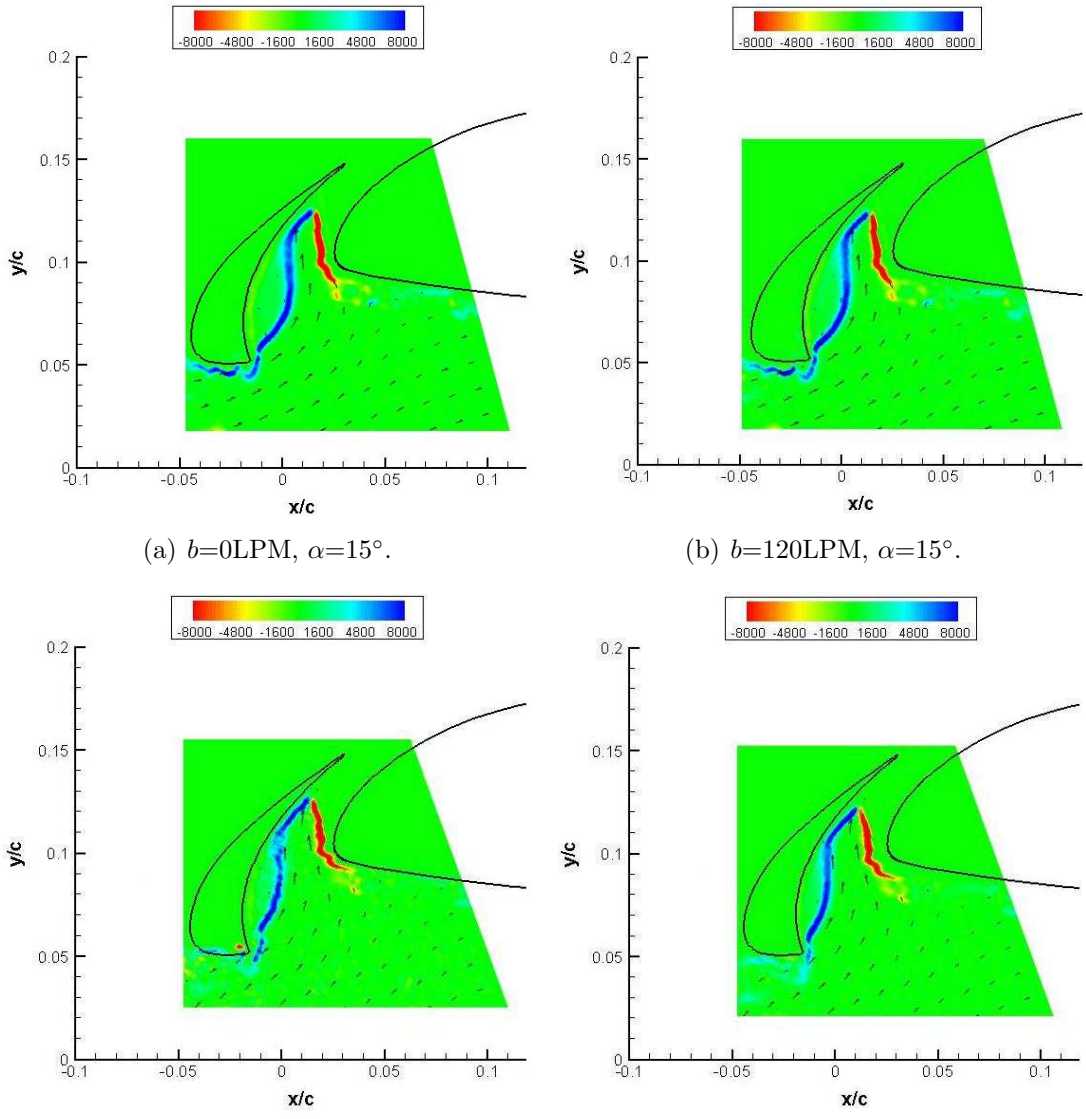

(a) b=0LPM, α=15°.

(b) b=120LPM, α=15°.

(c) b=0LPM, α=20°.

(d) b=120LPM, α=20°.

Figure 3.25: PIV spanwise vorticity plots (s^{-1}) showing the impact of blowing on the mean flow. v=25 m/s, α=15°, 20°.

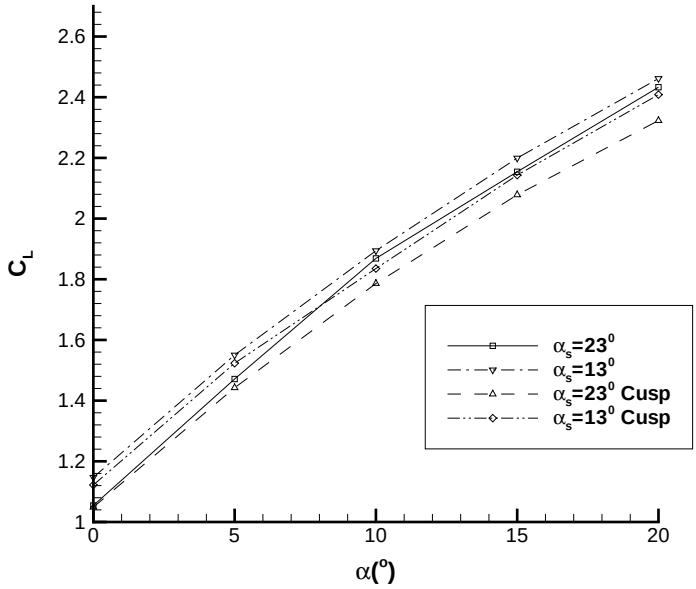

Figure 3.26: Experimental C_L vs α plot with and without the cusp extension, v=30 m/s.

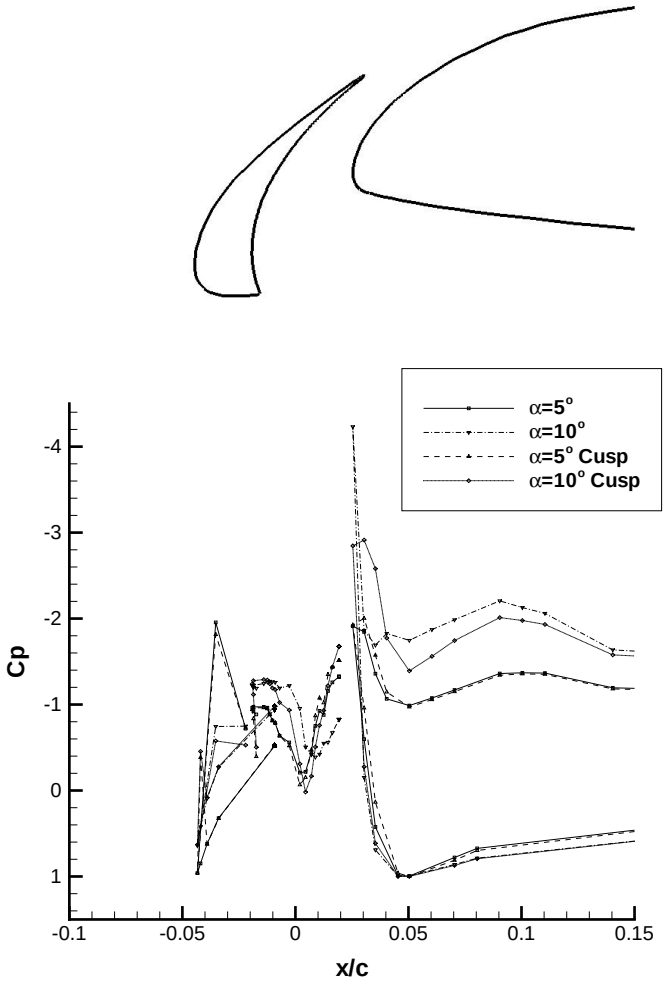

Figure 3.27: Experimental C_P plot showing the impact of adding the cusp extension, v=30 m/s.

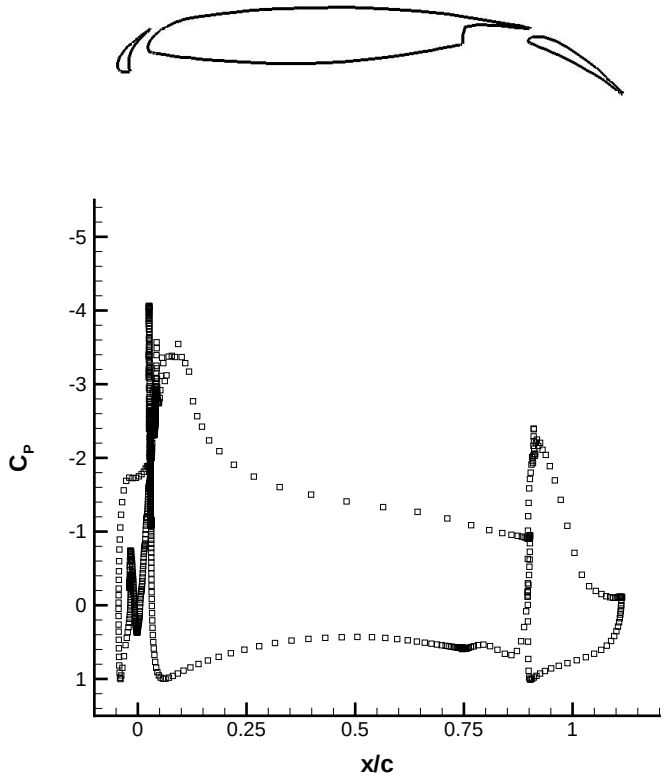

Figure 3.28: C_P plot in the reference conditions from the 3D grid, M=0.2.

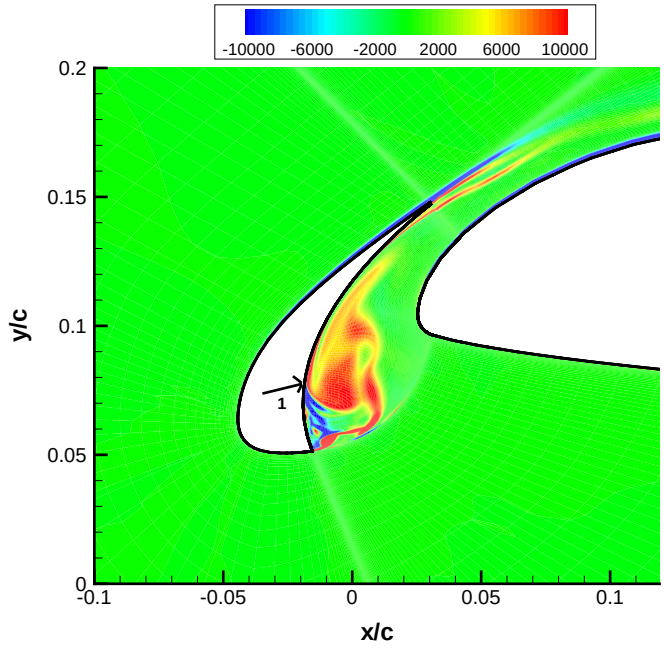

Figure 3.29: Instantaneous velocity magnitude plot in the reference conditions from the 3D grid (Normalized using the free-stream velocity v). M=0.2.

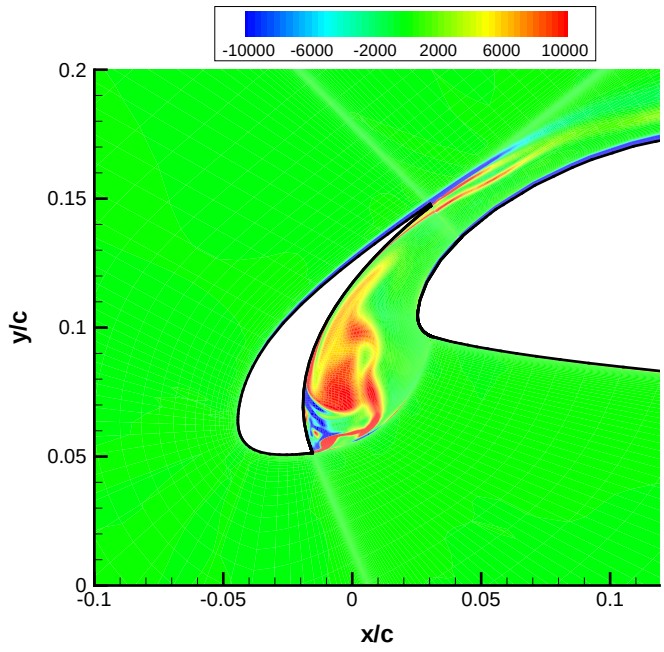

Figure 3.30: Instantaneous spanwise vorticity plot (s^{-1}) at the reference conditions from the 3D grid. M=0.2.

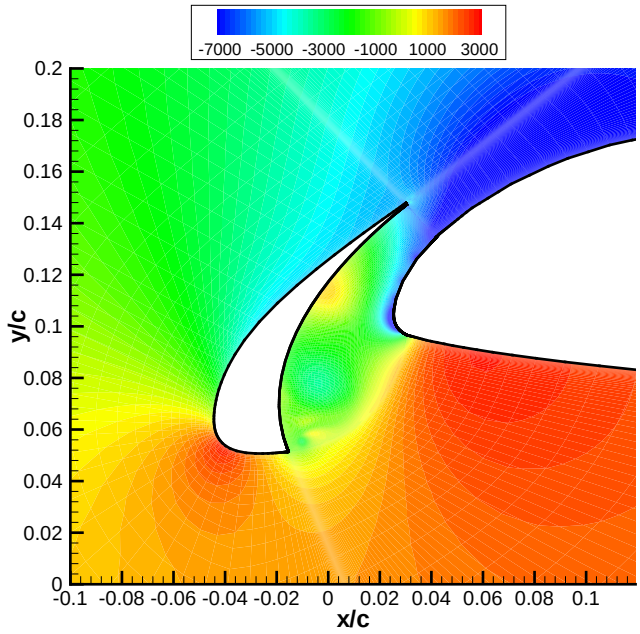

Figure 3.31: Instantaneous gauge pressure plot ($p - pref$, Pa) at the reference conditions from the 3D grid. M=0.2.

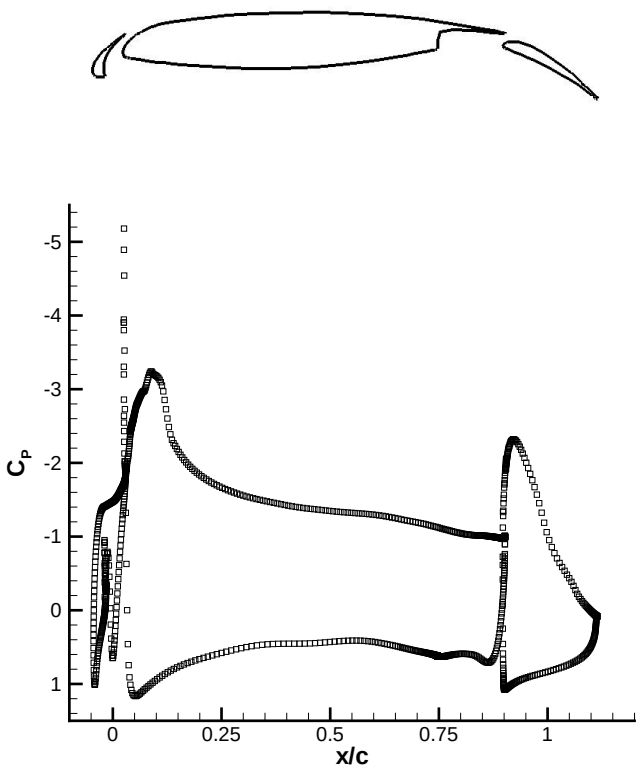

Figure 3.32: C_P plot from the 2D simulation, M=0.2.

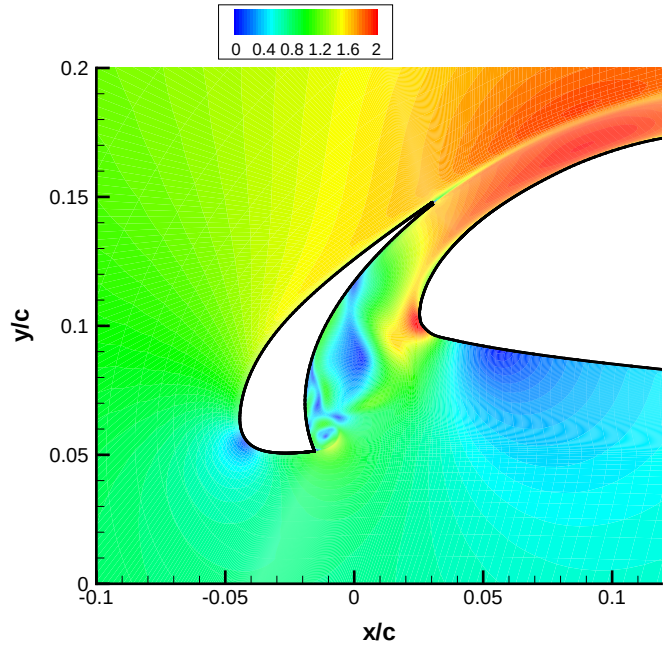

Figure 3.33: Instantaneous velocity magnitude plot at the reference conditions from the 2D grid (Normalized using free-stream velocity v). M=0.2.

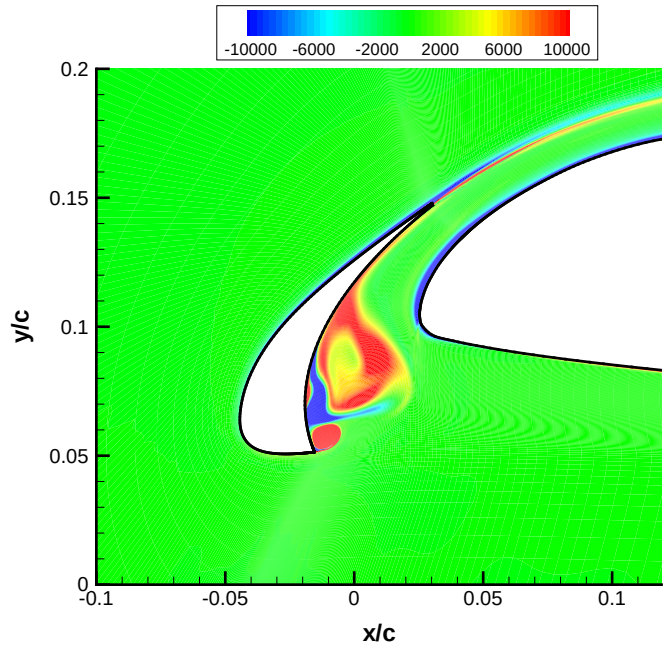

Figure 3.34: Instantaneous spanwise vorticity plot (s^{-1}) at the reference conditions from the 2D grid. M=0.2.

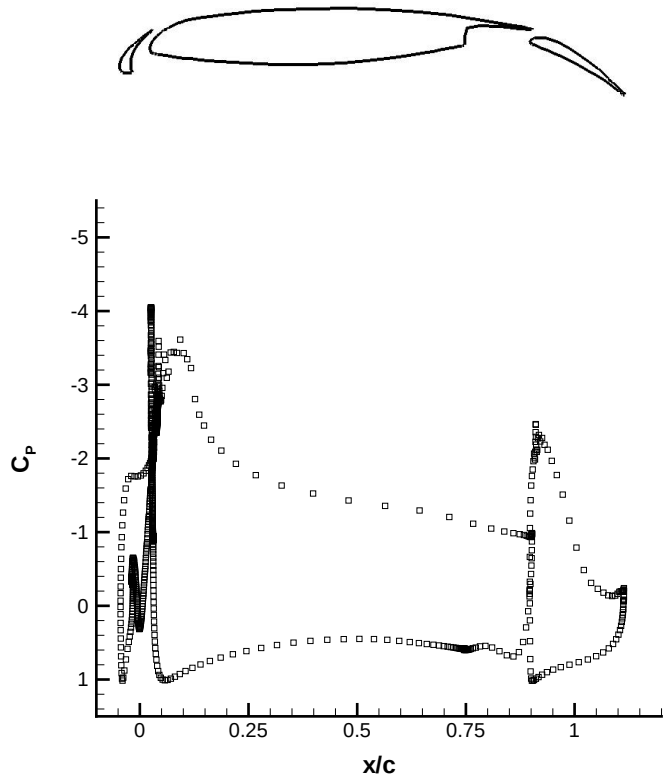

Figure 3.35: C_P plot with low rate blowing. b=120LPM, M=0.2.

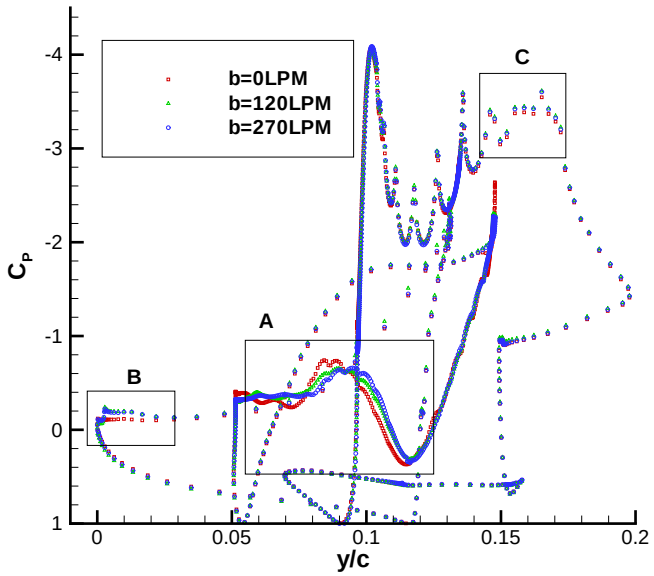

Figure 3.36: C_P vs y plot with varied blowing rates. M=0.2. (A) Slat cove surface, (B) Flap upper surface, (C) Main element, opposite to the slat trailing edge.

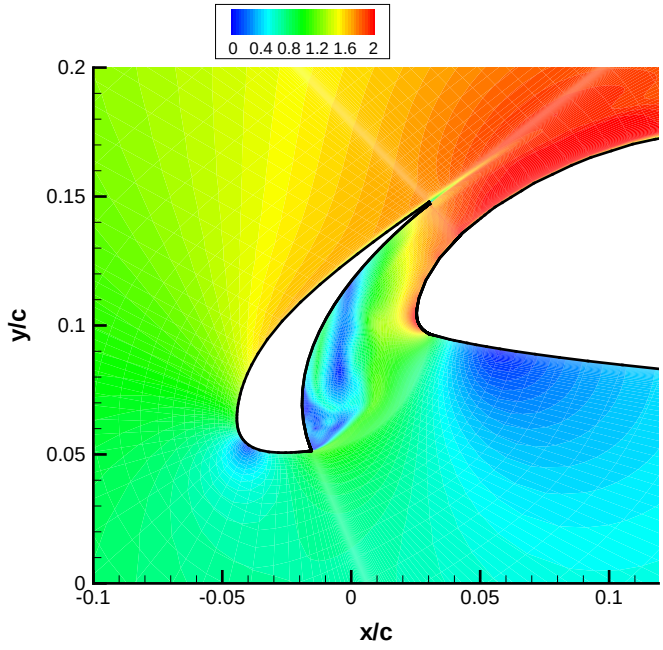

Figure 3.37: Instantaneous velocity magnitude plot with low rate blowing from the 3D grid (Normalized using free-stream velocity v). b=120LPM, M=0.2.

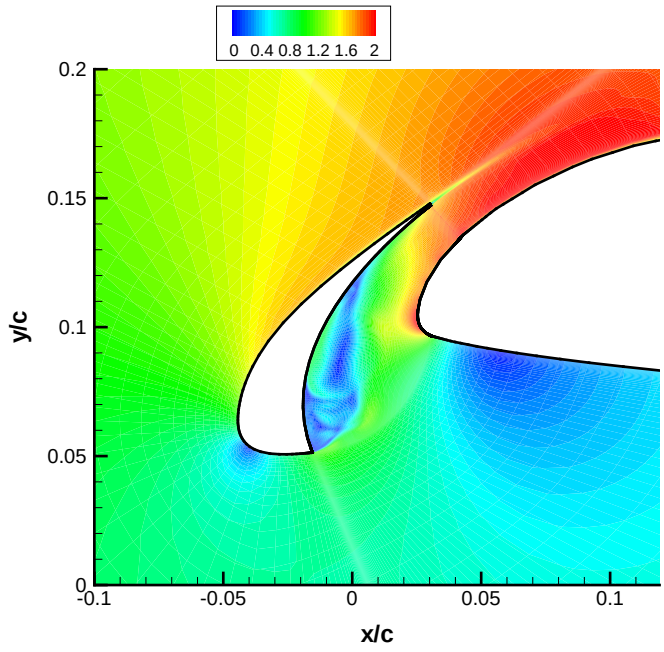

Figure 3.38: Instantaneous velocity magnitude plot with full rate blowing from the 3D grid (Normalized using free-stream velocity v). b=270LPM, M=0.2.

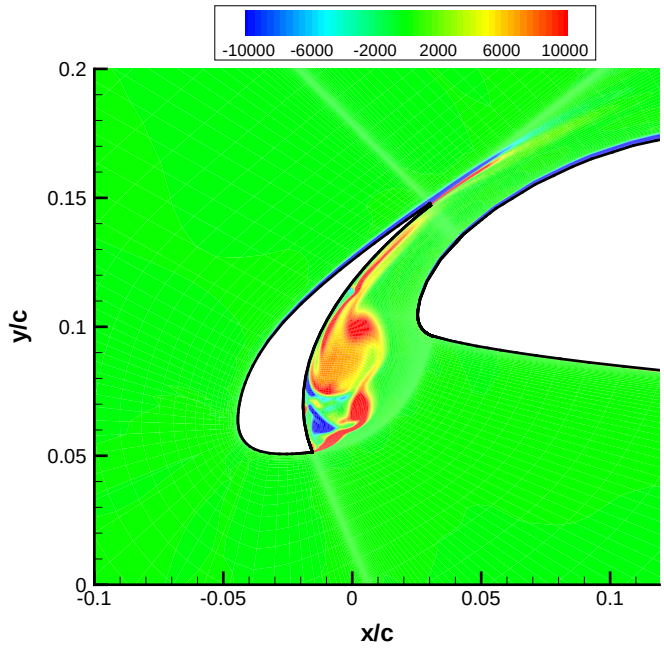

Figure 3.39: Instantaneous spanwise vorticity plot (s^{-1}) with full rate blowing from the 3D grid. b=270LPM, M=0.2.

Chapter 4

Aeroacoustic Results

4.1 Introduction

This chapter presents the aeroacoustic data from the study. The first section contains the experimental data, which were obtained using two techniques:

1. Flush mounted microphones on the model, which measured the local fluctuating pressure levels.

2. An acoustic array mounted directly above the model, which mapped the acoustic sources. The array data gave the spectra for the slat region and allowed calculation of the changes in the spectra.

The second section presents the aeroacoustic data obtained from the computational program. Near-field values came from monitoring points in the slat cove, which measured the pressure fluctuations (Figure 4.45 and Table 4.2). A FFT generated the local spectra from this data. The computational work also calculated the far-field directivity and the acoustic spectra of the far-field, using the FW-H equation on an integration surface.

The computational simulations complemented the experimental results by providing the far-field data but did not cover the range of conditions covered by the experimental work.

The third section brings together the different sets of results to explain the baseline results and the impact of the changes applied. The emphasis of the analysis was placed on linking the flow features found around the slat with the sound generated. This link assisted in the identification of the physical sound generation mechanisms. The identification of the sound generation mechanisms showed the physical reasons

for variations in sound levels. This section also contains work that examined the level of agreement between these sources and how they related to real aircraft.

4.2 Experimental results

4.2.1 Baseline results

The source maps from the slat were divided into fourteen 1/3 octave bands ranging from 1 kHz to 20 kHz. These plotted the SPL value (dB) on an imaginary grid placed in the plane of the aerofoil. The array data used 1/3 octave bands because it is a useful tool when examining broadband noise features but it does not pick up narrowband tonal features. At the lowest frequencies (below 2 kHz), the sound was dominated by the noise from the wind tunnel fan. The tunnel had a suck down arrangement so the fan was located just downstream of the test section, which resulted in the highest fan noise levels occurring downstream of the wing and lowest values occurring at the leading edge (Figure 4.1). From 2 kHz to 16 kHz the slat became the dominant noise source (Figures 4.2 and 4.3). The 20 kHz noise map produced unrealistic flow patterns due to the frequency limits of the microphones making this data unusable. The sound source strength distribution across the span of the model was non-uniform, indicating the flow exhibited some 3D variation in the distribution across the span. A spanwise non-uniform pattern was also detected when examining the separation line on the inside of the cove close to the slat cusp (Figure 4.4). The oil flow image shows that cellular features influenced the slat cove flow. At the reference conditions, five cells appeared and the centre section produced the highest sound levels in the array measurements. The model had a finite aspect ratio, which provided the main driving force for the observed flow variation across the span. However, the variation should have remained symmetrical about the centreline of the model for time-averaged quantities. As the cell pattern in Figure 4.4 is asymmetrical it indicates the presence of asymmetric imperfections in the shape of the wood and carbon fibre wing model. The spanwise variation in the tones was also found in array readings by Storms et al. [44]. However, their model included brackets and a half span flap, which added to the spanwise variation.

A measure of the acoustic spectra generated by the slat can be found by converting the SPL vales into fluctuating pressures then averaging the values across the area containing the slat and finding the resulting SPL value. Figure 4.5 shows the results from such integration at the reference conditions. The data followed the expected broadband pattern of a gradual reduction as the frequency was increased (Figure

4.5). The pattern found shows that the majority of the sound was generated at low frequencies with energy then transferred to higher frequencies as large unstable features decayed into smaller features. Altering the free-stream velocity changed the magnitude of the sound generation but did not have a large impact on the shape of the frequency spectra. The scaling of the spectra with velocity is addressed in section 4.4.1.

Addition of a trip strip to the slat did not alter the general shape of the frequency spectra generated by the slat. However, the trip strip did have an influence on the sound produced especially around 3-8 kHz. This frequency range is associated with shedding originating at the slat cusp, which fixing transition can remove. This thesis later shows that certain conditions generated a tonal feature in this frequency range.

The surface microphones for the reference conditions showed the surface pressure fluctuation was broadband in nature for all the microphone locations (Figure 4.6). The only significant feature was the tone observed at 470 Hz by microphone S2 on the outside of the slat. This tone appeared above broadband levels in many conditions, when the broadband unsteady surface pressure was low enough, and was not dependent on the model settings. This indicates it was a tone associated with the wind tunnel fan. The relative levels of the microphones show the unsteady surface pressure was highest at the slat gap (M1) and reduced towards the reattachment point (S3) and down to the cusp (S6). The microphones outside the cove had the lowest values indicating a local sound source rather than an external source, generated the majority of the unsteady surface pressure. The impact of changing velocity on the surface microphone was similar to the array results, with amplitude changes but similar frequency distribution (Figure 4.7). Examining the flow at lower frequencies shows that the peak broadband SPL occurred at 100-250 Hz suggesting the unsteadiness was driven by low frequency features.

With fixed transition, the flow at the gap was not significantly changed but there was an increase in the SPL in the cove at low frequencies (Figure 4.8).

4.2.2 Dependence on incidence

The aerofoil incidence had a large influence on the source distribution as measured by the acoustic array. Relative to the reference value of α=5°, the largest change was at α=0° where the slat ceases to generate enough sound to appear above the background levels on the source maps. Below 10 kHz the slat source strength reduced at increasing incidence. Above 11 kHz, the slat source strength matched the reference incidence value when the incidence was increased from α=5°. At higher frequencies, the pattern reversed and the slat source increased with incidence (Figure 4.9). The

pattern from the source maps was clarified by examining the SPL spectra of the slat (Figure 4.10).

The changes in the source pattern reflect a significant impact on the frequency spectra as incidence was varied. The integration of the data matched the flush mounted microphone readings in showing the quietest incidence was at α=0° . At 13 kHz there was a clear jump in SPL at high incidence (α=15, 20°) indicating the presence of a narrowband feature in this 1/3 octave band.

The differences are clearer when the change in SPL relative to α=0° is plotted (Figure 4.11). At α=5°, there was a significant increase in the sound production especially from 2 kHz to 11 kHz where there was an increase of up to 10 dB relative to α=0°. Below 8 kHz as the incidence was increased further there was a reduction in the difference relative to α=0°, resulting in little overall increase by α=20°. At higher frequencies, there was an increase in the sound levels at higher incidence. The increase was centred on 13 kHz matching the location found in the frequency spectra. The magnitude of the peak increased with increasing aerofoil incidence. This trend follows the pattern found with the surface microphones with α=5° being the loudest at low frequencies and high frequency features appearing at high incidence.

When the transition point was fixed using trip strips, at low frequencies the pattern was unchanged relative to α=0° (Figure 4.12). However, unlike the free transition case, the large increase at higher frequencies did not occur. The change was largest at high incidence around 13 kHz, indicating suppression of the tonal features. Plotting the difference generated by fixing the transition point highlights the changes generated (Figure 4.13). As well as removing the tones there was also a reduction in the level of the broadband noise generated at α=5° from 5-10 kHz. The only penalty for adding the trip strips was an increase in SPL level at α=20° of 4 dB at 2.5 kHz. However, this condition remained quieter than at lower aerofoil incidence settings.

The surface microphones followed the trend set out by the array results, with α=5° the loudest in most conditions and α=0° the quietest (Figure 4.14). The microphones also showed the reasons behind the high SPL readings at high frequency for α=15° and 20°. In these conditions, the tonal features generated are both loudest at the slat gap. At α=15° a high frequency tone was generated at 22 kHz and there was a rise in the SPL centred around 10 kHz. At α=20° there was a mid frequency tone at 13 kHz, which produced smaller sum-and-difference tones with a spacing of 2 kHz, along with a narrowband rise on SPL from 10-18kHz. A sum-and-difference tone occurs when a tone is generated in a flow that contains a driving frequency. Tones are generated on both sides of the original tone shifted by the frequency of the

driving frequency. The main tone matches the frequency predicted by the whistle mechanism of Tam and Pastouchenko [62]. The mid frequency tone was linked with a narrowband rise in broadband levels, which gradually reduced in magnitude as the aerofoil incidence reduces. The generation mechanism for this narrowband rise in SPL is linked to the feedback mechanism that generates the tone. When the feedback is in phase at the trailing edge the sound will be greatly amplified generating the tone. However, if the frequency is close to this value the feedback loop will still act and return sound that is almost in phase there will still be a reinforcement of the sound source. This amplification will be dependent on the phase shift of the feedback and will result in a narrowband hump centred on the tonal frequency. In the cove region, the tones were less important and there was a drop in the broadband noise levels. The array measurements showed a rise where the tones were located but the increase was only 5 dB indicating the impact of the tones was much smaller in the far-field than at the slat gap. Hence, the values taken in the cove region gave a better indication of the far-field levels (Figure 4.12).

With fixed transition, the broadband unsteady surface pressure levels were largely unchanged as was the high frequency tone. However, fixing transition did lead to some localized changes in the broadband SPL. There was a drop in SPL in the cove region at α=10° and an increase at the cusp at α=5°. These changes appeared on the array readings indicating that they were local features caused by a small change in the local unsteadiness. Fixing transition reduced the mid frequency tones. At the gap, they were still a major feature but in the cove region, the tones were no longer significant. Adding the trip strip aimed to promote transition to prevent laminar separation at the cusp, which could lead to the generation of a Kelvin-Helmholtz type single frequency instability in the shear layer. Removing this frequency altered the mid frequency tone and reduced the associated narrowband rise in SPL. The fact that tripping the separating boundary layer reduced the mid frequency tone indicates that the tone is produced by an amplification of instabilities within the shear layer, the growth rate of which is effected by tripping. The amplification around the mid frequency uses the feedback mechanism proposed by Tam and Pastouchenko [62], but the result of the amplification will depend on the original fluctuation amplitude allowing upstream changes to alter the mid frequency tone. The high frequency tone was unaffected by fixing transition, indicating it is caused by the blunt slat trailing edge. Tripping has a minimal impact on the trailing edge tone because it was not generated purely by the breakdown of a shear layer and the flow on the inside of the slat is not tripped allowing the possibility of relaminarization at the reattachment point. Overall, fixing transition acted to suppress tones

by preventing laminar separation at the cusp. However, tripping the flow added turbulence to the shear layer that the flush mounted microphones could pick up.

The general trend of the broadband sound reducing and high frequency sound increasing with increasing aerofoil incidence matched the trends found by Andreou et al. [47]. This work built on that study by showing that the high frequency trend at α=20° was associated with the mid frequency tone. The microphone array results also matched the earlier study by showing SPL invariance with aerofoil incidence at low frequency, but the surface microphones show that this is not the case and that the tunnel noise masks the slat noise. A similar aerofoil incidence trend was found by Storms et al. [44] including a drop in SPL at very low angles of attack. However, the highest value was found to occur at α=10° rather than α=5° indicating that this measurement is aerofoil geometry dependent.

4.2.3 Dependence on slat angle

At α_S=13°, as with the reference slat position of α_S=23°, the source maps show the slat source was not dominant at low frequencies. Over the range 1.6 kHz to 13 kHz, the slat source appears but the level was lower than the reference conditions especially at α=5°. The α=5° condition remained the loudest but the difference relative to higher incidence was reduced. At high frequencies (10 kHz+) the slat noise dropped below the background levels with the exception of the α=5° case where it generated a clear line source along the slat (Figures 4.15 and 4.16). The exception to the pattern, of reduced sound source levels at the low frequencies, occurs at 3.1 kHz with α=15° and α_S=13°. At this condition, there was a significant increase in the source strength indicating the presence of a narrowband feature (Figure 4.17).

The spectra obtained from the array readings at α_S=13° show, as expected, the general pattern was unchanged with the exception of the single point at 3.1 kHz (Figure 4.18). This increase only occurred at a specific frequency, indicating it was a narrowband or tonal feature rather than an increase in the broadband noise level. However, there were several smaller changes relative to the reference slat position case (Figure 4.10). The α=5° spectrum remained the highest SPL for most frequencies but was no longer significantly higher than the other lines. The change in slat angle also removed the rise observed at high incidence at around 13 kHz in Figure 4.11. In Figure 4.19 the change in SPL relative to α=0° is shown for α_S=13°. It is useful to compare this result to Figure 4.11 where the measurements for the reference condition of α_S=23° are shown. The increase in SPL at α=5° in Figure 4.11 was reduced by 3 dB at 2 kHz in Figure 4.19 and was less than 3 dB above 3 kHz. At high frequencies (10 kHz+), the SPL change relative to α=0° was lower

at α_S=13° than at α_S=23°, leaving less than 3 dB between the SPL at any incidence compared to a range of 10 dB with the reference slat. The one exception was the tone that occurs at α=15° but not at α=0°.

Combining the reduced slat angle with a reduced slat gap further reduced the impact of the incidence of the wing. The main changes in the spectra were significant reductions in the feature at 3.1 kHz and a reduction in the variation in SPL at low frequencies (Figure 4.20). Plotting the changes as the incidence was altered in Figure 4.21 shows that the change in SPL at low frequencies reduced by a further 2 dB due to reducing the slat gap compared to Figure 4.19.

Plotting the changes relative to the reference conditions show the overall changes due to altering the slat settings (Figure 4.22). Both of the settings with reduced slat angle gave a SPL reduction across the frequency range at both α=5° and α=10°. The improvement due to reducing the slat anlge was largest at α=5° due to the high SPL level of the reference conditions and the large improvement achieved by increasing the incidence to α=10°. The impact of reducing the slat gap was smaller, but was an advantage for frequencies up to 6 kHz. Above 6 kHz, the original gap setting was the better setting.

The location of the slat at the leading edge of the aerofoil means that the slat angle relative to the free-stream direction can become a useful factor in controlling slat noise. The broadband sound level generally reduced with increased angle between the slat and free-stream. The increase occurred either when the aerofoil incidence was increased or the flap angle was reduced. A 5° change in either of these variables results in a 5° change in the angle between the slat and free-stream flow, however, altering the aerofoil incidence had a greater influence on the broadband sound level. Figure 4.22 shows that a 5° increase in aerofoil incidence gave a larger SPL reduction than a 10° increase in slat angle up to 8 kHz. At higher frequencies the mid frequency tone resulted in an increase with increased aerofoil incidence but this did not occur with the reduced slat angle until α=20° (Figure 4.19), 10° higher than with the reference slat angle (Figure 4.11) showing that it was slat angle dependent. The greater importance of the aerofoil incidence relative to the slat angle, where tones were not an issue, occurred because increasing the aerofoil incidence increased the lift generated by the wing. The increased lift generated a local upwash around the slat, which effectively further increased the aerofoil incidence and further reduced the slat noise. The reduced gap setting was similar to the α_S=13° case but it did give a small reduction in SPL especially below 5 kHz.

With both slat settings at α_S=13° fixing transition had little impact with the exception of narrowband features at α=15° (Figures 4.23 and 4.24). The largest

narrowband feature was located at 3.1 kHz where there was a large SPL reduction especially with the standard gap setting where the tone was larger. Unlike at the reference slat position of α_S=23°, there were no large high frequency tones at α_S=13°, so fixing transition had little impact at high frequencies.

The surface microphone data recorded at α=5° show that there was no narrowband feature for any slat angle (Figure 4.25). At α=10° there was much greater variation in the levels found. For the cove microphones (S3, S6), the pattern matched the pattern found by the array, with a reduction in SPL for α_S=13° and little difference generated by reducing the slat gap. The best match to the array came from the cusp microphone (S6) which picked up the convergence from 5-8 kHz and the larger reduction away from this frequency (Figure 4.22). At the slat gap, the pattern was different with the reduced gap having the highest noise levels. However, the increase was due to the reduced gap size moving the sound source closer to the microphone rather than a higher source strength since the array SPL for α=10°, α_S=13°RG in Figure 4.22 is lower than the SPL at α=10°, α_S=13° with the standard gap width. At α=15° a new tonal feature was present when α_S=13° (Figure 4.26). This feature contained several tones over the range of 3-5 kHz (Figure 4.27). These features were sum-and-difference tones, which occur when a tonal feature interacts with another disturbance present in the flow. The magnitudes of the tones were highest at the reattachment point (S3) and slat gap (M1) indicating the sound originated at the reattachment point (Table 4.1). Due to the high aerofoil incidence, this location was downstream of microphone S3, which was the closest to the reattachment point. At the slat gap (M1), the highest peak occurred at 3.45 kHz. However, for the cove microphones, the tone at 4.05 kHz was the dominant feature. The spacing of the tones indicates the wind tunnel fan, which produced a tone at 470 Hz, generated the sum-and-difference part of the tones. The array image of this tone showed uneven distribution of the tone across the span and unlike other variation was highly asymmetrical (Figure 4.17). This pattern indicated a localized source for the tone due to a small spanwise variation in the model and high sensitivity to the model settings.

Away from the tone, the slat angle had less impact especially at the cusp (S6). At the slat gap (M1), the reference incidence had significantly higher high frequency sound but the far-field noise did not share this feature (Figure 4.22). At α=20° the pattern was similar with the reduced slat angle giving large SPL reductions at the slat gap (M1), small SPL reductions at S3 and no large reductions at the cusp (S6). As well as these broadband noise features, altering the slat incidence also removed the mid frequency tone giving an improvement at 13 kHz.

Plotting the spectra at different wing incidences together in Figure 4.28 shows

the variation with wing incidence was similar for all slat angles where no tones were present (α=5°, 10° and 20°). The SPL is highest for α=5° with reductions for higher incidence. For both of the slat conditions, microphone M1 gave higher values at α=5° and 10° than those observed in the cove and microphone S6 gave the best match to the array data.

Overall, it was found that acoustically it was beneficial to reduce the slat angle. This reduced the broadband SPL level (agreeing with Wild et al. [45]) and reduced the tonal content of the flow.

4.2.4 Influence of blowing

Switching on the blowing system added an additional noise source to the wing in addition to altering the aeroacoustic sound. The self-noise generated by the blowing system was determined by the blowing rate and was unaffected by the flow, allowing measurement with the wind off. The source maps show the blowing noise is concentrated to the right side of the internal chambers of the slat (Figures 4.29, 4.30 and 4.31). The locations of the sound sources indicate the air entering the plenum chambers, rather than the air exiting through the external skin of the slat generated this sound. Only two sections of the slat were significant noise sources despite all three haveing the blowing activated. This indicated an interaction between the jet entering the slat cove and the surrounding tubes for the pressure taps and microphone cables generated the noise. As the microphones and pressure taps were located at the centre-span point and exited via the right side of the slat as viewed in the array source maps, they are only present in two of the chambers. The spectra generated by the blowing showed an increase in SPL as the blowing rate increased (Figure 4.32). The SPL produced by the blowing did not produce any clear tones but did generate a narrowband local maximum between 5 kHz and 15 kHz.

With the wind activated, blowing noise partially covered both other local noise sources and background noise. These noise sources were flow speed dependent, so at low flow speeds, the blowing was a dominant source across the frequency spectrum but at higher free-stream velocities other noise sources masked the blowing noise at lower frequencies, limiting the impact of blowing self-noise to above 5 kHz. In a real system, the free-stream velocity is higher than in the tests and noise reduction by improved plenum design should reduce the impact of blowing noise relative to these tests. The emphasis should therefore move to reducing the aeroacoustic sound levels.

The spectra generated with blowing showed the blowing system produced a very confused picture at low frequencies (Figure 4.33). Up to 5 kHz, the blowing altered

the SPL by up to 3 dB either up or down. Above 5 kHz, there was a clear upward trend as the frequency increased. The increase in SPL above 5 kHz links directly to the blowing self-noise. By examining the sources from the starboard end of the wing, the blowing self-noise was not included and the increase is greatly reduced (Figure 4.34). At the wing tip, the increase only occurred above 10 kHz with a maximum increase of 4 dB at 20 kHz compared to increases of over 5 dB above 5 kHz.

The complex patterns generated by the blowing system as the slat setting and aerofoil incidence were altered required an examination of the spectra produced over a range of conditions to clarify the general trend. The array SPL spectra generated with the configurations with $0° \leq \alpha \leq 20°$, $13° \leq \alpha_S \leq 23°$ and normal and reduced slat gap were averaged and the minimum, mean and maximum SPL of the data set was plotted in Figure 4.35. Below 5 kHz, the pattern was to have little change in the mean SPL, with a variation of 3 dB in either direction. Above 5 kHz, the increase due to the blowing noise was clear and its magnitude increased with higher blowing rates. Blowing noise occurred for all slat angles with the value at α_S=13° at the top end of the range shown due to the lower no-blowing broadband levels at high frequency. The flow maps below 2 kHz show that the fan-noise dominated (Figure 4.1) and above 5 kHz, the blowing noise dominated (Figure 4.35) so the area of interest lies between 2 and 5 kHz. In this region, the trend was upward as the frequency increased but at 2.5 kHz, there was a small noise reduction for most conditions. However, this drop was less than 1 dB so it was much smaller than the scatter produced by the various slat angles, wing incidences and slat gap settings, which gives a range of around 4 dB.

Addition of a trip strip did not significantly alter the pattern when using blowing because it did not alter either the fan or blowing noise sources (Figure 4.36). The most significant change was the possible reduction found at 2.5 kHz was not present with fixed transition.

Figure 4.37 shows the effect of blowing on the wall pressure fluctuations. At the reference conditions, the impact of blowing was small at the reattachment point (S3) and slat gap (M1). However, there was an increase in SPL of 2 dB at the slat cusp (S6) up to 10 kHz. The changes measured locally did not match the array measurements but the surface microphones are aligned to the centre of one of the plenum chambers away from the jet flow entering the chambers. By not picking up the internal jet noise, the change generated by the blowing only contain the component caused by the blowing through the slat skin and changes to the flow in the cove.

Applying blowing at low aerofoil incidence produced no significant change so it

was not beneficial but there was no significant penalty. At higher aerofoil incidence, there was a small penalty noticeable above 5 kHz. With the reduced gap setting, the blowing still gave no large improvement and the noise was higher above 20 kHz.

At the reference conditions, a combination of fixing transition with blowing gave a small improvement at microphones M1 (slat gap) and S3 (reattachment point), but was a major noise source at S6 (slat cusp) below 10 kHz (Figure 4.38). The lack of an SPL increase in the rest of the cove indicates this was a local change caused by altering the recirculation zone size rather than an additional noise source.

The combination of blowing and fixing transition had most potential when applied to the three tonal features, which originate at the wing. For the low frequency tone (3-5 kHz) (Figure 4.39), blowing without fixing transition had little impact. However, fixing transition completely removed the tonal features.

For the mid frequency tone (13 kHz) (Figure 4.40), blowing without fixing transition gave a 3 dB reduction in the tone but increased the secondary peak at 15.5 kHz. Fixing transition gave a larger reduction but did not remove the tone. Fixing transition also strengthened the secondary tone and caused a small frequency shift. The delta plots show that adding blowing to the fixed transition case gave a further 2 dB reduction in the maximum SPL of the tone at microphone S3 (reattachment point) but less than 1dB at M1 (slat gap) and S6 (slat cusp). However, relative to a no-blowing case, the blowing increased the broadband noise level in the cove region, especially close to the cusp (microphone S6).

Blowing also had little impact on the high frequency tone (Figure 4.41). Fixing transition reduced the frequency of the tone from 22 kHz to 21 kHz but produced no large reduction in its magnitude. Fixing transition actually gave a small increase at the slat gap and a small reduction at S3 (reattachment point), with no change in magnitude at the cusp. For the fixed transition cases, the delta plots show the peak and trough caused by the shift in the frequency of the tone. Relative to fixing transition, the blowing had little impact especially at M1 (slat gap). The maximum increase due to blowing occurred at the slat cusp (S6) which had an increase of up to 5 dB.

Overall, the blowing was less successful in suppressing slat noise than blowing applied flap edges [136] largely because the blowing is located just upstream of the slat gap. Because the gap is a narrow high-speed flow, blowing cannot move instabilities away from walls, which is possible in geometries that are more open.

4.2.5 Dependence on cusp geometry

The addition of the slat cusp extension at the reference conditions reduced the surface pressure fluctuations (Figure 4.42). The improvement was largest at the slat gap (M1) where there was a reduction of up to 4 dB across the entire frequency spectrum. Away from the gap, the changes were less pronounced. Microphone S3 (reattachment point) gave a small reduction at high frequencies (>5 kHz) but little change at low frequencies. At microphone S6 (slat cusp), the cusp extension was beneficial at low frequencies but increased the sound level at high frequencies. Examining the change in SPL caused by adding the cusp shows that the cusp extension was clearly useful at most frequencies at the reattachment point and in the slat gap (Figure 4.43). Close to the cusp (S6) the extension was useful at low frequencies but generated a small SPL increase at around 9 kHz. The action of the extension was to reduce greatly the size of the region of flow located at the cusp, which contained interactions between the shear layer and the recirculated flow. Reducing this area allowed a smoother recirculation and less destabilization of the shear layer. Microphone S6 was located at the joint between the extension and the slat, which along with the finite thickness edges of the component, was likely to be the source of the increase in the high frequency noise.

As the aerofoil incidence was varied, the extension maintained its usefulness at the gap for most settings as shown by microphone M1 (Figures 4.44(a), (c) and (e)). At α=10° the extension gave large reductions above 5 kHz but increases below this value. At α=15° the impact was reduced with only small reductions at low frequencies. The cusp did not remove the high frequency tone present in this condition. For α=20° the extension did remove the tone and associated peaks. This gives a major reduction in the peak SPL value. As a penalty, a high frequency tone appeared at 20 kHz, however, it was 25 dB quieter than the original tone.

Away from the gap, the extension was less advantageous. At microphone S3 (reattachment point) the extension produced a large increase in the broadband noise level for α=10° up to 15 kHz. At higher incidence, the increase was smaller but still present. The tonal features, which occurred at α=20° were still removed but their original magnitude was lower, meaning the tone was of the same magnitude as its replacement at 20 kHz. At microphone S6 (slat cusp), the results were similar although the penalties at high incidence increased.

With the slat angle reduced from α_S=23° to α_S=13°, (Figures 4.44(a), (c) and (e))the extension maintained its effectiveness at the slat gap giving large reductions at α=5° but large increases at α=10°. At high incidence, the extension had less impact and did not remove the low frequency tones. However, the extension did

generate the mid frequency tones at α=15°, where tones are not present with a standard cusp (Figures 4.28 (a), (c) and (e)). In the cove, the extension had little impact with a small increase of around 3 dB observed at all aerofoil incidence settings.

Overall, the extension has some potential to reduce the noise level at the slat gap but produced increases in the cove region. The benefit was also limited to conditions where the trailing edge was aligned with the flow past the slat cusp. When the slat angle reduced, or the wing incidence increased, the alignment was lost and the impact of the extension reduced. The extension acted in a similar way to slat cove covers that have been tested by Dobrzynski et al. [41, 46] and produced a similar reduction in the broadband noise level. However, the extension in this study modified the slat to give it a representative slat cusp geometry, similar to the baseline case used by Dobrzynski et al.

4.3 Computational results

4.3.1 Baseline results

For the baseline 3D configuration, the flow was monitored using seven monitoring points located within the flow thought the slat cove region (Figure 4.45). The aerodynamic pressure spectrum was obtained at each of these locations (Figure 4.46). The most obvious feature was the narrowband feature observed at point te1, which was located close to the slat trailing edge. The narrowband feature was at 7 kHz with harmonics at 14 kHz and 21 kHz and a high broadband level. However, further downstream, at te2, the broadband level dropped significantly and the tones disappear, showing that this feature was not radiating sound. The large features found were caused by locating the monitoring point close to the trailing edge resulting in large aerodynamic pressure fluctuations that cover any aeroacoustic features. High broadband levels also occurred at s1, which was just downstream of the cusp where the SPL level was at its lowest. At the cusp, the shear layer did not have time to become unstable but this occurred further downstream. The recirculated flow acted on the shear layer just downstream of the cusp accelerating the destabilization. Further from the cusp, at s2, s3 and at the reattachment point (R), the SPL level was lower with little variation between the different monitoring points.

The exception to the pattern was low frequency sound levels. Below 3 kHz, the reattachment point had the highest SPL value and the level gradually reduced away

from this point.

The far-field directivity obtained from the baseline configuration had the overall shape of a dipole aligned with the slat trailing edge (Figure 4.47). The slat element generated the majority of this sound. The slat sound was roughly dipole in shape aligned to the slat trailing edge with a slight increase in the downstream direction. The main element also produced a dipole shape but it was orientated closer to vertical with the sound concentrated directly above and below the wing. The flap dipole aligned with the flap trailing edge but was not a significant contribution to the overall sound distribution. In the overall plot, there was noticeable interference between the components giving contributions to the far-field SPL as the pressures were linearly added at the observer locations to determine the overall SPL. This linear combination gave a jagged appearance to the directivity plot. However, over time the cancellation and reinforcement of the sound waves would vary creating a smoother shape. The directivity followed the basic dipole shape found by Singer et al. [84] but did not include the shielding effects that are present in that simulation. Emunds and Fischer [90] also found the dipole shape using pressure monitors around the slat. However, they found that the downward lobe was amplified by the slat gap but this was based on a 2D simulation because a wall integration surface was used rather than an off wall surface.

4.3.2 Influence of blowing

With low rate blowing applied to the model, the main impact occurred downstream of the blowing location (Figure 4.48). At te1, the sound level dropped significantly and the tonal features disappeared. This indicated that the blowing moved the disturbances away from the wall by creating a smooth, slow moving boundary layer. The modified boundary layer was an advantage close to the trailing edge at te1 with reduced SPL, but further downstream at te2 there was an increase in the SPL. In the cove, s1 remained the loudest although there was a large increase in the sound levels found at the cusp and reduction at s2. These changes indicate the cause was due to changes to the size of the recirculation zone rather than changes within the shear layer. At low frequencies, the location with the highest SPL was still the reattachment point but the value at the other monitors was no longer determined by the distance from this point.

At the higher blowing rate, the impact past the blowing point was greater, with a significant reduction at both te1 and te2 (Figure 4.49). In the cove region there was less variation between the monitoring points than at lower blowing rates although s1 was the loudest at most frequencies and the reattachment point remained the loudest

at low frequencies. The greater uniformity of the recirculation region indicated the blowing has increased the amount of disturbances held in the cove. The noise level increased at the cusp but the disturbances at the trailing edge reduced in magnitude.

Examining the individual monitoring points show how the impact of the blowing varied around the slat (Figure 4.50). At the cusp, there was a significant increase in SPL as the recirculation zone was better defined, but in the rest of the shear layer, there was a slight reduction in the SPL recorded. Blowing had little impact at the reattachment point but was a significant advantage at the slat trailing edge.

The far-field value with the blowing showed a significant reduction in the RMS pressure at the monitoring points especially in sound originating from the slat (Figure 4.51). The p_{RMS} reduced by a factor of around 0.5 in most directions, which corresponds to a 6 dB drop. However, this result looks un-physical, especially with respect to the reduction in the slat noise. The change was probably due to the majority of the sound originating at the slat trailing edge. The reduction in the sound at this location due to blowing was reflected in the far-field levels. However, the main element acts to shield this noise source, so, in reality, the far-field noise observed on the ground was radiated from inside the recirculation region where blowing was less advantageous. The shielding was also directional and this was visible when the far-field RMS pressure with blowing relative to the no-blowing value is plotted (Figure 4.52). In most directions, there was a significant drop due to the application of blowing. However, this was not the case in the downward section, especially slightly ahead of the aerofoil. In this direction, there was an increase in the sound observed at the far-field and this corresponds to flow un-shielded by the main element. To solve this issue, the integration surface would need to be well away from the aerofoil so it allowed the trailing edge to be shielded. However, moving the integration surface required an improved grid resolution to allow accurate simulation of the acoustics within a large integration region. The large increase in the upward direction was not physical and corresponded to the interactions between the elements, which form the aerofoil.

4.4 Discussion

4.4.1 Broadband noise

For the baseline configuration, both experimental and computational results gave a broadband distribution. The broadband sound level was highest from the reattachment point to the trailing edge with a lower level observed in the cove region.

The experimental results showed the reference condition gave the highest level of broadband noise of all the conditions tested. Examining the flow pattern for this condition using the PIV data showed that the reference condition was also the condition where the shear layer approaches the reattachment point closest to the wall normal. This angle is referred to as the shear angle (ϕ) in this thesis (Figure 4.53). The high incidence between the shear layer and wall increased the interaction between them and allowed greater movement of the reattachment point. The shape of the broadband spectra was similar for most conditions and the low frequency SPL defined their magnitude. The values of sound recorded by the surface microphones were linked to shear angles measured using PIV (Table 4.3). Plotting the values shows higher shear angles lead to increases in the SPL measured in the cove at low frequencies (Figure 4.54). The points gave a roughly linear trend, expressed as:

$$SPL_{S3} = 0.371\phi + 82.3 \tag{4.1}$$

$$SPL_{S6} = 0.606\phi + 60.6 \tag{4.2}$$

It is noticed that there is a greater change in SPL with the reattachment angle at S6, close to the cusp, than at S3, which is close to the reattachment point. This is significant and suggests that the shear layer separation angle is possibly mirroring the reattachment angle changes at different aerofoil angles and slat angles.

However, the difficulty in obtaining a reliable angle of the shear angle, due to its shape and the difficulty in getting PIV data close to the slat wall, limited the accuracy of the data. This prevented an accurate fitting of the trend line. For a given slat, this trend indicated the sound levels were reduced most effectively when the incidence of the aerofoil increased. However, it was clearly advantageous to reduce the slat angle. The influence of the main element on the angle at the low incidence settings also suggested increasing the slat gap was also an effective means of control, although it would have had aerodynamic penalties. This matches the trend for aerofoil incidence found in this study and earlier studies [44, 47]. This trend also matched studies that showed cove fillers [2, 110] or advanced slats with smoothed cusps [109] generated less noise. For these slat designs, the flow remained attached so the shear angle was zero. Figures 4.46, 4.48 and 4.50 show that the main contribution to the unsteady aerodynamic pressure at the locations monitored in the time-dependant CFD predictions also has a broadband SPL peak in the 1 kHz to 3 kHz range. The variations with α and α_S could not be verified by the acoustic array data due to the wind tunnel fan noise masking the wing noise in this frequency range. At higher frequencies, the wind tunnel acoustic array results followed the

same trend as the surface microphones with higher levels where the shear angle was largest but the presence of narrowband features in the local unsteady pressure distort the results. The trend was also limited to flows that passed through the gap, so it is not valid at low aerofoil incidences (α=0°).

The other main factor determining the broadband level was the free-stream velocity. The free-stream velocity determined the energy in the system, which then led to the sound level. The impact of velocity can be expressed by a velocity scale factor as shown in equation 4.3:

$$SPL_{v2} = 10Log_{10}\frac{{p'_{v_1}}^2}{{p_{REF}}^2}(\frac{v_2}{v_1})^n \tag{4.3}$$

where the scale factor n is found by examining the SPL measured at different free-stream velocities from cases with identical settings. Only the noise from non-blowing cases can be scaled by equation 4.3 because the blowing noise can significantly contribute to the sound levels recorded. The blowing component did not scale with free-stream velocity resulting in a greatly reduced value for n. Experimental data were obtained at three speeds 10 m/s, 20 m/s, and 30 m/s allowing the calculation of n using three pairs of data over a range of incidences and slat incidences (Figure 4.55). However, other factors complicated obtaining a single scale factor. At low frequencies, significant sound was generated by the wind tunnel fan, which did not scale at the same rate as the slat noise. At higher frequencies, the fan had less influence over the scale factor, but tonal features can generate increased values when activated. The impact of tonal features and fan noise was minimized in tests that used α=5° at 20 m/s and 30 m/s. These conditions are the loudest relative to the fan noise and do not contain any tonal feature (Figure 4.56). At these conditions, there was still a discrepancy in the scaling at low frequency (<5 kHz) and at high frequency (>5 kHz). At low frequency, the SPL scales with $v^{5.4}$. However, at high frequencies the scale factor was $v^{7.2}$. At higher frequencies (>13 kHz) the scale factor reduced but this was likely due to the increase in fan noise at high frequencies and the microphone limitations at 20 kHz. The difference between the low and high frequency scaling rate is not always apparent when looking at a plot of the spectra at different speeds (Figure 4.5) however this is an optical illusion caused by the steepening of the spectra at higher frequencies. Plotting the difference in the spectra there is a clear increase in the difference at higher frequencies (Figure 4.57).

The difference between low and high frequencies indicated that a dipole source generates the majority of the low frequency noise. However, the high frequency sound must have had a significant quadrapole component. For broadband noise,

the dipole source was most important with significantly higher SPL at lower frequencies. Scaling from v=30 m/s to M=0.2 will result in a relative increase in the high frequency noise which will increase by 25 dB as opposed to 19 dB for the low frequency sound (using scale factors of 7.2 and 5.4). However, the low frequencies will remain dominant.

The low frequency scale factor of 5.4 matched values of 5.3 and 5.7 found previously [50, 2]. The higher frequency factor of 7.2 contained significant narrowband contributions which are quadrapole in nature similar to those found by Dobryzynski et al. [46]. The transition point of 5 kHz was significantly lower than the 25 kHz found by Dobryzynski et al. but this value was largely determined by the tonal features and hence by the free-stream velocity which was run up to 60 m/s in the earlier study.

4.4.2 Narrowband noise

The surface mounted microphones embedded in the slat recorded that the aerodynamic pressure fluctuations a 4 kHz low frequency tone at α_S=13°, α=15° (Figure 4.39), a 13 kHz mid frequency tone at α_S=23°, α=20° (Figure 4.40) and a 21 kHz high frequency tone at α_S=23°, α=15° (Figure 4.41). The corresponding far-field acoustic array data showed a 3.1 kHz low frequency 1/3 octave SPL peak at α_S=13°, α=15° (Figure 4.18) and a 13 kHz mid frequency peak at α_S=23°, α=15° (Figure 4.10). This correlates the presence of tones in the mean wall aerodynamic surface pressure with acoustic noise at the low and mid frequency ranges. The variation in aerofoil incidence and slat angle allowed the impact of each of these tones to be measured, building on earlier studies, which did not find all the types of tone observed. Mapping of the appearance of tones followed on from work by Olson et al. [43], who examined the impact of slat angle and gap settings, by including the impact of aerofoil incidence. Using multiple surface microphones and the acoustic array also gave more information on the origin of the sound.

The low frequency tone was strongest at the reattachment point S3 (Figure 4.39(c)) and fixing transition can remove the tone (Figure 4.39(d)). This indicated the source of the tone had links to the laminar shear layer originating at the slat cusp explaining the tones reaction to fixing transition. The tone was not observed under most conditions indicating this was not caused by the shear layer acting alone. When the tone was active, it was possible for the recirculation region to act as a feedback mechanism, which caused the shear layer to break down and generate tones. The flow pattern for this condition obtained using PIV (Figure 3.22) shows the shear layer evolved into discrete vortices at this condition, but remained as a shear layer for

other conditions. The Q value for this condition also showed a staggered pattern in the vortices indicating greater instability in the shear layer (Figure 3.21) compared to the take off condition of α=5°. This change in local unsteady flow is likely to be linked to the acoustic feature that occurs in this condition. As well as appearing with α_S=13°, α=15° this tone was also observed at α_S=18°, α=20° (Figure 4.58). Only two conditions generated this tone and they both shared a common angle between the slat and the free-stream flow but different values of aerofoil incidence and slat angle. This indicates the resonance needed was dependent on the angle between the slat and the free-stream flow rather than on the incidence of the wing or slat. Finding the conditions where the tone appears builds on the study by Andreou et al. [47] who observed the tone and found it could be removed by tripping the flow. Takeda et al. [53] also found a tone originating from the cusp, although it occurred at a higher frequency due to a significantly different slat geometry. Kaepernick et al. [58] found that this tone had a Strouhal number of 0.21 based on the cusp trailing edge thickness, making the generation mechanism similar to that at the trailing edge (high frequency tone). However, in the current study the cusp os sharp and does not provide a reference dimension to determine a vortex shedding type in the separated flow.

The mid frequency tone was strongest at the trailing edge of the slat and was not removed by fixing transition. The location of this tone indicates it was generated either by the gap or by the blunt slat trailing edge. Equation 2.1 in Tam and Pastouchenko [62] was applied to the Airbus aerofoil of figure 2.1(b), tested with the reference gap. This predicted the tone frequency as 12.3 kHz. This frequency is a good match to the pattern observed for the mid frequency tone in Figure 4.40. When this tone did not occur, there was often a small SPL hump at this frequency like in Figure 4.14(e), indicating the mechanism was always active in generating noise but it only formed a tone under certain conditions. The gap selectively amplified flow instabilities over a particular frequency range determined by the gap velocity and width, but the noise output depends on the disturbances entering the gap. Broadband noise will simply be amplified to form a small hump whereas a tone requires a limit cycle to onset in the slat recirculation region. The hump increased in size with increased aerofoil incidence and slat angle. This result links the tone predicted by Tam and Pastouchenko to narrowband features that played an important part in the high frequency slat acoustics (see broadband section 4.4.1). An advance of the model by Tam and Pastouchenko could be to include a broadband distribution form into that model. This topic could be expanded in future work.

The mid frequency tone is also more dependent on the slat angle than the angle

between the slat and the free-stream flow, showing that the shape of the slat cove influences the magnitude of this feature. The impact of slat angle is clearly shown by the reduced importance of the tone at α_S=13° (Figure 4.28 (a), (c), (e)) compared to α_S=23° (Figure 4.14 (a), (c), (e)). The same figure show that the angle between the slat and free stream is not a good measure because configurations with constant angles between the slat and free stream do not have similar mid frequency characteristics, notable the pairs of α_S=23°, α=20° with α_S=13°, α=10° and α_S=23°, α=15° with α_S=13°, α=5°. The limited dependence on transition indicates the trigger is unlikely to be shear layer breakdown but it could be due to fluctuations in the shape of the recirculation region.

The high frequency tone also originated at the trailing edge and fixing transition did not remove this tone. The frequency of the tone did not match the expected gap tone and the finite thickness of the trailing edge was the most likely source. The flow at the trailing edge is not resolved by the PIV. However, the computational work shows that the flow past the trailing edge was approximately fifty percent higher than the free-stream velocity. This gives a local velocity of 45 m/s around the slat trailing edge. The frequency of the high frequency tone is 21 kHz (Figure 4.41). Using the 45 m/s trailing edge flow velocity and the $6.60\times10^{-4}c$ trailing edge thickness to normalize this frequency, a Strouhal number of 0.26 is obtained. This is a good match to the values found in other studies for trailing edge noise [44, 43].

4.4.3 Full scale values

To scale results to full-scale, there are two main factors to consider. The free-stream velocity for landing is generally around Mach 0.2. This is equal to the value used by most of the computational work but is 2.3 times larger than most of the experimental work. The second factor is the increase in size from the model chord of 0.8 m to a full-scale aircraft. For a single aisle aircraft such as the A320, the mean chord for the wing is 3.61 m although clearly this would vary along the span due to the wing taper. This represents an increase in scale by a factor of 4.5 relative to the experimental work and by 3.61 for the computational work, which used a chord of 1 m.

The sound level generated by the wing scaled by v^n, where v is the free-stream velocity and the exponent is six for a dipole source. Since SPL uses a logarithmic scale, the scale factor becomes a fixed addition to the SPL and an increase of velocity by a factor of 2.3 represents the addition of 21.3 dB for a dipole source.

The frequency scaling, which was important when investigating narrowband features, was determined by Strouhal scaling. The Strouhal number of a particular

feature should remain velocity independent. To scale from the model size and test speed of 30 m/s to the approach speed and size of an A320 aircraft resulted in a frequency scale factor of 0.5. Hence, the high frequency tone moves from 22 kHz to 11 kHz and the mid frequency tone moves from 13 kHz to 6.5 kHz and the low frequency tone moves to 2 kHz. For the computation results, the scale factor was 0.277. The tones reduced in frequency when scaled to full size so they all remain within hearing range for full-scale aircraft. However, on a full-scale aircraft slat, laminar separation does not occur. This removes the low frequency tone. The other tones did not occur in all conditions so they may not appear at full scale. The lack of tones observed in flyover tests indicates, that although the tones should scale to noticeable values, other factors prevent them from becoming prominent in the measured fly over tests.

A commercial civil aircraft wing also has sweep and taper, which would also influence the scaling of results from this study. The impact of these features is not easy to predict. Additional complications arise from additional features such as slat tracks, the landing gear and the influence of the fuselage, which this study did not cover.

4.4.4 Experimental/ computational agreement

The aeroacoustic results were based on the aerodynamic results so the differences due to the aspect ratio were reflected in these results. However, the shape of the spectra was consistent between the computational and experimental results along with the intensity distribution around the slat cove. Comparison of the tones was not possible as the simulations were carried out at α=5° where there was no tone in experiment. In the computational work, narrowband features were only detected at the trailing edge but this feature did not transmit the sound to the other monitoring points.

4.5 Summary

The microphone array identified the broadband sound sources on the wing and recorded 1/3 octave band far-field noise spectra. The aerofoil acted like a typical broadband noise source with the highest SPL at low frequencies and a reduction in SPL as the frequency increases. The array showed that there was a spanwise distribution in the sound source strength and this corresponded to a velocity distribution across the span.

The α=5° setting was the loudest for most conditions, especially at the reference slat settings. The SPL reduced as the aerofoil incidence was increased above α=5°. The quietest case was α=0°, although, at this incidence, the wing lift coefficient is too low for landing. For the reference slat at high incidence, there was a narrowband feature close to 13 kHz, which raised the SPL level above the α=5° value. Reducing the slat angle from α_S=23° to α_S=13° gave a small advantage across the spectra. In particular, it removed the high frequency feature and reduced the impact of aerofoil incidence on broadband noise particularly at low frequencies. The only increase occurred at 3 kHz due to the presence of a narrowband feature at this condition. Reducing the slat gap had less impact than changing the slat angle. It was generally advantageous below 6 kHz but a disadvantage at higher frequencies.

Fixing transition had little impact on the broadband noise SPL values. However, where there were narrowband features present, fixing the transition gave significant reductions in the SPL measured at low frequencies (3-5 kHz) and at mid frequencies (10-17 kHz).

The blowing system produced a significant additional sound source over the range 5-15 kHz. The additional sound was mainly self-noise, generated by the air entering the plenum chambers in the slat. This blowing noise originated at point sources inside the slat. Away from these sources, blowing did not add significantly to the flow noise. Below 5 kHz, there was no clear trend for the use of blowing. There was a possible improvement at 2.5 kHz but this only occurred at the free transition condition.

The shear angle and the free-stream velocity largely determined the broadband noise, with both strongly affecting the measured SPL. The SPL reduced as the shear angle reduced. This occurred when the aerofoil incidence increased or the slat angle reduced. Acting to reduce the shear angle generally reduced the size of the recirculation region, allowing a smoother flow passage through the cove region.

The velocity scaling indicates, that at low frequencies, dipoles generated the majority of the sound giving a scale factor of 5.4. However, at high frequencies, the scale factor was larger, indicating a significant quadrapole contribution.

Surface microphones show that all configurations produced broadband sound but there were four tones identified:

1. A tone at 470 Hz, which was not dependent on model settings and was due to the wind tunnel fan.

2. A low frequency feature, which produced tones over the range of 3-5 kHz, located at the reattachment point. This tone occurred at α=15° with α_S=13°.

3. A mid frequency tone at 13 kHz, located at the trailing edge. This tone occurred at α=20° with the reference slat settings.

4. A high frequency tone at 22 kHz, located at the trailing edge. This tone occurred at α=15° with the reference slat settings.

Fixing transition over the slat cusp completely removed the low frequency tone and significantly reduced the mid frequency tone. The three tones observed had three different causes. The low frequency tone was generated in the shear layer originating at the cusp. The mid frequency tone was a gap tone and the high frequency tone was generated by the blunt trailing edge of the slat. All three tones only occurred at certain conditions, despite all settings generating disturbances in the shear layer and at the slat gap and trailing edge, indicating the tones only occurred when the driving force was amplified. The narrow range of conditions that generate tones means that the tones are avoidable by adopting a suitable operational protocol at landing to fly the aerofoil off these conditions.

There were significant variations in the surface pressure records among the surface microphones with a clear change moving from the slat trailing edge to the cusp. The microphone at the cusp gave the best match to the array results with the microphone at the gap exaggerating the high frequency and tonal components of the far-field sound generated.

Scaling the results to a full-scale aircraft landing speed increased the SPL amplitude by around 20 dB relative to the experimental data due to the increased velocity. Additionally, scaling the test data to a full-scale aircraft wing chord results in the frequency of narrowband features reducing by a factor of two.

With the computational work, the monitoring points show for the baseline case that the SPL was highest in the shear layer just downstream of the cusp and close to the slat trailing edge at most frequencies. At the reattachment point the broadband surface pressure spectrum peaked at low frequencies. The far-field sound originated mainly from the slat and the main element, which both produced a dipole distribution aligned roughly with their trailing edges. The combined far-field noise radiations approximated to a dipole directivity with the majority of the sound directed either upstream, away from the ground, or downstream, towards the ground. Applying blowing reduced the unsteady aerodynamic pressure generated at the trailing edge of the slat. However, there was an increase at the slat cusp and no appreciable impact on the unsteady aerodynamic pressure at the reattachment point.

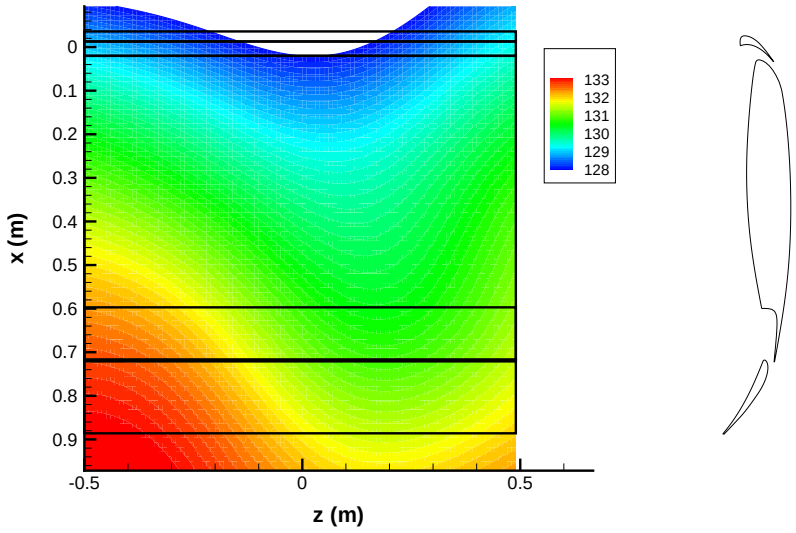

Figure 4.1: 1 kHz noise map showing SPL (dB) in the reference conditions. Free transition, v=30 m/s.

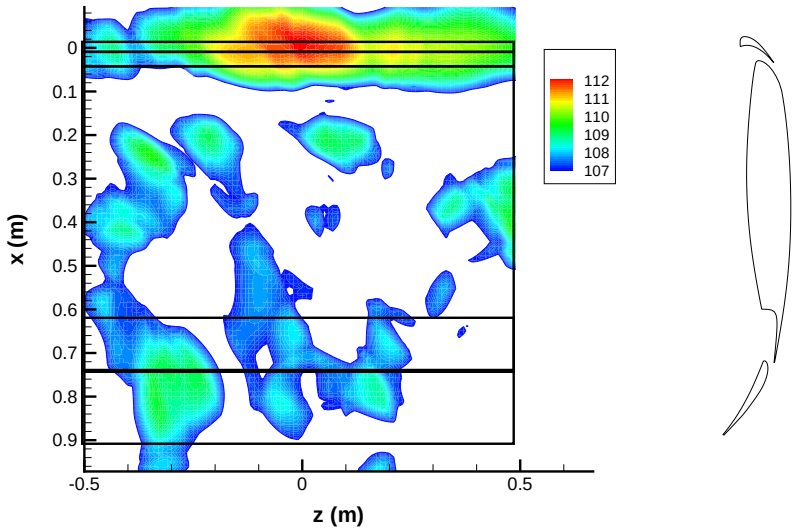

Figure 4.2: 3.1 kHz noise map showing SPL (dB) in the reference conditions. Free transition, v=30 m/s.

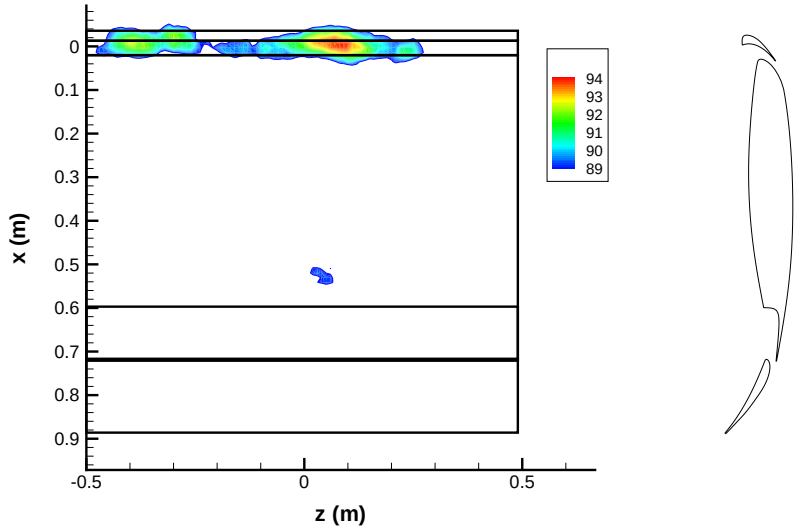

Figure 4.3: 10 kHz noise map showing SPL (dB) in the reference conditions. Free transition, v=30 m/s.

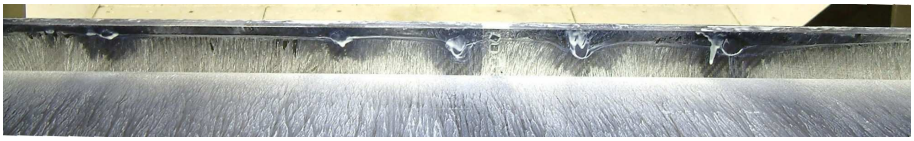

Figure 4.4: Oil flow photograph of the separation line in the cove in the reference conditions. Flow towards the camera, free transition.

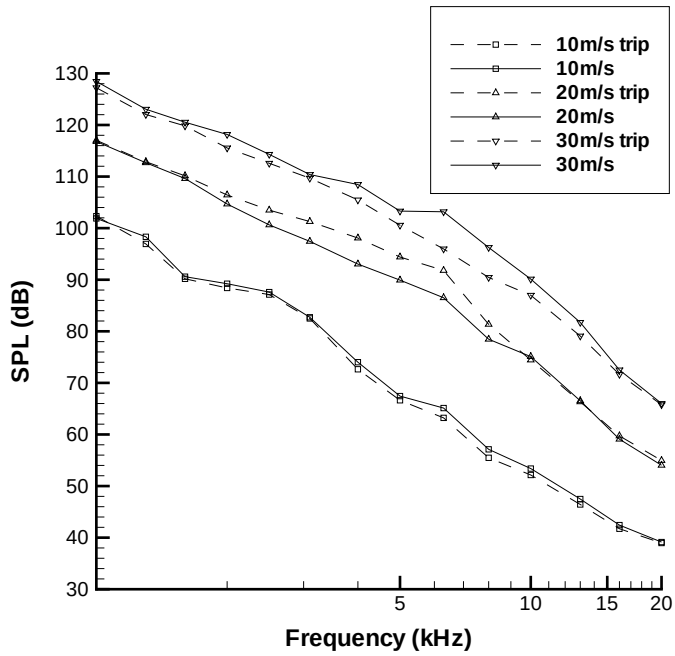

Figure 4.5: SPL spectra in the slat cove region measured at the array with the wing in the reference conditions. Free and fixed transition.

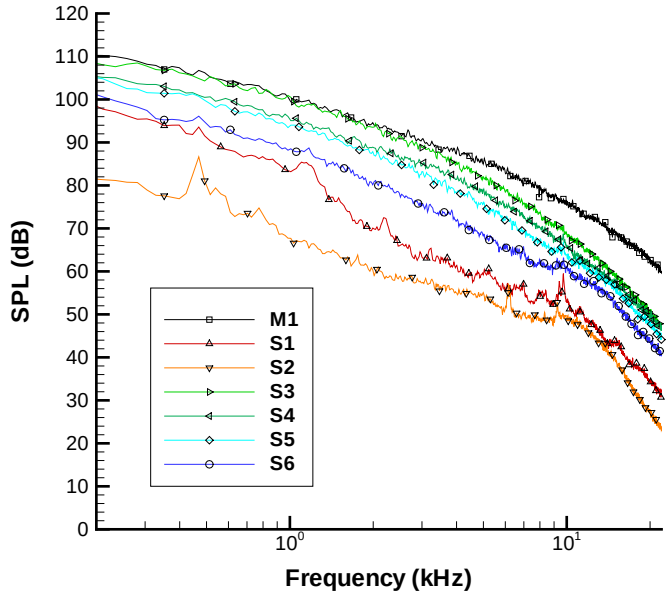

Figure 4.6: Surface microphone SPL spectra in the reference conditions, v=30 m/s.

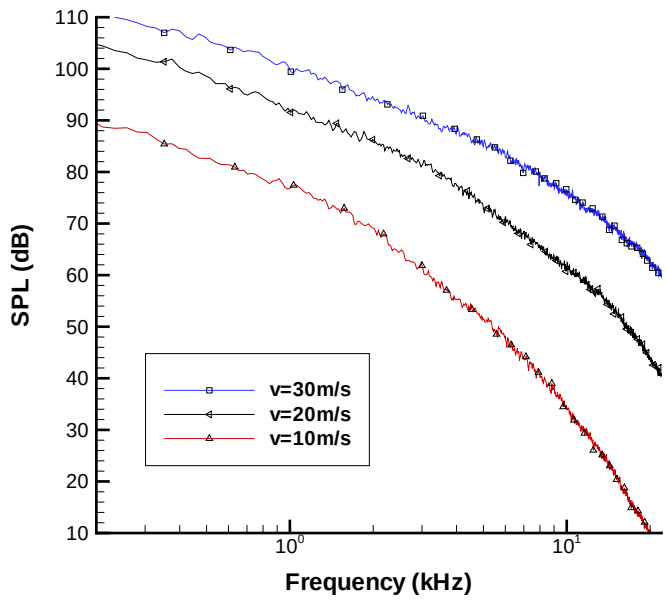

Figure 4.7: Surface microphone SPL spectra showing the influence of the free-stream velocity.

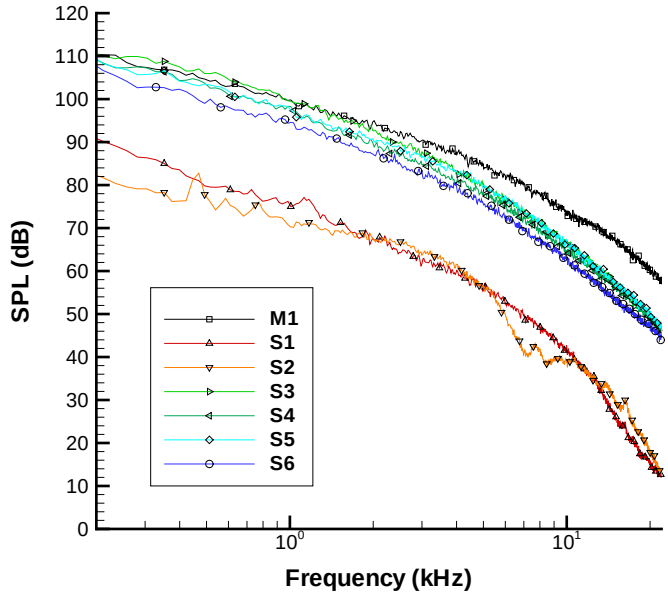

Figure 4.8: Surface microphone SPL spectra showing the influence of fixing transition in the reference conditions, v=30 m/s.

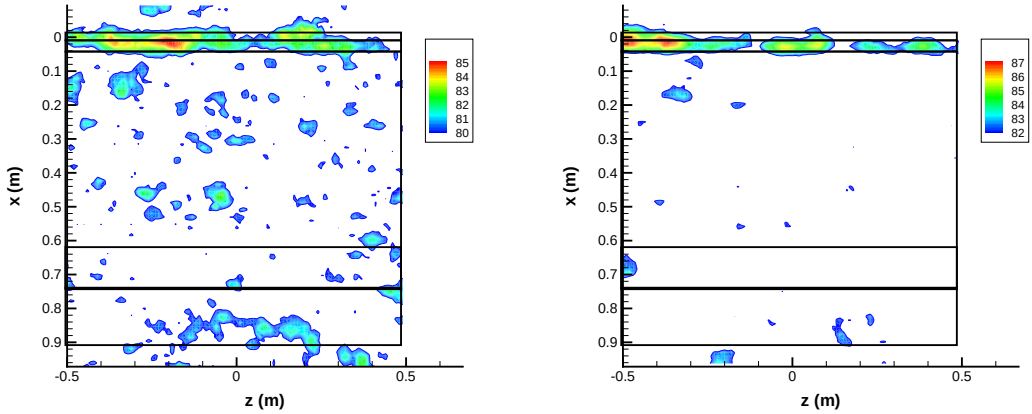

(a) α=5°.

(b) α=10°.

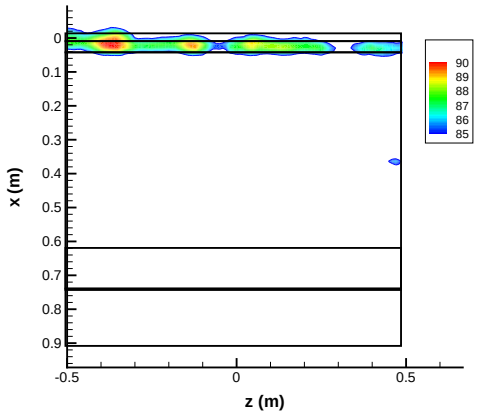

(c) α=15°.

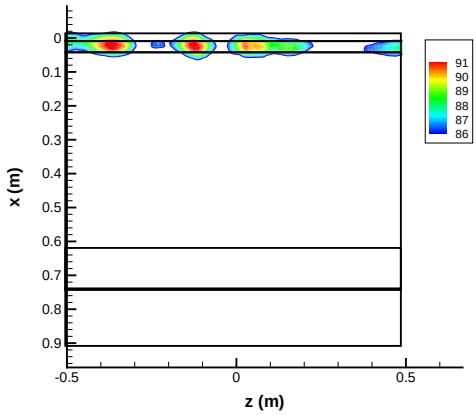

(d) α=20°.

Figure 4.9: Source maps showing SPL (dB) at 13 kHz with variation of the aerofoil incidence. Free transition, v=30 m/s.

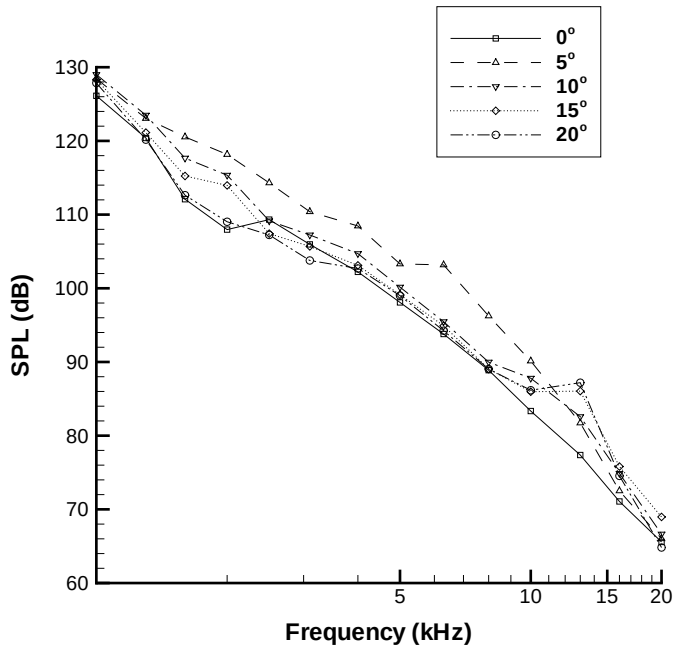

Figure 4.10: Impact of aerofoil incidence on the slat SPL spectra measured at the array with the wing in the reference conditions. Free transition, v=30ms.

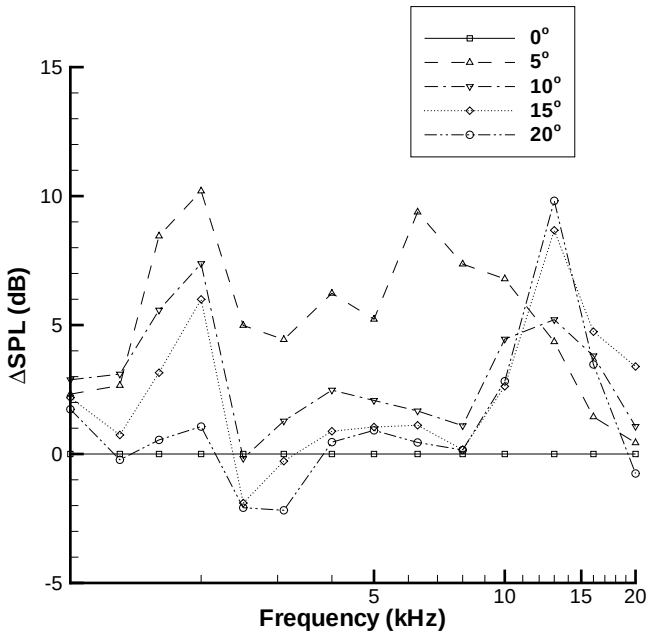

Figure 4.11: Change in SPL spectra due to incidence change relative to α=0°. Free transition, v=30 m/s.

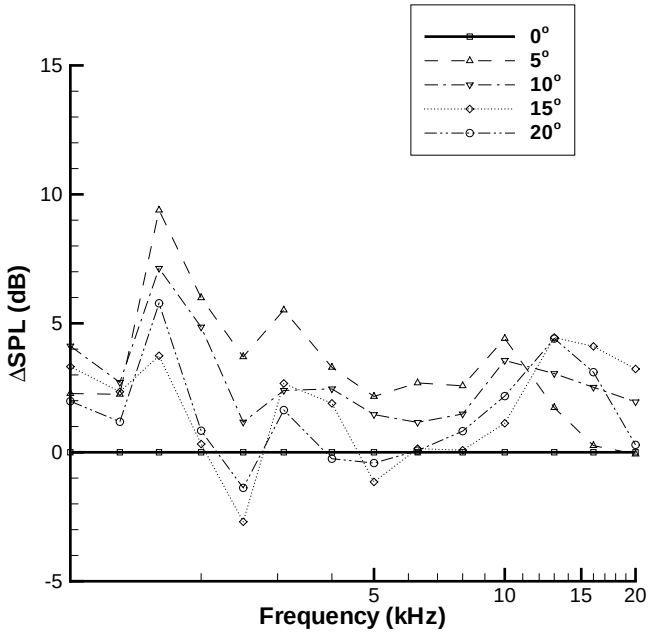

Figure 4.12: Change in SPL spectra due to incidence change relative to α=0°. Fixed transition, v=30 m/s.

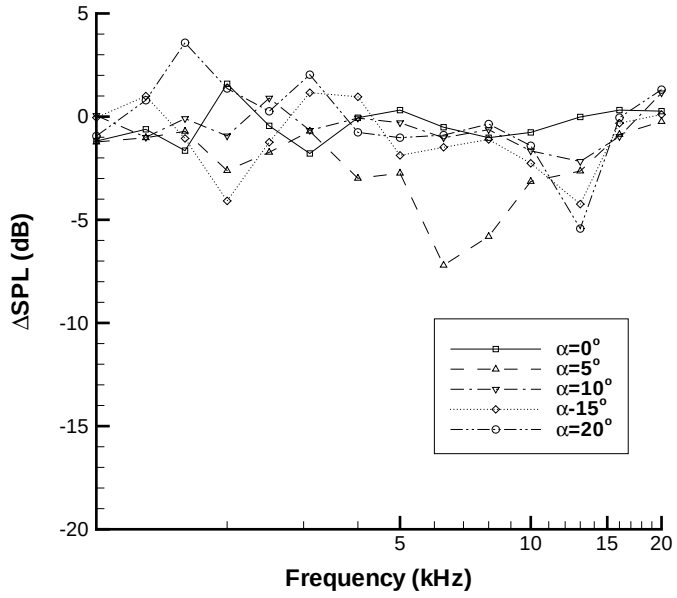

Figure 4.13: Change in SPL spectra due to fixing transition, v=30 m/s.

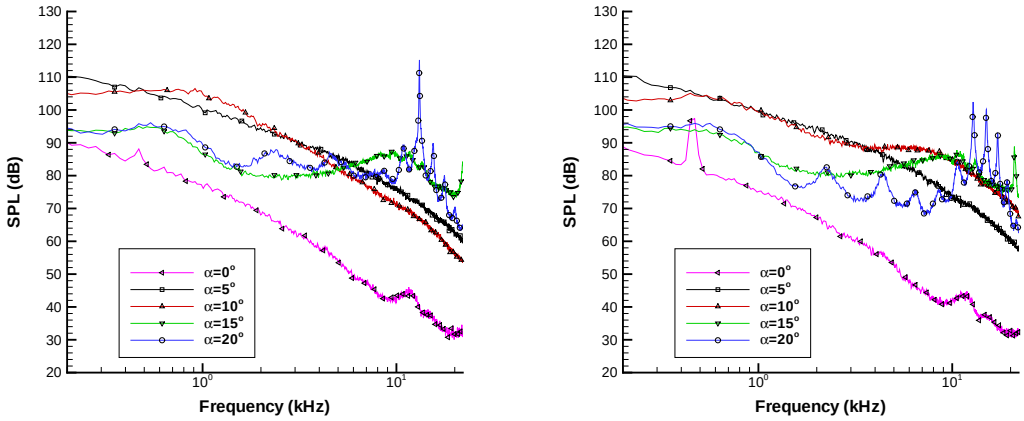

(a) M1, free transition.

(b) M1, fixed transition.

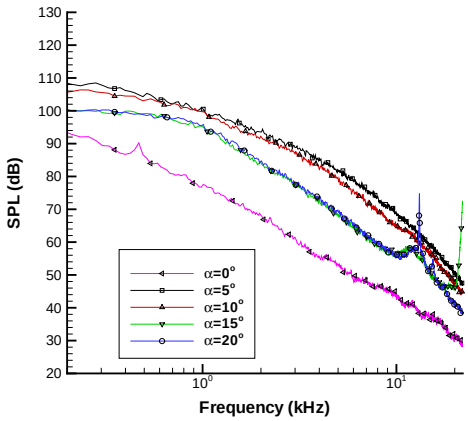

(c) S3, free transition.

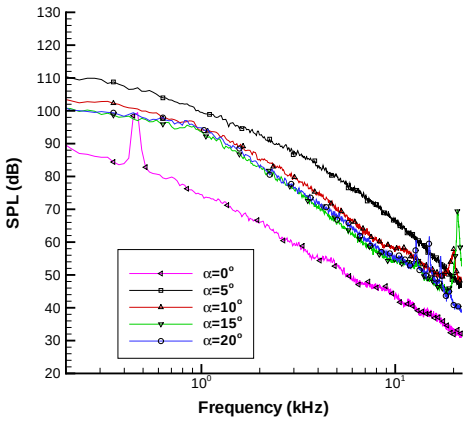

(d) S3, fixed transition.

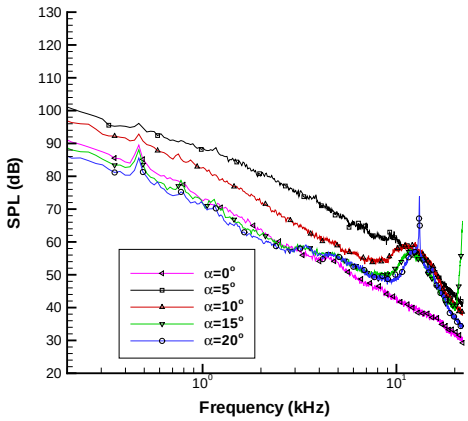

(e) S6, free transition.

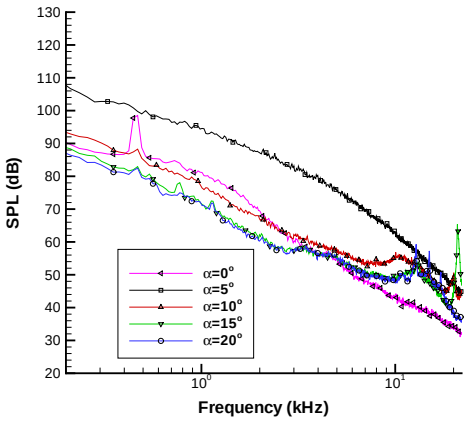

(f) S6, fixed transition.

Figure 4.14: Surface microphone SPL spectra showing the impact of the aerofoil incidence with free and fixed transition.

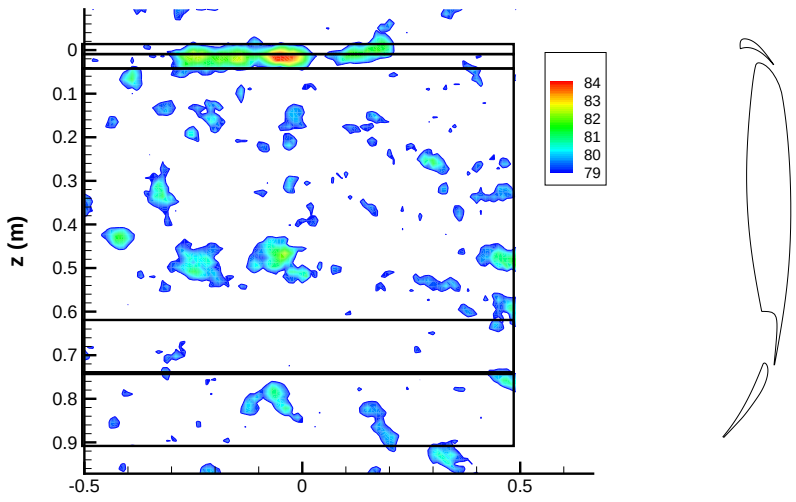

Figure 4.15: 13 kHz noise map showing SPL (dB) with α_S=13°. Free transition, α=5°, v=30 m/s.

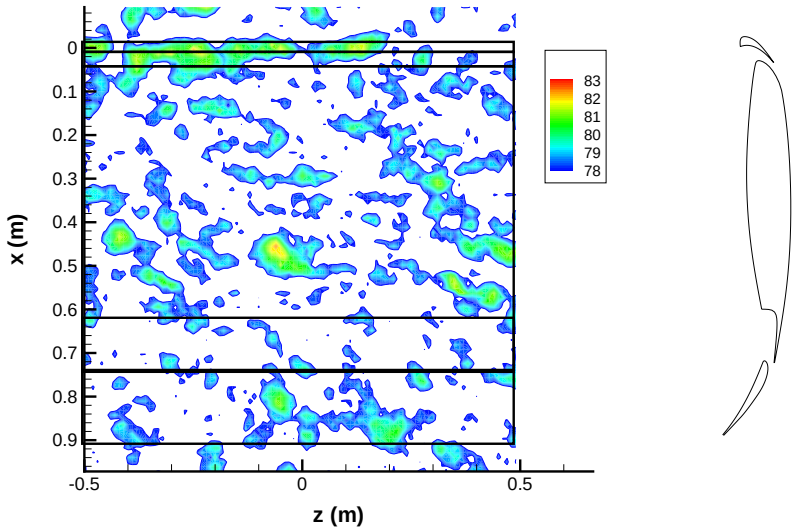

Figure 4.16: 13 kHz noise map showing SPL (dB) with α_S=13°RG. Free transition, α=5°, v=30 m/s.

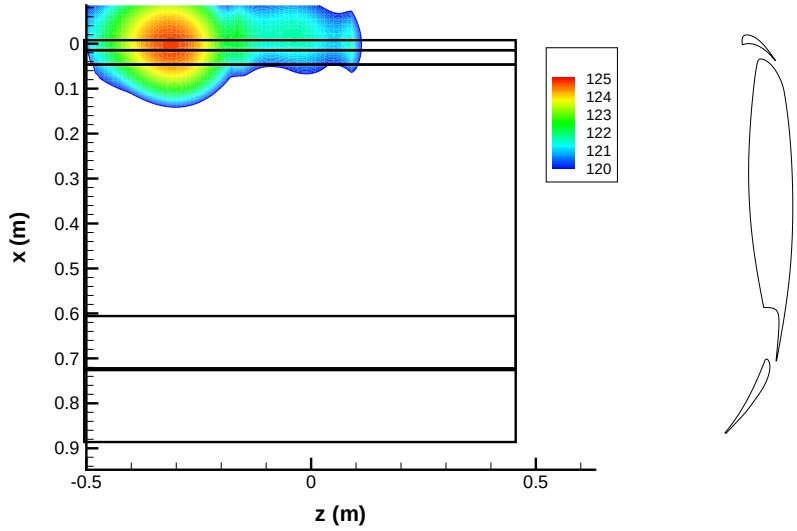

Figure 4.17: 3.1 kHz noise map showing SPL (dB) with α_S=13°. Free transition, α=15°, v=30 m/s.

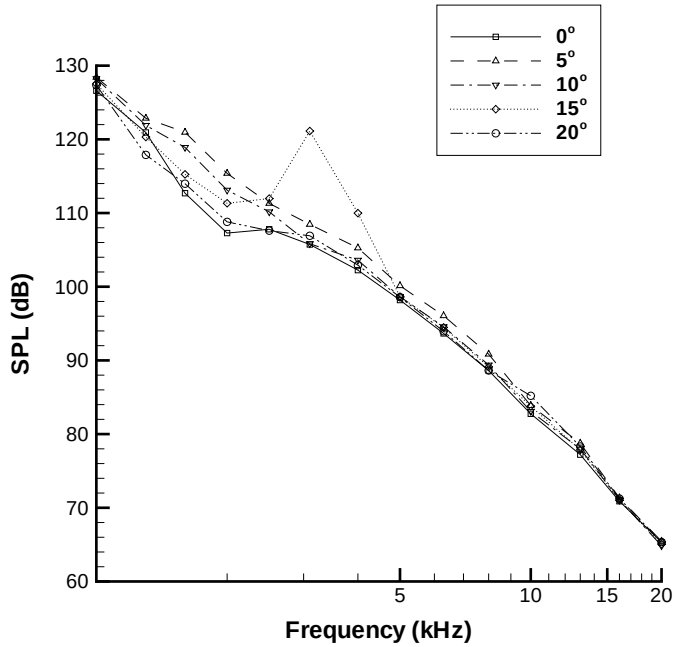

Figure 4.18: Impact of aerofoil incidence on the slat SPL spectra measured at the array with α_S=13°. Free transition, v=30 m/s.

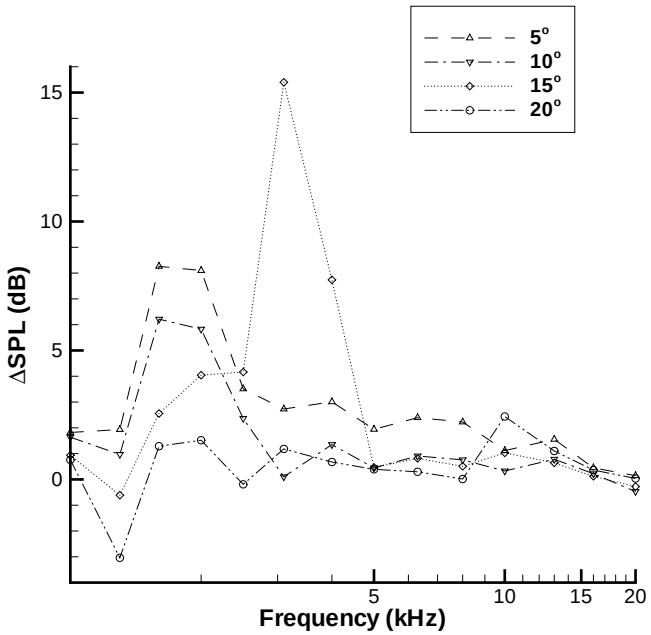

Figure 4.19: Change in SPL spectra due to incidence change relative to α=0° with α_S=13°. Free transition, v=30 m/s.

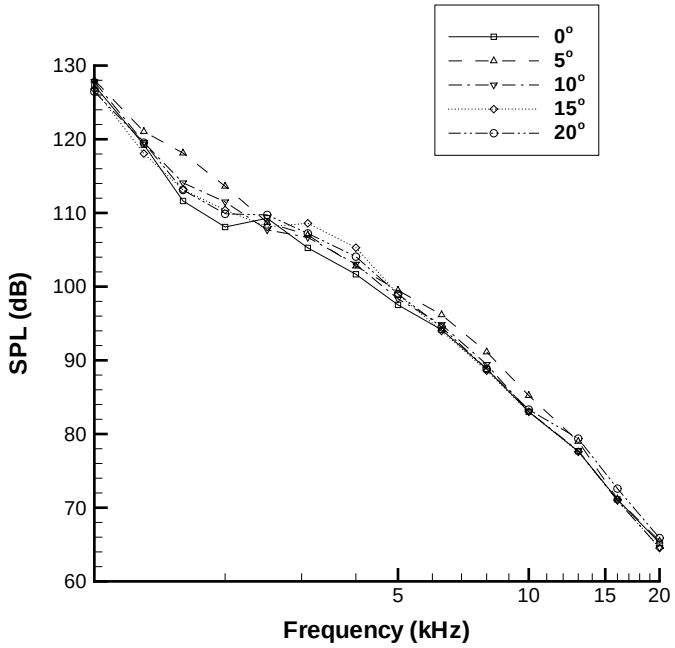

Figure 4.20: Impact of aerofoil incidence on the slat SPL spectra measured at the array with α_S=13°RG. Free transition, v=30 m/s.

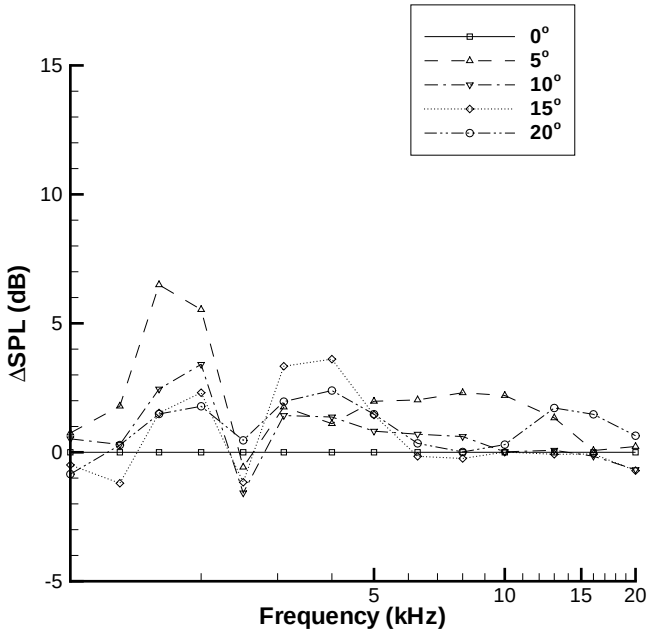

Figure 4.21: Change in SPL spectra due to incidence change relative to α=0° with α_S=13°RG. Free transition, v=30 m/s.

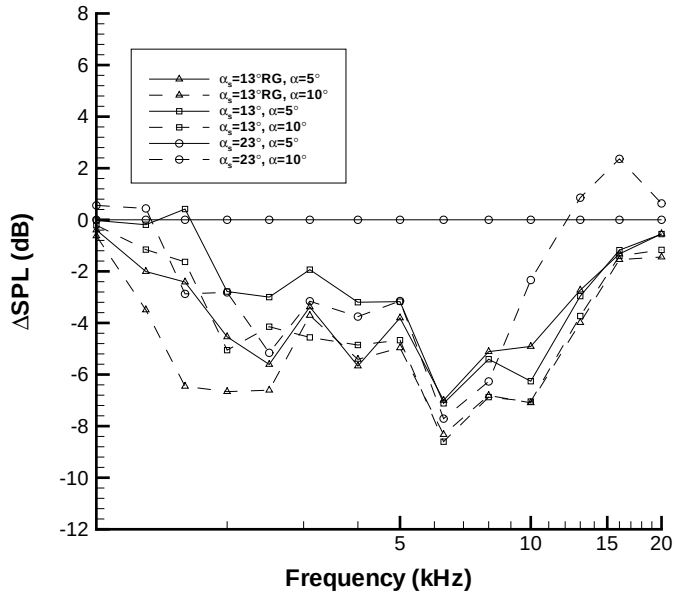

Figure 4.22: Change in SPL spectra relative to the reference conditions, v=30 m/s.

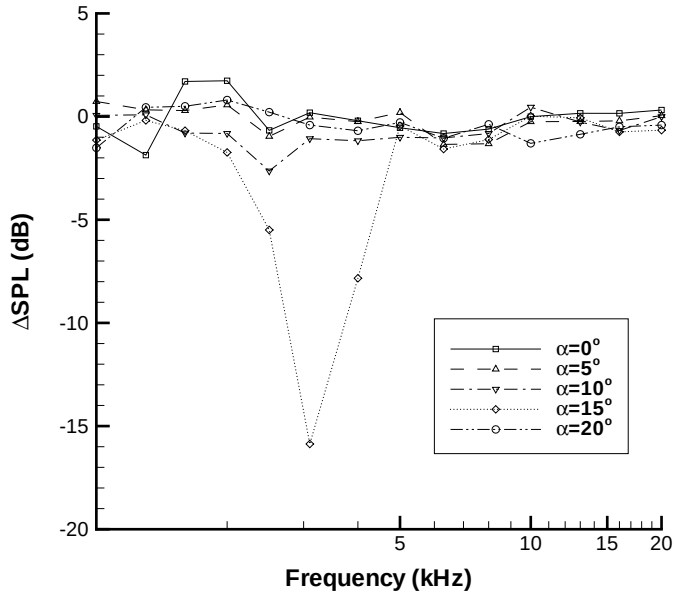

Figure 4.23: Change in SPL spectra due to fixing transition with α_S=13°, v=30 m/s.

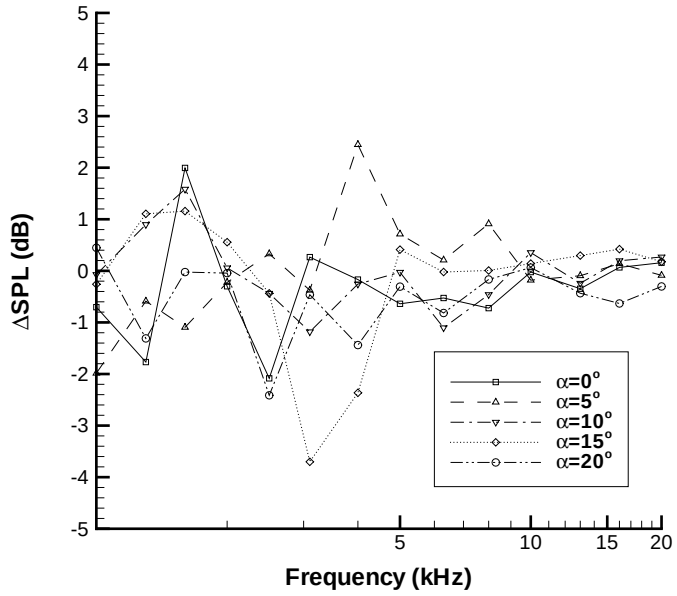

Figure 4.24: Change in SPL spectra due to fixing transition with α_S=13°RG, v=30 m/s.

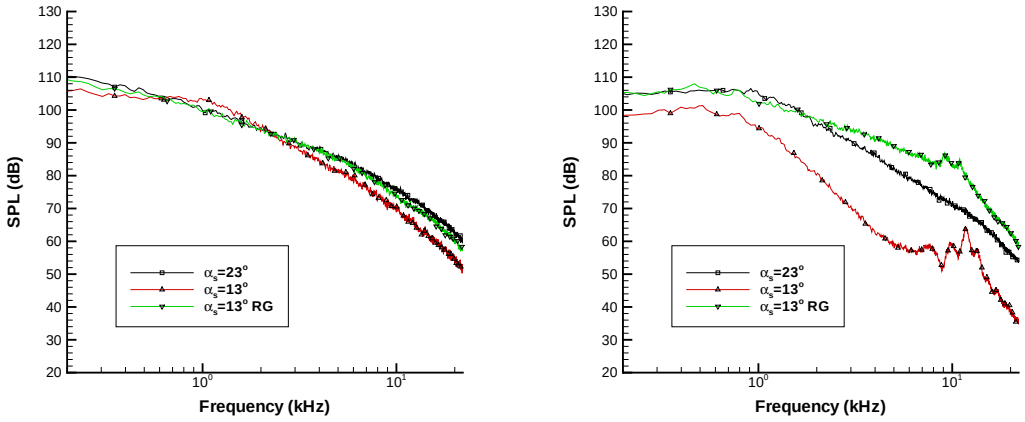

(a) M1, α=5°. (b) M1, α=10°.

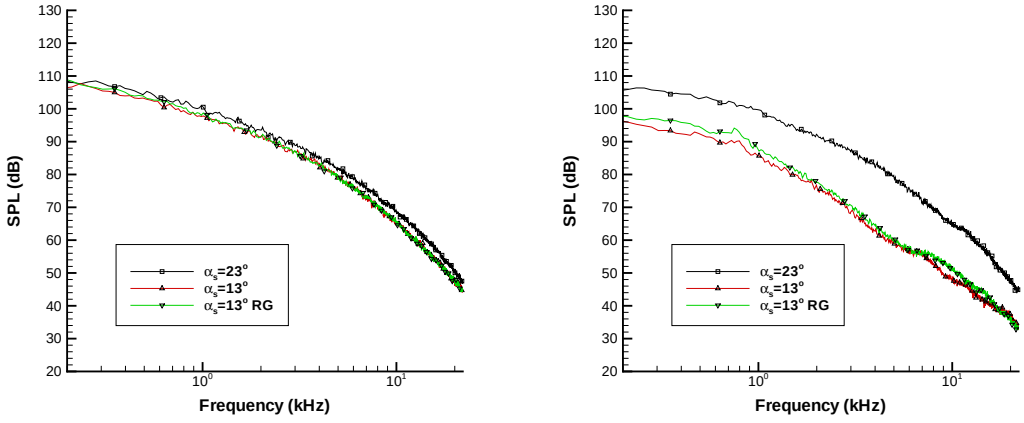

(c) S3, α=5°. (d) S3, α=10°.

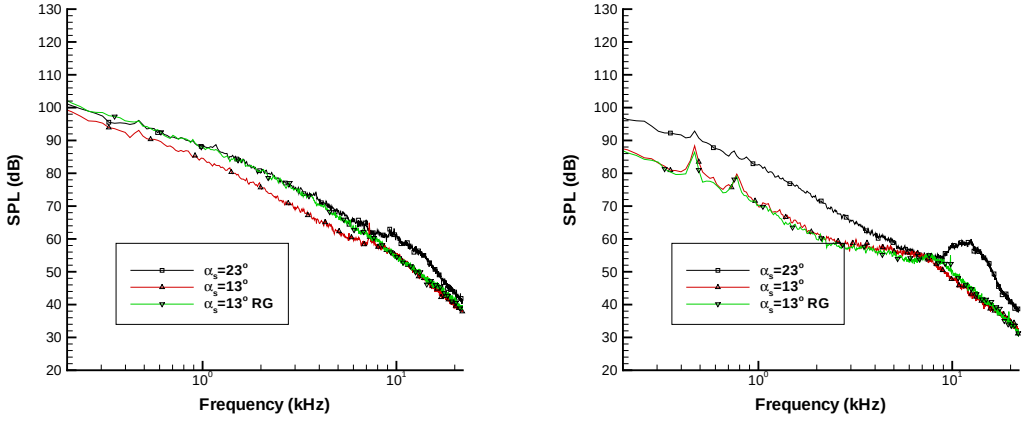

(e) S6, α=5°. (f) S6, α=10°.

Figure 4.25: Surface microphone SPL spectra showing the impact of the slat angle for α=5° and 10°, v=30 m/s.

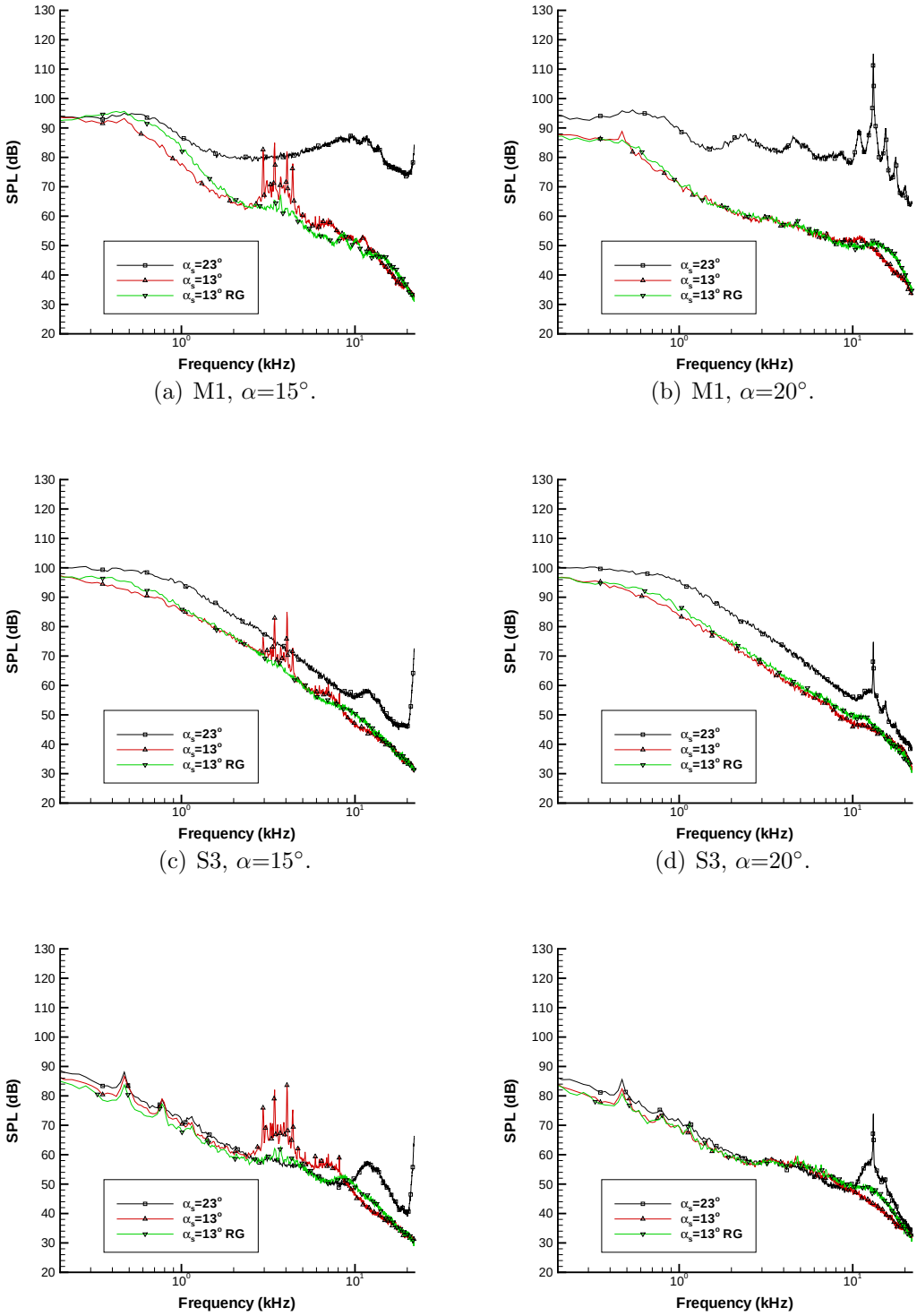

(a) M1, α=15°.

(b) M1, α=20°.

(c) S3, α=15°.

(d) S3, α=20°.

(e) S6, α=15°.

(f) S6, α=20°.

Figure 4.26: Surface microphone SPL spectra showing the impact of the slat angle for α=15° and 20°, v=30 m/s.

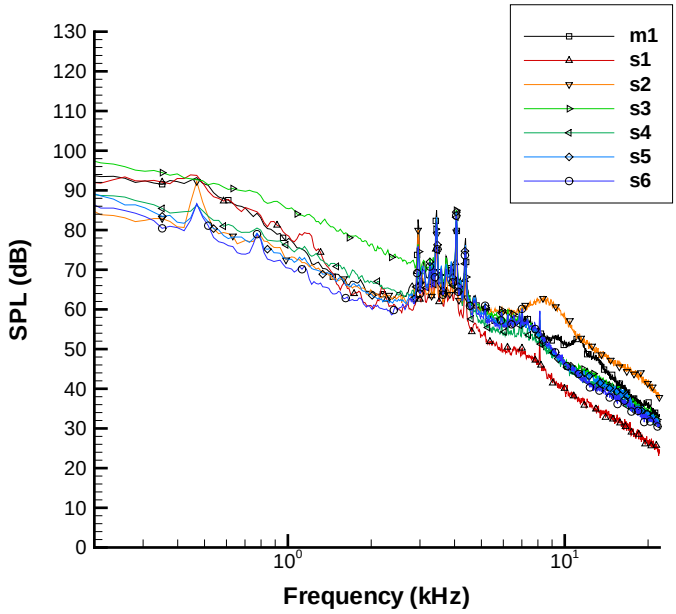

Figure 4.27: Surface microphone SPL spectra with α_S=13° and α=15°, v=30 m/s.

Frequency	2.95 kHz	3.45 kHz	4.05kHz	4.4 kHz
M1	83 dB	85 dB	82 dB	78 dB
S1	78 dB	78 dB	81 dB	69 dB
S2	80 dB	79 dB	79.5 dB	70.5 dB
S3	76.5 dB	78 dB	85 dB	73 dB
S4	69.5 dB	82 dB	83 dB	73 dB
S5	75 dB	83.5 dB	84.5 dB	76 dB
S6	76 dB	82 dB	84 dB	75 dB

Table 4.1: Surface microphone peak SPL values at α=15 and 20°, v=30 m/s.

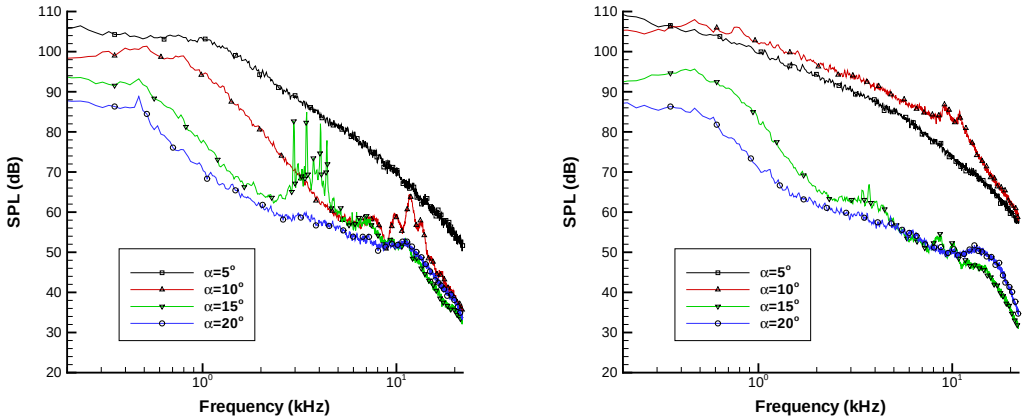

(a) M1, α_S=13°. (b) M1, α_S=13°RG.

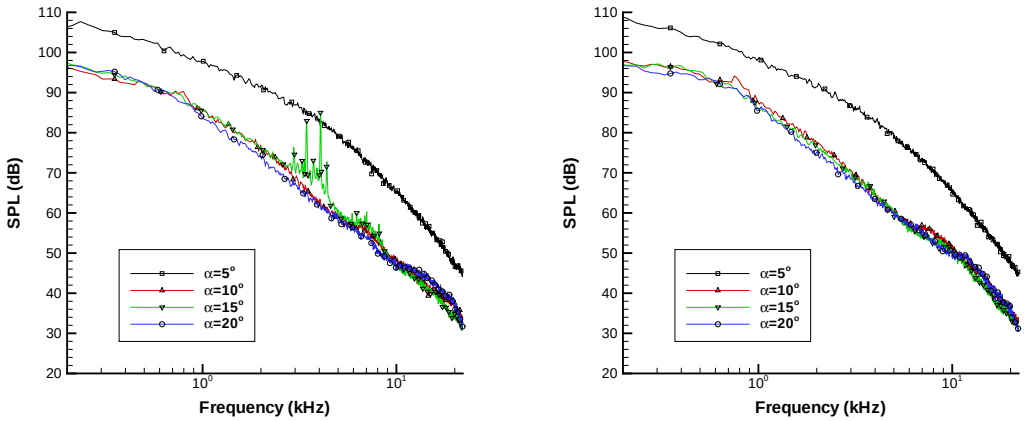

(c) S3, α_S=13°. (d) S3, α_S=13°RG.

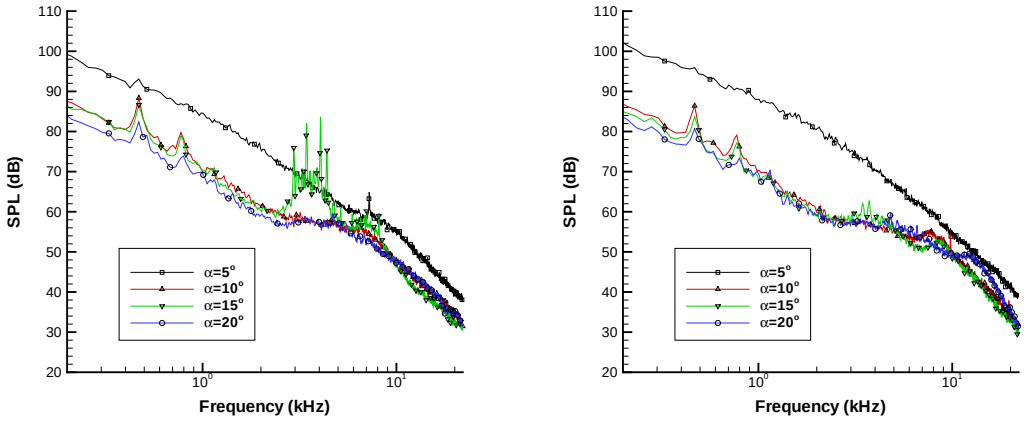

(e) S6, α_S=13°. (f) S6, α_S=13°RG.

Figure 4.28: Surface microphone SPL spectra showing the impact of the aerofoil incidence with α_S=13° with and without the reduced gap setting, v=30 m/s.

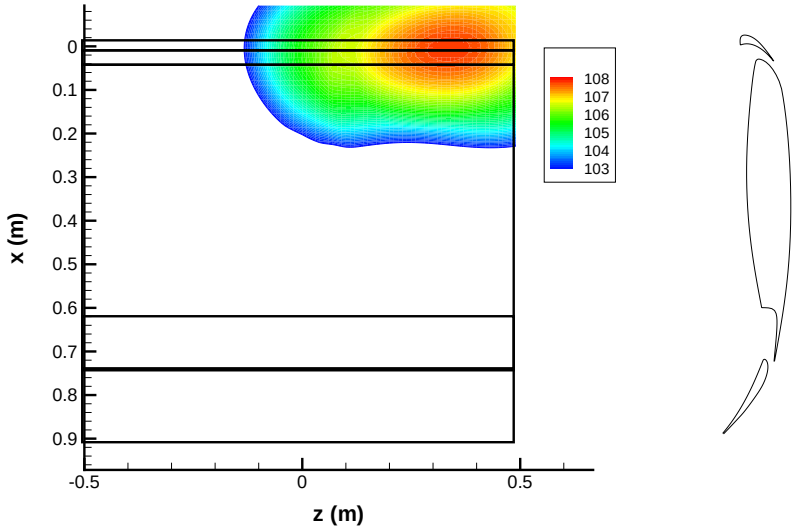

Figure 4.29: 2 kHz noise map showing SPL (dB) with b=120LPM. α=5°, v=0 m/s.

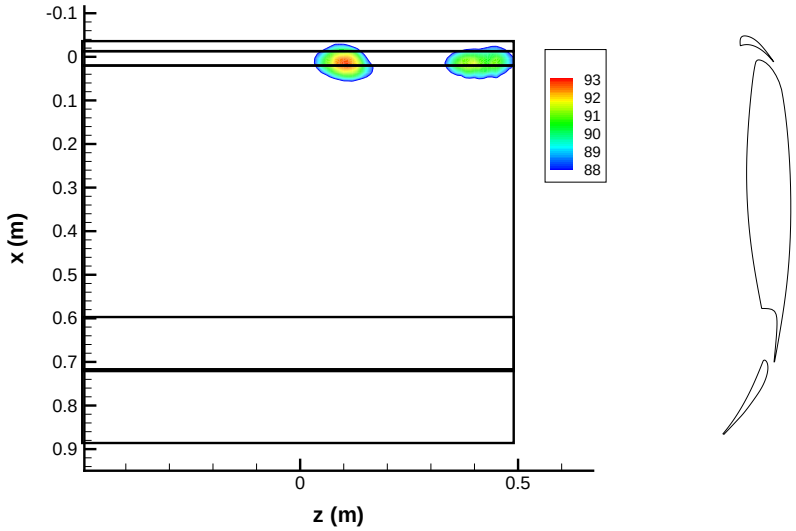

Figure 4.30: 10 kHz noise map showing SPL (dB) with b=120LPM. α=5°, v=0 m/s.

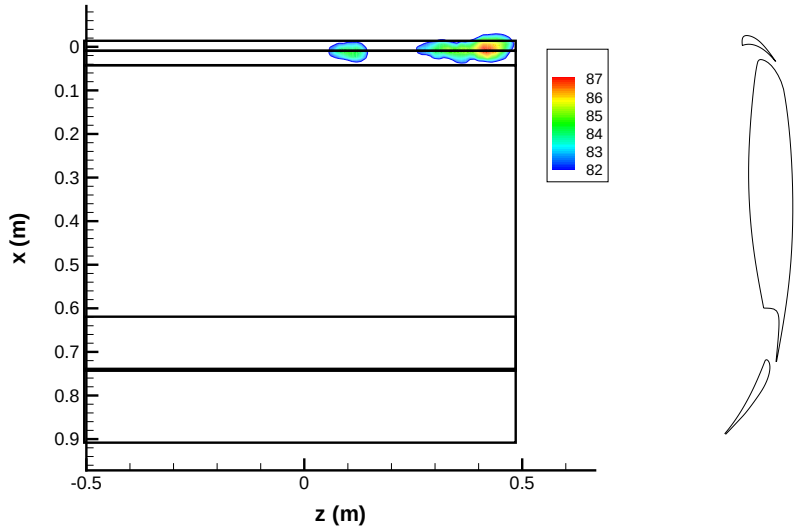

Figure 4.31: 13 kHz noise map showing SPL (dB) with b=120LPM. α=5°, v=0 m/s.

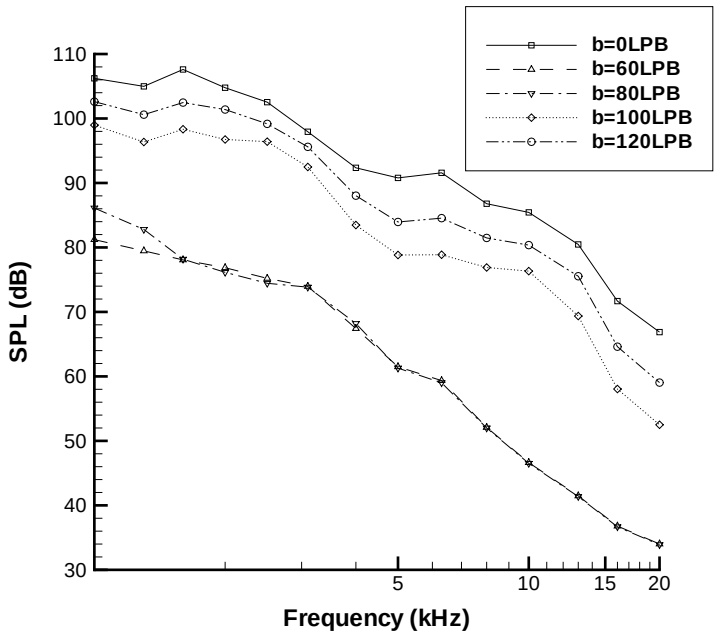

Figure 4.32: SPL spectra generated by the blowing system as measured by the array, v=0 m/s.

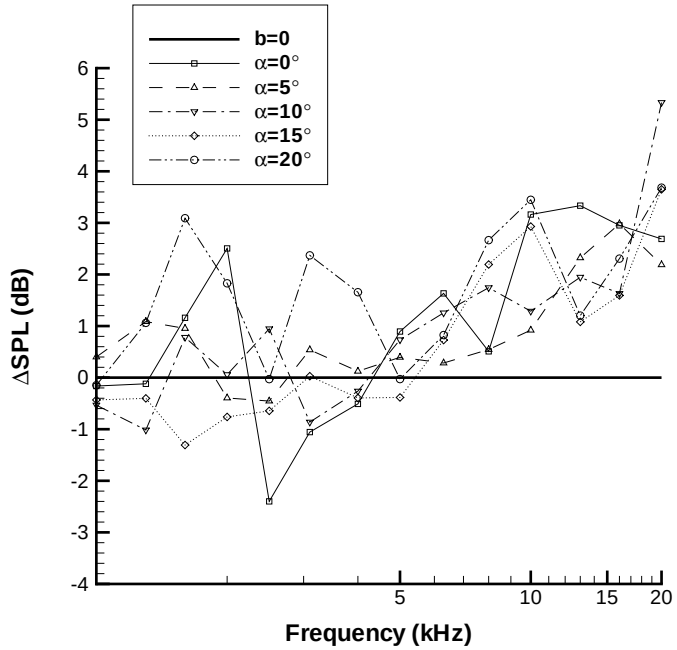

Figure 4.33: Change in SPL spectra due to blowing with the wing in the reference conditions. Free transition, v=30 m/s, b=120LPM.

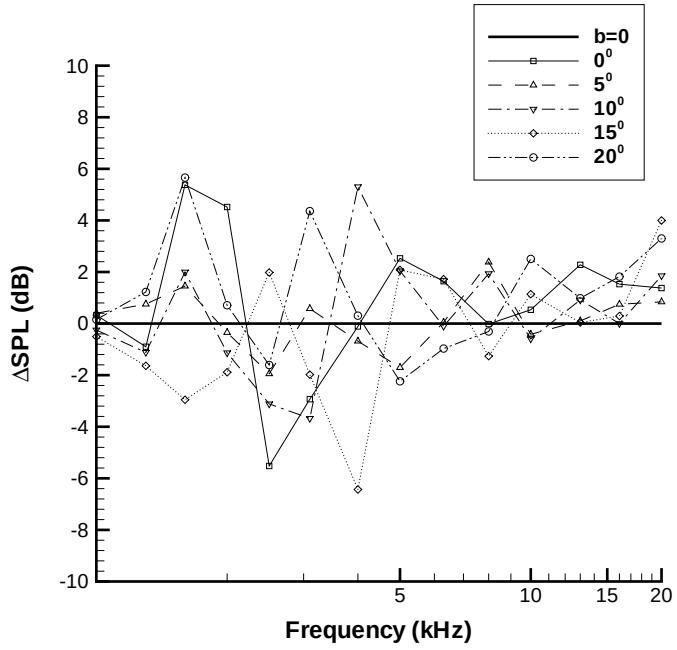

Figure 4.34: Change in SPL spectra for the starboard 1/6 of wing (away from the internal jet noise) due to blowing with the wing in the reference conditions. Free transition, v=30 m/s, b=120LPM.

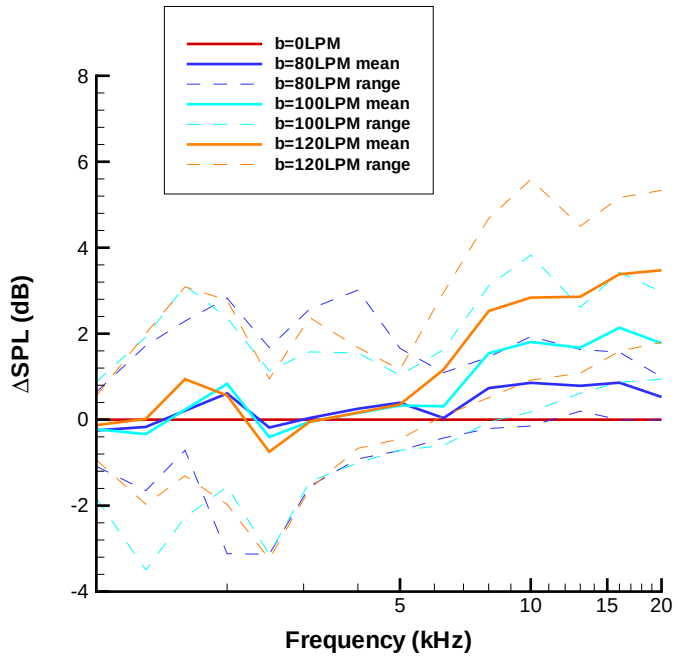

Figure 4.35: Range of SPL spectra with blowing at all free transition slat settings, v=30 m/s.

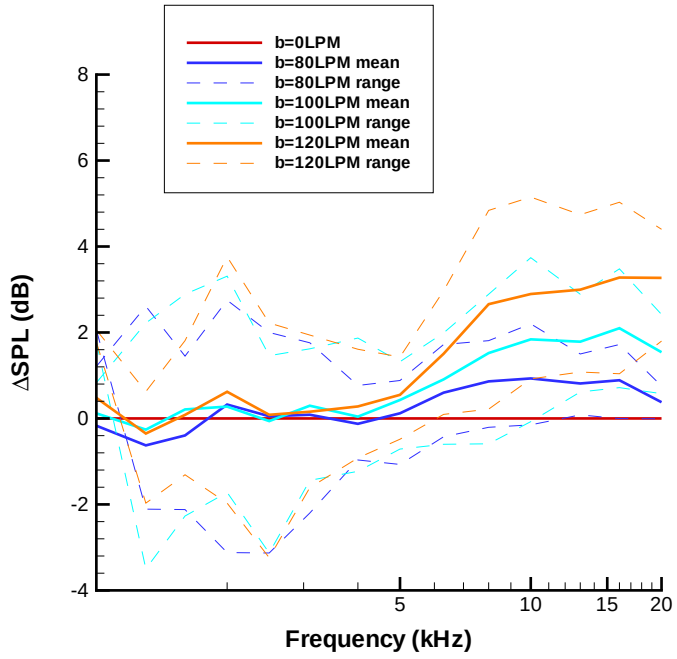

Figure 4.36: Range of SPL spectra with blowing at all fixed transition slat settings, v=30 m/s.

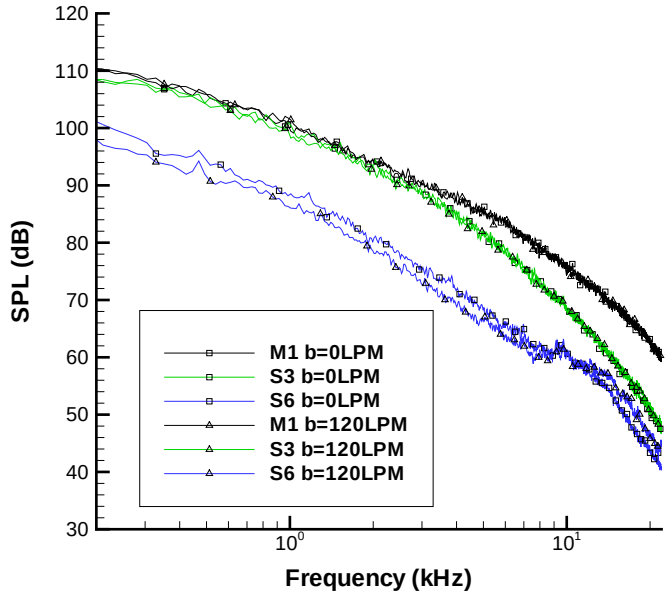

Figure 4.37: Impact of blowing on the surface microphone SPL spectra, v=30 m/s.

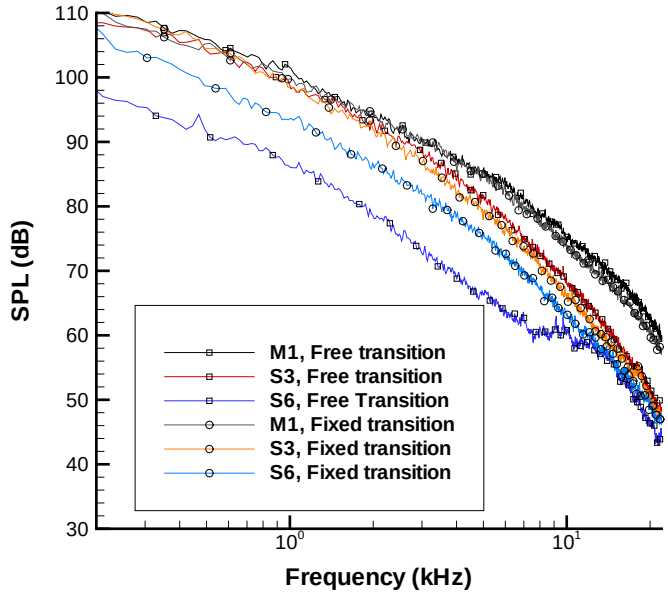

Figure 4.38: Surface microphone SPL spectra showing the impact of blowing and fixing transition for the reference conditions, v=30 m/s.

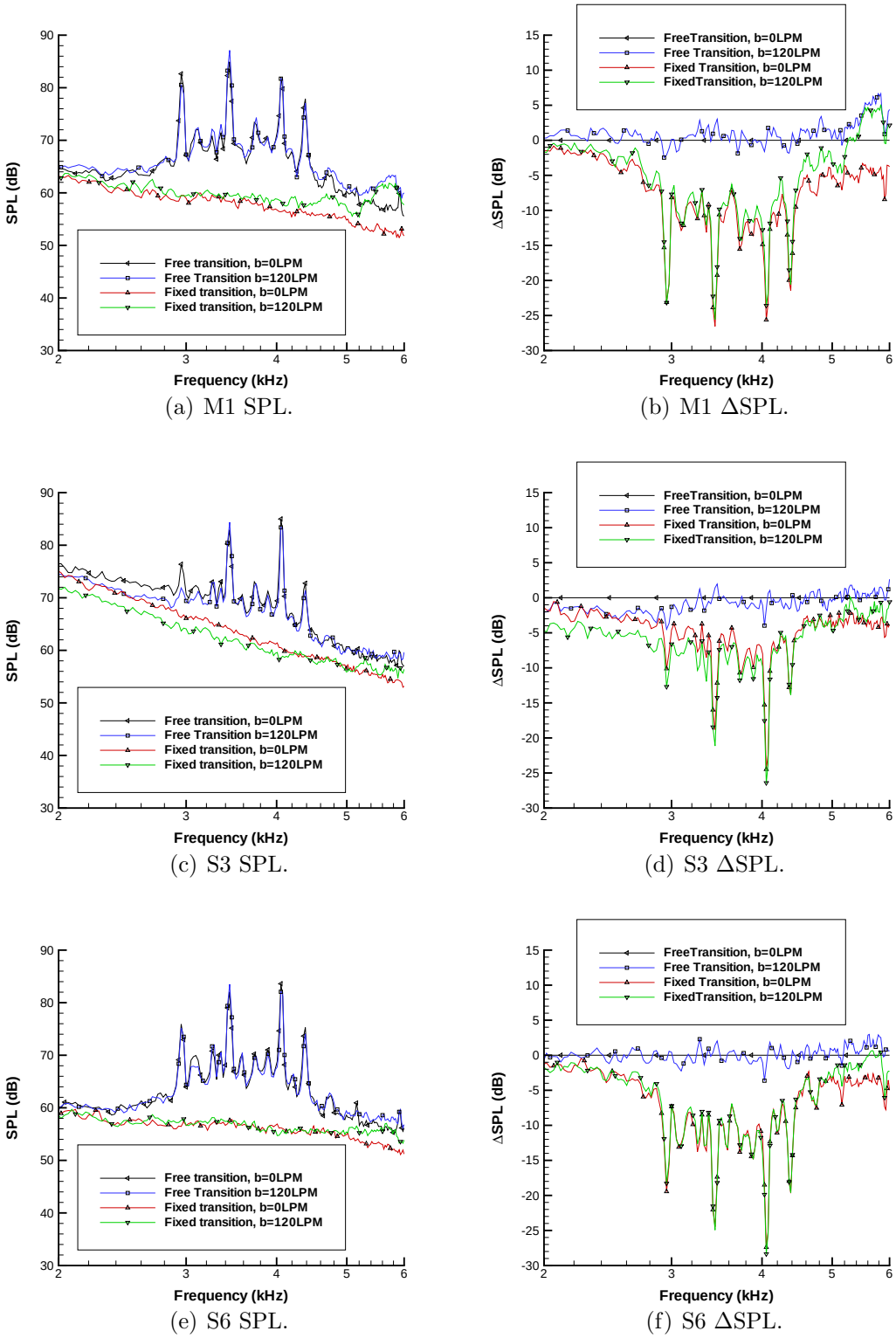

(a) M1 SPL. (b) M1 ΔSPL.

(c) S3 SPL. (d) S3 ΔSPL.

(e) S6 SPL. (f) S6 ΔSPL.

Figure 4.39: Surface microphone SPL spectra showing the impact of blowing and fixing transition on the low frequency tone (3-5 kHz). Delta values plotted relative to free transition no-blowing case. α_S=13°, α=15° v=30 m/s.

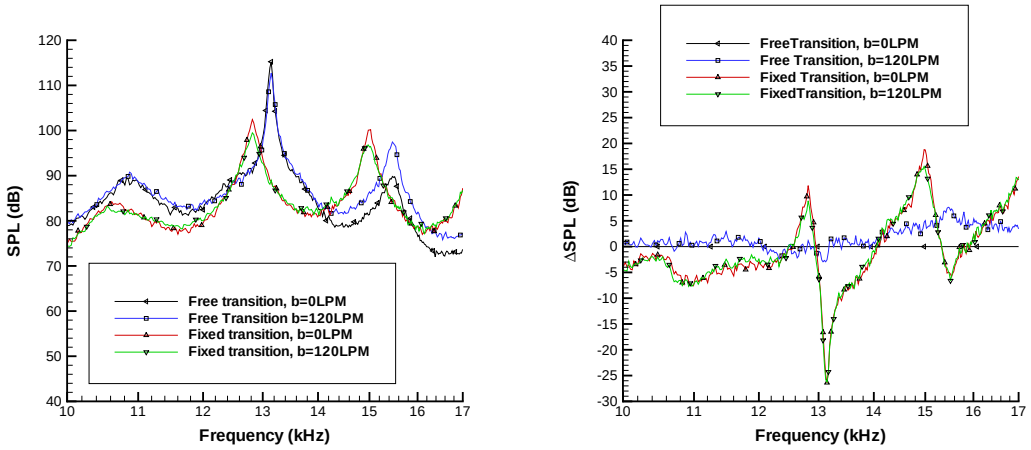

(a) M1 SPL.

(b) M1 ΔSPL.

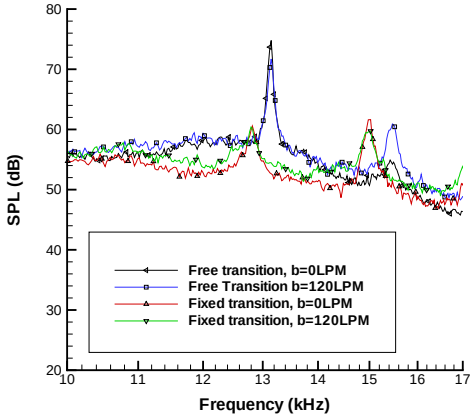

(c) S3 SPL.

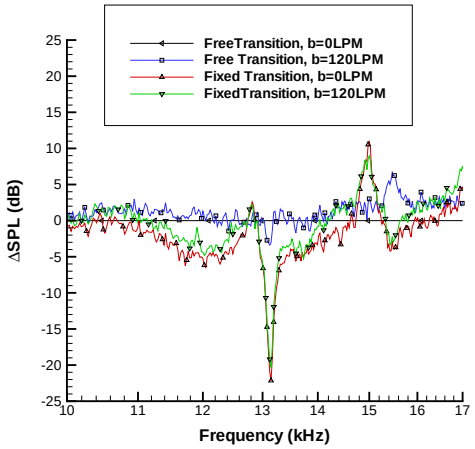

(d) S3 ΔSPL.

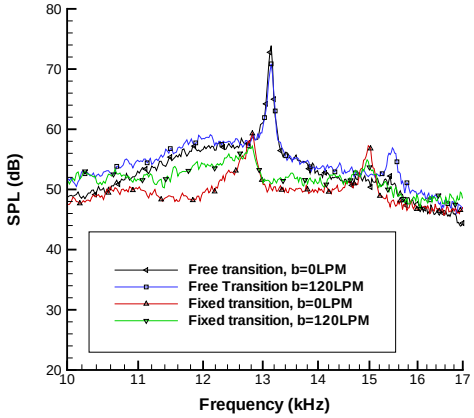

(e) S6 SPL.

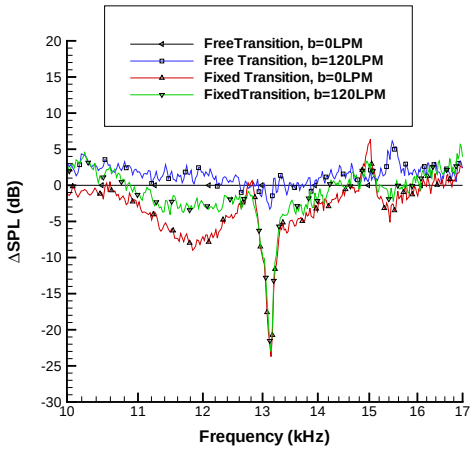

(f) S6 ΔSPL.

Figure 4.40: Surface microphone SPL spectra showing the impact of blowing and fixing transition on the mid frequency tone (12 kHz). Delta values plotted relative to free transition no-blowing case. α_S=23°, α=20° v=30 m/s.

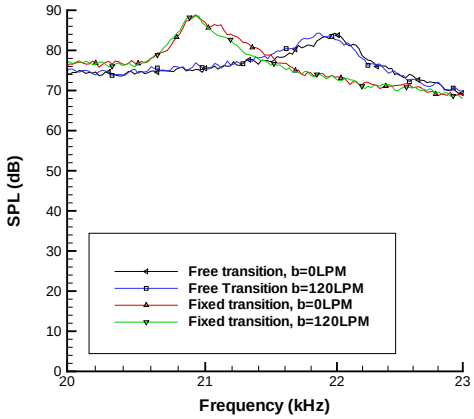

(a) M1 SPL.

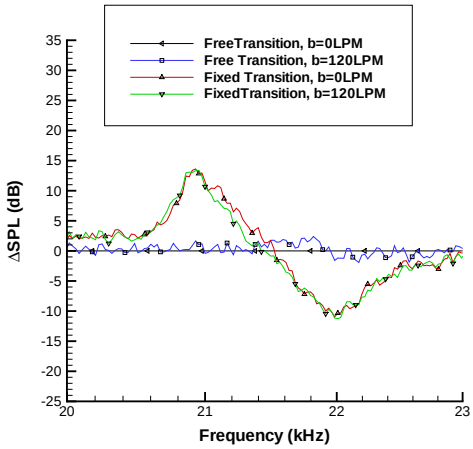

(b) M1 ΔSPL.

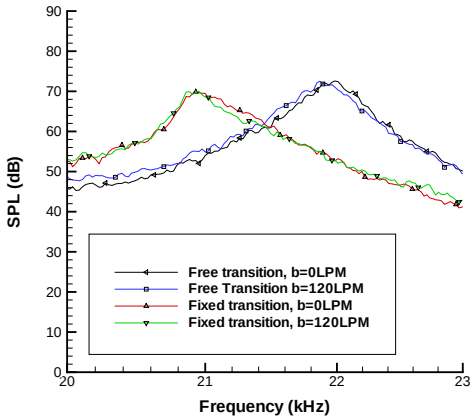

(c) S3 SPL.

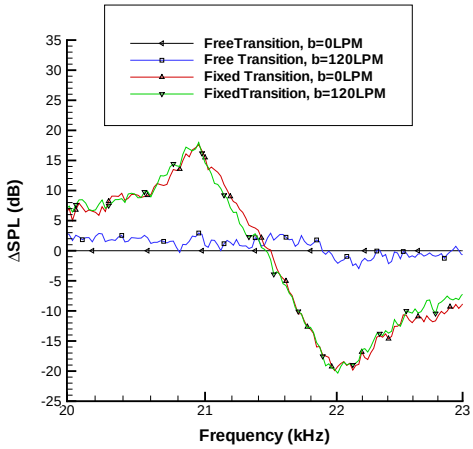

(d) S3 ΔSPL.

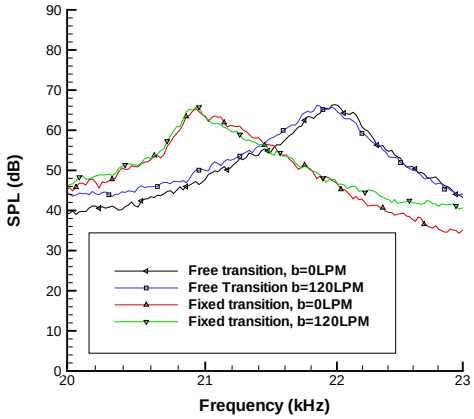

(e) S6 SPL.

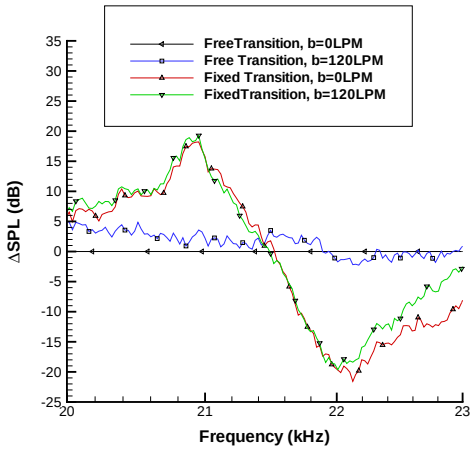

(f) S6 ΔSPL.

Figure 4.41: Surface microphone SPL spectra showing the impact of blowing and fixing transition on the high frequency tone (20 kHz). Delta values plotted relative to free transition no-blowing case. α_S=23°, α=15° v=30 m/s.

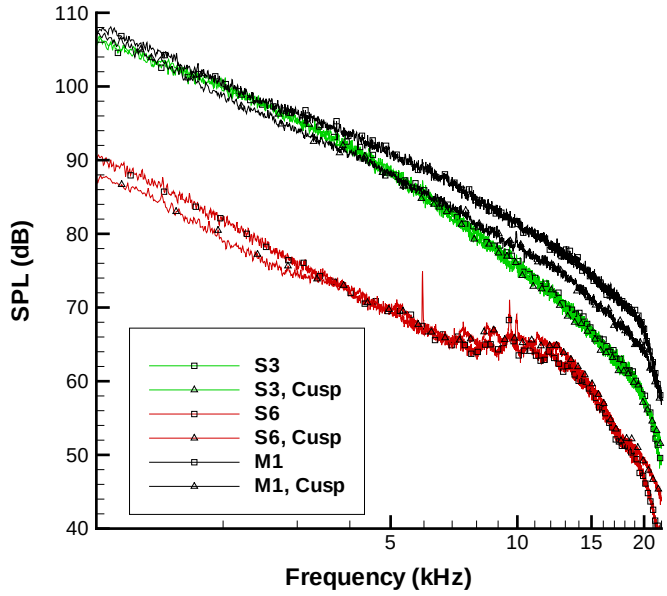

Figure 4.42: Impact of extending the slat cusp on the surface microphone SPL spectra in the reference settings, v=30 m/s.

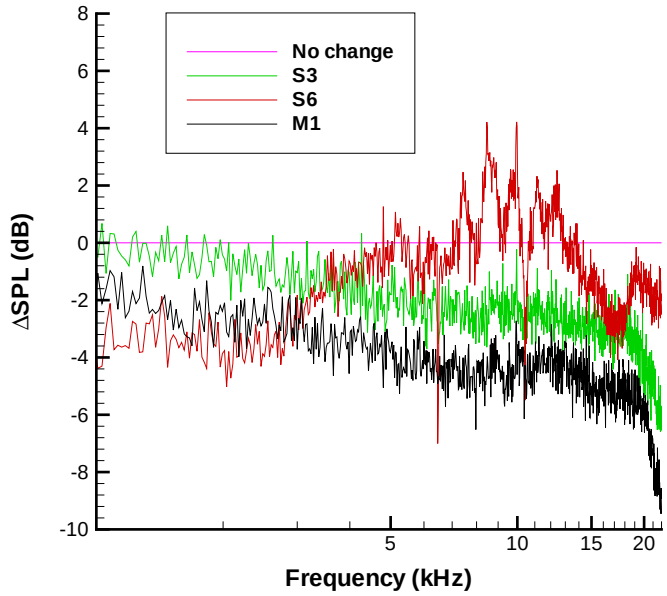

Figure 4.43: Change in SPL measured by the surface microphones due to extending the slat cusp in the reference settings, v=30 m/s.

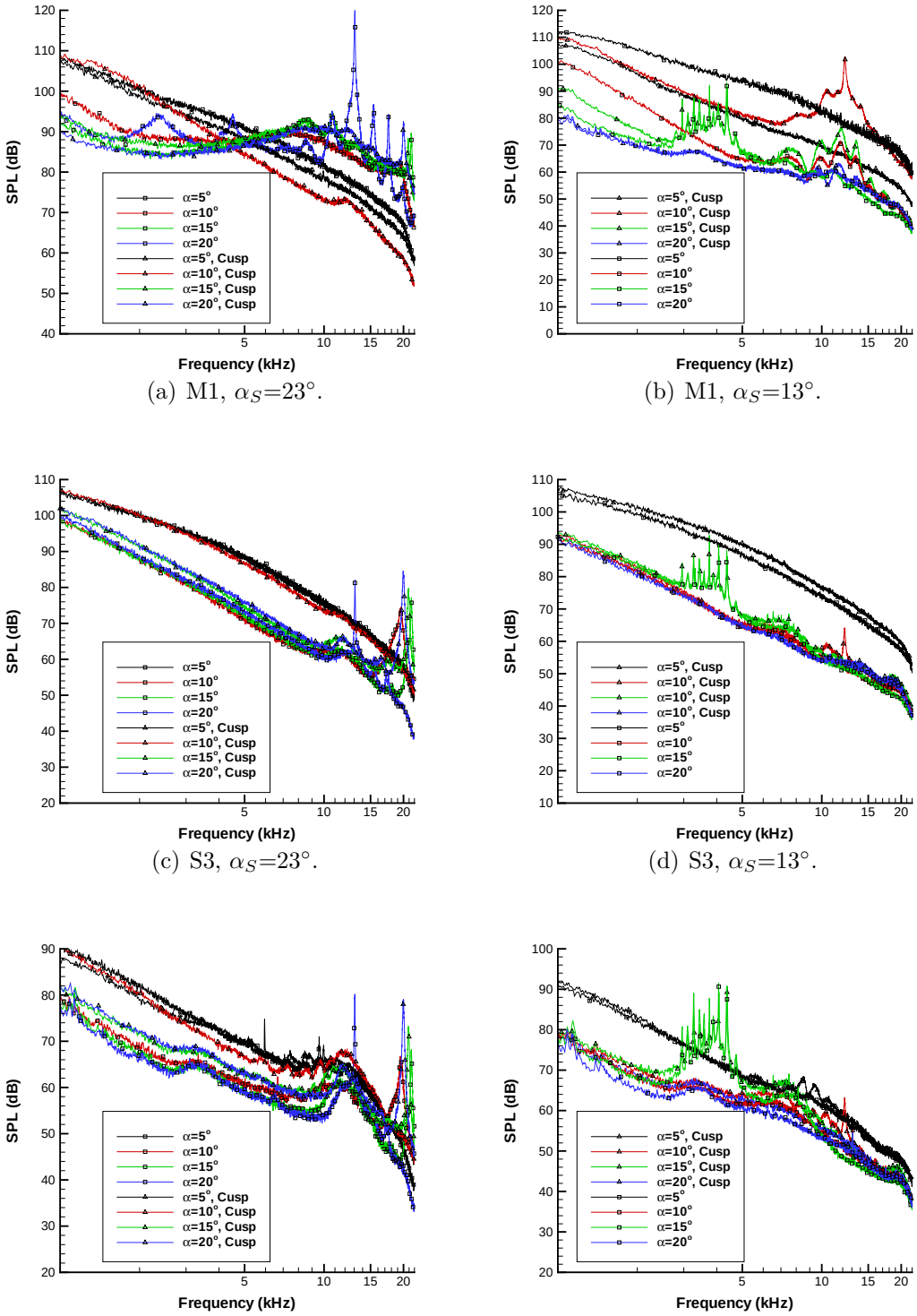

(a) M1, α_S=23°.

(b) M1, α_S=13°.

(c) S3, α_S=23°.

(d) S3, α_S=13°.

(e) S6, α_S=23°.

(f) S6, α_S=13°.

Figure 4.44: Surface microphone SPL spectra showing the impact of extending the slat cusp, v=30 m/s.

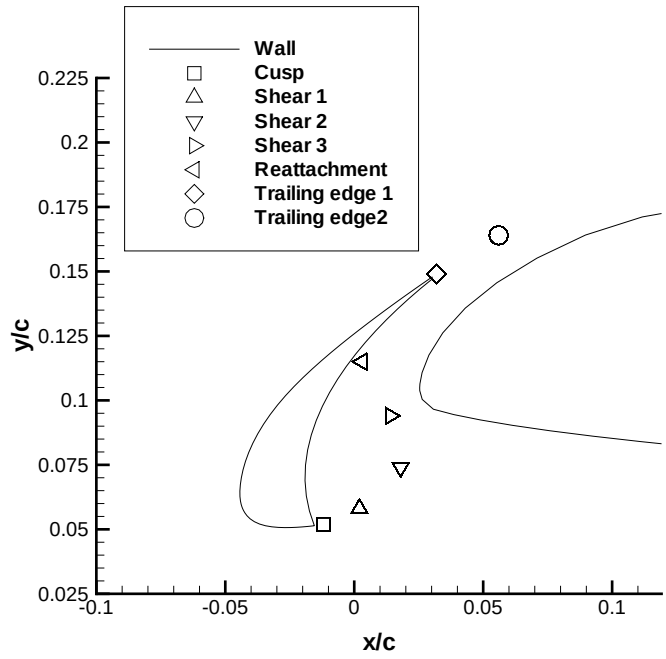

Figure 4.45: Monitoring point locations around the slat.

Monitoring point	x/c	y/c
Cusp (c)	-0.012	0.052
Shear 1 (s1)	0.002	0.058
Shear 2 (s2)	0.018	0.074
Shear 3 (s3)	0.014	0.094
Reattachment (R)	0.003	0.115
Trailing edge 1 (te1)	0.032	0.149
Trailing edge 2 (te2)	0.056	0.164

Table 4.2: Monitoring point coordinates.

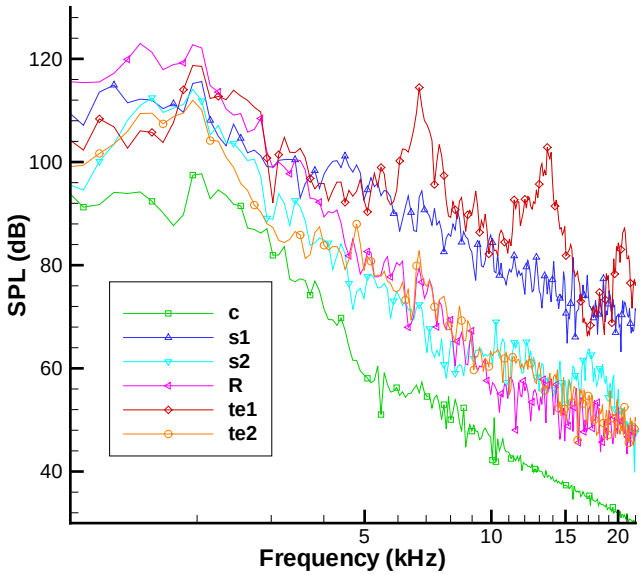

Figure 4.46: SPL spectra with the reference wing settings. M=0.2.

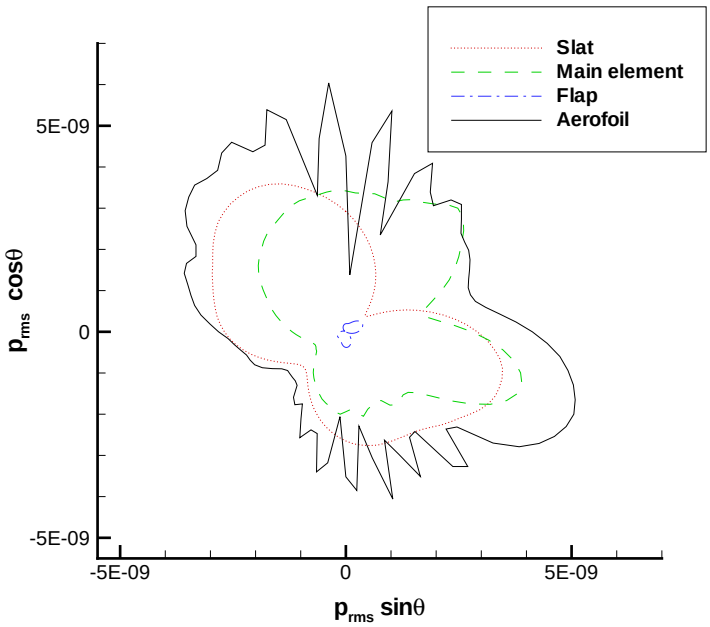

Figure 4.47: Far-field directivity plot for the reference wing settings. M=0.2, flow left to right.

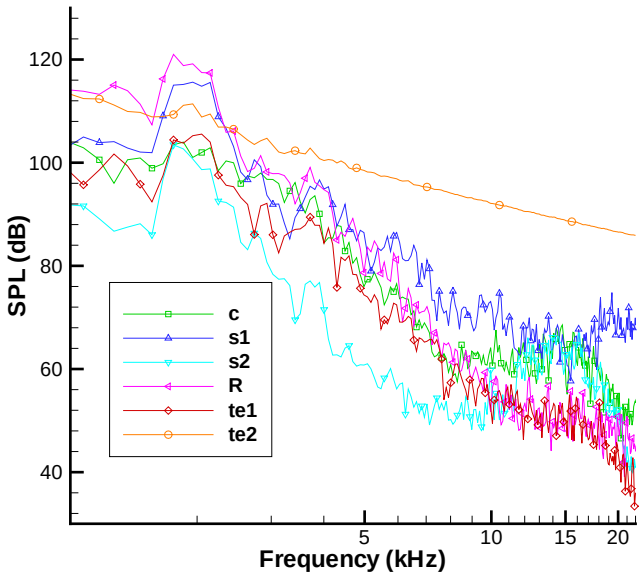

Figure 4.48: SPL spectra with low rate blowing. M=0.2, b=120LPM.

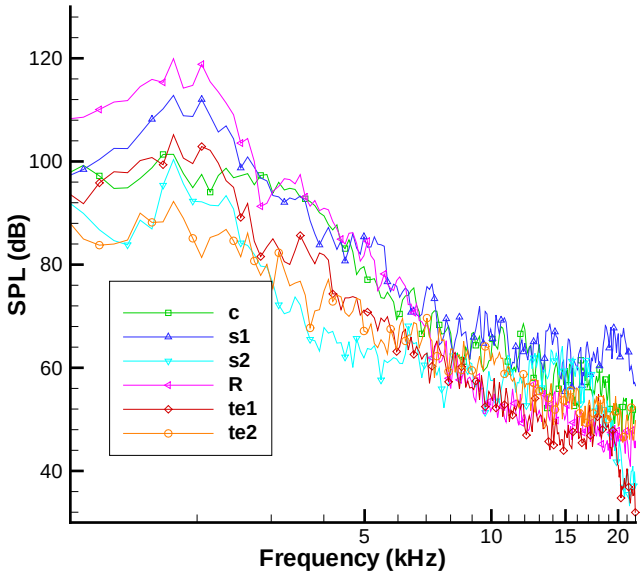

Figure 4.49: SPL spectra with high rate blowing. M=0.2, b=270LPM.

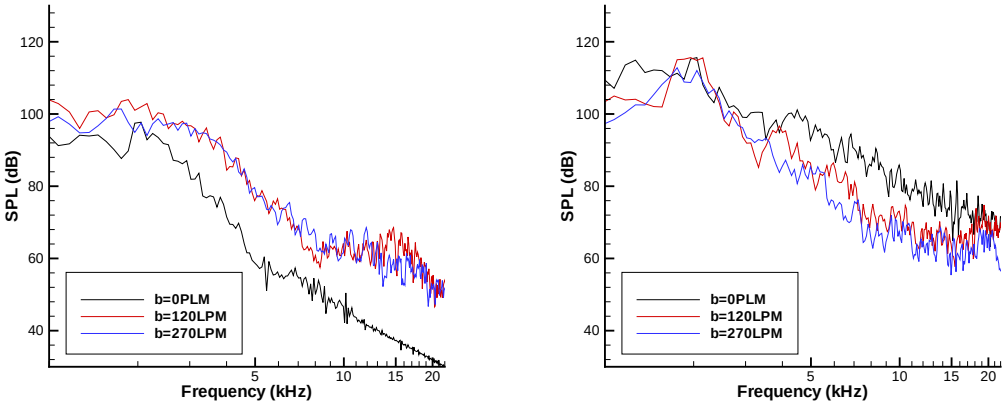

(a) Cusp.

(b) Shear 1.

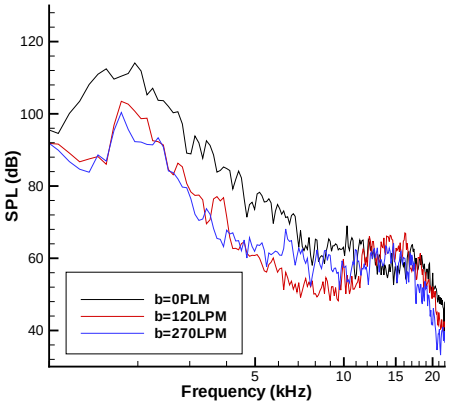

(c) Shear 2.

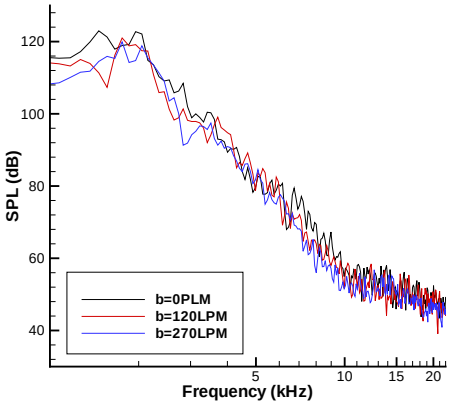

(d) Reattachment.

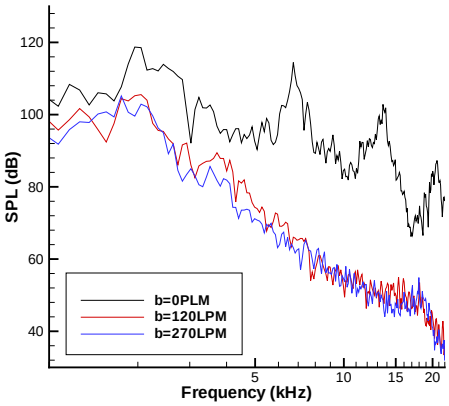

(e) Trailing edge 1.

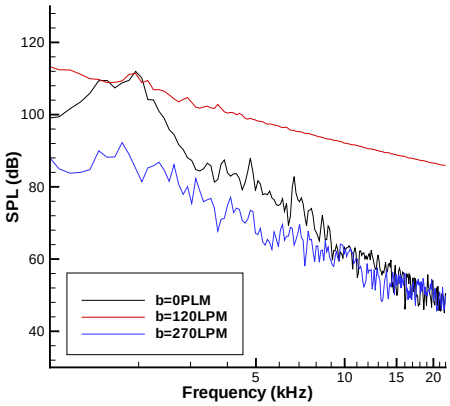

(f) Trailing edge 2.

Figure 4.50: Monitoring point SPL spectra showing the impact of blowing, M=0.2.

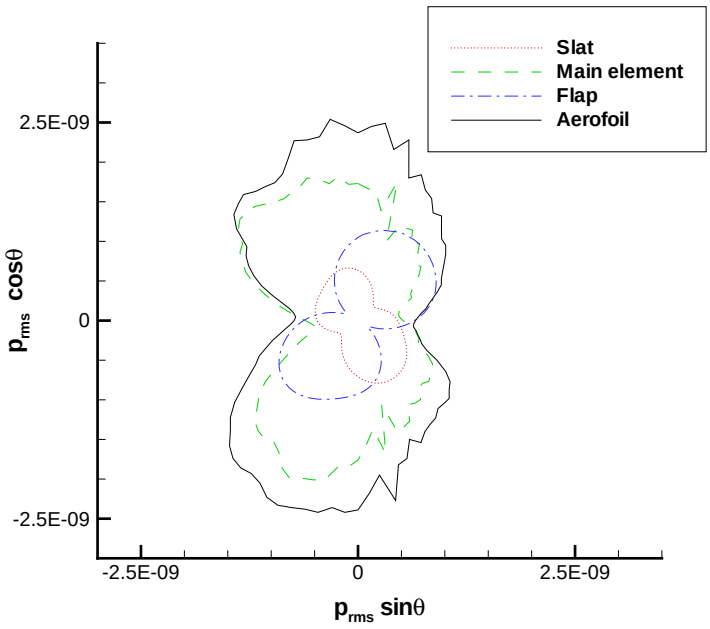

Figure 4.51: Far-field directivity plot with full rate blowing. M=0.2, b=270LPM, flow left to right.

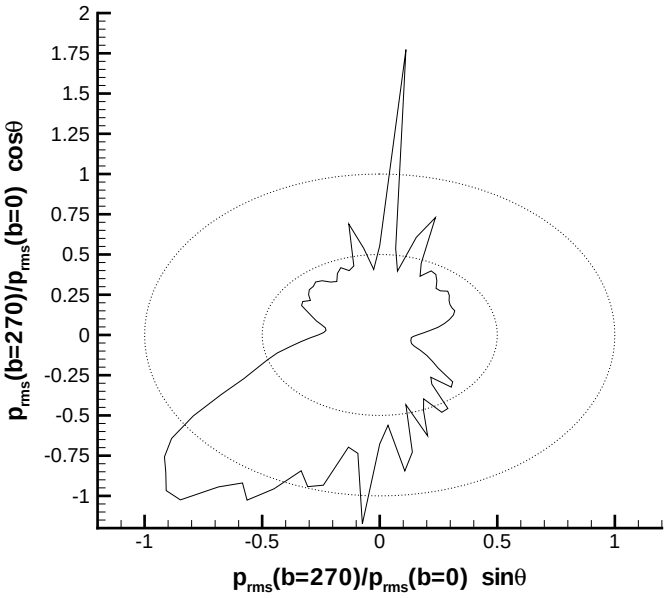

Figure 4.52: Relative far-field directivity plot showing the ratio of p_{RMS} with blowing relative to the no-blowing case. M=0.2, b=0,270LPM, flow left to right.

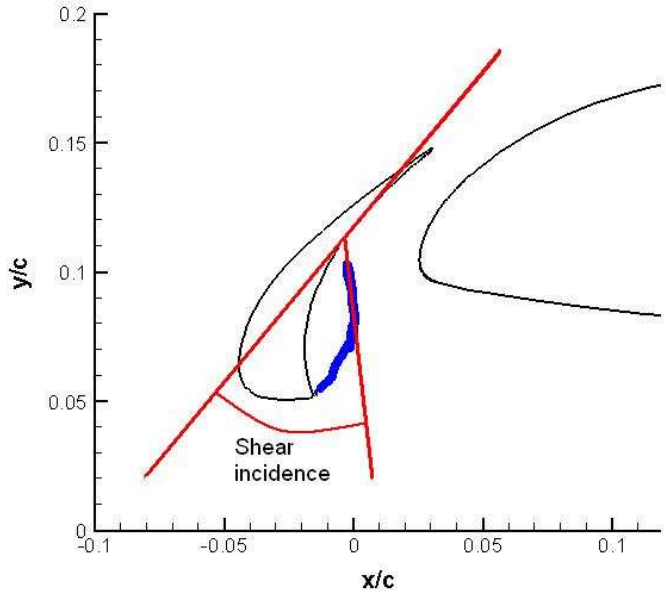

Figure 4.53: Definition of the shear angle.

α	α_S	Transition	Shear angle	S3 SPL	S6 SPL
5°	23°	free	70°	108 dB	101 dB
10°	23°	free	56°	106 dB	96 dB
15°	23°	free	51°	100 dB	88 dB
20°	23°	free	36°	100 dB	85.5 dB
5°	13°	free	64°	106 dB	99 dB
10°	13°	free	46°	96 dB	87.5 dB
15°	13°	free	49°	97 dB	86 dB
20°	13°	free	38°	96 dB	83 dB
5°	23°	fixed	70°	110 dB	108 dB
10°	23°	fixed	54°	103 dB	94 dB
15°	23°	fixed	45°	100 dB	88 dB
20°	23°	fixed	43°	100 dB	86 dB
5°	13°	fixed	57°	106 dB	98 dB
10°	13°	fixed	50°	95 dB	86 dB
15°	13°	fixed	36°	96 dB	85 dB
20°	13°	fixed	36°	96 dB	84 dB

Table 4.3: Shear angle and surface microphone SPL levels at 200 Hz.

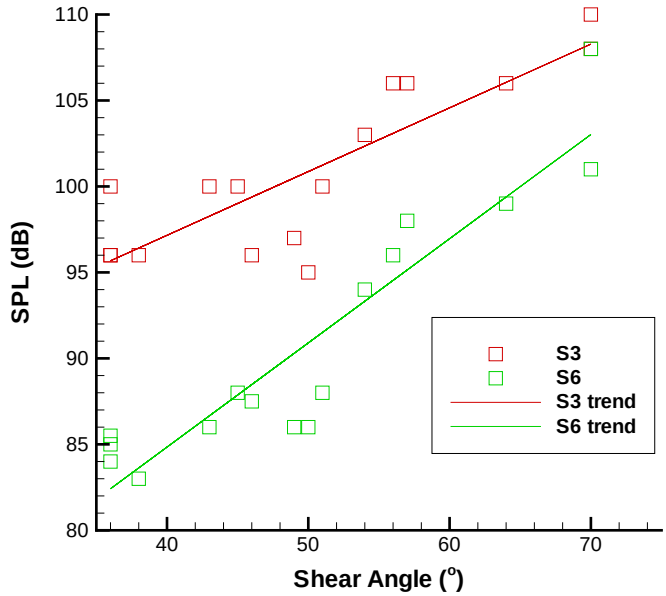

Figure 4.54: Surface SPL value at 200 Hz dependence on the shear angle.

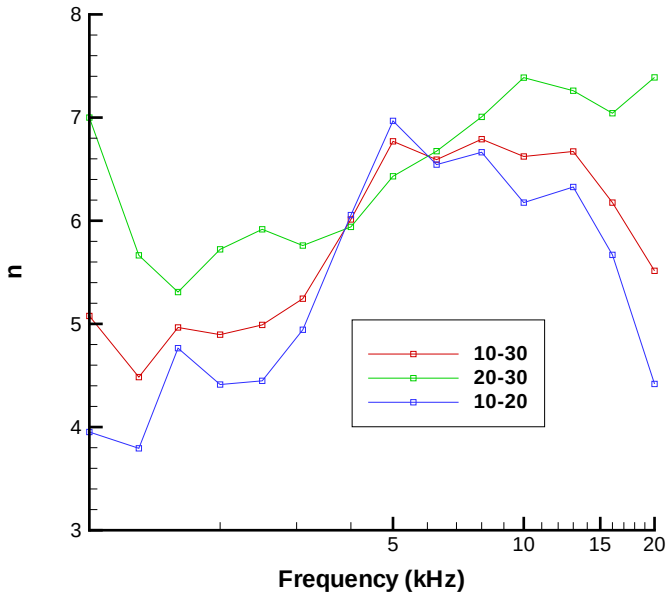

Figure 4.55: Velocity scale factor based on array data taken at 10, 20, 30 m/s.

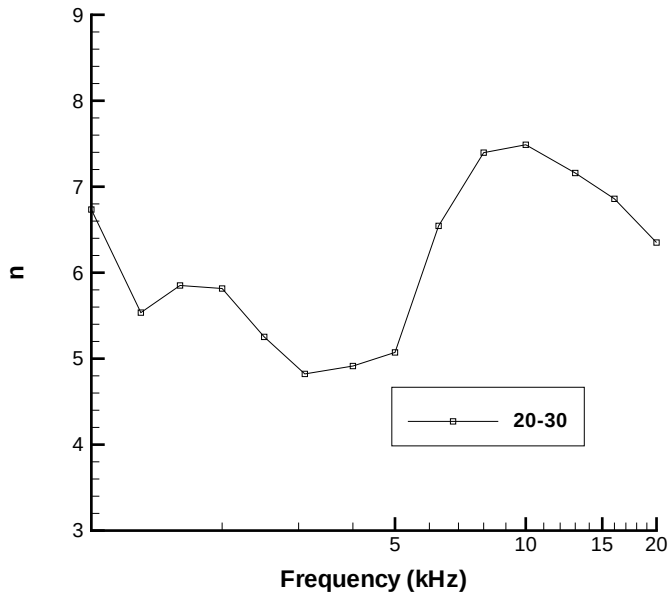

Figure 4.56: Velocity scale factor based on array data taken at 20 m/s and at 30 m/s with α=5°.

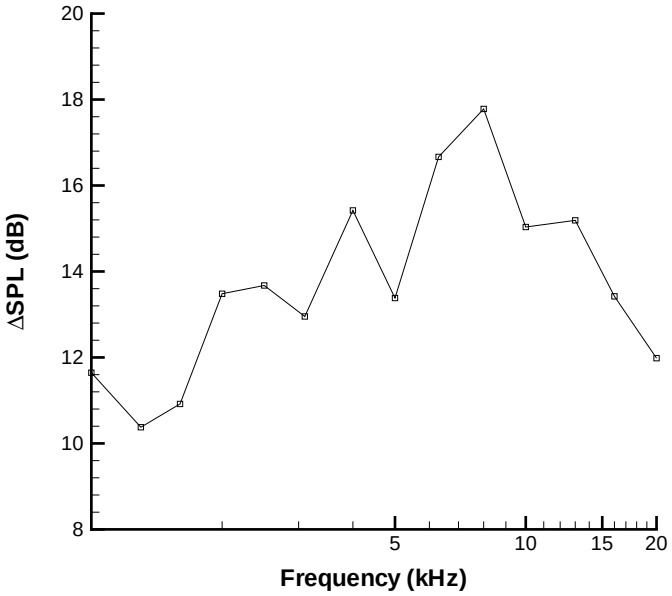

Figure 4.57: Change in SPL at reference condition between array data taken at 20 m/s and at 30 m/s.

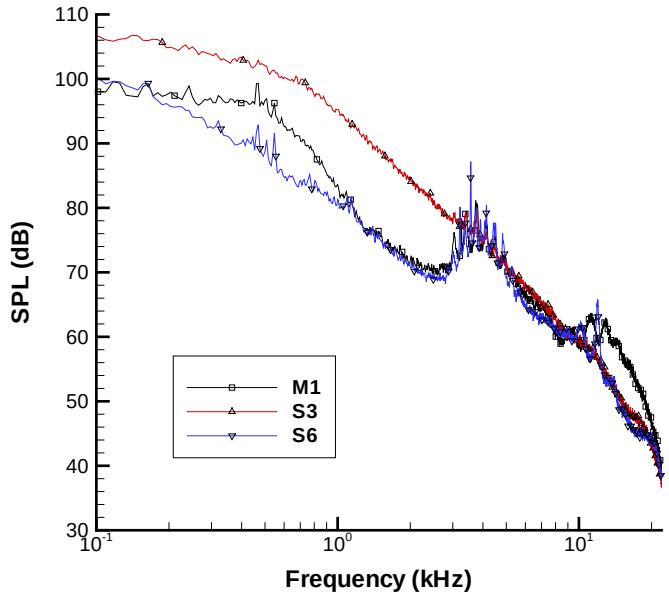

Figure 4.58: Surface microphone SPL spectra with α_S=18° and α=20°, v=30 m/s.

Chapter 5

Conclusion and future work

5.1 Introduction

The chapter provides a summary of the main findings of this study. The results demonstrate the impact of the various slat configurations investigated on the aerodynamics and aeroacoustics of the flow around a high-lift aerofoil.

5.2 Conclusion

This study has examined the impact of aerofoil incidence, slat angle, slat cusp geometry and blowing for a representative aerofoil design to map its aerodynamic and acoustic characteristics. This included the use of blowing at the reattachment point, which is a new area of study. The range of data also complemented earlier work and showed how the broadband SPL level and different tonal features changed depending on the configuration. This led to the link between the shear angle and the broadband sound level which was a new finding.

This is a summary of the main findings:

Broadband noise

The broadband noise generated by the slat system was loudest at the reference settings and reduced at higher aerofoil incidences. It was lowest at zero incidence because at this condition there is no significant flow through the slat cove region. Examining the PIV data showed that the angle at which the shear layer reattached to the slat was a key factor in the sound generated, with a reduction in the shear angle leading to reduction in the broadband noise.

Narrowband features

Three tones associated with the slat system have been identified:

1. A low frequency feature, which produced aerodynamic surface pressure tones over the range 3-5 kHz, located at the reattachment point. This tone occurred at α=15° with α_S=13°. The tone was related to the shear layer originating at the slat cusp so fixing transition removed the tone. The appearance of the tone is dependent on the angle between the slat and free-stream flow. This tone propagates to the far-field and corresponds to a large increase acoustic array SPL in the appropriate 1/3 octave band at α=15° with α_S=13°.

2. A mid frequency tone at 13 kHz, generated in the slat gap. This tone occurred at α=20° with the reference slat settings. Fixing transition to reduce the disturbances entering the gap reduced the magnitude of the tone. This tone also generated a narrowband hump that increases in magnitude with aerofoil incidence. This tone also propagates to the acoustic array and corresponds to an increase in the 1/3 octave band at 13kHz at α=15° and 20°.

3. A high frequency tone at 22 kHz, generated by the blunt trailing edge of the slat. This tone occurred at α=15° with the reference slat settings. This aerodynamic surface pressure tone was not detected by the acoustic array.

Baseline condition

For the baseline configuration, the sound generated was broadband in nature. Both the microphone array and surface microphones showed that the overall SPL level at this configuration was high. The PIV data at this configuration showed a recirculation zone that filled the majority of the slat cove region. The large recirculation region led to a high shear incidence angle and high broadband noise levels.

Dependence on the aerofoil incidence

The incidence of the aerofoil had the largest impact on determining the angle at which the flow separates from the cusp, the shear angle and broadband noise level. The incidence also controlled the lift generated by the aerofoil for a given configuration so its use in controlling sound is limited by aircraft operational requirements on approach.

Dependence on the slat angle

The aircraft operational requirements on approach dictate the aerofoil incidence range, but the slat angle had less influence on the lift generated. At the low aerofoil incidence of α=0°, the slat was of little use, so the slat would best be retracted in this incidence. Reducing the slat angle reduced the size of the recirculation zone and the shear angle, giving a reduction in broadband noise. This also increased the lift generated. At high aerofoil incidence, the slat is used to maintain attached flow over the wing suction side and broadband noise reduced at increasing aerofoil incidence.

Dependence on cusp geometry

The cusp extension tested provided a reduction in the broadband levels at low aerofoil incidence. However, for $\alpha \geq$10° there was an increase in the broadband sound generated and a reduction in lift. The usefulness of the cusp extension was limited to when the flow past the cusp aligned with the extension. Allowing a greater range of condition to use the extension requires adjustable extensions, which can flex so the wall at the cusp matches the natural direction of the shear layer in that condition, but this would require further study. At low speeds in the wind tunnel the cusp acted as an add-on device, but at full scale, the cusp geometry would be built into the structure of the slat.

Impact of blowing

Blowing was not effective in reducing the broadband sound generated by the slat system. Blowing had a limited impact on the narrowband aerodynamic surface pressure but was not as effective as fixing transition and had little impact on the forces generated in most conditions. Blowing also acted as a source of additional high frequency noise especially where there were high-speed jets formed such as where the flow enters the plenum chambers.

Impact of flow transition

Fixing transition had little influence on the lift, flow patterns or broadband sound generated by the slat. However, fixing transition did remove or reduce tonal and narrowband features. It was possible to remove the low frequency tone completely because it develops from the shear layer, but, with the gap tone, only a reduction in amplitude was possible. Little change was possible with the trailing edge tone. Full-scale aircraft feature transition to turbulent flow ahead of the slat, so the tones removed by fixing transition are less important in a full scale application.

5.3 Future work

In order to create a quiet slat system, the main task is to reduce the broadband sound generated. For real world applications, the noise level must be reduced over a range of lift settings. This study indicated the best way of controlling the broadband sound was to reduce the shear angle. The next step is to examine methods of controlling the shear angle. Altering the geometry on the inside of the slat wall, adjusting the slat settings or employing a form of flow control could achieve this aim. However, this study shows the slat settings had a larger impact on the sound generated and were much easier to adjust than any active flow control method. In particular, using a high aerofoil incidence where ever possible and having an appropriate slat angle for the conditions appears to be the way forward. These passive means also have the advantage of not requiring an additional power supply or generating additional noise.

Bibliography

[1] "Computational Aeroacoustic Research Initiative on Airframe Noise," *European Fifth Framework Programme*, March 2000.

[2] L. C. Chow, "Reduction of Airframe and Installation Noise," Tech. Rep., European Community, Brite-Euram IV programme, 2001.

[3] D. P. Lockard and G. M. Lilley, "The Airframe Noise Reduction Challenge," *AIAA Paper 2004-213013*, 2004.

[4] S. R. Maddah and H. H. Bruun, "An Investigation of Flow Fields Over Multi-Element Aerofoils," *Transactions of the ASME*, Vol. **124**, March 2002, pp. 154–165.

[5] N. Alemdaroglu, "Experimental Investigation of Flow Around a Multielement Airfoil," *AGARD CP-515*, 1993.

[6] I. R. M. Moir, "An Experimental Investigation of the Optimum Slat Setting on a Combat Aircraft Model," *AGARD CP-515*, 1993.

[7] F. O. Thomas, R. C. Nelson and X. Liu, "Experimental Investigation of the Confluent Boundary Layer of a High Lift System," *AIAA Journal*, Vol. **38**, No. 6, June 2000, pp. 978–988.

[8] F. W. Spaid, "High Reynolds Number, Multielement Airfoil Flowfield Measurements," *Journal of Aircraft*, Vol. **37**, No. 3, May-June 2000, pp. 499–507.

[9] M. Pott-Pollenske, J. Alvarez-Gonzalez and W. Dobryzynski, "Effect of Slat Gap on Farfield Radiated Noise and Correlation with Local Flow Characteristics," *AIAA Paper 2003-3228*, 2003.

[10] W. O. Valarezo, C. J. Dominik and R. J. McGhee, "Multielement Airfoil Performance Due to Reynolds and Mach Number Variations," *Journal of Aircraft*, Vol. **30**, No. 5, September-October 1993, pp. 689–694.

[11] B. C. Hardy, "An Experimental Investigation of Attachment-Line Transition of the Slat of a Combat Aircraft Model," *AGARD CP-515*, 1993.

[12] A. Séraudie, J. Perraud and F. Moens, "Transition Measurement and Analysis on a Swept Wing in High Lift Configuration," *Aerospace Sciences and Technology*, Vol. **7**, 2003, pp. 569–576.

[13] J. C. Lin and C. J. Dominik, "Parametric Investigation of a High-Lift Airfoil at High Reynolds Numbers," *Journal of Aircraft*, Vol. **34**, No. 4, July-August 1997, pp. 485–491.

[14] D. Landman and C. P. Britcher, "Experimental Investigation of Multielement Airfoil Lift Hysteresis due to Flap Rigging," *Journal of Aircraft*, Vol. **38**, No. 4, July-August 2001, pp. 703–708.

[15] A. Gopalarathnam and M. S. Selig, "Multipoint Inverse Method for Multielement Airfoil Design," *Journal of Aircraft*, Vol. **35**, No. 3, May-June 1998, pp. 398–404.

[16] K. Jacob, "A Fast Computing Method for the Flow Over High-Lift Wings," *AGARD CP-515*, 1993.

[17] K. de Cock, "High-Lift System Analysis Method Using Unstructured Meshes," *AGARD CP-515*, 1993.

[18] L. J. Johnston and L. Stolcis, "Prediction of the High-Lift Performance of Multi-Element Aerofoils Using an Unstructured Navier-Stokes Solver," *AGARD CP-515*, 1993.

[19] W. K. Anderson, D. L. Bonhaus, R. J. McGhee and B. S. Walker, "Navier-Stokes Computations and Experimental Comparisons for Multielement Airfoil Configurations," *Journal of Aircraft*, Vol. **32**, No. 6, November-December 1995, pp. 1246–1253.

[20] W. O. Valarezo and D. J. Mavriplis, "Navier-Stokes Applications to High-Lift Airfoil Analysis," *Journal of Aircraft*, Vol. **32**, No. 3, May-June 1995, pp. 618–624.

[21] A. Moitra, "Automated CFD Analysis of Two-Dimensional High-Lift Flows," *Journal of Aircraft*, Vol. **39**, No. 4, 2002, pp. 662–667.

[22] S. E. Rogers, N. L. Wiltberger and D. Kwak, "Efficient Simulation of Incompressible Viscous Flow over Multi-Element Airfoils," *AGARD CP-515*, 1993.

[23] T. E. Nelson, D. W. Zingg and G. W. Johnson, "Compressible Navier-Stokes Computations of Multielement Airfoil Flows Using Multiblock Grids," *AIAA Journal*, Vol. **32**, No. 3, March 1994, pp. 506–511.

[24] T. E. Nelson, D. W. Zingg and G. W. Johnson, "Numerical Solution of the Navier-Stokes Equations for High-Lift Configurations on Structured Composite Grids," *AGARD CP-515*, 1993.

[25] M. E. M. Stewart, "Domain Decomposition Algorithm Applied to Multielement Airfoil Grids," *AIAA Journal;*, Vol. **30**, No. 6, June 1992, pp. 1457–1461.

[26] S. Kim, J. J. Alonso and A. Jameson, "Design Optimization of High-Lift Configurations using a Viscous Adjoint-Based Method," *AIAA Paper 2002-0844*, January 2002.

[27] M. Nemec, D. W. Zingg and T. H. Pulliam, "Multipoint and Multi-Objective Aerodynamic Shape Optimization," *AIAA Journal*, Vol. **42**, No. 6, June 2004, pp. 1057–1065.

[28] C. L. Rumsey, E. M. Lee-Rausch and R. D. Watson, "Three-Dimensional Effects in Multi-Element High Lift Computations," *Computers and fluids*, Vol. **32**, 2003, pp. 631–657.

[29] M. R. Khorrami, M. E. Berkman, F. Li and B. A. Singer, "Computational Simulations of a Three-Dimensional High-Lift Wing," *AIAA Paper 2002-2804*, 2002.

[30] C. L. Rumsey and T. B. Gatski, "Recent Turbulence Model Advances Applied to Multielement Airfoil Computations," *Journal of Aircraft*, Vol. **38**, No. 5, September-October 2001, pp. 904–910.

[31] T. B. Gatski and C. G. Speziale, "On Explicit Algebraic Stress Models for Complex Turbulent Flows," *Journal of Fluid Mechanics*, Vol. **254**, 1993, pp. 59–78.

[32] P. R. Spallart and S. R. Allmaras, "A One Equation Turbulence Model for Aerodynamic Flows," *Le Recherche Aerospatiale*, Vol. **1**, 1994, pp. 5–21.

[33] P. Godin, D. W. Zingg and T. E. Nelson, "High-Lift Aerodynamic Computations with One- and Two-Equation Turbulence Models," *AIAA Journal*, Vol. **35**, No. 2, February 1997, pp. 237–243.

[34] P. Catalano and M. Amato, "An Evaluation of RANS Turbulence Modelling for Aerodynamic Applications," *Aerospace Science and Technology*, Vol. **7**, 2003, pp. 493–509.

[35] M. Breuer, N. Jovičić and K. Mazaev, "Comparison of DES, RANS and LES for the Separated Flow Around a Flat Plate at High Incidence," *International Journal for Numerical Methods in Fluids*, Vol. **41**, 2003, pp. 357–388.

[36] I. Mary and P. Sagaut, "Large Eddy Simulation of Flow Around an Airfoil Near Stall," *AIAA Journal*, Vol. **40**, No. 6, June 2002, pp. 1139–1145.

[37] J. U. Schlüter, S. Shankaran, S. Kim, H. Pitsch, J. J. Alonso and P. Moin, "Integration of RANS and LES Flow Solvers for Simultaneous Flow Computations," *AIAA Paper 2003-85*, 2003.

[38] C. P. van Dam, S. M. Los, S. J. Miley, V. E. Roback, L. P. Yip, A. Bertelrud and P. M. H. W. Vijgen, "In-Flight Boundary-Layer State Measurements on a High-Lift System: Slat," *Journal of Aircraft*, Vol. **34**, No. 6, November-December 1997, pp. 748–756.

[39] L. P. Yip, P. M. H. W. Vijgen, J. D. Hardin and C. P. van Dam, "In-Flight Pressure Measurements on a Subsonic Transport High-Lift Wing Section," *Journal of Aircraft*, Vol. **32**, No. 3, May-June 1995, pp. 529–538.

[40] N. J. Burnside, S. M. Jaeger, B. R. Reinero, W. C. Horne and P. T. Soderman, "Array Design and Performance For a Large Scale Airframe Noise Study," *AIAA Paper 2002-2576*, 2002.

[41] W. Dobrzynski, B. Gehlhar and H. Buchholz, "Model and Full Scale High-Lift Wing Wind Tunnel Experiments Dedicated to Airframe Noise Reduction," *Aerospace Science Technology*, Vol. **5**, 2001, pp. 27–33.

[42] T. Ito, Y. Yakokawa, H. Ura, H. Kato, K. Mitsuo and K. Yamamoto, "High-Lift Device Testing in JAXA 6.5 m x 5.5 m Low-Speed Wind Tunnel," *AIAA Paper 2006-3643*, 2006.

[43] S. Olson, F. O. Thomas and R. C. Nelson, "A Preliminary Investigation into Slat Noise Production Mechanisms in a High-Lift Configuration," *AIAA Paper 2000-4508*, 2000.

[44] B. L. Storms, J. A. Hayes, J. C. Ross and P. J. Moriarty, "Aeroacoustic Measurements of Slat Noise on a Three-Dimensional High-Lift System," *AIAA Paper 99-1957*, 1999.

[45] J. Wild, M. Pon-Pollenski and B. Nagel, "An Integrated Approach for Low Noise Exposing High-Lift Devices," *AIAA Paper 2006-2843*, 2006.

[46] W. Dobrzynski, K. Nagakura, B. Gehlhar and A. Buschbaum, "Airframe Noise Studies on Wings with Deployed High-Lift Devices," *AIAA Paper 98-2337*, 1998.

[47] C. Andreou, W. Graham and H. C. Shin, "Aeroacoustic Study of Airfoil Leading Edge High-Lift Devices," *AIAA Paper 2006-2515*, 2006.

[48] Y. P. Guo and M. C. Joshi, "Noise Characteristics of Aircraft High Lift Systems," *AIAA Journal*, Vol. **41**, No. 7, July 2003, pp. 1247–1256.

[49] J. A. Hayes, W. C. Horne, P. T. Soderman and P.H. Bent, "Airframe Noise Characteristics of a 4.7% Scale DC-10 Model," *AIAA Paper 97-1594*, 1997.

[50] S. Perennes and M. Roger, "Aerodynamic Noise of a Two-Dimensional Wing with High-Lift Devices," *AIAA Paper 98-2338*, 1998.

[51] R. Davy and H. Remy, "Airframe Noise Characteristics of a 1/11 Scale Airbus Model," *AIAA Paper 98-2335*, 1998.

[52] R. Davy, F. Moens and H. Remy, "Aeroacoustic Behaviour of a 1/11 Scale Airbus Model in the Open Anechoic Wind Tunnel Cepra 19," *AIAA Paper 2002-2412*, 2002.

[53] K. Takeda, X. Zhang and P. A. Nelson, "Unsteady Aerodynamics and Aeroacoustics of a High-Lift Device Configuration," *AIAA Paper 2002-0570*, 2002.

[54] S. Oerlemans and P. Sijtsma, "Acoustic Array Measurements of a 1:10.6 Scaled Airbus A340 Model," *AIAA Paper 2004-2924*, 2004.

[55] D. Blacodon, "Spectral Analysis of Airframe Noise of an Aircraft Model A320/A321," *AIAA Paper 2005-2809*, 2005.

[56] S. Moreau, M. Roger and V. Jurdic, "Effect of Angle of Attack and Airfoil Shape on Turbulence-Interation Noise," *AIAA Paper 2005-2973*, 2005.

[57] K. Pashal, L. Jenkins and C. Yao, "Unsteady Slat-Wake Characteristics of a High-Lift Configuration," *AIAA Paper 2000-0139*, 2000.

[58] K. Kaepernick, L. Koop. and K. Ehrenfried, "Investigation of the Unsteady Flow Field Inside a Leading Edge Slat Cove," *AIAA Paper 2005-2813*, 2005.

[59] K. Takeda, G. B. Ashcoft, X. Zhang and P. A. Nelson, "Unsteady Aerodynamics of Slat Cove Flow in a High-Lift Device Configuration," *AIAA Paper 2001-0706*, 2001.

[60] L. N. Jenkins, M. R. Khorrami and M. Choudhari, "Characterization of Unsteady Flow Structures Near Leading Edge Slat:Part I PIV Measurements," *AIAA Paper 2004-2801*, 2004.

[61] A. Agarwal and P. J. Morris, "Investigation of the Physical Mechanisms of Tonal Sound Generation by Slats," *AIAA Paper 2002-2575*, 2002.

[62] C. K. W. Tam and N. Pastouchenko, "Gap Tones," *AIAA Journal*, Vol. **39**, No. 8, August 2001, pp. 1442–1448.

[63] M. R. Fink, "Noise Component Method for Airframe Noise," *Journal of Aircraft*, Vol. **16**, No. 10, October 1979, pp. 659–665.

[64] Y. P. Gou, K. J. Yamamoto and R. W. Stoker, "A Component Based Empirical Model for Airframe Noise Prediction," *AIAA Paper 2002-2574*, 2002.

[65] N. Molin, M. Roger and S. Barré, "Prediction of Aircraft High-Lift Device Noise using Dedicated Analytical Models," *AIAA Paper 2003-3225*, 2003.

[66] M. G. Smith and L. C. Chow, "Aerodynamic Noise Sources on High Lift Slats and Flaps," *AIAA Paper 2003-3226*, 2003.

[67] S. Hosder, J. A. Schetz, B. Grossman and W. H. Mason, "Airframe Noise Modeling Appropriate for Multidisciplinary Design and Optimization," *AIAA Paper 2004-0698*, 2004.

[68] M. Lummer, J. W. Delfs and T. Lauke, "Simulation of the Influence of Trailing Edge Shape on Airfoil Sound Generation," *AIAA Paper 2003-3109*, 2003.

[69] M. Lummer, J. W. Delfs and T. Lauke, "Simulation of Sound Generation by Vortices Passing the Trailing Edge of Airfoils," *AIAA Paper 2002-2578*, 2002.

[70] M. J. Lighthill, "On Sound Generated Aerodynamically: I. General Theory," *Proceedings of the Royal Society*, Vol. **A211**, 1952, pp. 564–587.

[71] M. J. Lighthill, "On Sound Generated Aerodynamically: II. Turbulence as a Source of Sound," *Proceedings of the Royal Society*, Vol. **A222**, 1954, pp. 1–32.

[72] J. E. Ffowcs Williams and D. L. Hawkings, "Sound Generation by Turbulence and Surfaces in Arbitrary Motion," *Philosophical Transactions of the Royal Society*, Vol. **A264**, May 1969, pp. 321–342.

[73] K. S. Brentner and F. Farassat, "Analytical Comparison of the Acoustic Analogy and Kirchhoff Formulation for Moving Surfaces," *AIAA Journal*, Vol. **36**, No. 8, 1998, pp. 1379–1386.

[74] F. Farassat and M. K. Myers, "Extension of Kirchhoff's Formula to Radiation from Moving Surfaces," *Journal of Sound and Vibration*, Vol. **123**, No. 3, March 1988, pp. 451–460.

[75] K. Takeda, X. Zhang and P. A. Nelson, "Linearized Euler Simulations of Leading-Edge Slat Flow," *AIAA Paper 2003-0364*, 2003.

[76] K. Takeda, X. Zhang and P. A. Nelson, "Computational Aeroacoustic Simulation of Leading-Edge Slat Flow," *Journal of sound and vibration*, Vol. **270**, 2004, pp. 559–572.

[77] E. Manoha, C. Herrero, P. Sagaut and S. Redonnet, "Numerical Prediction of Airfoil Aerodynamic Noise," *AIAA Paper 2002-2573*, 2002.

[78] M. Terracol, E. Labourasse, E. Manoha and P. Sagaut, "Simulation of the 3D Unsteady Flow in a Slat Cove for Noise Prediction," *AIAA Paper 2003-3110*, 2003.

[79] E. Manoha, S. Redonnet, M. Terracol and R. Guenanff, "Numerical Simulation of Aerodynamic Noise," *European Congress on Computational Methods in Applied Sciences and Engineering*, 2004.

[80] M. G. Macaraeg, "Fundamental Investigation of Airframe Noise," *AIAA Paper 98-2224*, 1998.

[81] M. E. Berkman, M. R. Khorrami, M. Choudhari and S. S. Sadowski, "Investigation of High-Lift Flowfield of an Energy Efficient Transport Wing," *Journal of Aircraft*, Vol. **37**, No. 1, January-February 2000, pp. 45–52.

[82] M. R. Khorrami, M. E. Berkman and M. Choudhari, "Unsteady Flow Computation of a Slat with a Blunt Trailing Edge," *AIAA Journal*, Vol. **38**, No. 11, November 2000, pp. 2050–2058.

[83] B. A. Singer, D. P. Lockard, K. S. Brentner, M. R. Khorrami, M. E. Berkman and M. Choudhari, "Computational Aeroacoustic Analysis of Slat Trailing-Edge Flow," *AIAA Paper 99-1802*, 1999.

[84] B. A. Singer, D. P. Lockard and K. S. Brentner, "Computational Aeroacoustic Analysis of Slat Trailing-Edge Flow," *AIAA Journal*, Vol. **38**, No. 9, September 2000, pp. 1558–1564.

[85] M. R. Khorrami, B. A. Singer and M. E. Berkman, "Time-Accurate Simulations and Acoustic Analysis of Slat Free-Shear Layer," *AIAA Paper 2001-2155*, 2001.

[86] M. Khorrami, B. Singer and D. Lockard, "Time-Accurate Simulations and Acoustic Analysis of Slat Free-Shear-Layer: Part II," *AIAA Paper 2002-2579*, 2002.

[87] M. R. Khorrami, B. A. Singer and M. E. Berkman, "Time-Accurate Simulations and Acoustic Analysis of Slat Free Shear Layer," *AIAA Journal*, Vol. **40**, No. 7, July 2002, pp. 1284–1291.

[88] M. R. Khorrami and M. M. Choudhari and L. N. Jenkins, "Characterization of Unsteady Flow Structures Near Leading-Edge Slat: Part II 2D Computations," *AIAA Paper 2004-2802*, 2004.

[89] M. R. Khorrami, M. Choudhari, B. A. Singer, D. P. Lockard and C. L. Streett, "In Search of the Physics: The Interplay of Experiment and Computation in Slat Aeroacoustics," *AIAA Paper 2003-0980*, 2003.

[90] R. Emunds and M. Fischer, "Effect of Slat Settings (Gap and Overlap) on Slat Noise Based on a Test Vortex Injected Upstream of the Slat-Hook," *AIAA Paper 2006-2665*, 2006.

[91] R. Ewert, "Slat Noise Trend Predctions using CAA with Stochastic Sound Sources from a Random Particle Mesh Method (RPM)," *AIAA Paper 2006-2667*, 2006.

[92] M. M. Choushari and M. R. Khorrami, "Slat Cove Unsteadiness: Effect of 3D Flow Structures," *AIAA Paper 2006-211*, 2006.

[93] T. Imamura, S. Enomoto and K. Yamamoto, "3D Unsteady Flow Computations in a Slat Cove Using Large Eddy Simulation," *AIAA Paper 2006-2668*, 2006.

[94] P. Sagaut, E. Manoha, C. Herrero, M. Terracol and E. Labourrasse, "Numerical Simulation of Acoustic Sources and Noise Propagation on 2D Wings," *Proceedings of the 3rd SWING Aeroacoustics workshop*, September 2002.

[95] J. H. Casper, D. P. Lockard, M. R. Khorrami and C. L. Streett, "Investigation of Volumetric Sources in Airframe Noise Simulations," *AIAA Paper 2004-2805*, 2004.

[96] D. P. Lockard and P. J. Morris, "Radiated Noise from Airfoils in Realistic Mean Flows," *AIAA Journal*, Vol. **36**, No. 6, June 1998, pp. 907–914.

[97] S. Nagarajan and S. K. Lele, "Sound Generation by Unsteady Airfoil Motions: A Study Using Direct Computation & Acoustic Analogy," *AIAA Paper 2005-2915*, 2005.

[98] J. Wang, H. Yao, E. Benard, R. Cooper, S. Raghunathan, J. Tweedie and D. Riordan, "Identification of Aircraft Noise at Landing - an Approach to Integrate Noise Control Technologies into Aircraft Design," *AIAA Paper 2005-2811*, 2005.

[99] J. F. Piet, U. Michel and P. Böhning, "Localization of the Acoustic Sources of the A340 with a Large Phased Microphone Array During Flight Tests," *AIAA Paper 2002-2506*, 2002.

[100] R. W. Stoker, Y. Guo, C. Streett and N. Burnside, "Airframe Noise Source Locations of a 777 Aircraft in Flight and Comparisons with Past Model Scale Tests," *AIAA Paper 2003-3232*, 2003.

[101] W. Qiao and U. Michel, "A Study on the Vortex Shedding Noise from the Wake of Aircraft Wings," *AIAA Paper 2000-1973*, 2000.

[102] J. D. Johnson and D. E. Dudgeon, "Array Signal Processing - Concepts and Techniques," *Prentice-Hall*, 1993.

[103] P. Sijtsma and R. W. Stoker, "Determination of Absolute Contributions of Aircraft Noise Components using Fly-Over Array Measurements," *AIAA Paper 2004-2958*, 2004.

[104] G. M. Lilley, "A Quest for Quiet Commercial Passenger Transport Aircraft for Take-Off and Landing," *AIAA Paper 2004-2922*, 2004.

[105] D. Reckzeh, "Aerodynamic Design of the High-Lift-Wing for a Megaliner Aircraft," *Aerospace Science and Technology*, Vol. **7**, 2003, pp. 107–119.

[106] B. L. Storms, J. A. Hayes, S. M. Jaeger and P. T. Soderman, "Aeroacoustic Study of Flap-Tip Noise Reduction using Continuous Moldline Technology," *AIAA Paper 2000-1976*, 2000.

[107] C. L. Streett, J. H. Casper, D. P. Lockard, M. R. Khorrami, R. W. Stoker, R. Elkoby, W. F. Wenneman and J. R. Underbrink, "Aerodynamic Noise Reduction for High-Lift Devices on a Swept Wing Model," *AIAA Paper 2006-212*, 2006.

[108] M. R. Khorrami and D. P. Lockard, "Effects of Geometric Detail on Slat Noise Generation and Propagation," *AIAA Paper 2006-2664*, 2006.

[109] S. R. Maddah, T. Gough, B. Pierscionek and H. H. Bruun, "Investigation of Slat Heel Effect on the Flow Field Over Multi-Element Aerofoils," *Experimental Thermal and Fluid Science*, Vol. **25**, 2002, pp. 651–658.

[110] W. C. Horne, K. D. James, N. Burnside and S. M. Jaeger, "Measurements of 26% Scale 777 Airframe Noise in the NASA Ames 40 by 80 Foot Wind Tunnel," *AIAA Paper 2005-2810*, 2005.

[111] M. G. Smith, Leung Choi Chow and N. Molin, "Attenuation of Slat Trailing Edge Noise using Slat Gap Acoustic Liners," *AIAA Paper 2006-2666*, 2006.

[112] Z. Ma, M. Smith, S. K. Richards and X. Zhang, "Slat Noise Attenuation Using Acoustic Liner," *AIAA Paper 2005-3009*, 2005.

[113] M. Herr and W. Dobrzynski, "Experimental Investigations in Low Noise Trailing Edge Design," *AIAA Paper 2004-2804*, 2004.

[114] P. T. Soderman, F. Kafyeke, N. J. Burnside, R. Chandrasekharan, S. M. Jaeger and J. Boudreau, "Airframe Noise Study of a CRJ-700 Aircraft Model in the NASA Ames 7 by 10 Foot Wind Tunnel No.1," *AIAA Paper 2002-2406*, 2002.

[115] M. M. Choudhari, D. P. Lockard, M. G. Macaraeg, B. A. Singer, C. L. Streett, G. R. Neubert, R. W. Stoker, J. R. Underbrink, M. E. Berkman, M. R. Khorrami and S. S. Sadowski, "Aeroacoustic Experiments in the Langley Low-Turbulence Pressure Tunnel," *NASA /TM-2002-211432*, February 2002.

[116] J. Ortmann and J. Wild, "Effect of Acoustic Slat Modifications on Aerodynamic Properties of High-Lift Systems," *AIAA Paper 2006-3842*, 2006.

[117] M. R. Khorrami and M. M. Choudhari, "Application of Passive Porous Treatment to Slat Trailing Edge Noise," *NASA/TM-2003-212416*, 2003.

[118] D. Angland, X. Zhang, L. C. Chow and N. Molin, "Measurements of Flow around a Flap Side-Edge with Porous Edge Treatment," *AIAA Paper 2006-213*, 2006.

[119] J. C. Lin, S. K. Robinson, R. J. McGhee and W. O. Valarezo, "Separation Control on High-Lift Airfoils via Micro-Vortex Generators," *Journal of Aircraft*, Vol. **31**, No. 6, November-December 1994, pp. 1317–1323.

[120] R. H. Thomas, M. M. Choudhari and R. D. Joslin, "Flow and Noise Control: Review and Assessment of Future Directions," *NASA TM-2002-211631*, 2002.

[121] R. H. Thomas, M. M. Choudhari and R. D. Joslin, "Flow and Noise Control: Towards a Closer Linkage," *ICAS 2002 Congress*, 2002.

[122] F. Innes, H. H. Pearcy and D. M. Sykes, "Improvements in the Performance of a Three Element High Lift System by the Application of Airjet Vortex Generators," *Aeronautical Journal*, August-September 1995, pp. 265–274.

[123] S. S. Ravindran, "Active Control of Flow Separation Over an Airfoil," *NASA TM-1999-209838*, 1999.

[124] L. G. Pack, N. W. Schaeffler and C. S. Yao, "Active Control of Separation from the Slat Shoulder of a Supercritical Airfoil," *AIAA Paper 2002-3156*, 2002.

[125] J. Kiedaish, H. Nagib and B. Demanett, "Active Flow Control Applied to High-Lift Airfoils Utilizing Simple Flaps," *AIAA Paper 2006-2856*, 2006.

[126] R. H. Cabell, M. A. Kegerise, D. E. Cox and G. P. Gibbs, "Experimental Feedback Control of Flow Induced Cavity Tones," *AIAA Paper 2002-2497*, 2002.

[127] R. Petz and W. Nitshe, "Active Control of Flow Separation on a Swept Constant Chord Half Model in a High-Lift Configuration," *AIAA Paper 2006-3505*, 2006.

[128] S. Nakahsima and S. Akishita, "Numerical Analysis on Self-Excited Tone Noise Control in a Two-Dimensional Airfoil Wing," *AIAA Paper 98-2368*, 1998.

[129] N. J. Pern, J. D. Jacob and R. P. LeBeau, "Characterization of Zero Mass Flux Flow Control for Separation Control of an Adaptive Airfoil," *AIAA Paper 2006-3032*, 2006.

[130] S. Yarusevych, J. G. Kawall and P. E. Sullivan, "Effect of Acoustic Excitation on Airfoil Performance at Low Reynolds Numbers," *AIAA Journal*, Vol. **41**, No. 8, August 2003, pp. 1599–1601.

[131] G. M. Lilley, "Circulation Control for Quiet Commercial Aircraft," *AIAA Paper 2006-2842*, 2006.

[132] L. Shaw, "Active Control for Cavity Acoustics," *AIAA Paper 98-2347*, 1998.

[133] L. Shaw, "High Speed Application of Active Flow Control for Cavity Acoustics," *AIAA Paper 2000-1926*, 2000.

[134] P. Micheau, L. Chatellier, J. Laumonier and Y. Gervais, "Active Control of a Self-Sustaining Pressure Fluctuation due to Flow Over a Cavity," *AIAA Paper 2004-2851*, 2004.

[135] L. Huang, P. G. Huang, R. P. LeBeau and T. Hauser, "Numerical Study of Blowing and Suction Control Mechanism on NACA0012 Airfoil," *Journal of Aircraft*, Vol. **41**, No. 5, September-October 2004, pp. 1005–1013.

[136] J. E. Grove, R. M. Berkbeck and J. M. Kreher, "Acoustic and Separation Characteristics with Bay Leading Edge Blowing," *AIAA Paper 2000-1904*, 2000.

[137] E. A. Gillies, "Multipoint Sensor Control of Vortex Shedding," *AIAA Paper 2000-1933*, 2000.

[138] S. Chan, X. Zhang and S. Gabriel, "The Attenuation of Cavity Tones using Plasma Actuators," *AIAA Paper 2005-2802*, 2005.

[139] L. Koop, K. Ehrenfried and A. Dillmann, "Reduction of Flap Side Edge Noise by Active Flow Control," *AIAA Paper 2002-2469*, 2002.

[140] L. Koop, K. Ehrenfried and A. Dillmann, "Reduction of Flap Side-Edge Noise: Passive and Active Flow Control," *AIAA 2004-2803*, 2004.

[141] S. Zheng and M. Zhuang, "A New Conceptual Design For Active Noise Control With Controllable Impedance Liners," *AIAA Paper 2002-2518*, 2002.

[142] C. L. Chin, J. L. Lee and G. P. Mathur, "Analytical Modeling of Active/Passive Smart Foam Noise Control Treatment in Aerospace Vehicles," *AIAA Paper 2002-2414*, 2002.

[143] P. A. Nelson, "Active Techniques and their Potential for Application in Aeroacoustics," *AIAA Paper 2000-2100*, 2000.

[144] R. W. Gilbey, "Lift-Interference and Blockage Corrections for Two-Dimensional Subsonic Flow in Ventilated and Closed Wind Tunnels," Tech. Rep., ESDU 76028, November 1976.

[145] , "Tecplot User's Manual: Version 9.0," *Amtec Engineering, Inc*, 2001.

[146] J. Weiss, "The Dynamics of Enstophy Transfer in Two-Dimensional Hydrodynamics," *Physica D*, Vol. **48**, 1991, pp. 273–294.

[147] A. Okuba, "Horizontal Dispersion of Floatable Particles in the Vicinity of Velocity Sinularities such as Convergences," *Deep-Sea Research*, Vol. **17**, 1970, pp. 445–454.

[148] K. R. Holland and P. A. Nelson, "Sound Source Characterisation: The Focussed Beamformer vs The Inverse Method," *Tenth International Congress on Sound and Vibration*, July 2003.

[149] G. K. Batchelor, "An Introduction to Fluid Dynamics," *Cambridge University Press*, 1967.

[150] "Fluent 6.1 User's Guide," *Fluent Inc.*, 2003.

[151] B. van Leer, "Towards the Ultimate Conservative Difference Scheme. V. A Second-Order Sequel to Godunov's Method," *Journal of Computational Physics*, Vol. **32**, No. 1, July 1979, pp. 101–136.

[152] G. B. Ashcroft, "A computational and Experimental Investigation into the Aeroacoustics of Low Speed Flows," *PhD Thesis, University of Southampton*, September 2003.

[153] F. Farassat and G. P. Succi, "The Prediction of Helicopter Discrete Frequency Noise," *Vertica*, Vol. **7**, No. 4, 1983, pp. 309–320.

[154] X. Chen and X. Zhang, "High Sorage FW-H Solver," *Aerodynamics and Fligh Mechanics Research Group Internal Report*, November 2004.

[155] B. Greschner, F. Thiele, A. Gurr, D. Casalino and M. C. Jacob, "Prediction of Sound Generated by a Rod-Airfoil Configuration using a Cubic Explicit Algebraic Stress Model for Detached Eddy Simulation and the Generalised Lighthill/FW-H Analogy," *AIAA Paper 2006-2628*, 2006.

[156] J. D. Anderson Jr, *Fundamentals of Aerodynamics, Second Edition*, McGraw Hill, 1991.

Appendices

Appendix A

Tunnel corrections

The forces recorded contained two main additional components that distort the data.

1. Additional forces caused by the presence of the struts and endplates.
2. The model generating blockage in the tunnel resulting in a change in the freestream flow.

The compensation for the struts and endplates was achieved by removing tare values taken by running the tunnel with only the struts and endplates (Table A.1).

To compensate for the wind tunnel blockage the forces are adjusted using the method detailed in EDSU 76 028 [144]. The correction was largely determined by the blockage of the tunnel. The tunnel area was $8.17\,\mathrm{m}^3$ with the blockage aerofoil incidence dependant. The force corrections are given in Table A.2.

α	$\text{Lift}_{10\,m/s}$	$\text{Lift}_{20\,m/s}$	$\text{Lift}_{30\,m/s}$	$\text{Drag}_{10\,m/s}$	$\text{Drag}_{20\,m/s}$	$\text{Drag}_{30\,m/s}$
0°	2.2 N	3.2 N	7.4 N	19.4 N	73.2 N	159.0 N
5°	1.2 N	3.5 N	6.5 N	18.5 N	71.0 N	153.0 N
10°	2.2 N	5.6 N	7.4 N	18.4 N	70.2 N	150.4 N
15°	1.4 N	5.0 N	7.3 N	17.7 N	69.5 N	149.2 N
20°	1.9 N	5.7 N	6.4 N	17.7 N	69.7 N	147.8 N

Table A.1: Tare values.

α	Blockage Area	Relative blockage	Force Reduction
0°	$0.107\,\text{m}^3$	0.013	0.76 %
5°	$0.137\,\text{m}^3$	0.020	1.26 %
10°	$0.225\,\text{m}^3$	0.028	1.79 %
15°	$0.282\,\text{m}^3$	0.035	2.33 %
20°	$0.337\,\text{m}^3$	0.041	2.88 %

Table A.2: Force correction values.

Appendix B

Blowing rates

Measuring the flow rate entering the plenum chambers using a flow rate meter allowed adjustment of the blowing to 60, 80, 100 and 120LPM. To obtain the mass flow rate the pressure of the air passing through the meter is needed to calculate the air density. This used two pressure measurements, taken using a digital manometer. Firstly, the pressure of the air supplied to the flow meter was measured relative to the freestream by closing the valve in the flow meter. Secondly, the pressure drop across the flow meter was measured to obtain the pressure drop due to restricting the flow to give the desired flow rate. The pressure at the flow meter was the pressure of the air supplied less the drop caused by the pressure drop in the valve.

The C_P plots show that at the blowing location the value of $C_P \approx 0$ so the standard atmosphere pressure of 101,325 Pa can be used. Over the range of conditions, there are small changes in the local pressure but, due to the low velocity of 30 m/s, these changes will be relatively small and have little impact on the density. The air supply was at 373,500 Pa above the pressure in the test section giving an absolute value of 474,825 Pa. The pressure drop through the valve varied from 85,000 to 312,500 Pa allowing the air density to be obtained and the mass flow rates calculated as up to 9.43×10^{-3} kg/s (Table B.1).

After passing through the flow meter, the air entered the plenum chamber and exited into the slat cove. Upon reaching the cove, the air will have returned to close to atmospheric pressure and density allowing calculation of the jet velocity. The slat contained 400 1mm diameter holes giving an area of 3.142×10^{-4} m^2. This corresponds to a maximum jet velocity of 24.49 m/s (Table B.2).

These estimates contain inaccuracies because not all of the pressure drop is across the value increasing the pressure in the flow meter. In addition, the air passing through the blowholes will not reach atmospheric pressure at the exit reducing the mean jet velocity, although the centre of the jet will exceed the mean value.

b	p in	p drop	Measurement p	ρ	Mass flow
0 LPM	474,825 Pa	373,500 Pa	101,325 Pa	1.225 kg/m^3	0 kg/s
60 LPM	474,825 Pa	312,500 Pa	162,325 Pa	1.963 kg/m^3	1.96×10^{-3} kg/s
80 LPM	474,825 Pa	241,500 Pa	233,325 Pa	2.821 kg/m^3	3.76×10^{-3} kg/s
100 LPM	474,825 Pa	185,000 Pa	289,825 Pa	3.504 kg/m^3	5.84×10^{-3} kg/s
120 LPM	474,825 Pa	85,000 Pa	389,825 Pa	4.713 kg/m^3	9.43×10^{-3} kg/s

Table B.1: Blowing rates.

b	Mass flow in	Volume flow	Jet velocity
0 LPM	0 kg/s	0 m^3/s	0 m/s
60 LPM	1.96×10^{-3} kg/s	1.60×10^{-3} m^3/s	5.10 m/s
80 LPM	3.76×10^{-3} kg/s	3.07×10^{-3} m^3/s	9.77 m/s
100 LPM	5.84×10^{-3} kg/s	4.77×10^{-3} m^3/s	15.17 m/s
120 LPM	9.43×10^{-3} kg/s	7.69×10^{-3} m^3/s	24.49 m/s

Table B.2: Jet velocity.